In vivo analysis of junctional dynamics underlying angiogenic cell behaviors

Inauguraldissertation

zur

Erlangung der Würde eines Doktors der Philosophie

vorgelegt der

Philosophisch Naturwissenschaftlichen Fakultät

Der Universität Basel

von

Loïc Aurélien Sauteur

aus Saint Martin, Fribourg

Basel, 2016

Genehmigt von der Philosophisch Naturwissenschaftlichen Fakultät

auf Antrag von

Prof. Dr. Markus Affolter

Prof. Dr. Gerhard Christofori

Basel den, 24. März 2015

Prof. Dr. Jörg Schibler

Dekan

List of abbreviations

4xnr	4x non-repetitive
4xUAS	4 times non-repetitive UAS
A	adenine
aa	amino acid
AJ	adherens junction
Akt	Protein kinase B
AMIS	apical membrane initiation sites
Amp	ampicillin
Ang1	Angiopoietin-1
ARP2/3	Actin related protein 2/3
Bmp	Bone morphogenetic protein
bp	base pair
C	cytosine
Cam	chloramphenicol
CAR	Coxsackie and Adenovirus Receptor
Cas	CRISPR-associated
CCV	common cardinal vein
Cdh5	Cadherin 5 (vascular endothelial cadherin)
cDNA	complementary DNA
CoDA	context-dependent assembly
CRISPR	clustered regularly interspaced short palindromic repeats
crRNA	CRISPR RNA
CVP	caudal vein plexus
Cxcl	CXC-motif ligand
Cxcr	CXC-motif receptor
DA	dorsal aorta
DLAV	dorsal longitudinal anastomotic vessel
Dll4	Delta-like-4
DNA	deoxyribonucleic acid
dpf	days post-fertilization
DSBs	double strand breaks
dsDNA	double stranded DNA
e.g.	example given
EC	endothelial cell
ECM	extracellular matrix
EMCCD	electron multiplying charge coupled device
ESAM	Endothelial cell-selective adhesion molecule
F-actin	filamentous actin
Flt1	Fms-like tyrosine kinase 1
Fmnl3	Formin-like 3
FoxO1	Forkhead transcriptional repressor

FR	Folate receptor
FRAP	fluorescence recovery after photobleaching
FRET	fluorescence resonance energy transfer
G	guanine
G-actin	Globular actin
GAP	GTPase activating protein
GEF	guanine-nucleotide-exchange factor
gp	guinea pig
GPI	Glycosylphosphatidylinositol
gRNA	single-guide RNA
GSK	Glycogen synthase kinase
HIF1	Hypoxia inducible factor-1
hpf	hours post-fertilization
HR	homologous recombination
hr	hour
HyD	hybrid detector
Hz	hertz
i.e.	id est (that is)
ICAM-1	Intercellular adhesion molecule
ISV	intersegmental vessel
Jag1	Jagged 1
JAIL	junction-associated intermitted lamellipodia
JAM	Junction adhesion molecule
Kan	Kanamycin
kb	kilobase
KD	knock down
Kdrl	Kinase insert domain receptor-like
lat. B	latrunculin B
LMA	low melting agarose
MAGI1	Membrane-associated guanylate kinase
min	minute
MO	morpholino oligonucleotide
N	any DNA nucleotide
n/a	not available
NA	Numerical aperture
NEU	N-ethyl N-nitrosourea
NHEJ	non-homologous end joining
NICD	Notch intracellular domain
NPF	Nucleation-promoting factor
Nrarp	Notch-regulated ankyrin repeat protein
o/n	overnight
OD$_{600}$	Optical density at 600nm wavelength
PAM	Protospacer adjacent motif
Par	Partitioning defective
PCR	Polymerase Chain Reaction
PCV	posterior cardinal vein

Pdxl2	Podocalyxin-2
PFA	paraformaldehyde
PI3K	Phosphatidylinositol-4,5-bisphosphatase 3-kinase
PlGF	Placental growth factor
PMT	Photon Multiplying Tube
PTU	1-Phenyl-2-thiourea
r1	rabbit one
r2	rabbit two
RGNs	RNA-guided nucleases
RNA	Ribonucleic acid
rpm	rounds per minute
RT	room temperature
RVD	repeat variable diresidue
SA	segmental artery
sec	second
SH3	Src homology 3
SIV	subintestinal vessels
SNPs	single nucleotide polymorphisms
Spec	spectinomycin
Str	streptomycin
SV	segmental vein
SV40	Simian virus 40
sVEGFR1	soluble Vascular endothelial growth factor receptor 1
T	thymine
T3SS	type III secretion system
T7EI	T7 endonuclease I
TALEN	Transcription activator-like effector nuclease
Temp.	temperature
Tet	tetracycline
TF	transcription factor
TILLING	targeting induced local lesion in genomes
TJ	tight junction
tracrRNA	trans-activating crRNA
UAS	upstream activation sequence
UCHD	Utrophin calponin homology domain
UTR	untranslated region
VE-cad	Vascular endothelial cadherin (Cdh5)
VE-PTP	Vascular endothelial phosphatase
VEGFA	Vascular endothelial growth factor A
VEGFR	Vascular endothelial growth factor receptor tyrosine kinase
wt	wild-type
ZFN	Zinc finger nucleases
Zo-1	Zonula occludens 1

Abstract

The blood circulatory system delivers nutrients and oxygen to tissues and organs. Moreover, the circulatory system retains high plasticity throughout an organism's life, which is important for physiological processes, such as wound healing, but also during pathological processes, such as tumor growth.

Blood vessels can sprout from existing ones, a process called angiogenesis, to create a more branched network that reaches avascular and the most distal parts of an animal body. The morphogenetic processes that underlie angiogenesis can be studied at cellular resolution in the zebrafish embryo. Moreover, the fast development of the embryo allows to follow these processes in real-time. In the trunk, where metameric vessels sprout from the dorsal aorta, cells migrate collectively in a hierarchy defined by a leading endothelial cell at the tip of the sprout and several following cells, called stalk cells. Once the tip cells reach the level of the dorsal neural tube, they extend laterally and initiate the anastomosis process with tip cells from the neighboring segments. Eventually, cells rearrange and form a patent lumen, which allows blood circulation.

Angiogenic sprout outgrowth and anastomosis involve complex cell behaviors and cell-cell interactions, which need to be precisely orchestrated. The molecular mechanisms underlying these cellular activities are not known. However, proteins that mediate endothelial specific cell adhesion are good candidates to promote concerted cell behaviors. The goal of my thesis was (i) to characterize the cell shape changes that occur during angiogenic sprouting, (ii) to analyze the function of VE-cadherin in this process and (iii) to analyze the role of VE-cadherin and Esama, as candidate proteins, in the initiation of endothelial cell-cell interaction at the onset of vascular anastomosis.

I found that two major cell behaviors contribute to angiogenic sprouting. While cell migration is predominantly used by the tip cell, elongation of the stalk is mainly achieved by extensive stalk cell elongation, rather than by pulling forces exerted by the tip cell.

VE-cadherin, which is the major component of adherens junction of endothelial cells, is required for concerted angiogenic cell junctional elongation. The absence of VE-cadherin in stalk cells leads to a disorganized cortical F-actin network, which reflects the elongation defects. Furthermore,

the loss of VE-cadherin function can be phenocopied by inhibiting actin polymerization.

Anastomosis is initiated by filopodial contacts between endothelial cells. The formation of these contacts is thought to be mediated by endothelial specific adhesion molecules, which provide adhesion as well as cell type specificity. We have previously shown that VE-cadherin plays an important role in anastomotic contact formation. However, our observation that tip cells can still generate contacts in the absence of VE-cadherin, prompted us to investigate the role of a second endothelial-specific adhesion molecule, Esama, during anastomosis.

In my thesis I generated a targeted mutation in the zebrafish *esama* gene using TALEN technology and started to analyze the loss of function. Embryos mutant for *esama* are viable and do not show major vascular defects, except for small, transient gaps in junctional rings. However, zebrafish embryos lacking both, VE-cadherin and Esama, show frequent detachments of stalk from tip cells, ineffective cell-type specific recognition and strongly protrusive cell morphologies. All together, the phenotypes of the *ve-cadherin* mutants are aggravated by the simultaneous absence of Esama. Moreover, the double mutant shows junctional discontinuities, seen as big gaps within the junctional rings between stalk cells.

Our results support a model for angiogenic sprout elongation by cell shape changes orchestrated by VE-cadherin. VE-cadherin connects the actin cytoskeletons of neighboring stalk cells and drives the cell elongation by localized actin polymerization at the edges of the elongating junctions. Esama and VE-cadherin have partly overlapping functions during angiogenic sprouting and anastomosis. Both proteins are required for endothelial contact formation during anastomosis, but also for the maintenance of structural integrity during angiogenic sprouting.

Chapter I

Introduction

1.1. Morphogenetic and molecular control of blood vessel formation

Like all animals, unicellular organisms require oxygen and nutrients which they take up by passive diffusion. Multicellular organisms rely on more sophisticated delivery systems to distribute chemicals to every tissue of their bodies. For this purpose, tubular structures have proven useful and hence, they are found in many places in a vertebrate organism, e.g. lungs, kidneys and the cardiovascular system. These structures are highly branched, which increases the surface area of these organs and facilitates chemical exchange processes, or can reach into distal parts of a body to deliver nutrients and energy.

The development of tubular structures starts early in development and is genetically hardwired, as is the branching processes of a tubular organ (Affolter et al., 2009). Invertebrate and vertebrate organisms share the morphogenetic concepts underlying the development of branched organs, such as the tracheal or cardiovascular systems, respectively. Not only the morphogenetic concepts seem conserved, also the genetic pathway and molecular players are highly related (Affolter et al., 2009).

The cardiovascular system of a vertebrate is the first organ to form and is well suited to study branching morphogenesis. In adult organisms it serves to deliver oxygen, nutrients and hormones throughout the body and removes waste metabolites. During embryogenesis the formation and function of many organs rely on the development of vascular function. Therefore, the correct embryonic development of the vascular system is crucial and defects can lead to malformations and often to embryonic death.

The first vessels form by a mechanism referred to as vasculogenesis, which create the first and biggest functional circulatory loops. However, most blood vessels arise by a process called sprouting angiogenesis in which vessels form from existing ones. These processes give rise to a branched vascular network, which reaches the most distal parts of an animal body.

6

1.1.1. Vasculogenesis

The development of the cardiovascular system has fascinated embryologists for centuries. The heart is one of the first organs to form in the vertebrate embryo and the only one that is constantly in motion. Evolution gave rise to the cardiovascular system to meet the tissues' requirements for nutrients, oxygen and waste removal. Whilst the embryo grows, new blood vessels form, branch and reach the most distal tissues to deliver everything needed for fast growth.

Although the heart is one of the first organs to develop, it does not start to pump until the first vascular loops have been formed. In contrast to expectations, these first circulatory loops do not emerge form the heart. Rather, cells gather together to form a tube and only later connect to the heart. Vasculogenesis gives rise to the axial blood vessels, therefore creating the first circulatory loops. In a second process, this primary vascular network is remodeled into more branched circulatory beds – a process known as angiogenesis, which will be introduced in chapter 1.1.2.

The cells that contribute to blood vessels during vasculogenesis are angioblasts (precursors of endothelial cells) and originate from the lateral plate mesoderm. These cells migrate individually and aggregate in clusters to form a cord-like structure. Vasculogenesis involves cell-cell and cell-extracellular matrix (ECM) interactions and is tightly regulated at the genetic level.

1.1.1.1. Vasculogenesis in zebrafish

The circulatory systems of different species vary in their patterns, since the genome does not specify the position of every single connection in such complex circuits. However, the networks do look similar, because early development of the cardiovascular system is restricted by evolutionary and also physical and physiological constraints.

In contrast to mammals, where vasculogenesis gives raise to a paired dorsal aorta (DA), only one DA is formed in the embryonic axis in zebrafish (*Danio rerio*). The DA of zebrafish runs through the trunk in the posterior direction and is led back by the posterior cardinal vein (PCV). Initially, the DA

forms from angioblasts that emerge 13 hours post-fertilization (hpf), where they arise in two stripes in the posterior lateral mesoderm. Single angioblasts migrate towards the embryonic midline, where they coalesce and at 17 hpf start to form a tube (Lawson and Weinstein, 2002a). These cells are of arterial origin and shortly afterward, the PCV starts to form from the DA by ventral sprouting (Herbert et al., 2009).

Genetic analysis, combined with in vivo time-lapse analysis, has revealed the signaling pathways that contribute to the formation of the DA and the PCV. The arterial fate of angioblasts is determined by growth factors arising from ventral somites. In the notochord, Sonic hedgehog signals induce the secretion of the Vascular Endothelial Growth Factor A (VEGFA) in the ventral somites. The VEGFA signal is sensed by angioblasts, and functions not only by attracting the cells to the midline, but also by inducing arterial determinants (Lawson and Weinstein, 2002b; Lawson et al., 2002). VEGFA sensed by angioblasts leads to the expression of the arterial marker EphrinB2a, downstream of Notch signaling (Lawson et al., 2002). Therefore, the role of Notch in angioblasts is to repress venous fates. Yet, the VEGFA gradient appears to induce the arterial differentiation in the dorsal-most angioblasts, while the more ventrally located cells express EphB4a. The repulsive Ephrin signaling is thus supposed to drive the ventral sprouting of angioblasts that will give rise to the PCV (Herbert et al., 2009 and reviewed in Ellertsdóttir et al., 2010).

1.1.2. Angiogenesis

Angiogenesis describes the outgrowth of new blood vessels from existing ones and is not only found in physiological (e.g. developing organism or wound healing processes), but also in pathological conditions (e.g. tumors). Every metabolically active tissue requires the supply of nutrients and oxygen, which are delivered by close-by small blood vessels, known as capillaries. These metabolic requirements regulate angiogenic activity, leading to denser capillary network in the tissues. While physiological angiogenesis is induced by hypoxic cues, sprouting angiogenesis during embryonic development seems to be mostly genetically hardwired.

The formation of new blood vessels is accomplished via: (i) sprouting angiogenesis and (ii) intussusceptive angiogenesis (the latter describes the splitting of one vessel into two). In my thesis I will focus on sprouting angiogenesis as the main angiogenic mechanism and intussusception as a vascular remodeling mechanism (briefly described in chapter 1.1.2.3).

1.1.2.1. Sprouting angiogenesis

In zebrafish, different vessels can serve as model case to study sprouting angiogenesis. The best-studied blood vessels for this process are intersegmental vessels (ISVs).

ISVs are metamerically organized segmental arteries (SAs) and veins (SVs), located along the zebrafish trunk (Isogai et al., 2001). In a first angiogenic wave, pairs of SAs sprout bilaterally from the DA around 20 hpf, commencing close to the head and continuing in a posterior direction. The sprouts grow dorsally along the somite boundary, up to the level of the neural tube, where they extend laterally, anastomose (around 32 hpf) and give rise to the dorsal longitudinal anastomotic vessel (DLAV). A second wave of angiogenic sprouting starts form the PCV, which connects either to the SAs, converting them to SVs; or grow up to the horizontal myoseptum, where they contribute as progenitor cells to the lymphatic vasculature (Isogai, 2003) and reviewed by Ellertsdóttir et al., 2010).

Angiogenic stimulus

A growing embryo relies on the supply of oxygen and nutrients. As just described, the early vascular development during embryogenesis seems to be genetically hardwired and the first circulatory loops arise before blood flow has started. In early development the small size of an embryo allows for passive diffusion of oxygen through the tissue. However, hypoxia regulates the growth of new vessels at later stages during physiological and pathological processes. For example, passive diffusion permits the growth of a tumor mass up to the size of 1mm^3 (Patel-Hett and D'Amore, 2011).

Endothelial cells (ECs) embedded in vessels are activated by angiogenic cues, which lead to the extension of filopodia and cell migration. Hypoxic tissue is able to induce angiogenesis by secretion of proangiogenic signals. The main proangiogenic cue for blood vessel outgrowth is secreted VEGFA. The secretion of VEGFA is triggered in cells deprived of oxygen by the production of the transcription factor hypoxia inducible factor-1 (HIF1) (reviewed in Pagès and Pouysségur, 2005).

Tip cell selection

Activation of ECs embedded in vessels lead to the extension of filopodia, which facilitate their migration towards the source of VEGFA. The activated ECs do not leave the vessel individually; they are followed by several other ECs and migrate collectively. This collective cell migration is usually led by a single EC at the tip, termed "tip cell". The trailing cells are called "stalk cells", since they build the trunk of the sprouting vessel (see Figure I-1).

Different signaling pathways control the correct patterning of tip and stalk cells during sprout outgrowth. First, a single EC is selected to guide the sprout which is accomplished by growth factor signaling. Vascular endothelial growth factor receptor 2 (VEGFR2) located on the EC's membrane binds diffusing VEGFA. This interaction activates the receptor's tyrosine kinase, leading to the activation of the EC and extension of filopodia (Gerhardt et al., 2003). Next, it must be ensured that not all EC that sense VEGFA leave the blood vessel and become tip cells. This is achieved by cell-cell communication, i.e. lateral inhibition. Activation of EC by VEGF signaling induces the transcription Delta-like-4 (Dll4), which interacts with its Notch1 receptor on neighboring

10

ECs (Hellström et al., 2007). Dll4 interaction with Notch1 receptor on neighboring stalk cells induces the cleavage of the intracellular domain of the receptor. This peptide (Notch intracellular domain; NICD) transcriptionally downregulates VEGFR2 and thus makes stalk cells less responsive to VEGFA (reviewed by Andersson et al., 2011). This lateral inhibition mechanism ensures that only the EC that senses the highest concentration of growth factor is selected to lead the angiogenic sprout to the source, and also defines leading cell (tip cell) versus trailing cell (stalk cell) identity.

A further mechanism underlying Notch signaling controls the selection of a single tip cell. While NICD leads to the downregulation of VEGFR2 (Williams et al., 2006), it increases the transcription of VEGFR1 (Funahashi et al., 2010). VEGFR1, which also binds VEGFA, has little kinase activity and, furthermore, stalk cells secrete a soluble isoform of VEGFR1 (sVEGFR1), which suggests that it acts as negative regulator of angiogenic sprouting. Mouse and zebrafish models with genetic deletions for VEGFR1 or sVEGFR1 show hypersprouting activity, thus VEGFR1 acts as a sink for VEGFA (Chappell et al., 2009; Kendall and Thomas, 1993; Krueger et al., 2011 and reviewed in Siekmann et al., 2013).

In summary, VEGF signaling induces angiogenic sprouting through VEGFR2. Notch signaling defines tip versus stalk cell identity by lateral inhibition and regulates VEGFA levels by inducing expression of decoy-acting VEGFR1 and downregulation of VEGFR2 in stalk cells.
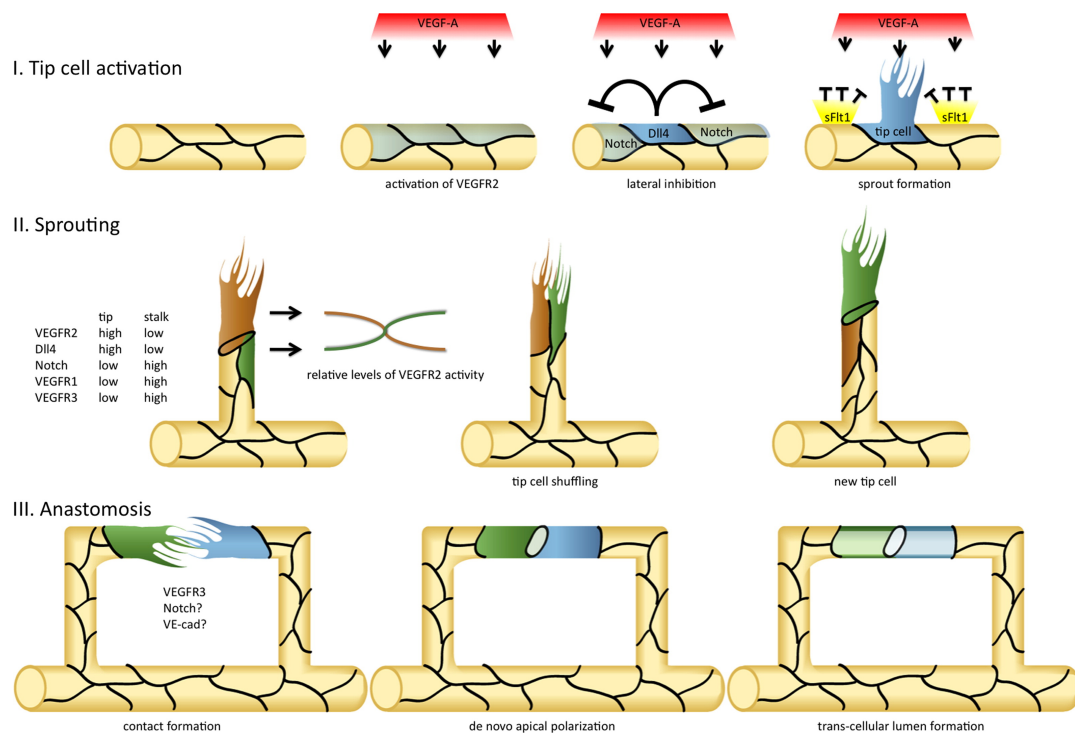
Figure I-1:   The cycle of angiogenic sprouting

Tip cell activation: The VEGFA signal triggers angiogenic sprouting of ECs in existing vessels. Notch signaling ensures by lateral inhibition that a single EC is selected to guide the sprout (blue cell, rich in Notch ligand Dll4) and thus increases VEGFR2 transcription. Flanking cells express membrane-bound and soluble isoforms of VEGFR1, which act as a decoy and reduces VEGF signaling. *Sprouting*: the tip cell has strong migratory activity and extends filopodia towards the growth factor source. Tip cell – stalk cell identity is kept through Notch signaling. Fluctuations in VEGFR2 signaling lead to competition for tip cell position amongst cells of the sprout. *Anastomosis*: filopodia engage in homotypic interactions establishing a junctional ring. Within the junctional ring the membranes are apically polarized, creating a luminal pocket. Lumen is pushed through the stalk and connects the luminal pocket creating a patent lumen. Adapted from Siekmann et al., 2013 with permission from Elsevier.

Sprout outgrowth

The path of an outgrowing sprout is spatially tightly defined and often leads through dense tissue. Therefore, for proper outgrowth, the sprout has to clear its way by breaking down ECM components, and this task is taken over by proteolytic enzymes (such as metalloproteinases), secreted from ECs (reviewed by van Hinsbergh and Koolwijk, 2008). The direct involvement of

12

proteolytic enzymes for way clearance during sprout outgrowth in zebrafish has not been investigated so far. García-Vilas et al. investigated the anti-angiogenic properties of a plant-derived hyaluronic acid biosynthesis inhibitor. They could show *in vitro* that, due to the compound, changes in the ECM decreased EC adhesiveness but also changed the expression level of matrix metalloproteinase-2 in ECs. Further, pharmacological treatment of zebrafish embryos showed disturbed ISV outgrowth *in vivo* (García-Vilas et al., 2013). These results might indicate (i) a role of ECM components in vascular morphogenesis and/or (ii) involvement of metalloproteinases during angiogenic sprouting. Although metalloproteinases are needed for angiogenic processes in mice, tissue-invading ECs do not depend on metalloproteinases; they can switch to an amoeboid mode, which allows them to push into the surrounding ECM. However, metalloproteinases can release pro- and anti-angiogenic factors that are stored in the ECM (reviewed by Michaelis, 2014).

In the case of the zebrafish ISV sprout outgrowth, the tip cell leads the way and is followed by several overlapping stalk cells and all of them proliferate (Blum et al., 2008). The angiogenic sprouts find their way along the somitic boundaries and do not invade the somitic tissue. However, after reaching the horizontal myoseptum, they grow straight up to the level of the neural tube (reviewed by Ellertsdóttir et al., 2010; Schuermann et al., 2014).

Like axonal guidance of neurons, ECs rely on attractive and repulsive guidance cues and it is intriguing that many of the involved molecules are shared amongst these different cell types. As described above, one of the major attractive signals during sprout outgrowth is VEGFA. However, to ensure the correct guidance of angiogenic sprouts, they have to be prevented from growing into vital tissues, such as the somites during segmental vessel formation. This is achieved by Semaphorin-Plexin signaling, where the Semaphorin ligands are expressed on the membrane of ventral somites and interact with Plexin receptors on ECs. Genetic alterations, like the *out of bounds* (*plexinD1*) mutant in zebrafish, lead to undirected sprouting and invasion of somites (Childs et al., 2002; Torres-Vázquez et al., 2004).

Despite being thoroughly described, Semaphorin - Plexin interactions are not the only guidance cues that contribute during sprout guidance. Some examples of other guidance cues can be found in Table I-1 (and reviewed by

Larrivée et al., 2009). Importantly, combinations of signaling pathways are involved in the selection and the guidance of angiogenic sprouts in different vascular beds. This reduced redundancy prevents signaling interference and thus ensures stereotypic vascular network formation (reviewed by Ellertsdóttir et al., 2010; Schuermann et al., 2014; Siekmann et al., 2013).

Table I-1: Examples of signaling interactions during vascular morphogenesis

Receptor	Ligand	Context	References
Bmpr2a and/or Bmpr2b	Bmp2b	Ventral PCV sprouting to form the CV	Wiley et al., 2011
Cxcr4a	Cxcl12b	Sprouting and anastomosis of hindbrain central arteries of zebrafish, tip cell identity	Bussmann et al., 2011
Cxcr4b	Cxcl12a	EC migration in the CV plexus	Torregroza et al., 2012
EphB4a	EphrinB2a	Arterial (EphrinB2) and venous (EphB4) segregation during DA and PCV formation	Herbert et al., 2009
Notch1	Dll4	Lateral inhibition, tip versus stalk cell identity, patterning of angiogenic sprout, cell behavior (shuffling)	Hellström et al., 2007
PlexinD1	Semaphorin3A / Semaphorin3Ab	Repulsive guidance of ISVs	Childs et al., 2002; Quillien et al., 2014
Roundabout4	Slit	Restriction of growth path (repulsion) and timing of ISV outgrowth	Bedell et al., 2005; Park et al., 2003
Unc5b	Netrin-1a	Repulsive guidance in the dorsal trunk	Lu et al., 2004
CD146	Netrin-1a	Attractive signal for parachodal vessel formation	Tu et al., 2015
VEGFR2	VEGFA	Induction of angiogenic sprouting	Gerhardt et al., 2003
VEGFR1 and sVEGFR1	VEGFA	Decoy receptor for VEGFA	Chappell et al., 2013; Kendall and Thomas, 1993; Krueger et al., 2011
VEGFR3	VEGFC	Venous sprouting from PCV to connect to ISVs	Hogan et al., 2009
VEGFR3	VEGFC	Primordial hindbrain channel formation	Covassin et al., 2006
VEGFR2-VEGFR3	VEGFA	Receptor heterodimer that might contribute to ISV sprouting	Covassin et al., 2006

Anastomosis

Circulatory loops do not form until dead-ended sprouts connect to each other. ISVs of the zebrafish trunk are a special type of such dead-ended sprouts, where each T-shaped sprout has two dead ends. Thus, every ISV will connect to its neighboring vessel, in a process called blood vessel fusion or anastomosis (Blum et al., 2008; Herwig et al., 2011). As a consequence of anastomosis, the tip cells become quiescent and hence have less protrusive activity. Quiescence is one of the first steps of vessel maturation; more will be covered on this subject in chapter 1.1.2.4.

The process of anastomosis starts by filopodial interaction between two neighboring tip cells. A single contact point is sufficient to maintain and expand the contact (Lenard et al., 2013). While the initial contact can be visualized by a single spot of junctional material deposition, this junctional spot transforms into a ring as the tip cells crawl over each other and increase their mutual surface (see Figure I-2). At the same time cell polarization processes create a new apical compartment at the contact site, a luminal pocket between the two tip cells (Figure I-2), whose membranes are marked by the apical marker Podocalyxin 2 (Pdxl2) (Herwig et al., 2011).
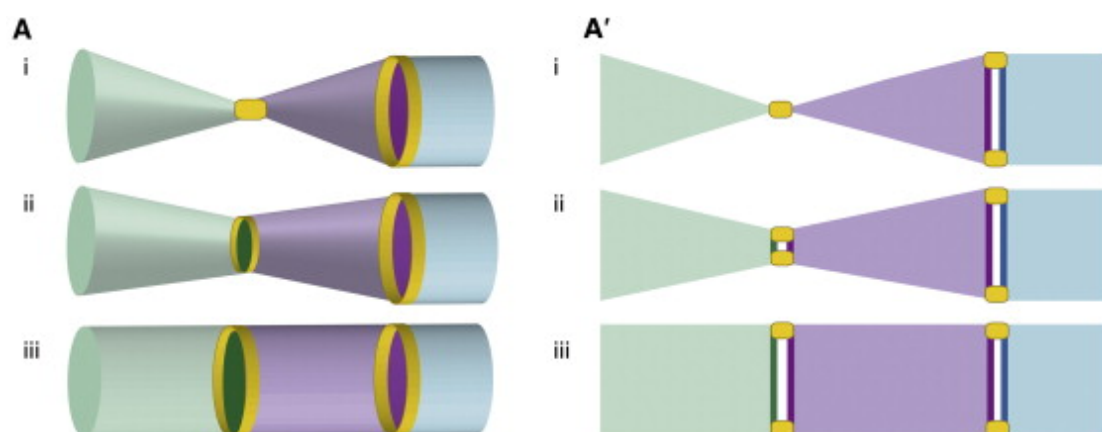
Figure I-2: Cellular mechanism of anastomosis

(**A**) Contact formation during angiogenesis; (A') shows a cross-section through the cells. (i) Junctional components (yellow) are deposited at the contact site of the two tip cells (green and purple). As the cells crawl over each other the junctional spot

expands to a ring (i-iii in A) and the enclosed membrane compartment becomes apically polarized (dark green and dark purple membranes in A and A'), which creates a luminal pocket between the two cells (seen in the cross-section; ii-iii in A'). Adapted from Herwig et al., 2011 with permission from Elsevier.

How the tip cells recognize each other so specifically is less clear, but adhesive proteins on the cell membrane (i.e. junctional proteins) are supposed to play a major role. When *vascular endothelial cadherin* (*ve-cad*), also known as *cadherin 5* (*cdh5*), is genetically deleted, tip cells have difficulty in recognizing each other. The deletion of *ve-cad* does, however, not abrogate tip cell interaction, it rather results in several filopodial contacts that are each expanded and eventually fused to a single mutual contact (Lenard et al., 2013). However, other studies have implied the involvement of macrophages that bridge filopodia between two tip cells, facilitating anastomosis (Fantin et al., 2010). Following on this line, mouse studies suggested a mechanism, where macrophages participate in the anastomotic process by secreting VEGFC, which turn the EC into a more quiescent – stalk cell-like – state (Tammela et al., 2011).

1.1.2.2. Lumen formation

Blood vessels, similar to other branching organs, have to form tubes and a variety of morphogenetic mechanisms can generate vascular tubes.

Cord hollowing

The mechanism of cord hollowing is best characterized for vasculogenic processes (Jin et al., 2005). ECs, assembled in a vascular cord, establish cell-cell connections via cell junctions and subsequently polarize. At the center of the cord, cells deposit sialomucins (e.g. Pdxl) on their apical membranes, which lead to the separation of these membranes due to electrostatic repulsion of the negatively charged sialomucins. Subsequent cell shape changes allow establishment of a patent lumen (Strilić et al., 2010; 2009). During angiogenesis, multicellular tubes (tubes consisting of several ECs) generate lumen in ways that resemble the cord hollowing mechanism (Blum et al., 2008; Herwig et al., 2011). Here, several luminal pockets, between EC, are joined by cell rearrangements (see Figure I-3 B). Importantly, this is a mechanism independent of blood flow.

Lumen ensheathment

Blood vessel formation via lumen ensheathment resembles to some extent the formation of the neural tube of vertebrates, which occurs by a mechanism called wrapping (reviewed by Lubarsky and Krasnow, 2003). Lumen ensheathment has been described as a novel mechanism of lumen formation for the common cardinal veins (CCVs aka ducts of Cuvier) of zebrafish. The CCV (located on the yolk) is part of the venous system and responsible to collect all the blood to deliver it back to the heart. The CCV initially develops by vasculogenic processes, where ECs arrange into a monolayer on top of the yolk. With the onset of blood flow, the EC monolayer starts to migrate towards the heart in an angiogenic manner. After the cell sheet connects to the endocardial ECs, the lumen ensheathment starts by folding around the blood stream (Helker et al., 2013).

Intracellular lumen formation by vacuole fusion

Individual cells generate vesicles that coalesce within the cell to form vacuoles. Several of these vacuoles will fuse within the cell, forming one

luminal space, which, by exocytosis, interconnects with neighboring lumens giving rise to a multicellular tube (Bayless et al., 2000 and reviewed in Iruela-Arispe and Davis, 2009; Lubarsky and Krasnow, 2003). This type of lumen formation hollows up the cells and has been observed in different lumen generating cell types *in vivo* and *in vitro* (reviewed by Iruela-Arispe and Davis, 2009). In zebrafish vacuole fusion has been proposed, but needs better investigation especially using better cellular resolution to ensure the observed vacuoles are not artifacts from collapsed lumens (Ellertsdóttir et al., 2010; Kamei et al., 2006).

Budding

In some instances an angiogenic sprout, connected to a vessel with continuous lumen, extends, while simultaneously the blood pressure expands the lumen up to, and sometimes into, the tip of the sprout (Baer et al., 2009; Lenard et al., 2013). This process of vessel lumenization is called budding and predominantly occurs in larger capillaries that are constantly perfused; it can be regarded as a result of membrane invagination, another process introduced in the next section.

Transcellular lumen by membrane invagination

Herwig et al. described that during anastomosis a new apical compartment is defined at the contact point between two tip cells (Herwig et al., 2011). The apical compartment contains apical markers, such as Pdxl2, which, as described for cord hollowing, act anti-adhesive. This luminal pocket will fuse with other luminal compartments, which can be achieved by two distinct morphogenetic processes, involving: (i) cell rearrangements, which, as described above, is reminiscent of the cord hollowing process and creates a multicellular tube with extracellular lumen (see Figure I-3 B). Or (ii) by cell membrane invagination, which is dependent on blood pressure (Herwig et al., 2011; Lenard et al., 2013). For the latter process, an existing lumen (e.g. from a budding sprout) will push the membrane of a former tip cell through it and fuse with the luminal pocket generated by anastomosis (see Figure I-3 C). This process creates unicellular (seamless) tubes with a transcellular lumen. Usually, unicellular tubes are

transformed to multicellular tubes at later time points, which involves further cell rearrangements, such as cell splitting (Lenard et al., 2013). Multicellular tubes are thought to be more stable.
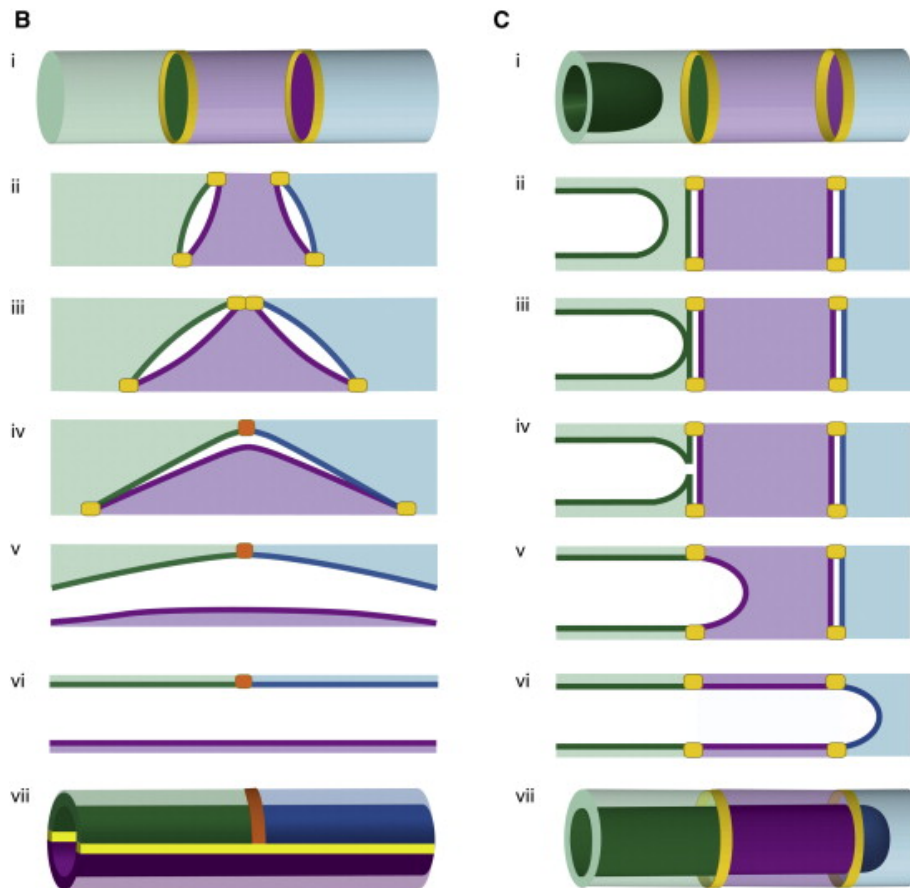
Figure I-3: Cellular model for multicellular and transcellular lumen formation
(**B**) Multicellular lumen formation by cord hollowing mechanism. Cells rearrange, which bring luminal pockets (enclosed by yellow junctions) closer together (ii-iii in B). Two luminal pockets fuse with each other (iv in B); further cell rearrangements open up the tube (v-vi in B), which leads to the formation of a multicellular tube. (**C**) Cell membrane invagination creates a unicellular tube with transcellular lumen. Blood pressure pushes the apical membrane (dark green) of the green cell through the cell body (i-iii in C). The two apical membranes (dark green) fuse (iv in C) and the invagination continues fist in the purple cell, then in the blue cell (v-vi in C). This creates a unicellular, seamless tube with transcellular lumen (vii in C). Adapted from Herwig et al., 2011 with permission from Elsevier.

1.1.2.3.   Vascular remodeling

The primary vascular network that has been created by extensive sprouting needs to be refined, which has been well characterized in the retina vasculature of the mouse (reviewed by Dorrell and Friedlander, 2006; Ribatti and Crivellato, 2012). Remodeling of the vasculature requires the generation of (other) new vessels (by sprouting or vessel splitting – intussusception), retraction of redundant ones (pruning) and adjustments in vessel diameters (which is also accomplished during vessel maturation).

Intussusception

The splitting of an existing vessel into two smaller ones creates additional vessel segments. This process, intussusception, is thought as an adaptive mechanism to regulate the flow velocity in vessels (reviewed in LeBlanc et al., 2012). This vessel splitting, in contrast to my categorization, is often regarded as an alternative form of angiogenesis (see chapter 1.1.2.1).

Intussusception has been characterized in different model organisms, such as chick embryos or the mouse. During intussusception, mural cells invade in the middle of a blood vessel, forming a pillar (Djonov et al., 2002). Interendothelial cell contact formation and junctional remodeling precedes vessel perforation, which then splits the vessel. As previously mentioned, activation of intussusception seems to be triggered by flow dynamics within the vessel, but also by VEGF signaling (reviewed in LeBlanc et al., 2012). The tissue invasion is usually started by interaction of tyrosine-protein kinases receptor (Tie2) on EC and angiopoietin-1 (Ang1) ligand on surrounding mesenchymal cells, which usually regulates EC motility and pericyte recruitment (Patan, 1998). The pillar then passes through the vessel, creating a hole, which expands longitudinally, splitting the vessel in two (reviewed by Makanya et al., 2009).

Pruning

Not much is known about the morphogenetic processes that lead to vessel pruning. Leukocyte-mediated EC apoptosis has been shown to be involved in vessel pruning (Ishida et al., 2003). However, more recently, pruning of zebrafish vascular connections has been described as a reverse

mechanism of vascular tube fusion and might not rely extensively on apoptosis (Chen et al., 2012; Kochhan et al., 2013; Lenard et al., *in press*).

The retraction of vascular tubes can be induced by the drop of pressure (sensed by shear stress and pressure) or by hyperoxia (suppression of VEGF signaling) (reviewed by Ribatti and Crivellato, 2012). This is the case in the mouse retina, where vascular pruning was shown to be induced by suppression of VEGF signaling, directed by neuronal cells (Stone et al., 1995).

1.1.2.4.   Maturation and Stabilization

The last step during angiogenesis is the maturation and stabilization of vascular loops. This creates blood vessels that are resistant to stress, increased blood pressure and inflammatory responses. Moreover, it makes blood vessels highly adaptable to environmental changes and ready to function throughout an organism's lifespan. After vascular remodeling, different cell types (e.g. pericytes, smooth muscle cells, fibroblasts, inflammatory cells etc.) are recruited to blood vessel and ECM components are deposited to maintain vessel integrity. ECs secrete factors that recruit and differentiate mural cell precursors to smooth muscle cells and pericytes, promoting vascular stabilization and maturation. Different molecular regulators have been involved in the regulation of vessel stabilization (reviewed in Ribatti and Crivellato, 2012), such as endothelial cell receptors Tie1 and especially Tie2, and their ligands angiopoietins (i.e. Ang1) (Puri et al., 1995; Suri et al., 1996). The angiopoietin signaling seems to be conserved also in zebrafish (Sessa et al., 2012).

1.1.3. Signaling during angiogenesis

Different aspects of angiogenic sprouting are controlled by a wealth of signaling pathways (Table I-1, page 14). Among these, VEGF, Notch, Wnt, Angiopoietin/Tie2, TGFβ, FGF, Slit/Robo, Semaphorin/Plexin, Netrin/Unc5b are the best studied. In this section I want to focus on two of the most important pathways during angiogenesis, VEGF and Notch signaling.

1.1.3.1.   VEGF signaling

VEGF signaling is the principal regulator of angiogenesis and controls, for example, EC migration, proliferation, survival and junctional permeability of blood vessels (Phng and Gerhardt, 2009).

The VEGF family of signaling molecules consists of five members (VEGFA-D and Placental Growth Factor [PlGF]), which act as homodimers and are processed by splicing or by metalloproteinases, which influences their ability to bind to receptors or their diffusion (by regulating the binding to ECM components, such as heparan sulfate).

The VEGF signals are perceived by the members of the VEGF-receptor family of tyrosine kinases VEGFR1 (or Fms-like tyrosine kinase 1; Flt1), VEGFR2 (or kinase insert domain receptor-like; Kdrl or Flk1) and VEGFR3 (or Flt4). These transmembrane receptors bind their ligands through extracellular immunoglobin-like loops and signal by their intracellular split tyrosine kinase domain (reviewed in Koch et al., 2011). Generally, VEGFR1 is expressed in ECs, macrophages and monocytes, VEGFR2 by ECs and VEGFR3 is specific for lymphatic endothelial cells. There are, however, some exceptions where all three receptors are expressed in ECs, can form homo- and heterodimers, bind to different growth factors with different affinities, and thus have different impacts during vascular biology. An additional level of complexity is achieved by the fact that VEGF receptors can also form heterodimer with other receptors, such as Neuropilins (Favier et al., 2006; Gu et al., 2003). Moreover, VEGF signaling can be subject to the output of other signaling pathways, for example Plexin/Semaphorin (Zygmunt et al., 2011).

As I described before, both forms of VEGFR1 (membrane bound and soluble) are considered as decoy receptors for VEGFA and therefore

22

important to limit angiogenic sprouting by attenuating the VEGFA signaling output (see also Figure I-4). In agreement with this view, loss of VEGFR1 function leads to an increase in tip cell numbers and a hypersprouting phenotype (Krueger et al., 2011). Furthermore, this correlates with ectopic expression of VEGFR3, which is usually upregulated in tip cells in a Notch-dependent manner (Krueger et al., 2011). VEGFR1 therefore seems to help to fine tune VEGF signaling. However, in the mouse, the loss of VEGFR1 function has been associated with decreased EC migration and defective sprout formation (Kearney et al., 2004). Therefore, angiogenic responses are precisely fine-tuned by the bioactive availability of VEGFA and spatio-temporal receptor activation.

VEGFR2 transduces the main signals for vascular processes, i.e. inducing vascular permeability, EC migration, proliferation, cytoskeletal organization and thus the formation of vascular tubes (see Figure I-4). The different signaling readouts are transmitted through its different tyrosine phosphorylation sites (reviewed in Koch et al., 2011). Chemical blockage of the tyrosine kinase of VEGFR2 abrogates all angiogenic responses. Another process, vascular permeability, is increased by the VEGFA-VEGFR2 induced disassembly of junctional complexes (i.e. VE-cad, β-catenin) through activation of cytoplasmic tyrosine kinases, and similar mechanisms are supposed to initiate and regulate angiogenesis (Esser et al., 1998 and reviewed in Koch et al., 2011).

Although best described for lymphatic development, VEGFR3 is expressed early on in the primary vascular plexus (Kaipainen et al., 1995). During vascular development in zebrafish, VEGFR3-VEGFC signaling plays crucial roles during secondary sprouting (from the PCV) and these sprouts contribute to either lymphatic or vascular networks by connecting to SeA and transforming them to SeV (Hogan et al., 2009). Furthermore, VEGFR3 is regulated by Notch-dependent signaling, which increases its transcription in tip cells, therefore modulating angiogenic responses in cooperation with VEGFR2 (Siekmann et al., 2013).
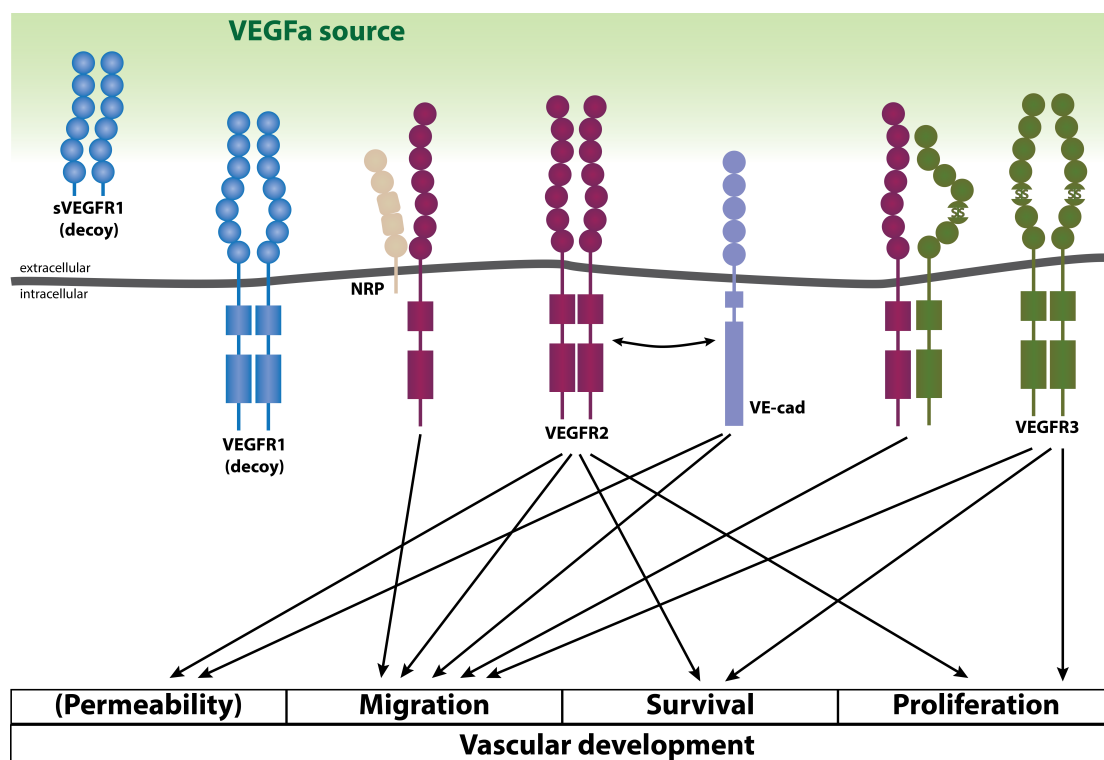
Figure I-4: VEGF signaling

Schematic representation of VEGFA - VEGF receptor interactions during vascular development. VEGFR1 and its soluble isoform, sVEGFR1, have little or no tyrosine kinase activity respectively, and act as VEGFA decoy receptors. VEGFR3 is predominantly responsible for lymphangiogenesis (responding to VEGFC and -D), but is also found in angiogenic ECs. The VEGFR2 homodimer is the most potent VEGFA signal transducer, and regulates vascular development at the level of cell migration, survival, proliferation and also permeability. VEGFR2 can also form heterodimers with VEGFR3 or Neuropilin (NRP) and promote angiogenesis. Furthermore, VE-cadherin (VE-cad) interacts also with VEGFR2 and is thought to attenuate VEGFR2 signaling.

1.1.3.2. Notch signaling

Notch signaling is involved in many cell types and processes during development, including tissue patterning, cell fate specification and morphogenesis (Lewis, 1998). In vertebrates, there are 5 ligands and 4 Notch receptors, which interact by cell surface exposure. The Notch receptors are named Notch1 to Notch4, and ligands are Jagged 1 (Jag1), Jag2, Delta-like 1 (Dll1), Dll3 and Dll4. Only a subset of these molecules are expressed in ECs,

i.e. Notch1, Notch4, Dll1, Dll4, Jag1 and Jag2 (reviewed by Benedito and Hellström, 2013; Phng and Gerhardt, 2009).

The role of Delta/Notch signaling has been best described during cell fate specification by lateral inhibition. Generally, Delta ligand binding induces high Notch levels and suppresses Delta in signal-receiving cells. As a consequence, groups of cells express either high levels of Delta or Notch, which leads to the formation of different cell types (reviewed by Lewis, 1998). Unlike in other signaling pathways, Notch signals are not amplified and act in a stoichiometric fashion. Notch signals are fine-tuned at the level of NICD, where many posttranslational modifications adjust the signaling output (reviewed in Andersson et al., 2011). Binding of the ligand to the receptor induces proteolytic cleavages of the Notch receptor. Metalloproteinases cut Notch receptor in the extracellular space and γ-secretase cleaves it in the transmembrane domain. The latter cleavage releases NICD from the membrane, which is translocated to the nucleus and leads to the transcription regulation of target genes by interacting with the transcription factor complex CSL (Kao et al., 1998; Struhl and Adachi, 1998). One important outcome of nuclear NICD is the expressional downregulation of the Notch ligand, which is important for lateral inhibition and serves as a negative feedback (Lewis, 1998).

During angiogenesis, VEGFA activates the EC and induces Dll4 expression, which interacts with Notch1 receptor on neighboring cells, altering its transcriptional profile to a more quiescent state (i.e. downregulation of VEGFR2 and upregulation of VEGFR1) (Hellström et al., 2007; Holderfield et al., 2006; Kappas et al., 2008). In this way, Notch signaling limits VEGF-induced angiogenic behaviors, although the exact mechanisms are not understood in detail and are sometimes contradictory (Siekmann et al., 2013). Nevertheless, the interplay of Notch and VEGF ensures that only one tip cell is selected and leads the sprout. Indeed, the suppression of Notch signaling, by genetic deletion of *dll4* causes excessive proliferation and hypersprouting (Leslie et al., 2007). Dll4 has thus an antiangiogenic role by upregulating Notch in neighboring cells. However, Jag1, a less potent Notch ligand, was shown to counteract the Dll4 repressive signals, rather acting in a proangiogenic manner (Benedito et al., 2008).

During sprout outgrowth, stalk cells perceive VEGFA signals at reduced and variable levels. Those receiving higher levels will compete for the tip cell position (Arima et al., 2011; Jakobsson et al., 2010) (see Figure I-1), which is explained by the activating potential of VEGFA. Furthermore, during this competition, fluctuations of Notch, Dll4 and VEGFR2 levels in stalk and tip cells are observed. The fluctuations were proposed to regulate VE-cad dynamics, allowing stalk cells to overtake a tip cell via cortical protrusions (Bentley et al., 2014). More details about this mechanism will be discussed in chapter 1.2.2.2.

Another mechanism by which Notch regulates the angiogenic readouts of VEGF signaling is the adhesiveness of ECs to the ECM. Experiments done in cell culture and in the chick chorioallantoic membrane showed that Notch1 and Notch4 activation leads to an increase in EC-ECM adhesion through β1-integrins and hence reducing the EC's response to VEGF (Hodkinson et al., 2007; Leong et al., 2002).

Eventually, newly formed vascular loops need to be stabilized, a process that is also regulated by Notch signaling. Notch in EC activates Notch-regulated ankyrin repeat protein (Nrarp), which acts as negative regulator of Notch signaling and integrates into Wnt signaling. The proper balance of Notch and Wnt in ECs determines their activity, however the upstream Wnt ligands and receptors have not been identified (Phng et al., 2009).

There is much more to Notch signaling: it integrates in many different pathways, such as VEGF or Ephrin, and in turn, can be altered by many more signals (e.g. Wnt or Bmp pathways). More information about these processes is summarized in Benedito and Hellström, 2013; Phng and Gerhardt, 2009; Siekmann et al., 2013.

26

1.2. Endothelial cell junction, cytoskeleton and polarity

During organ formation, cells assemble and shape the emerging structure by a multitude of collective and individual cell behaviors, such as proliferation, cell shape changes or cell migration. Collective cell behaviors often depend on physical cell-cell interactions, which are conferred by adhesive molecules presented at the cell surface. When cells physically interact with each other, they form junctions in a cell-type specific manner. Through these junctions, the cytoskeletons of neighboring cells are cross-linked, which thus define the shape and stiffness of a cluster of cells or even an organ. Not only do the junctions crosslink the cells, they also form a sealing barrier that can be selectively permeable, still allowing the exchange of signals amongst the cells to coordinate the cell behaviors of the community. Especially during early development of an organism, the junctions are vital for collective migration, to cluster cells at the right position and to determine their fate through signaling. Therefore, the junctions are fundamental to shape and organize organs in a developing organism.

In blood vessels, endothelial cell junctions play vital roles in many different contexts such as inflammation and homeostasis (reviewed in Dejana, 2004). However, they are all-important to generate the vascular network in first place.

Here, I focus on how junctions regulate actin cytoskeletal dynamics (e.g. cell shapes or motility), cell polarity; and focus on specific junctional components and their roles during angiogenesis.

1.2.1. Overview of endothelial cell junctions

Endothelial cell junctions can be divided into adherens junctions (AJs) and tight junctions (TJs). In contrast to junctional complexes of other cell types, endothelial cell junctions lack components such as desmosomes. Further, their organization is less defined, whereas in most epithelial cells TJs are found more apically, in endothelial cells they overlap with AJs. Junctions contain transmembrane molecules that engage in a homophilic fashion and mediate adhesion between cells (see Figure I-5).
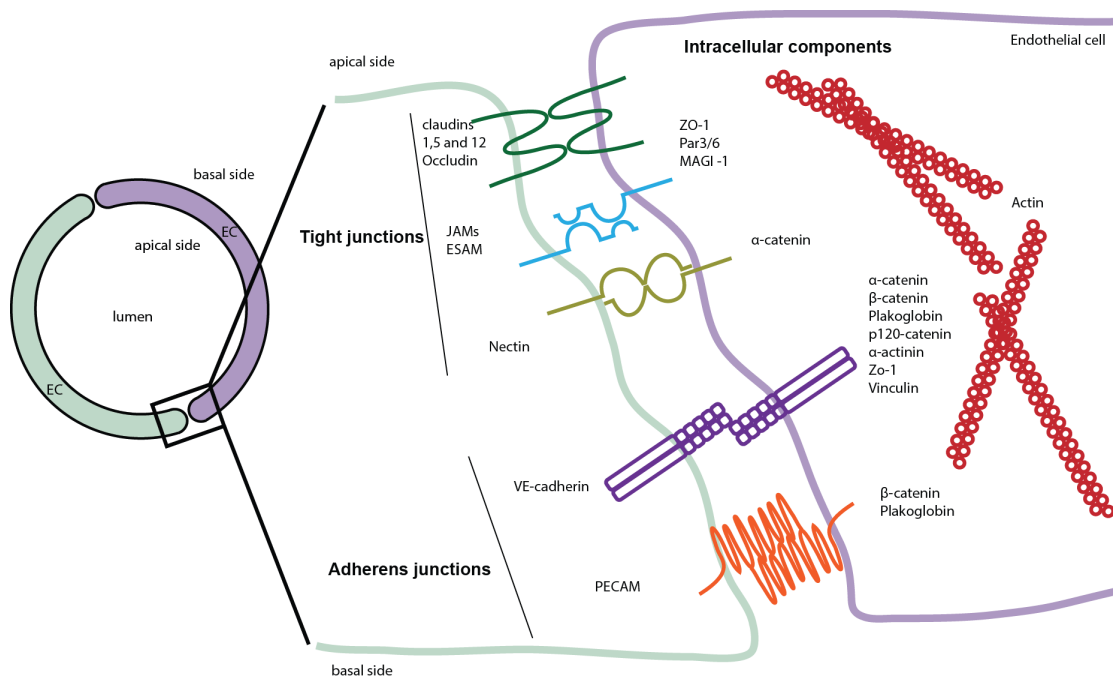
Figure I-5:   Endothelial cell-cell junction

A cross-section of a vascular tube is shown on the left and a magnification of the junctional interface between two endothelial cells is schematically represented on the right. Here, the TJs and AJs are separated whit TJ components more apically and AJ components more basolaterally located. Next to the transmembrane adhesion molecules, many cytoplasmic proteins (intracellular components) can associate with the junctional complex to stabilize it, transduce signals or link it to cellular organelles, such as the cytoskeleton. After Dejana, 2004.

28

In the mature endothelium, the role of AJs is to mediate cell-cell adhesion and to regulate endothelial permeability, hence acting as gatekeepers for leukocyte transmigration (Dejana et al., 2009). Moreover, they are needed for the establishment of new cell-cell connections, remodeling of the actin cytoskeleton and local signaling, but also signaling at the transcriptional level (Harris and Nelson, 2010). As for TJs, they show size and ion selectivity and seal the endothelium to prevent the leaking of solvents (Nitta, 2003).

AJs contain cadherins (e.g. VE-cad), which associate with catenins that link the junctional complex to the cell cytoskeleton. Proteins characteristic for TJs are Claudins, Occludins, Nectins and proteins of the Junction Adhesion Molecule (JAM) family and finally Claudin5, which is the main component of endothelial TJs (Taddei et al., 2008). Next to the adhesive properties, junctions contain and interact with molecules that function as signal transducers to communicate positional information (polarity), survival cues or other signals. Due to the selective expression of these junctional proteins, different combinations are thought to mediate cell specific properties, including cell-cell specific recognition (reviewed in Dejana, 2004).

In vitro studies support models for adhesion molecules during angiogenesis in maintenance of dynamic properties that allow the cells to migrate, rearrange and respond to external cues, such as growth factors. Once sprouts have met and lumen has established, junctional complexes mature, stabilize and signal to switch the cells to a more quiescent state (reviewed in Dejana, 2004). While the importance of endothelial junctions is generally recognized during vascular development, very little is known of how they support the cellular dynamics of angiogenic sprouting.

1.2.1.1. VE-cadherin

Cadherins are the first adhesion molecules that have been identified and therefore, have been the subject of many studies. There are different classes of cadherin molecules, but here I consider only classical cadherins, to which VE-cad belongs. VE-cad is single-pass transmembrane protein, which mediates homophilic, calcium-dependent adhesion.

Structure and homology of VE-cad and other cadherins

The extracellular domain of classical cadherins contains five cadherin repeats that interact in a homotypic manner (Figure I-6). The conserved intracellular domain attaches the cadherin to the cytoskeleton and interacts with a subset of different cytoplasmic proteins. Like other cadherins, VE-cad engages in cis- and trans-interactions but its expression is restricted to the endothelium.

Cadherins homophilic engagement occurs over a tryptophan residue at their amino-terminal end (first extracellular cadherin repeat), which binds the cell adhesion recognition domain (a tri-residue) on a neighboring cadherin. These amino acids are encoded in the first extracellular cadherin repeat. The homology between the first cadherin repeats of VE-cad and other cadherins is low, and although the amino-terminal tryptophan is conserved, the cell adhesion recognition domain is not. As for the cytoplasmic tail of VE-cad, sequence analysis revealed further differences, suggesting unique roles for VE-cad in the endothelium (reviewed in Vincent et al., 2004).

Adhesion

The exact mode of homophilic VE-cad interaction has not been defined yet. However, *in vitro* and *in vivo* studies propose roles for the first and fourth cadherin repeat during angiogenesis, while the first repeat also mediates barrier function (Corada et al., 2002).

Not only the extracellular domain of cadherins is important to mediate proper cell-cell adhesion. In the absence of specific intracellular binding partners, cadherins do not exhibit proper adhesion. The most important binding partners are α-, β-, p120-catenin, Vinculin and Plakoglobin, while α-catenin and Vinculin bind VE-cad indirectly through β-catenin (Figure I-6) (Navarro et al., 1995 and reviewed by Vincent et al., 2004). Best

characterized are β-catenin-α-catenin interactions, where β-catenin directly binds VE-cad and also α-catenin, and the latter connects to actin filaments (Figure I-6). With these binding partners, the VE-cad-catenin complex is coupled to the actin cytoskeleton, which is required for proper adhesion and later also for the stabilization and maturation of the junctional complex (Ozawa et al., 1990 and reviewed by Vasioukhin and Fuchs, 2001; Vincent et al., 2004).
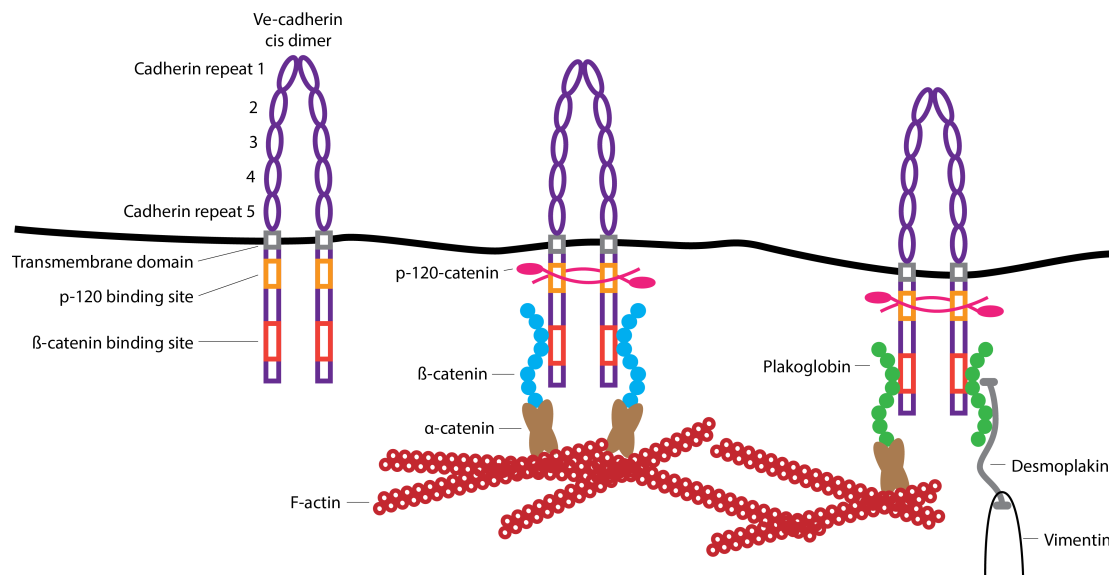
Figure I-6: Schematic representation of Ve-cadherin and cytoskeletal interactions

VE-cad engages in homotypic manner through its first extracellular cadherin repeat. Binding of p-120-catenin to the juxtamembrane domain of VE-cad stabilizes the complex at the membrane. VE-cad has been shown to interact with intracellular proteins leading to the association with actin and intermediate (Vimentin) cytoskeletal components. β-Catenin and Plakoglobin bind to the distal catenin binding site of VE-cad, and both can link the junctional complex to F-actin by binding α-catenin. In addition, Plakoglobin links the junctional complex to intermediate filaments by binding to Desmoplakin, leading to the association with Vimentin filaments. After Vincent et al., 2004.

Maturation of junctional complexes

Cadherins are amongst the first proteins to accumulate at novel cell-cell contacts (reviewed by Ebnet, 2008; Irie et al., 2004). Similar to other cell types, a crucial step in EC junction maturation involves recruitment of TJ components and, in the case of the endothelium, one of these proteins is Claudin5. VE-cad, through β-catenin, recruits Phosphatidylinositol-4,5-bisphosphatase 3-kinase (PI3K), which is involved in many different signaling pathways. Nevertheless, the recruitment of PI3K activates Akt (protein kinase B), which leads to derepression of the *claudin5* locus (by exclusion of β-catenin and forkhead transcriptional repressor FoxO1) and leads to the maturation of the junction (Taddei et al., 2008).

Another molecular interaction during junction maturation is the association of vascular endothelial phosphatase (VE-PTP) with the VE-cad extracellular domain (the fifth cadherin repeat), which helps in stabilizing the junctions. VE-PTP can dephosphorylate Tie2, and VEGFR2 located at the junctions. This complex (VE-cad, VE-PTP, Tie2 and VEGFR2) then regulates vascular quiescence, EC polarity and lumen formation (Hayashi et al., 2013).

In mature junctions, VE-cad reduces apoptotic and proliferative signaling (Dejana et al., 2009). In contrast, during angiogenesis, transient homophilic VE-cad interactions have other downstream consequences. These interactions might also involve association with growth receptors, such as VEGFR2, hence endothelial survival cues are down-regulated, but they might also alter migratory cell behaviors (reviewed by Bravi et al., 2014). This suggests that the degree of junctional maturity and its composition leads to differential signaling.

Regulation of actin at the junctions alters adhesive properties

An important aspect of AJ and TJ function is their interaction with the underlying actin cytoskeleton, which supports the stabilization of, and maturation of junctions. Activation of Rac and Cdc42 GTPase, for example, strengthens the cytoskeleton at the junctions. In contrast, VE-cad dependent stimulation of Rho small GTPase activates ROCK, which phosphorylates myosin and pulls on cell-cell junctions, inducing gaps that increase

32

permeability (required e.g. during inflammation) (reviewed by Bravi et al., 2014; Spindler et al., 2010).

Furthermore, many interactions of VE-cad with small GTPases, but also their regulators guanine-nucleotide-exchange factors (GEFs) and GTPase activating proteins (GAPs), have been investigated and have been shown to regulate VE-cad's activity, association with the cytoskeleton, but also signaling downstream of VE-cad (reviewed in Bravi et al., 2014; Dejana et al., 2008; Lampugnani and Dejana, 2007; Vincent et al., 2004).

Cell signaling downstream of VE-cad

Cell-cell interactions impact on many cell-signaling pathways, which do not only alter the cell's transcriptome, but also cell survival. Also endothelial contact formation was shown to reduce cell proliferation in a VE-cad-dependent manner (Caveda et al., 1996). More recent analyses have revealed that VE-cad homophilic interactions actually alter EC proliferation in both directions. Interestingly, increase in proliferation was associated with Rho mediated actin cytoskeleton tension, which facilitates crosstalk between cell-cell and cell-ECM adhesion and hence alters cell spreading (involving cell shape, cell-substrate adhesion and cell migration) (Nelson and Chen, 2003; Nelson et al., 2004).

One major VE-cad-dependent signaling pathway is mediated by the association with or dissociation from β-catenin. β-catenin is the canonical effector of Wnt signaling and can modulate the transcriptional activity by its nuclear presence. In mature junctions, β-catenin is mostly found associated to VE-cad at the junctions and excluded from the nucleus, while in weak (remodeling) junctions it is concentrated in the nucleus (Clevers and Nusse, 2012). The signaling contribution of β-catenin that dissociates from junctions is debated. However, availability of β-catenin is proteolytically regulated; when not bound by cadherins it is rapidly degraded (which is dependent on e.g. glycogen synthase kinase (GSK)-3 β) (reviewed in Bravi et al., 2014; Vincent et al., 2004).

Recycling of VE-cad

Endocytosis of VE-cad from the junctions usually leads to higher permeability. However, the local availability of VE-cad at the junctions

modulates also the signaling activity downstream of VE-cad. The local amount of VE-cad protein can be modulated via different ways. One mechanism is the dissociation of p120-catenin from the juxtamembrane domain of VE-cad, which leads to VE-cad endocytosis and thus also higher vascular permeability. On the other hand, clathrin-dependent endocytosis can be induced in VEGF-dependent interaction of β2-arrestin with VE-cad (Gavard and Gutkind, 2006); or by serine or tyrosine phosphorylation of VE-cad cytoplasmic tail (Orsenigo et al., 2012). Several factors have been shown to mediate phosphorylation of VE-cad (e.g. VEGF, TNF-α or intercellular adhesion molecule ICAM-1), but the molecular mechanisms are poorly understood. However, VE-PTP phosphatase, Src, Pyk2 tyrosine kinase or p21-activated kinase are some of the molecules that seem to be involved. Furthermore, phosphorylation of VE-cad associated proteins, such as β-catenin or p120-catenin, have also been implicated in VE-cad turnover (reviewed by Bravi et al., 2014; Harris and Nelson, 2010).

VE-cadherin couples the cytoskeleton to the junction

In AJs of epithelial cell-cell junctions, E-cadherin links to the actin cytoskeleton, while desmosomal cadherins interact with intermediate filaments (Vimentin). In ECs, which are devoid of desmosomes, VE-cad, through its more distal cytoplasmic tail, links to both the actin and the intermediate filament cytoskeleton (Figure I-6) (reviewed by Vincent et al., 2004). As mentioned just above, the cytoskeletal anchorage to the junctions is vital for the strength of a junction. However, the cytoskeleton is involved in most, if not all, cellular activities, such as cell migration and cell shape. Therefore, junctions can alter the actin cytoskeleton and alter cell behaviors.

In adhesive cells, filamentous actin (F-actin) usually assembles in an apical ring overlapping with the AJ. The junctional complex is supposed to be physically and functionally linked to the cytoskeleton. While β-catenin acts as a main cytoskeletal linker, Plakoglobin (a desmosomal protein) has some overlapping functions with β-catenin, it can mediate linkage of VE-cad to the actin cytoskeleton, but also to intermediate filaments (Figure I-6) (reviewed in Ratheesh and Yap, 2012).

The cadherin binding protein p120-catenin is another protein which interacts with the juxtamembrane domain of cadherins (Figure I-6); p120-catenin, however, is not exclusively found at cell junctions, but also at the leading edge of a migrating cell, controlling cell protrusions. Therefore, p120-catenin was proposed to link actin dynamics at the junction and at the leading edge of the cell (Boguslavsky et al., 2007), which is important for migration, e.g. in the tip cell of an angiogenic sprout. Furthermore, p120-catenin has important roles in VE-cad turnover and membrane localization (Figure I-6), and was also shown to regulate the activity of Rho family GTPases, such as RhoA, Rac and Cdc42. Together VE-cad and the Rho GTPases can locally modify actin dynamics through the localization and availability of VE-cad and p120-catenin (Navarro et al., 1995 and also reviewed in Vincent et al., 2004). Furthermore, endocytosis of Cadherins occurring via clathrin-dependent and -independent pathways were shown *in vitro* to be coordinated by the actin cytoskeleton (Yarar et al., 2005). During disassembly of junctional complexes, internalized VE-cad can activate Cdc42 (probably through its juxtamembrane domain), which regulates the actin cytoskeleton (e.g. membrane protrusions) (Kouklis et al., 2003).

Taken together, these changes in actin dynamics reflect adaptation of ECs to e.g. angiogenic cues, and therefore the cell-cell interface can alter cell behaviors.

1.2.1.2. Endothelial cell-selective adhesion molecule

Recently a new member of junctional proteins has been characterized: Endothelial cell-Selective Adhesion Molecule (Esam). Esam expression, like VE-cad, is restricted to the endothelium. Compared to VE-cad much less is known about the roles of Esam during vascular development.

Expression of Esam

Esam was first described in 2001 (Hirata Ki et al., 2001) and its expression in the mouse was found to be restricted to ECs, platelets and megakaryocytes (Hirata Ki et al., 2001; Nasdala et al., 2002). In zebrafish, next to ECs and the endocardium, Esam was also found to be expressed in a subset of neurons in the brain, which include the epiphysis/pineal gland (Wong et al., 2009).

Structure of Esam and interaction partners

Esam belongs to the JAM immunoglobulin superfamily of molecules, which are expressed on leukocytes and platelets and in TJs of epithelial and endothelial cells. This superfamily is characterized by an extracellular V-type and a membrane-proximal C2-type immunoglobulin domain, a single transmembrane domain and a cytoplasmic tail, containing a terminal PDZ domain binding motive (reviewed in Ebnet et al., 2004; Garrido-Urbani et al., 2014). To date, seven JAM members have been identified; classical JAMs, comprising JAM-A, JAM-B and JAM-C, and four related proteins: JAM-4, JAM-L, CAR (Coxsackie and Adenovirus Receptor) and Esam. Amongst these molecules, only JAM-B, JAM-C and Esam are expressed in ECs and not in epithelial cells (reviewed by Garrido-Urbani et al., 2014).

The JAM adhesion molecules can engage in homophilic, and most of these proteins can also interact with heterophilic ligands. Esam was shown to engage in homotypic, calcium-independent interactions (Hirata Ki et al., 2001; Kimura et al., 2010); however, heterophilic interactions with unknown ligands have been proposed (Inoue et al., 2010).

The cytoplasmic domain (120aa in mouse and human; 167aa in zebrafish) of Esam is structurally related to the cytoplasmic tails of JAM-4, JAM-L and CAR, while classical JAMs have shorter cytoplasmic tails (40-50aa). Esam's cytoplasmic tail contains a motive (PXXP), which interacts with SH3 (Src homology 3) domain signaling molecules, but no tyrosine residues that could be subject to phosphorylation (Hirata Ki et al., 2001). In ECs, Esam localizes to TJs and overlaps with cytoplasmic Zonula occludens 1 (Zo-1). Esam harbors conserved cytoplasmic PDZ domain binding motive and *in vitro* assays showed selective binding of PDZ domain proteins (Nasdala et al., 2002; Stalker et al., 2009). Zo-proteins or Par3, for example, are not binding partners of Esam, but they do bind JAMs (Ebnet et al., 2003; Nasdala et al., 2002; Wegmann et al., 2004). Moreover, Esam and its PDZ domain binding motive are required for junctional localization of MAGI1 (a membrane-associated guanylate kinase protein), while not all JAMs (actually only JAM4) interact with MAGI1 (Kimura et al., 2010; Wegmann et al., 2004). These interactions suggest differential roles of JAMs and Esam. Other PDZ domain molecules were shown to be able to bind to the Esam cytoplasmic tail *in vitro*,

but NHERF-1 was confirmed to interact with Esam in platelets (Stalker et al., 2009).

Functions of Esam during vascular morphogenesis

Esam null mutant mice were shown to be viable, without any vascular defects (Ishida et al., 2003). However, studies demonstrated that in Esam mutant mice, tumor angiogenesis was reduced which coincided with smaller tumor size, but also fewer vessels and disturbed vessel morphology. Further, Esam deficient cells, *ex vivo* and *in vitro,* show reduced angiogenic potential and migratory behavior, while overexpression of Esam accelerated tube formation *in vivo* (Cangara et al., 2010; Ishida et al., 2003).

Nevertheless, Esam is present in ECs during vascular development, suggesting specific roles, but its contributions for tube morphogenesis have not been investigated so far.

Involvement of Esam in cytoskeleton regulation and cell signaling

Membrane-associated guanylate kinase (MAGUK) proteins, despite their inactive kinase domain, contain several PDZ domains and are supposed to interact with many different cytosolic proteins. Zo-1, as MAGI1, also belongs to the MAGUK family. However, MAGI1, unlike Zo-1, does not contain a SH3 domain. Moreover, MAGI1 was shown to bind to cytoplasmic proteins, such as β-catenin, or α-actinin-4, implying roles in signaling and actin cytoskeletal dynamics (Wegmann et al., 2004). The latter has been confirmed: the inter-action of Esam and MAGI1 was shown to stimulate local actin polymerization via MAGI1-dependent RhoA activation (but not Rac) (Kimura et al., 2010).

Other roles of Esam during health and disease

In this short section I want to highlight some findings about Esam that are not relevant for my thesis. However, they underscore the importance of this molecule in the etiology of human diseases.

Esam is selectively involved in neutrophils and leukocytes, but not lymphocytes, extravasation at the step of diapedesis (Khandoga et al., 2009; Wegmann et al., 2006) and also inflammation-dependent vessel permeability regulation (Wegmann et al., 2006). Knockdown experiments supported the idea that Esam regulates activation of Rho GTPase to control the opening of

TJs (Wegmann et al., 2006). With this view, Esam was shown to be important for the maintenance of the glomerular endothelium. Mice lacking Esam showed higher albumin in the urine during high glucose treatment, suggesting vascular defects during diabetic diseases (Hara et al., 2009 and reviewed in Luissint et al., 2014). Moreover, soluble Esam was used as a marker for kidney failure during worsening of diabetes and atherosclerotic diseases (Kacso et al., 2013; Park et al., 2014).

Since Esam is also expressed on platelets, scientists looked into thrombus formation. As just mentioned, soluble fractions of Esam were found in plasma associated with atherosclerosis, making it a possible biomarker for atherosclerosis (Park et al., 2014; Rohatgi et al., 2009). Interestingly, Esam localizes to platelet-platelet contacts but also acts as a negative regulator during thrombus formation, since Esam deficient platelet aggregates were larger and more stable, compared to the control (O'Connor et al., 2009; Stalker et al., 2009). Furthermore, Esam seems to bind monocytes in an heterophilic manner, via an unknown ligand and thus supports the recruitment of immune cells to the atherosclerotic lesion (Inoue et al., 2010).

Other studies proposed Esam as an hematopoietic stem cells marker (Yokota et al., 2009). However, a subset of CD4$^+$ dendritic cells expresses Esam at high levels (Lewis et al., 2011).

During cancer diseases Esam was also associated with lymph node metastasis (Clasper et al., 2008).

Taken together, these studies support roles for Esam in stability and maintenance of junctions (mediated downstream of Esam), thrombus formation and immune cell recruitment.

1.2.2. Junctions and the actin cytoskeleton

A vertebrate body relies on its (bone) skeleton to have a given shape and move its body parts, without it we would all be just meat bags. Similarly, each cell in a body requires a cytoskeleton to take up a shape and perform tasks. Unlike bones, cells can change their neighboring cells and connect to other partners. The connections that build up (junctions) permit cells to engage with several partners (more than two other cells) and to build up a complex cell community. Eventually, the shape of an organ is given by the cytoskeleton of the cells and the specific connection they have made with each other.

The structural units of the actin cytoskeleton are actin monomers (globular (G-) actin), which assemble in two-stranded helical filaments (F-actin). F-actin can further gather as actin bundles or form a branched network. Many proteins can promote or block filament polymerization, stabilize the filaments, stimulate filament branching or attach filaments to the plasma membrane. Furthermore, actin filaments are very dynamic structures. They are not only in constant turnover, but also can generate contractile forces with the help of non-muscular myosin, making the junctional actin more dynamic and increase its F-actin content.

In this section I want to focus on actin forms that are present at junctions, and some aspects on the regulation of their dynamics. However, the following findings have been obtained mostly from *in vitro* experiments.

1.2.2.1. Assembly of F-actin at the junctions

As mentioned before, cadherins interact with the actin cytoskeleton and these interactions are important for cell-contact formation. Upon homophilic cadherin interactions, actin regulatory proteins are recruited to the adhesion site (Kovacs et al., 2002). Once the cell contact has formed, junctional actin remains highly dynamic and both, filamentous and branched F-actin, have been observed at these junctions. Furthermore, the actin nucleation activity is strongest at the junctional membrane. Actin nucleators at the junctions are Formins (such as Formin1) and Actin-related protein 2/3 (ARP2/3), while the latter is mainly found at cadherin based junctions (for review see Michael and Yap, 2013; Ratheesh and Yap, 2012). While Formins bind the barbed end

(growing end) of an actin filament, the ARP2/3 complex binds at the side of a filament and promotes, with association of nucleation-promoting factors (NPFs), the growth of a new filament (see Figure I-7) (reviewed in Michael and Yap, 2013; Ratheesh and Yap, 2012).

The activity of NPF and thus, actin polymerization, is regulated by Rho-family GTPases, such as Rac or Cdc42 and their GEFs (e.g. Tiam1 or Tuba, respectively). For example, homophilic cadherin engagement leads to the recruitment of Rac1 and Tiam1 to the new cell junctions in a cadherin-dependent manner. Actin nucleation is then initiated by Rac1-dependent activation NPFs (i.e. WAVE1 and WAVE2) of ARP2/3 (Kraemer et al., 2007; Otani et al., 2006; Yamazaki et al., 2007). The mechanism causing actin to be organized into a junctional ring is still not fully understood. However, a proposed model suggests that the initial actin network is elongated and these filaments are bundled into a ring shape (Michael and Yap, 2013).

Once a junctional ring has been formed dynamics are maintained and both, polymerization and depolymerization, occurs. Furthermore, non-muscular myosin (e.g. MyosinVI or isoforms of MyosinII), found at the junctions, can exert tension and deform junctional actin to different shapes (Smutny and Yap, 2010; Smutny et al., 2010).
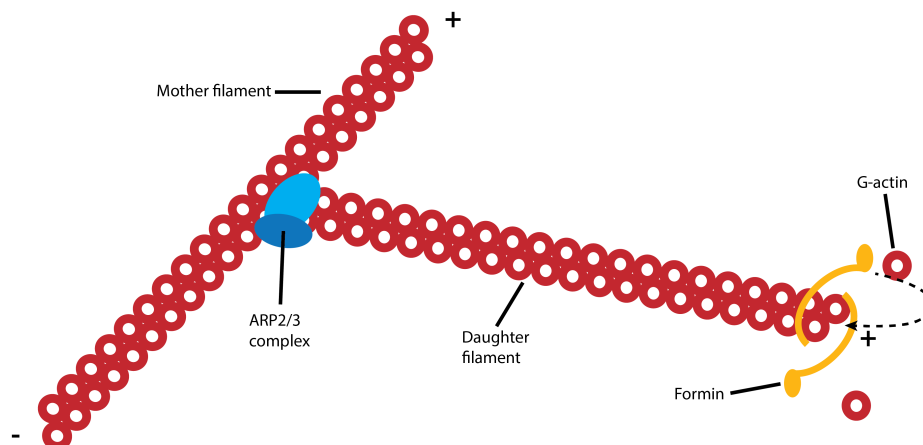
Figure I-7:   Actin filament nucleation

The ARP2/3 complex promotes filament branching by binding an existing filament (mother filament). The association of nucleation-promoting factors (NFPs, not shown) with ARP2/3 complex promotes the polymerization of the new branch. Formins bind the barbed end (+) of actin filaments and promote incorporation of G-actin into the filament. After Ratheesh and Yap, 2012.

1.2.2.2. Cytoskeletal regulation of the cell-cell interface

Several *in vitro* studies demonstrated subcellular differences in junctional coupling of actin and actin dynamics. Before junctions form *de novo*, a cell has a certain shape that is given by its cortical actin, e.g. an isolated cell may be spherical. When contacts form between two cells, their cortical actin rearranges and the tension within the cortical actin controls this process. The adhesive properties of junctional components (e.g. cadherins) have little function in the expansion of the cell-cell contact. However, cadherins are needed to couple the cortexes of the two cells and the modulation of cortical tension will drive the contact expansion (Maître et al., 2012). In a steady state, an actin belt runs parallel and overlaps with VE-cad in endothelial cells. Reorganization of the endothelial cell sheet locally reorganizes the actin cytoskeleton and F-actin attaches perpendicular to cell-cell contacts (referred as remodeling junctions). Here, Vinculin, a mechanosensing protein, prevents opening of the junction due to pulling forces exerted by the cytoskeletal remodeling (Huveneers et al., 2012). Another study showed that the local absence of VE-cad drives the formation of lamellipodia (marked by the ARP2/3 complex). This local lamellipodia formation, termed JAIL (junction-associated intermitted lamellipodia), facilitates the formation of new AJs (Abu Taha et al., 2014). In context of this *in vitro* study, JAIL allows sealing of the endothelial monolayer. If, how, and why, JAIL formation occurs *in vivo* needs to be determined. However, JAIL represents an adaptive mechanism, whereby local differences in junctional components drive polarized cell movements and/or cell shape changes.

With respect to sprouting angiogenesis, we know that the stalk and tip cells are very dynamic, and that there is a constant competition for tip cell position amongst the EC of an outgrowing sprout. The sensing of VEGFA and the integration of Notch signaling regulates these dynamics. Computational models, supported by *in vivo* data, have shown that fluctuation in these signaling pathways also regulate local turnover of VE-cad at the junctions (Bentley et al., 2014). This allows differential adhesion, which facilitates overtaking of cells during sprouting. The differential adhesion was also associated with local cell protrusions that support the migration of the cells.

These cell protrusions might represent the occurrence of JAIL during sprouting, however these have not been defined in this study.

Taken together, the actin cytoskeleton regulates the formation of junctions, but is also regulated by the junctions, through e.g. the Rho-family GTPases. The tight regulation of these processes vary in different contexts and more work is needed to understand the subtle changes occurring at cellular and subcellular levels during junctional complex.

1.2.3. Junctions and the cell polarity

ECs interact with different partners on their luminal or basal side, but how do these cells know where apical or basal is? Moreover, when ECs start sprouting, they leave their niche with defined apical-basal polarity. While they reorient their apical-basal axis, they also gain a directional polarity (front to rear). How are these polarities regulated during angiogenic sprouting or when there is no lumen?

1.2.3.1. Apical-basal polarity orchestrated at the cell-cell boundary

First described in *Caenorhabditis elegans*, proteins that are needed for asymmetrical cell division play important roles in apical-basal cell polarity signaling. Such proteins involve partitioning defective proteins (such as Par1 through Par6), small GTPase Cdc42, atypical protein kinase C (aPKC) and others that are usually found at the cell cortex (reviewed in Goldstein and Macara, 2007). These determinants are needed for asymmetrical cell division. However, apical-basal polarity is defined by similar mechanisms in cell communities or when two cells engage in homotypic interactions.

When two migrating cells meet, they form junctions and then they have to define apical (at the cell-cell contact) versus basal polarity. Hence, junctions are thought to form prior to polarization and are subsequently recruiting proteins that organize the cell's apical-basal polarity.

In epithelial cells, the formation of new junctions triggers cadherin-dependent activation of Cdc42, which then activates aPKC. The latter is a component of the core polarity complex (consisting of Par3, Par6 and aPKC itself). This polarity complex is then tethered to the most apical side of the junctions, the TJ, by interaction with JAMs. These interactions are thought to drive cell polarization processes (reviewed in Ohno, 2001). Although conserved amongst species, there might be differences in different cellular contexts.

1.2.3.2. Polarization processes in angiogenic sprouts

In regard to angiogenic sprouts, two different polarities have to be considered: apical-basal and directional (front versus rear) polarity. On the

one hand, ECs in the angiogenic sprout need positional information in respect to where they sit in axial axis (front versus rear). Additionally, during the outgrowth of the sprout, ECs overlap and this is important for subsequent lumen formation, which requires correct apical-basal polarity.

Apical-basal polarization in the angiogenic sprout

Endothelial cell culture experiments showed that VE-cad is necessary for the recruitment of polarity determinants (such as Par3 and aPKCz) and subsequent lumen formation (Lampugnani et al., 2010). This confirms that, similar to epithelial cells, cell junctions form prior to polarization in the endothelium. Moreover, like in epithelial cells, JAMs (JAM2 and JAM3) can also recruit the polarity complex to the endothelial junctions (through Par3) (Ebnet et al., 2003). Furthermore, activated Cdc42 appears to play a role in the recruitment of the cell polarity complex and the maintenance of polarity (Rojas et al., 2001).

Apical-basal polarization in the angiogenic sprout is poorly investigated. Recent investigation showed, that ECs in mouse retina or zebrafish ISV sprouts do polarize (Hayashi et al., 2013; Pelton et al., 2014). Research has show that apical membrane, labeled by Pdxl, accumulates between tip and juxtaposed trailing cell at the cell-cell interface. Furthermore, it was shown that aPKCz is required for cell-cell pairing and subsequent polarization (Pelton et al., 2014). Others showed that although downregulated in stalk cells, VEGFR2 has important roles, especially in the context of lumen formation and thus cell polarization. VE-PTP (via Tie2 receptor) dephosphorylates VEGFR2 associated in junctional complexes of stalk cells, reducing its activity. Therefore, VEGFR2 does not phosphorylate VE-cad (see also Figure I-4 for VEGFR2 and VE-cad interactions), which results in correct cell polarization, lumen formation and vascular quiescence (Hayashi et al., 2013). Thus, junctions appear to initiate the cell polarization process in ECs, similar to observations made during epithelial cell polarization.

An interesting property of tip cells is that they generate a second apical compartment when they anastomose (Blum et al., 2008; Herwig et al., 2011; Lenard et al., 2013). How this special polarization is regulated at the molecular level remains to be explored.

44

Defining front and rear

Once a tip cell has been selected, also its leading edge is specified. The tip cell has to interpret the signals and organize itself to orchestrate sprout outgrowth. The alignment of nucleus, Golgi, actin and microtubule cytoskeleton into rear to front position is one of the first steps of cell migration (Michaelis, 2014). In cell sheets, cadherin at cell-cell junctions was shown to orchestrate this polarization process in a Cdc42 dependent manner during migration (Desai et al., 2009), which eventually leads to the generation of lamellipodia at the leading edge. Lamellipodia formation needs the local inhibition of myosin dependent contraction, thus local loss of RhoA. Furthermore, lamellipodia formation is a tightly controlled process that does not only depend on Cdc42, but also on Rac activity (reviewed by Michaelis, 2014).

Sensing of growth factors by tip cells is commonly believed to occur over VEGFR2 in filopodial extension. However, a tip cell's filopodial extensions are dispensable to sense the VEGFA gradient (Phng et al., 2013). Nevertheless, the absence of filopodia delays the angiogenic process, especially anastomosis, due to the decreased migration speed of ECs.

As for the stalk cells in the sprout, it is unknown how they define front and rear. However, differential Notch and VEGF signaling (and maybe cell junctions) could contribute to directional determinants in stalk cells.

1.3. Zebrafish genetics

In this section I discuss the recently developed technologies, which I have used for targeted genome engineering. Reverse genetic tools will be generally introduced, but the focus lies on TALEN technology. However, this section is not directly related to the biological questions I have addressed in my thesis, but serves to help to better understand targeted mutagenesis in the zebrafish.

1.3.1. Forward genetics

The first genetic mutations in zebrafish were generated by **γ-irradiation** of sperm or fertilized eggs (Chakrabarti et al., 1983). Since the 1990s, chemical mutagenesis – by treating adult fish with **ENU** (N-ethyl N-nitrosourea) – was used in forward genetic screens to identify genes that are essential for embryonic zebrafish development (Driever et al., 1996; Haffter et al., 1996). More recently, reporter gene based screens allowed the isolation of genes, which are important for the formation of certain organs, such as the cardiovascular system (Jin et al., 2007).

1.3.2. Reverse genetics

While forward genetic screens led to the discovery of several hundreds of genetic loci, not all essential developmental genes could be identified although the screens were done to apparent saturation. For these reasons, the need for a reverse genetic approach became obvious. However, traditional targeted mutagenesis as in the mouse, was prohibited in the zebrafish system due to the lack of embryonic stem cell technology. Finally, to circumvent this obstacle, different strategies, such as morpholino-mediated knockdown, TILLING or gene-specific endonucleases, were established. These strategies are described below.

1.3.2.1. TILLING

TILLING (Targeting Induced Local Lesion in Genomes), a reverse genetics approach based on sequencing ENU-mutagenized fish, was one of the next steps in targeted zebrafish genome manipulation (Kettleborough et al., 2013). The "Wellcome Trust Sanger Institute" established a TILLING-based zebrafish mutation project (Kettleborough et al., 2013), which offers a big variety of knockout alleles. However, the time-consuming identification of point mutations and fish breeding limits the processing of requests.

1.3.2.2. Gene silencing

Gene knockdown strategies in zebrafish make use of **morpholino** antisense technology (for review see Bedell et al., 2011; Bill et al., 2009). Morpholino oligonucleotides (MO) are synthetic derivatives of DNA containing two major changes: (i) morpholine rings replace the deoxyribose backbone making it enzymatically non-degradable, and (ii) non-ionic linkage, which causes less toxicity and makes the oligonucleotide cell permeable (Summerton and Weller, 1997). These antisense oligonucleotides are injected into 1-cell stage eggs and bind target RNA either at the start codon (translation start blocking) or at splice acceptor or donor sites (inhibition of precursor mRNA splicing). This knockdown strategy is efficient until 50 hpf (Nasevicius and Ekker, 2000). The gene silencing efficiency can continue for several more days, depending on the MO availability in the embryo. Electroporation techniques make MO applicable also to adult fish tissues (Thummel et al., 2011). However, some MOs do not work well, produce artifacts or bind RNA unspecifically causing secondary phenotypes, which are sometimes difficult to interpret and separate from specific ones (for review see Eisen and Smith, 2008). Recently it has become apparent that some of the reported morphant phenotypes could not be reproduced by genetic mutations (A. Krudewig, personal communication; Kok et al., 2015; van Impel et al., 2014). These results make mutant alleles unavoidable to study the function of genes.

1.3.2.3. Targeted mutagenesis

Introduction of customized DNA nucleases has ushered zebrafish research into a new era of reverse genetics: zinc finger nucleases and mainly

TALEN and CRISPR/Cas9 are now widely used to generate desired genomic alterations (for review see Schulte-Merker and Stainier, 2014). But how can these nucleases induce mutations?

DNA double strand breaks (DSBs) activate the cell's intrinsic DNA repair mechanisms: homologous recombination (HR) or non-homologous end joining (NHEJ). During HR the cell uses a homologous template (e.g. unbroken sister chromatid) to repair the break site. NHEJ is an error-prone process where the two broken ends are joined without the help of a homologous template and this usually leads to insertions or deletions. The cell's choice of the DNA repair mechanism (NHEJ or HR) depends on the phase of the cell cycle and the nature of the DSB (for detailed review see Chapman et al., 2012). Nonetheless, NHEJ appears to be the major repair mechanism (Carroll, 2014; Mao et al., 2008).

To introduce DSBs specifically at a desired locus the zebrafish community uses different synthetic molecules and deploys error-prone NHEJ, which induce frame-shift mutations and thus premature stop codons. The DSBs-inducing synthetic molecules will be introduced in order of appearance.

ZFN

Zinc Finger Nucleases (ZFNs) were the first synthetic endonucleases being used to induce DSBs in the zebrafish genome to alter desired loci (Doyon et al., 2008; Meng et al., 2008). Before being used in zebrafish ZFNs have been successfully used in other model organisms, such *as Arabidopsis thaliana, Drosophila melanogaster* and rats, but also in different stem cell cultures (for review see Urnov et al., 2010).

The specific repetitive zinc finger modules used in ZFNs were discovered in a transcription factor of *Xenopus laevis* (Miller et al., 1985), and bind approximately 3 base pairs (bp) each. Each module is built up of approximately 30 amino acids (aa) and interacts with given base pairs by binding into the major groove of the DNA helix.

To realize a designed endonuclease, the DNA binding zinc finger array needs to be fused to a DNA cleavage domain. Generally the cleavage domain of the FokI restriction enzyme is used, because this enzyme's DNA binding and DNA cleavage domain are functionally separated (Li et al., 1992). For a

ZFN to work, its cleavage domain (FokI domain) has to dimerize. Therefore two ZFNs are needed, they are oriented in opposite directions and their DNA binding domains have to be spaced correctly so the FokI domains can dimerize appropriately (Figure I-8).

Although ZFNs have been successfully used in several organisms, including zebrafish, they come with a big disadvantage: not every locus is targetable. Each module recognizes three base pairs and each ZFN should consist of at least 3 modules, this makes it difficult and sometimes even impossible, to find a target site at the desired locus. Further, a single zinc finger module that works fine in one context might not do so in a different one (Ramirez et al., 2008). If ZFN are constructed using a context-dependent assembly (CoDA) platform the probability for functional multifinger arrays are increased. Using CoDA, potential ZFN target sites are found only every 500bp (Sander et al., 2011b).
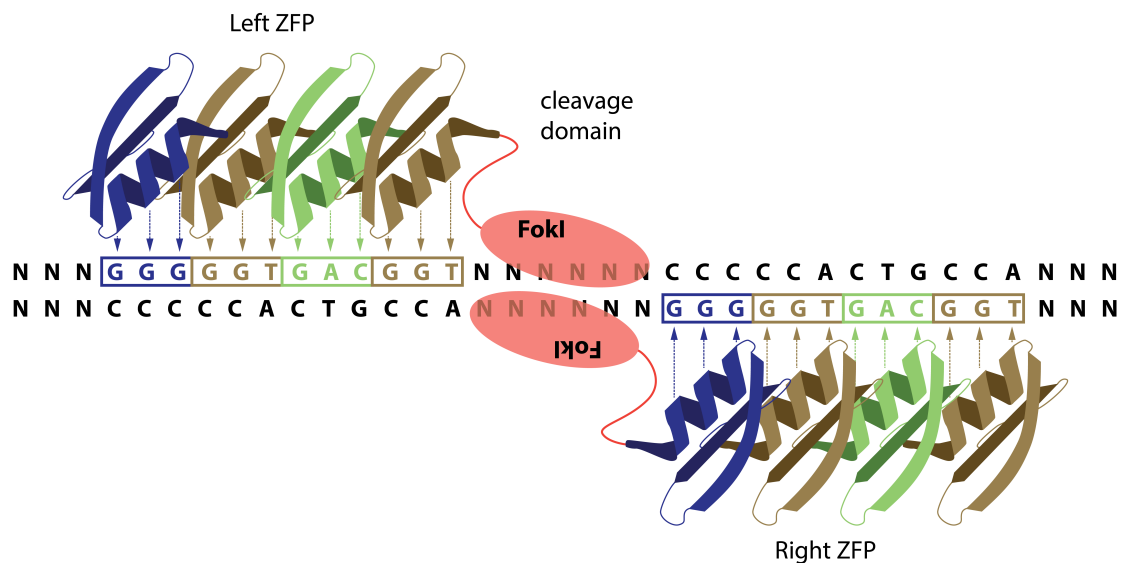
Figure I-8:   Structure of zinc finger nucleases

Schematic representation of a zinc finger nuclease (ZFN) dimer binding its target DNA sequence. Each ZFN contains an array of three to six zinc finger modules (four are shown here) and is fused to the cleavage domain of FokI. Two ZFN are needed for FokI domains to dimerize and cleave the DNA between the DNA-binding modules. After Urnov et al., 2010.

TALEN

Transcription Activator-Like Effectors (TALEs) originate from plant pathogens of the genus *Xanthomonas*. These bacteria use their type III secretion system to inject TALEs through cell walls into host cells. Once in the cell, TALEs enter the nucleus, bind effector-specific sequences and alter target gene transcription expression, favoring the bacterial colonization (Bogdanove et al., 2010).

TALE proteins contain a N-terminal domain that binds a thymidine residue, a DNA binding domain in the middle and a C-terminal domain. The TALEs DNA recognition domain is built in a modular fashion, where each module consists of 33aa to 35aa. However, they are not analogous to any other DNA-binding motive. The last repeat in a TALE is only a partial module, referred to as half repeat. The aa sequence of these modules is highly conserved, with an exception of two adjacent aa in the middle of the element. These two aa are called repeat variable diresidue (RVD) and biochemical and bioinformatics analyses have identified the RVD's specificity to DNA nucleotides (Boch et al., 2009; Moscou and Bogdanove, 2009). There are many RVDs with different affinities to different nucleotides, however the following RVDs have high affinities for single DNA nucleotides: NH for guanine, NG for thymine, HD for cytosine and NI for adenine (for review see Scott et al., 2014).

The mode of TALE-DNA interaction is very specific: the array of tandem TALE repeats wraps around and into the major groove of the DNA double helix in a helical fashion. Every repeat on its own has an α-helical secondary structure, which is broken by the RVD. This break produces a finger-like protrusion with the RVD at the tip pointing towards the DNA double helix and permits interaction with a single nucleotide (Deng et al., 2014; Mak et al., 2012). (Crystal structures that resolved the mode of TALE-DNA interactions are beautifully illustrated by Mak et al., 2012).

The modular structure of TALEs allows rapid construction of sequence specific DNA binding proteins, which can be further engineered to TALE nucleases (TALENs) by fusing the TALE to the catalytic domain of the FokI restriction enzyme (Figure I-9) (Christian et al., 2010). Two neighboring TALENs can induce DSB at a desired locus. Many methods to generate

TALENs were developed (for review see Scott et al., 2014). The foremost technique uses Golden Gate cloning strategy (see methods 2.2.4.1); here plasmids are picked from a big library digested with one type IIS restriction enzyme (e.g. BsaI) (Cermak et al., 2011). This enzyme recognizes a given palindrome but cuts outside of the recognition site, which creates a unique overhang (sticky end), allowing directional cloning (for details consult chapter 2.2.4). This cloning strategy allows generation of TALENs within five days.

TALEN technology has been thoroughly used in a wide variety of organisms (Carroll, 2014) and has quickly been added to the zebrafish genetic toolbox (Huang et al., 2011; Hwang et al., 2014; Sander et al., 2011a). This may be due to the advantage that TALEN come with only one restriction: the target sequence has to start with a thymine. This makes virtually every locus targetable. However, construction of TALENs requires some consideration, because not every RVD binds DNA with the same strength. Some of the "weaker" RVDs can also have preferences for a second nucleotide, reducing the specificity of the TALEN. Therefore, at least 3 "strong" RVDs must be present in the TALE and long stretches of low affinity RVDs should be avoided (Streubel et al., 2012). Further, also the DNA state influences the success of TALENs (Scott et al., 2014). In some cases the binding of TALEs to transcriptionally inactive chromatin is greatly reduced. Indeed, many studies suggest that DNA methylation reduces TALE(N) binding efficiency. CpG dinucleotides are heavily methylated in vertebrate genomes. This is a major concern for TALEN efficacy, since it is well-known that the RVD that binds cytosine (HD) does not bind methylated cytosine (Valton et al., 2012).
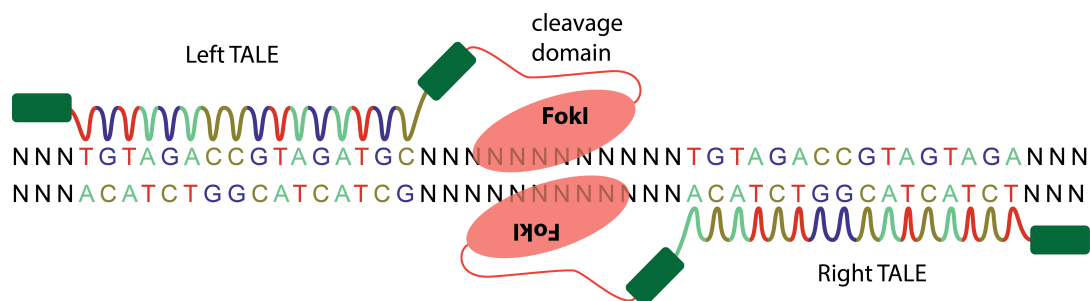
Figure I-9:   Schematic representation of TALEN

A TALE repeat domain recognizes a single DNA nucleotide, while an array of such repeats recognizes a stretch of DNA. A pair of TALENs oriented in opposite

directions, allows the dimeric FokI nuclease domains to cleave the DNA within the spacer region. Subsequent NHEJ creates insertion or deletion mutations.

CRISPR/Cas9

Bacteria and archaea possess an adaptive immune system that protects them from foreign DNA (e.g. viruses or plasmids). This immune system is encoded by clustered regularly interspaced short palindromic repeats (CRISPR) and the associated CRISPR-associated (Cas) proteins. CRISPR loci are arrays of short repetitive sequences that are "spaced" by sequences that are homologous to foreign DNA. Upon infection, the bacteria's Cas proteins incorporate small fragments of the invading DNA into the CRISPR array. They then use this new information as a template for crRNA (CRISPR RNA), which forms a complex with Cas proteins to degrade the invading genome (for review see Charpentier and Marraffini, 2014). In this way the CRISPR-Cas system provides a system to cleave DNA in sequence specific manner, which has been very rapidly adapted to the genome engineering toolbox.

The type II CRISPR system is one of the best-studied bacterial immune systems and requires only three components to mediate sequence specific cleavage. These three components have been derived from *Streptococcus pyogenes* and are: (i) Cas9 protein, which harbors two nickase domains (one for each DNA strand) to induce DBS together; (ii) the crRNA, which contains the target information (~20bp); and (iii) the tracrRNA (trans-activating crRNA). In *S. pyogenes*, crRNA and tracrRNA form a duplex (due to overlapping homology region), which is then able to guide Cas9 to an invading DNA molecule. Proper targeting by Cas9 also requires the presence of a protospacer adjacent motif (PAM; usually a triplet of 5'-NGG) next to crRNA target sequence on the invading DNA (Carroll, 2014; Charpentier and Marraffini, 2014; Scott et al., 2014). Implementing this system for genome engineering has been simplified by fusion of crRNA and tracrRNA to a chimeric single-guide RNA (gRNA), which reduces the requirements to two CRISPR/Cas components (Jinek et al., 2012) (Figure I-10).

Immediately after the chimeric gRNA efficacy had been validated (Jinek et al., 2012), groups started to use the CRISPR/Cas system to target the genes of their model organisms and cell lines. Simultaneously with reports in cell culture, zebrafish groups published efficient genome modifications (Hwang et al., 2013), claiming highly effective gene knock-in (Auer et al., 2014) and concurrent biallelic disruption of multiple genomic targets (Jao et al., 2013). Other studies determined more detailed requirements for the gRNA. For example, the targeting region, usually 20bp, can be shortened to 17bp or 18bp, which still allows efficient mutagenesis (Fu et al., 2014). Longer gRNA targeting regions with up to 22bp were shown to work efficiently (Ren et al., 2014), giving a dynamic range of 17-22bp to search for target sites. Moreover, a correlation between GC content of the PAM proximal 6 nucleotides and mutagenicity has been observed, where higher content usually improved the results (Ren et al., 2014).

The quick progress in genome modification with CRISPR/Cas has been possible, because the system requires only one protein for any target, while the short gRNAs are easily and quickly produced. This is in contrast to ZFNs or TALENs technologies, where every target requires 2 different proteins and the synthesis of the constructs is time-consuming. So far the CRISPR/Cas system seems to work without any drawbacks, but scientists argue that the off-target effect has to be considered. Several reports have shown that the gRNA guiding process allows mismatches (Seruggia and Montoliu, 2014) and since there is only one targeting sequence, the probability for off-target is higher than for ZFNs or TALENs, where two targeting sequences work together. For efficient on-target guidance the "seed" region of the target region is crucial. The seed sequence is determined by the 8-12 bases located 5' to the PAM in the DNA (respectively 3' of the target-homology region in the gRNA; see also Figure I-10 where the seed sequence corresponds to the numbered bases 1 to 12) (Cong et al., 2013; Jinek et al., 2012). A more recent study argues that the first 5 nucleotides adjacent to the PAM are a vital part of the seed sequence to guide Cas9 to the target (Wu et al., 2014). They further suggest a model, whereby gRNA loaded Cas9 recognizes PAM, locally melts the DNA to allow the short seed sequence to pair. Subsequent DNA unwinding and pairing distal to the PAM induces Cas9 mediated DSB.
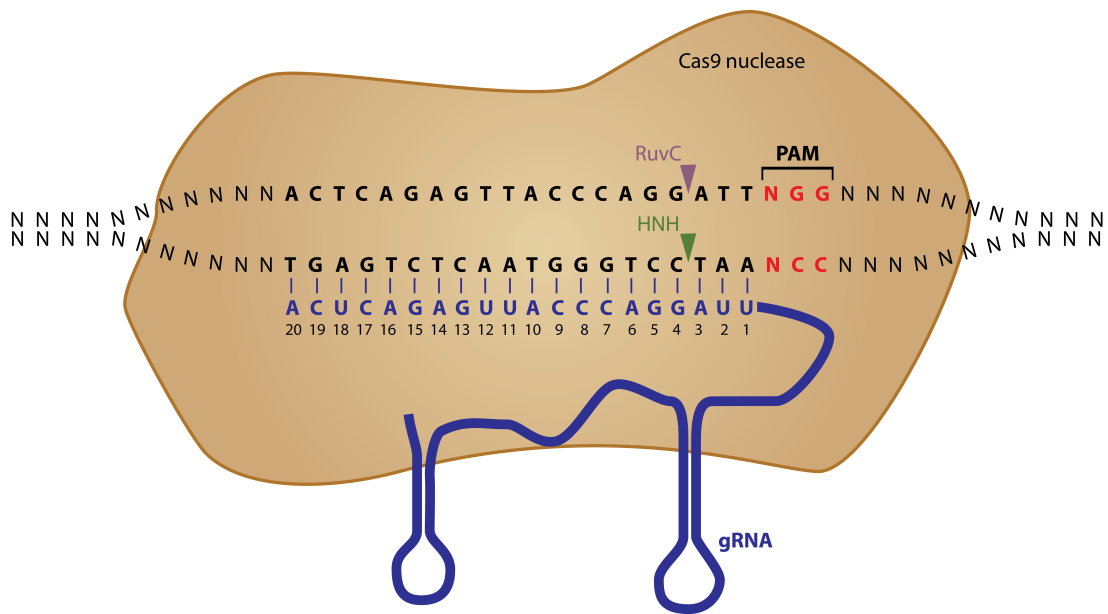
Figure I-10:   Schematic representation of Cas9 based DNA targeting

Cas9 protein is guided by chimeric gRNA (red) to the complementary sequence (20bp) in the genome (blue sequence) that is followed by the PAM sequence. Once this complex has formed, Cas9 protein induces a DSB with its two nickase domains (RuvC and HNH). After Sander and Joung, 2014.

54

1.4. Aim of the thesis

Organ morphogenesis requires coordinated cell behaviors to shape complex multicellular structures. Each cell contributes during these processes and cell-cell interaction and communication are indispensable. During vascular morphogenesis, ECs remain associated to each other through adhesive interactions mediated at the cell junctions. The Affolter lab has investigated the cell behaviors that contribute during angiogenic sprouting, using live imaging at single cell resolution. The aim of my thesis was to analyze how the junctional proteins VE-cad and Esama contribute to these dynamic cell behaviors during angiogenic sprouting and blood vessel fusion.

Chapter II

Materials and Methods

2.1. Materials

2.1.1. Buffer, Media and Solutions

Name	Composition
Alkaline Tris buffer	100mM Tris-HCl pH9.5 50mM MgCl2 100mM NaCl 0.1% Tween-20
BCIP solution	50mg 5-bromo-4-chloro-3-indolyl phosphate (BCIP, Sigma) in N,N-dimethylformamide (anhydrous) store at -20°C in the dark
Blocking solution	5% normal goat serum 1% BSA 0.1% Triton X-100 0.01% sodium azide in PBST
Blocking solution (in situ)	2% sheep serum 2mg/ml BSA 0.01% sodium azide 1x PBST
DNA loading buffer (10x)	30% (v/v) glycerol 20% (w/v) Orange G in ddH$_2$O store at -20°C
E3 (50x)	250mM NaCl 8.5mM KCl 16.5mM CaCl2 16.5mM MgSO4 adjust pH7.0-7.4 (with Na$_2$CO$_3$)
egg water	1:2000 Methylene blue solution (final 0.0005%) 1x E3
Hybridization Mix	5x SSC 50% deionized Formamide 50µg/ml Heparin 500µg/ml torula RNA (Sigma) adjust to pH6 (460µl 1M citric acid per 50ml solution) store at -20°C
LA	0.3% Agar in LA autoclave add antibiotics after cooling down to 50°C

Labeling solution	225µl NBT solution 50ml Alkaline Tris Buffer 175µl BCIP solution
LB	1% (w/v) tryptone 0.5% (w/v) yeast extract 1% (w/v) NaCl ddH$_2$O autoclave
LB w/o salt	1% (w/v) tryptone 0.5% (w/v) yeast extract ddH$_2$O autoclave
Methylene blue solution	1% Methylene Blue (Sigma) ddH$_2$O
Morpholino stock solutions	300nmol MO were dissolved in 300µl ddH$_2$O final concentration is 1mM (~8ng/nl)
NBT solution	50mg Nitro Blue Tetrazolium (NBT, Sigma) 70% N,N-dimethylformamide ddH$_2$O store at -20°C in the dark
PBS (10x)	1.37M NaCl 27mM KCl 100mM Na2HPO4 18mM KH2PO4 ddH$_2$O autoclave
PBST	1x PBS 0.1% Tween-20
PBSTX	0.5% Triton X-100 in PBST
PFA (4%)	heat 500ml 1xPBS pH7.2 to 60°C (under the hood) add 40g Paraformaldehyde add 2N NaOH drop by drop until PFA dissolved cool down, adjust volume to 1l with 1x PBS filtrate store at -20°C
PTU (50x; 2mM)	0.15% (w/v) 1-Phenyl-2-thiourea (PTU) (Sigma-Aldrich) in egg water
SSC (20x)	3M NaCl 300mM NaCitrate ddH$_2$O adjust pH7 autoclave
Stop solution (in situ)	1x PBS pH5.5 1mM EDTA 0.1% Tween-20

TAE (50x)	2M Tris Base 5.71% (v/v) glacial acetic acid 50mM EDTA ddH$_2$O autoclave
TBE (5x)	445mM Tris Base 445mM Boric Acid 10mM EDTA (pH 8.0) Filtering by 0.22µm filter delays precipitation.
Tricaine (25x)	0.4% (w/v) Tricaine (Sigma) ddH$_2$O adjust pH7.0 with 1M Tris HCl store at -20°C

2.1.2. Antibiotics

Antibiotic	Stock concentration	Working concentration
Ampicillin	100 mg/ml	100 µg/ml
Kanamycin	50 mg/ml	50 µg/ml
Streptomycin	10 mg/ml	50 µg/ml
Chloramphenicol	34 mg/ml	34 µg/ml
Tetracycline	3 mg/ml	10 µg/ml
Spectinomycin	50 mg/ml	50 µg/ml

2.1.3. Bacterial strains

Name	Genotype	Source
Top10	F- *mcrA* Δ(*mrr-hsd*RMS-*mcr*BC) φ80*lacZ*ΔM15 Δ*lacX74 rec*A1 *ara*D139 Δ(*araleu*)7697 *gal*U *gal*K *rps*L (Str^R) *end*A1 *nup*G	Invitrogen
ccdB survival	*F-mcrA Δ(mrr-hsdRMS-mcrBC) Φ80lacZΔM15 ΔlacX74 rec*A1 *ara*Δ139 Δ(*ara-leu*)7697 *gal*U *gal*K *rps*L (Str^R) *end*A1 *nup*G *fhuA*::IS2	Invitrogen

60

2.1.4. Fish lines

Name	Allele Designation	Description	Reference
kdrl:EGFPnls	UBS1	transgene	Blum et al., 2008
fli1ep:gal4ff	UBS3	transgene	Herwig et al., 2011
UAS:EGFPhZO1, cmlc:EGFP	UBS5	transgene	Herwig et al., 2011
VE-cadherin 4bp deletion	UBS8	mutant	Sauteur et al., 2014
VE-cadherin 9bp deletion	UBS9	mutant	Sauteur et al., 2014
5xUAS:VEcadΔC-EGFP	UBS12	transgene	Lenard et al., 2013
BAC(kdrl:mKate2-CAAX)	UBS16	transgene	Lenard et al., 2013
4xUAS:FR-mKate2	UBS17	transgene	This study
4xUAS:EGFP-UCHD	UBS18	transgene	This study; Sauteur et al., 2014
Esama 10bp deletion (Exon2)	UBS19	mutant	This study
4xUAS:mRuby2-UCHD	UBS20	transgene	This study
4xUAS:mRuby2-UCHD	UBS21	transgene	This study
4xUAS:mClav-UCHD		transgene	This study
4xUAS:mCherry-zfpdxl		transgene	This study
fli1a:EGFP	y1	transgene	Lawson and Weinstein, 2002b
kdrl:EGFP	s843	transgene	Jin et al., 2005
UAS:RFP		transgene	Asakawa et al., 2008
UAS:lifeact-EGFP		transgene	unpublished, Marina Mione lab, KIT (previously in Milan)
UAS:EGFP		transgene	Marina Mione lab, KIT; Feng et al., 2010
tp1:venus-PEST	s940	transgene	Ninov et al., 2012

2.1.5. Plasmids and cDNA clones

Plasmid name	Description	Anti-biotic	Reference
Esama_probe	*esama* cDNA in TOPO blunt vector (Invitrogen); for in situs; SP6 antisense (linearize with XhoI); T7 sense control (linearize with BamHI)	Kan	gift from Nicole Müller-Sienerth at Wellcome Trust Sanger Institute, Cambridge
Esamb_probe	*esamb* cDNA was amplified with P40 and P41 from pME18S-FL3_ESAMb_cDNA and cloned into pBSIIKS (Addgene) with KpnI and SacI; for in situs; T7 antisense (linearize with Acc65I); T3 sense control (linearize with SacI)	Amp	This study
fli1a probe	no sequence information available; for in situs; T7 antisense (linearize with BamHI)	N/A	handed over by Elin Ellertsdottir
pcDNA3-mRuby2	mammalian expression vector encoding far-red fluorescent protein mRuby2	Amp	addgene; Lam et al., 2012
pCS2-transposase	Tol2 transposasse; linearize with NotI	Amp	Kwan et al., 2007
pCS2+GFP-UCHD	vector containing EGFP fused to utrophin calponin homology domain	Amp	Bement lab, Burkel et al., 2007
pFUS_A	lacZ flanked by BsaI sites for the insertion of TALEN array of RVD 1 to 10	Spec	addgene; Cermak et al., 2011
pFUS_A_E111A	pFUS_A containing forward first array of RVDs for targeting *esama* exon1	Spec	This study
pFUS_A_E112A	pFUS_A containing reverse first array of RVDs for targeting *esama* exon1	Spec	This study
pFUS_A_E221A	pFUS_A containing forward first array of RVDs for targeting *esama* exon2 site 2	Spec	This study
pFUS_A_E222A	pFUS_A containing reverse first array of RVDs for targeting *esama* exon2 site 2	Spec	This study
pFUS_A_E311A	pFUS_A containing forward first array of RVDs for targeting *esama* exon3 site 1	Spec	This study
pFUS_A_E312A	pFUS_A containing reverse first	Spec	This study

	array of RVDs for targeting *esama* exon3 site 1		
pFUS_A_E321A	pFUS_A containing forward first array of RVDs for targeting *esama* exon3 site 2	Spec	This study
pFUS_A_E322A	pFUS_A containing reverse first array of RVDs for targeting *esama* exon3 site 2	Spec	This study
pFUS_B_E111B	pFUS_B containing forward second array of RVDs for targeting *esama* exon1	Spec	This study
pFUS_B_E112B	pFUS_B containing reverse second array of RVDs for targeting *esama* exon1	Spec	This study
pFUS_B_E221B	pFUS_B containing forward second array of RVDs for targeting *esama* exon2 site 2	Spec	This study
pFUS_B_E222B	pFUS_B containing reverse second array of RVDs for targeting *esama* exon2 site 2	Spec	This study
pFUS_B_E311B	pFUS_B containing forward second array of RVDs for targeting *esama* exon3 site 1	Spec	This study
pFUS_B_E312B	pFUS_B containing reverse second array of RVDs for targeting *esama* exon3 site 1	Spec	This study
pFUS_B_E321B	pFUS_B containing forward second array of RVDs for targeting *esama* exon3 site 2	Spec	This study
pFUS_B_E322B	pFUS_B containing reverse second array of RVDs for targeting *esama* exon3 site 2	Spec	This study
pFUS_B1 to pFUS_B10	lacZ flanked by BsaI sites for the insertion of TALEN array of RVD 11 to N-1	Spec	addgene; Cermak et al., 2011
pHD1 to pHD10	TALEN RVD for cytosine	Tet	addgene; Cermak et al., 2011
pLR-HD	TALEN last half repeat for cytosine	Spec	addgene; Cermak et al., 2011
pLR-NG	TALEN last half repeat for thymine	Spec	addgene; Cermak et al., 2011
pLR-NH	TALEN last half repeat for guanine	Spec	addgene; Cermak et al., 2011
pLR-NI	TALEN last half repeat for adenine	Spec	addgene; Cermak et al.,

			2011
pmClavGR2-NT	expression vector encoding photoconvertible reporter mClavGR2 (for N-terminal fusions)	Amp	Allele Biotech
pME18S-FL3_ESAMb_cDNA	*esamb* EST cDNA clone (IMAGp998L2215582Q)	Amp	GeneCube LifeSciences
pmKate2-N	mammalian expression vector encoding far-red fluorescent protein mKate2	Kan	Evrogen
pNG1 to pNG10	TALEN RVD for thymine	Tet	addgene; Cermak et al., 2011
pNH1 to pNH10	TALEN RVD for guanine	Tet	addgene; Cermak et al., 2011
pNI1 to pNI10	TALEN RVD for adenine	Tet	addgene; Cermak et al., 2011
pT2_4xUAS:eGFP-UCHD	Tol2, 4xUAS, eGFP fused to Utrophin 1aa-261aa	Amp	This study; Sauteur et al., 2014
pT2_4xUAS:FRmKate2	FR-mKate2 with 4xUAS from PUC57_4Xnr	Amp	This study
pT2_4xUAS:mCHERRYzfpodo	Tol2, 4xUAS, mCherry fused to zf Podocalyxin 2, cloned from pT2UASmCHERRYzfpdxl_cmlcEGFP	Amp	This study
pT2_4xUAS:mClav-UCHD	Tol2, 4xUAS, mClav fused to Utrophin 1aa-261aa	Amp	This study
pT2_4xUAS:mRuby2-UCHD	Tol2, 4xUAS, mRuby2 fused to Utrophin 1aa-261aa	Amp	This study
pT25xUASFRGFP	FR-GFP cloned into pT25xUASMCS	Amp	Zurzolo lab; Paladino et al., 2008
pT2UASmCHERRYzfpdxl_cmlcEGFP	Tol2, 5xUAS, mCherry fused to zf Podocalyxin; heart specific GFP	Amp	unpublished, Yannick Blum
pT2UASMCS_FRmKate2	Tol2, 5xUAS, folate receptor sorting sequence fused to mKate2	Amp	This study
pUC57_4Xnr	Synthetic DNA containing MCS and 4x non-repetitive UAS (designed by Lukas and Yannick)	Amp	Lukas Herwig, Yannick Blum, This study
RCIscript_GoldyTALEN	TALEN backbone with central lacZ flanked by Esp3I sites for directional replacement with TALEN DNA binding domain	Amp	addgene; Bedell et al., 2012; Carlson et al., 2012

64

RCIscript_Goldy TALEN_E111	Forward TALEN for *esama* Exon1 (RVDs replaced lacZ of RCIscript_GoldyTALEN); linearize with SacI	Amp	This study
RCIscript_Goldy TALEN_E112	Reverse TALEN for *esama* Exon1 (RVDs replaced lacZ of RCIscript_GoldyTALEN); linearize with SacI	Amp	This study
RCIscript_Goldy TALEN_E221	Forward TALEN for *esama* Exon2 site 2 (RVDs replaced lacZ of RCIscript_GoldyTALEN); linearize with SacI	Amp	This study
RCIscript_Goldy TALEN_E222	Reverse TALEN for *esama* Exon2 site 2 (RVDs replaced lacZ of RCIscript_GoldyTALEN); linearize with SacI	Amp	This study
RCIscript_Goldy TALEN_E311	Forward TALEN for *esama* Exon3 site 1 (RVDs replaced lacZ of RCIscript_GoldyTALEN); linearize with SacI	Amp	This study
RCIscript_Goldy TALEN_E312	Reverse TALEN for *esama* Exon3 site 1 (RVDs replaced lacZ of RCIscript_GoldyTALEN); linearize with SacI	Amp	This study
RCIscript_Goldy TALEN_E321	Forward TALEN for *esama* Exon3 site 2 (RVDs replaced lacZ of RCIscript_GoldyTALEN); linearize with SacI	Amp	This study
RCIscript_Goldy TALEN_E322	Reverse TALEN for *esama* Exon3 site 2 (RVDs replaced lacZ of RCIscript_GoldyTALEN); linearize with SacI	Amp	This study
RCIscript-T7_GoldyTALE N_E221	RCIscript_GoldyTALEN_E221 with T7 instead of T3 promoter; linearize with BstEII and BsaI	Amp	This study
RCIscript-T7_GoldyTALE N_E222	RCIscript_GoldyTALEN_E222 with T7 instead of T3 promoter; linearize with BstEII and BsaI	Amp	This study

2.1.6. Oligonucleotides

2.1.6.1. Morpholino oligonucleotides

MO working concentration is described in Buffer, Media and Solutions 2.1.1. The MOs were kept at RT in tightly sealed vials or tubes.

MO	Sequence	Source / Reference
cdh5-splice	TTTACAAGACCGTCTACCTTTCCAA	Nicoli et al., 2007
Esama-ATG	GTTTTGCTGAAGTTCGTCTCTCCAT	This study
Esama-MO1	GGAGGTACTGAAAGAGACAGAATGG	O'Connor et al., 2009
Esama-E2I2	TAAAAGGCAATCACCATTTCAGTGC	This study main MO
STD-control	CCTCTTACCTCAGTTACAATTTATA	GeneTools, LLC

2.1.6.2. Primers

Generally the primer stock solutions (100µM) and the working solutions (5µM) were kept at -20°C.

Primer	Name	Sequence
cdh5_1	cdh5-FWD	TTGGTGTAACTGACAATGGGG
cdh5_2	cdh5-REV	ACAGTCTTGGTGTTACCATTGGG
cdh5_3	cdh5-WT-FWD	ATCCCCGTTTTCGATTCTGAC
cdh5_4	cdh5-ubs8-REV	CTGATGGATCCAGATTGGAATC
P1	FR-mKate2_1.1_fwd	GAATTCCCGGAGAGCCACCTCCTCT
P2	FR-mKate2_1.2_rev	TGTTCTCCTTAATCAGCTCGCTCACCATGGCCTCGCTTATTAGTTTTTGTTCTGC
P3	FR-mKate2_2.1_fwd	TGCGACCTCCCTAGCAAACTGGGGCACAGAcccgggGCCATGAGTGGGGCTGGGCCCTGGG
P4	FR-mKate2_2.2_rev	GTTAACTTGTTTATTGCAGCTTATA
P5	FR-mKate2_3.1_fwd	GCAGAACAAAAACTAATAAGCGAGGCCATGGTGAGCGAGCTGATTAAGGAGAACA
P6	FR-mKate2_3.2_rev	CCCAGGGCCCAGCCCCACTCATGGCcccgggTCTGTGCCCCAGTTTGCTAGGGAGGTCGCA
P11	SV40_HpaI_rev	CGATGTTAACTTGTTTATTGCAGCTTATA
P12	eGFP-Utro_AgeI_fwd	CGATACCGGTCGCCATTCTGCCTGGGGAC
P30	gESAMa_seq1_fwd	ATGGTCTTTCAGTCAGCGAG

66

P36	eGFP_screen_fwd	ACGTAAACGGCCACAAGTTCAG
P37	TAL1_fwd	ttggcgtcggcaaacagtgg
P40	ESAMb_cloning_fwd_Kpnl	ATGCGGTACCCACACTGTCCTCCATAGCCAC
P41	ESAMb_cloning_rev_Xhol	ATGCCTCGAGGCTTTATAGCTTCCTGCTCATG
P42	pCR8_F1	ttgatgcctggcagttccct
P43	pCR8_R1	cgaaccgaacaggcttatgt
P44	TAL_R2	ggcgacgaggtggtcgttgg
P45	SeqTALEN_5-1	catcgcgcaatgcactgac
P55	ESAMaE2_seq4_rev	GTGTGGCAGTTTAATTCAAATC
P94	cdh5_HA1_control_fw	ACAGTGTGTTTGCATCATTG
P95	gal4ff_HA1_control_rev	AGTAGCGACACTCCCAGTTG
P99	ESAMaE2-totWT-fwd	GGATGTGATCCAAGGGAAG
P101	ESAMaE2-mut10bp-rev	CCACCATCTTCCCTCCA
PLH55	TOPO_rev_EGFP_gateway	TTACTTGTACAGCTCGTCCATG
PLH189	5'galP4	CGCTACTCTCCCAAAACCAAAAGG
PLH190	3'galP4	TCTCTTCCGATGATGATGTCGCAC
PLH200	seq_3'lifeact-gfp	GTTGTGGCTGTTGTAGTTGTAC

2.1.7. Antibodies

2.1.7.1. Primary antibodies

Name	Host species	Usage	Remarks	Reference
α-ve-cadherin	Rat	1:200	generation partially by Dimi Bieli; tested by Charles Betz	unpublished
α-Zo-1	Mouse	1:100		Invitrogen
α-Esam-a	Rabbit (#1)	1:200	Main Esam-a antibody	This study Sauteur et al., 2014
α-Esam-a	Rabbit (#2)	1:100		This study
α-Esam-a	Guinea pig	1:200		This study
α-Pdxl-2	Rabbit	1:200		Herwig et al., 2011

2.1.7.2.   Secondary antibodies

Name	Host species	Usage	Source
α-rat Alexa 647	Goat	1:700	abcam
α-mouse Alexa 568	Goat	1:1000	abcam
α-mouse Alexa 633	Goat	1:1000	abcam
α-rabbit Alexa 405	Goat	1:700	abcam
α-rabbit Alexa 568	Goat	1:1000	abcam
α-rabbit Alexa 633	Goat	1:1000	abcam

2.1.8. Microscopes and binoculars

2.1.8.1.   Confocal microscopes

If not indicated differently, these microscopes are point scanning confocal microscopes.

Microscope	Manufacturer	Information	Objectives
SP5MP	Leica	PMT; HyD	10x air; NA=0.3 20x air; NA=0.7 40x water; NA=1.1 63x glycerol; NA=1.3
SP5 Matrix	Leica	PMT; HyD	10x air; NA=0.3 40x water; NA=1.1 63x glycerol; NA=1.3
Ultraview (spinning disk)	Perkin Elmer	EMCCD	40x oil; NA=1.25-0.75 63x water; NA=1.2 100x oil; NA=1.4-0.7
3i (spinning disk)	3i	EMCCD	40x water; NA=0.75 63x oil; NA=1.4 100x oil; NA=1.4
LSM700	Zeis	PMT	40x oil; NA=1.3 63x oil; NA=1.4
FV1000 (at EMBL, Heidelberg)	Olympus	SIM scanner for manipulation with pulsed laser (355, 375 and 532nm)	30x silicon; NA=1.05

68

2.1.8.2.   Microscopes

Microscope	Manufacturer	Information	Objectives
Dissecting scope Leica DM 6000 B	Leica	Dissecting scope with CryLaS FTSS355-50 laser	10x air; NA=0.3 20x air; NA=0.4 40x water; NA=0.8 63x water; NA=0.9
Nikon Microphot-FXA (DIC)	Nikon		4x air; NA=0.13 10x air; NA=0.3 20x air NA=0.5 40x air; NA=0.7

2.1.8.1.   Fluorescence binoculars

Microscope	Manufacturer	Information
Leica M205 FA	Leica	Fluorescence binocular

2.2. Methods

2.2.1. Zebrafish protocols

2.2.1.1. Fish maintenance

Zebrafish were raised and maintained at standard conditions as described in "The Zebrafish Book" (Westerfield, 2000). Embryos were staged by hpf at 28.5°C (Kimmel et al., 1995).

Embryo dechorionation

Embryos (>24hpf) were either dechorionated with forceps (Dumont #5F) or chemically with Pronase (Roche). For chemical dechorionation Pronase stock solution (5mg/ml) was added to 1x E3 (usually 100µl per petri dish) containing the embryos and incubated until the first embryo was freed from his chorion. Thereafter, the remaining chorions were removed by gently pipetting the embryos up and down and the reaction was immediately stopped, by washing the embryos 4 times in 1x E3.

Pigmentation inhibition

For imaging, the embryo pigmentation was inhibited by incubation in 1x E3 supplemented with 1x PTU starting from ~26hpf.

DNA, MO and RNA injections

Borosilicate glass needles for injections were produced from capillaries (outer diameter 1.0mm, inner diameter 0.5mm, 10cm length; Sutter Instruments) with a needle puller (Sutter Instruments). Freshly laid eggs were mounted into the grooves of molded agarose (1% in 1x E3) in petri dishes and covered with egg water. Glass needles were loaded with injection mixture using Microloader tips (Eppendorf) (according to Table II-1), broken at the tip with forceps and finally the needle was connected to FemtoJet Injector® (Eppendorf). The constant pressure was set to minimum and the injection pressure was adjusted (visually, while injecting) to a volume of approximately 5nl. The single cell (one-cell stage) of the freshly laid eggs was then injected.

MO sequences are found in chapter 2.1.6.

Table II-1:   Injection mixes

Purpose	Injection mix	Injection volume
Tansgenesis	15ng/µl Tol2 transposase mRNA 20-60ng/µl plasmid in ddH$_2$O	2-4nl
MO knock down	0.1-0.2mM MO (~0.8-1.6ng/nl) in 1% phenol red	4-10nl
Mutagenesis	~150ng/µl of each TALEN mRNA optionally: 30ng/µl GFP mRNA for injection control (mRNA done by Rebecca Billig)	2-8nl

2.2.1.2.   DNA extraction by alkaline lysis

DNA extraction by alkaline lysis were performed according to Meeker et al., 2007. Briefly, larval fin biopsies, single embryos or adult fin biopsies were placed in 10µl, 50µl or 200µl 50mM NaOH respectively. Lysis was performed at 95°C for 5-20min (until the tissue was dissolved), cooled down to 4°C and neutralized by adding 1/10th volume of 1M Tris HCl pH8. Prior use in PCR, the cell debris were pelleted by centrifugation.

2.2.1.3.   Genotyping

Adult fin clip

Adult zebrafish were anesthetized in 1x E3 containing 1x tricaine. Paralyzed fish were placed on a sterile surface and the caudal fin was spread. A razor blade was pressed vertically onto the distal part of the caudal fin and a pipette tip was used to slide along the razor blade, cutting off the fin. The DNA of the tissue sample was extracted by alkaline lysis (see section 2.2.1.2). Fin clipped fish were kept individually in single cages containing egg water (to prevent infections) until genotypes were determined (maximally 7 days).

Larval fin clips

Larval fin biopsies were obtained as described by Wilkinson et al., 2013. Briefly, zebrafish larvae (3 to 5 days old) were anesthetized in 1x E3 containing 1x tricaine. Paralyzed larvae were placed onto a petri dish lid that has been lined with strip of autoclave tape and the excess liquid was removed. With a microscalpel the fin biopsy was cut off distal to blood circulation loops (within the ventral pigment gap, see also Wilkinson et al.,

2013). The tissue sample was removed using a P20 pipette and processed by alkaline lysis (see section 2.2.1.2). Individual larvae were placed into 24 well plates containing 1x E3 until genotypes were resolved. Larvae of the same genotype were then pooled and raised to adulthood at standard conditions.

UBS8 PCR

To identify wt versus UBS8 heterozygous or homozygous individuals a PCR with four primers was performed according to Table II-2 and Table II-3. The allele unspecific product (548 bp) generated by the two external primers is outcompeted by the shorter wt specific (387 bp) and/or the UBS8 specific product (195 bp) (see also Figure S2 in Sauteur et al., 2014).

Table II-2:   UBS8 genotyping mixture

Component	Final concentration
DNA template	(~1µl genomic DNA)
Titanium Taq Buffer 10x	1x
Primer chd5_1	0.5µM
Primer chd5_2	0.5µM
Primer chd5_3	0.5µM
Primer chd5_4	0.5µM
dNTPs	125µM
Titanium Taq DNA polymerase	0.1-0.2x

Table II-3:   UBS8 thermocycling reaction

Step	Temperature	Duration	
Initial denaturation	96°C	2min	
Denaturation	96°C	30sec	35 cycles
Annealing	66°C	30sec	
Extension	70°C	20sec	

UBS19 PCR

To identify wt versus UBS19 heterozygous or homozygous individuals a PCR with four primers was performed according to Table II-4 and Table II-5 (Figure III-15 C). The allele unspecific product (482 bp) generated by the two external primers is outcompeted by the shorter wt specific product (356 bp) and/or the UBS19 specific product (142 bp).

Table II-4:   UBS19 genotyping mixture

Component	Final concentration
DNA template	(~1µl genomic DNA)
Titanium Taq Buffer 10x	1x
P30	1.25µM
P55	1.25µM
P99	1.25µM
P101	1.25µM
dNTPs	250µM
Titanium Taq DNA polymerase	0.1-0.2x

Table II-5:   UBS19 thermocycling reaction

Step	Temperature	Duration	
Initial denaturation	95°C	2min	
Denaturation	95°C	30sec	31 cycles
Annealing	62°C	30sec	
Extension	68°C	30sec	
Final extension	68°C	5min	

Gal4 PCR

To genotype for TgBAC(*cdh5:Gal4FF*)[mu101] primer P94 and P95 were used in a PCR according to Table II-7 and Table II-8 (58°C annealing and 30 sec extension). Positive individuals produce a PCR product of 320 bp size.

To genotype for Tg(*fli1ep:gal4ff*)[ubs3] primer PLH189 and PLH190 were used in a PCR according to Table II-7 and Table II-8 (58°C annealing and 30 sec extension). Positive individuals produce a PCR product of 292 bp size.

EGFP PCR

To genotype for Tg(*UAS:EGFP*) primer P36, PLH55 and PLH200 were used in a PCR according to Table II-7 and Table II-8 (58°C annealing and 30 sec extension). Positive individuals produce a PCR product of ~400 and ~700 bp size.

2.2.1.4.   Tol2 transposase *in vitro* mRNA transcription

Generally, mRNA was transcribed with Ambion kits. 1µg of NotI-linearized pCS2FA-transposase plasmid was used to transcribe mRNA with mMESSAGE mMACHINE® SP6 Transcription Kit (Ambion) according to manufactures protocol. The LiCl precipitated RNA was resuspended to ~500ng/µl, aliquoted and stored at -80°C until usage.

2.2.1.5.   Immunohistochemistry

Embryos were raised in egg water until 24hpf and thereafter in 1x E3 containing 1x PTU until the desired developmental stage and fixed in 2% PFA o/n at 4°C. PFA was washed of by several washes in PBST and the specimens were subsequently permeabilized for 2hr at RT in PBST containing 0.5% Triton X-100 (Sigma). To saturate for nonspecific binding sites for the antibody, the embryos were incubated in Blocking solution o/n at 4°C. The specimen were incubated in primary antibody (diluted in Blocking solution) o/n at 4°C. The primary antibody solution was recollected and used in other experiments. The specimen were washed more than 6 times in PBST during 6-8 hr at RT and then incubated in secondary antibody (diluted in Blocking solution) o/n at 4°C. After the incubation the secondary antibody solution was recollected for usage in other experiments, the specimen were washed more than 6 times in PBST during 6-8hr at RT and imaged subsequently.

2.2.1.6.   *in situ* hybridization

The *in situ* hybridization protocol was adapted form (Thisse and Thisse, 2014).

DIG-labeled RNA probe synthesis

DIG-labeled RNA was transcribed from linearized plasmid template with the appropriate (T3, T7 or SP6) RNA polymerase and ingredients (according to Table II-6) for 2hr at 37°C.

Table II-6:   DIG RNA labeling reaction

1µg linearized plasmid
1x DIG RNA labeling mix (Roche)
1x Transcription buffer (Roche)
20U RNase inhibitor (Roche)
40U RNA polymerase (Roche)
Up to 20µl Nuclease Free H_2O (Ambion)

Template DNA was then degraded by incubation with 2U TURBO DNase I (Ambion) for 15min at 37°C, and the RNA was precipitated using LiCl (protocol and reagents of Ambion mMessage mMachine transcription kits). Pre- and post-precipitation RNA were checked on Ethidium Bromide gel. RNA was frozen at -80°C until use.

Preparation of the embryos

Eggs were collected right after they were laid and raised to the desired developmental stage (e.g. 30hpf), while the formation of pigments was prevented. The chorions were chemically removed before fixation in 4% PFA (o/n) at 4°C.

The embryos were dehydrated by incubation in 100% Methanol for 15min at RT, during this process the Methanol was exchanged once. Thereafter the embryos (in Methanol) were incubated -20°C for more than 2hr.

The embryos were successively rehydrated in Methanol dilutions (75% / 50% / 25% (v/v) Methanol and PBST, each step for 5min) and finally washed 4 times for 5min in PBST. Then, the embryos were permeabilized with Proteinase K (Roche) (10µg/ml in PBST) at RT. Depending on their developmental stage, the incubation with Proteinase K was prolonged (e.g. embryos at 28hpf for 15min, or 36hpf for 20min). Proteinase K was inhibited by fixation of the embryos in 4% PFA for 20min at RT and subsequently washed 4 times for 5min in PBST.

In situ hybridization

The embryos (less than 100) were prehybridized in 700µl Hybridization mix for 5hr at 67°C. Then the Hybridization mix was replaced with 200µl fresh one, containing 50ng DIG-labeled RNA probe and 5% Dextran Sulfate (Merck Millipore) and the incubation was continued o/n at 67°C. The next day, the buffer was successively exchanged to 0.2x SSC. Therefore, the embryos were incubated in each of the following pre-warmed (67°C) mixes for 10min: 100% Hybridization mix (w/o RNA and heparin), 75% / 50% / 25% (v/v) Hybridization mix in 2x SSC, and 2x SSC. Finally the embryos were washed twice 30min in pre-warmed 0.2x SSC at 67°C.

Thereafter, the SSC was progressively replaced with PBST by incubating the embryos at RT in 75% / 50% / 25% (v/v) 0.2x SSC in PBST and finally 100% PBST 10min for each step.

In situ labeling reaction

After the buffer exchange to PBST, the embryos were blocked for 3-4hr at RT in Blocking solution (*in situ*) and the AP-anti-DIG antibody (Roche) was applied onto the samples, diluted 1:5000 in Blocking solution (*in situ*). After

o/n incubation at 4°C, the antibody was washed away by 6 times 15min PBST incubations.

To prevent the formation of precipitates the samples were washed once in alkaline Tris buffer devoid of $MgCl_2$ and subsequently incubated twice for 5min in normal alkaline Tris buffer. To start the colorimetric reaction, the embryos were incubated at 37°C in freshly made labeling solution and monitored. The incubation time varies a lot, however for my reactions, I had to incubate fli probe labeled embryos for 4-5hr at 37°C. Finally, the labeling reaction was stopped by washing twice in Stop solution (*in situ*).

The embryos were kept in Stop solution at 4°C in the dark until usage or placed in 100% Glycerol (Sigma-Aldrich) o/n at room temperature to be imaged the next day. Embryos were mounted in Glycerol on glass slides for imaging on a Nikon Microphot-FXA microscope.

2.2.2. Image acquisition and analysis

2.2.2.1.   Specimen mounting

Before mounting, embryos were anesthetized in 1x E3 containing 1x tricaine and selected on a fluorescent binocular (Leica M205 FA).

0.7% low melting agarose (LMA) (Sigma) was dissolved in 1x E3. Before usage, the LMA was melted in the microwave and supplemented with 1x tricaine and 1x PTU (not necessary for fixed samples). The LMA mixture was kept at 50°C during mounting. A glass bottom dish (MatTek) was coved with LMA and allowed to cool down a bit. Life embryos or tail of fixed specimen (cut off with a razor blade) were dropped with a fish pipette into the agarose drop and orientated with a handle with eyelash.

2.2.2.2.   Confocal imaging

Generally, laser intensities and detector intensities or exposure times were set to obtain single saturated pixels. For recording 3D images (stacks of focal planes) the step size in z-directions was set from 0.1µm to 1µm for objectives with magnification higher than 20x, for objectives with magnification with 10x or 20x the section thickness was set to 1µm to 4µm.

For short and o/n time lapse recordings the incubation chamber of the confocal microscope was set to 28.5°C. When recording single images of live or fixed sample, the imaging was done at RT.

Point scanning confocal imaging

The majority of microscopy was performed on point scanning confocal microscopes (e.g. Leica SP5). Here the point scanner was set to 400Hz, 700Hz or 1000Hz. In some occasions the resonanz scanner option was chosen (8000Hz). For time-lapse imaging the interval between to time points was set to 5 to 10min. If multiple positions were recorded simultaneously the number of positions was chosen so that two time points were not further than 9 to 10min apart form each other.

Spinning disk confocal imaging

Spinning disk confocal microscopy was usually chosen for high temporal resolution (with ∆t<1min). Here, the laser intensities and exposure times were adjusted to obtain best signal to noise ratio and least photobleaching.

2.2.2.3.   Laser microsurgery

Confocal microsurgery

Confocal tip cell ablation was performed on an Olympus FV1000 confocal microscope with 355nm pulsed laser (at EMBL ALMF Heidelberg, Germany). Movies were recorded suing a 30x silicone immersion objective with a frame size of 640x640 pixels and a z-step size of 0.8µm. A stack was acquired before tip cell ablation. For laser microsurgery, the lasering plane was recorded only. Lasering was performed in this plane, using a tornado movement of the laser at 65% power for three consecutive frames. Thereafter, imaging in the confocal plane was continued for some seconds (~1min). Subsequently, stacks were acquired for several hours with 7min interval.

Dissecting scope microsurgery

Laser ablation experiments were performed with a dissecting scope (Leica DM 6000 B) equipped with a single-pulse laser. However, with this setup the highest useable magnification is a 20x dry objective and therefore does not allow high-resolution imaging. The lasering was performed with a power of 86, a speed of 2, specimen balance of 0 and an offset of 80. Tip cells were ablated manually with very short pulses (less than 2 seconds) to induce least tissue damage. For subsequent live imaging, specimen were brought to a confocal microscope (e.g. Leica SP5) or fixed for immunostainings.

2.2.2.4.   Image deconvolution

Only oversampled (∆z < 0.2µm), high-resolution (>1024x1024pixel) images were used for deconvolution. Raw data was uploaded on to the server (HRM: smb://131.152.25.73/hrm_data/) and processed over the online interface (https://huygens.bc2.unibas.ch/hrm/). Results were retrieved from the server.

2.2.2.5.   Image analysis

Image analysis was done using Fiji (open source, ImageJ) and Imaris (Bitplane).

Junctional ring quantification

For a more specific junctional signal two junctional stains (Zo-1 and Esama) were intersected using the co-localization function in Imaris (Bitplane) software. This co-localization channel was used to reconstruct the junctions in 3D in semi-automated manner (with the Filament tracking module of Imaris). The 3D coordinates of the junctions were exported as a list of data points, which could be handled by a custom made Python script (by Nikolaus Ehrenfeuchter). In brief, the Python script for volumetric calculation selects the two most distant points in the list and divides the junctional area by tessellation along the junctional circumference. The value for area was then calculated by summing up the areas of single polygons that were produced by the tessellation step. The junctional perimeter was calculated as well. More information and links to Python scripts are indicated in (Sauteur et al., 2014).

2.2.3. Molecular biology protocols

2.2.3.1. Preparation of electrocompentent cells

A fresh colony was picked to inoculate LB w/o salt containing the appropriate antibiotics and grown o/n at 37°C with 200 rpm. In the following morning, the culture was diluted 1:100 in LB w/o salt (without antibiotics), grown to OD_{600} = 0.6-0.8 and cooled down in an ice slurry. Bacteria were pelleted in a precooled centrifuge, washed once in 10% glycerol (sterile and ice cold) and resuspended in 10% glycerol in a 100th of the initial volume. Bacterial suspension was aliquoted and used immediately or frozen in liquid nitrogen for storage at -80°C.

2.2.3.2. PCR amplification

Taq polymerase

Taq DNA polymerase (NEB) was usually used for amplifications that did not require high fidelity (e.g. genotyping).

Table II-7:   PCR with Taq DNA polymerase

Component	Final concentration
DNA template	variable
ThermoPol buffer 10x	1x
Forward Primer	0.5µM
Reverse Primer	0.5µM
dNTPs	200µM
Taq DNA Polymerase	1-2 units

Table II-8:   Thermocycling reaction with Taq DNA polymerase

Step	Temperature	Duration	
Initial denaturation	95°C	30sec	
Denaturation	95°C	30sec	30 cycles
Annealing	50-65°C	30sec	
Extension	68°C	1min/kb	
Final extension	68°C	5min	

Phusion polymerase

Phusion High Fidelity DNA polymerase (NEB) was generally used for reactions that require high fidelity (e.g. cloning).

Table II-9:   PCR with Phusion DNA polymerase

Component	Final concentration
DNA template	variable
HF buffer 10x	1x
Forward Primer	0.5µM
Reverse Primer	0.5µM
dNTPs	200µM
Phusion DNA Polymerase	1-2 units

Table II-10:   Thermocycling reaction with Phusion DNA polymerase

Step	Temperature	Duration	
Initial denaturation	98°C	30sec	
Denaturation	98°C	30sec	30
Annealing	50-70°C	30sec	cycles
Extension	72°C	30min/kb	
Final extension	72°C	5-10min	

2.2.3.3.   Restriction enzyme digestion

General restriction

Plasmid or purified PCR products were digested with appropriate restriction enzyme(s) according to Table II-11. The mixtures were incubated for 1-3 hr at 37°C and analyzed by gel electrophoresis. For subsequent cloning the fragments were purified by gel extraction using NucleoSpin Gel and PCR Clean-up (Macherey-Nagel).

Table II-11: Restriction enzyme digestion

Component	Final concentration
DNA	1-5µg
NEB buffer 10x	1x
Enzyme	5-10 units

Amplicon restriction digest

To screen for palindrome alteration after genome modification (by TALEN or CRISPR) 5µl of PCR product of locus of interest were directly digested in 20µl containing 10 units restriction enzyme with 1x corresponding NEB buffer. Mix was incubated for 3-4 hr at 37°C and analyzed by gel electrophoresis.

T7 endonuclease I Assay

T7 endonuclease I assay (T7EI) allows the specific cleaving double stranded DNA (dsDNA) at mismatches, e.g. for mutation screening. The protocol is was adapted from (Jao et al., 2013; Reyon et al., 2012). Briefly, the region of interest was amplified by PCR (e.g. from genomic DNA of mutagenized embryos), checked on a gel for only one single band and purified using NucleoSpin Gel and PCR Clean-up. 200ng of purified PCR product were supplemented with 1x NEB Buffer 2 (NEB) and heteroduplexed by melting at 95°C for 5min, cooling down to 85°C at a speed of 2°C/sec and further slowly (0.1°C/sec) cooled down to RT (25°C). Heteroduplexed DNA was incubated for 15min at 37°C with 10U of T7 endonuclease I in a reaction volume of 20µl and subsequently analyzed on Ethidium bromide gel.

2.2.3.4. Ligation

The amount of backbone and insert was calculated according to Equation II-I, which equals in a ration of 1:5 (backbone : insert). The reaction was set up in a minimal volume (i.e. 10µl) of fresh 1x Reaction Buffer (NEB) containing 400 units of T4 DNA Ligase (NEB). The mixture was incubated o/n at 16°C, in the morning for additional 2hr at RT and subsequently used to transform electrocompetent cells.

Equation II-I: backbone (b) to insert (i) ratio for ligation.

bp, length of the backbone or insert in number of nucleotides.

$$m_b[ng] \times \frac{5 \times bp_i}{bp_b} = m_i[ng]$$

2.2.3.5.　　　Transformation of electrocompetent cells

Electrocompetent cells were thawed on ice mixed with construct (20-100ng) or plasmid (<500pg) into a Gene Pulser/Micro Pulser 1mm Cuvette (Bio-Rad) and electroporated at 1.8kV with a MicroPulser (Bio-Rad). Subsequently the cells were resuspended in LB (without antibiotics) and incubated for 1hr at 37°C. Dilutions of cells were plated on LA with appropriate antibiotics.

2.2.3.6.　　　Plasmid purification

Plasmids that were used to inject directly into one-cell staged eggs were purified using NucleoBond® Xtra Midi Plus EF (Machery-Nagel) kit. Others with NucleoBond® Xtra Midi Plus (Machery-Nagel) kit when needed in big quantities or for smaller quantities with NucleoSpin® Plasmid (Machery-Nagel).

2.2.3.7.　　　Sequencing

Sequencing was performed at Microsynth using barcode labeled tubes. Reactions mixtures were assembled as indicated on the company's website (www.microsynth.ch).

2.2.4. TALEN assembly

2.2.4.1. Golden gate reactions

TALENs were chosen and assembled as described by (Cermak et al., 2011), using their plasmid kit deposited at Addgene. Importantly, TALEN sites (15-20 RVDs spaced by 15-24 nucleotides) that contain a restriction palindrome in the spacer region were chosen to facilitate mutation screening afterwards.

Briefly, the first Golden Gate reaction assembles the RVD modules in directed fashion. The RVD modules are encoded in plasmids pAAx, where AA stands for the RVD (e.g. HD, NH, NI or NG) and x stands for the position of the RVD in the array. The first 10 RVD clones plus the pFUS_A plasmid are mixed, while RVD 11 to N-1 plus pFUS_B plasmid are assembled in a separate reaction. In a cycling reaction, BsaI cuts the plasmids, creating unique overhangs that are ligated in ordered fashion (see Table II-12 and Table II-13).

Table II-12: Golden Gate reaction I assembly

Component	Amount
RVD containing plasmid RVD_1-RVD_{10} or RVD_{11}-RVD_{N-1}	150ng each
Array plasmid (pFUS_A or pFUS_B) A or B_{N-11}	150ng
BsaI (NEB)	10U
T4 DNA ligase (NEB)	2000U
T4 DNA ligase buffer 10x (NEB)	1x
H_2O	Up to 20µl

Table II-13: Restriction-ligation cycling reaction I

Temperature	Duration	
37°C	5min	10 cycles
16°C	10min	
50°C	5min	
80°C	5min	

After the cycling and heat inactivation reactions, 25nmol of ATP and 10U of Plasmid Safe DNase (Epicentre) were added and incubated for 1hr at 37°C to degrade linearized DNA products. Subsequently, bacteria (*E. coli* Top10)

were transformed with 1µl reaction mix and plated on LA containing Spectinomycin (50µg/ml), X-gal (20µg/ml), and IPTG (100µM). The next day, transformants negatively selected for β-galactosidase expression and check for the correct construct by PCR. Colony PCR was assembled with P42 and P43 and a bit of the colony (instead DNA) according to Table II-7 a run according to Table II-8 (55°C annealing and 1.75min extension). Correct transformants show a smear and a laddering of bands, with the strongest band at approximately 120 times the number of assembled RVDs (e.g. for 10 RVDs the strongest band is around 1.2kb). The correct colonies were expanded and plasmid DNA was extracted with NucleoSpin® Plasmid.

The next Golden Gate reaction assembles the A and B intermediary arrays together with the last (half repeat) RVD into the TALEN backbone (RCIscript_GoldyTALEN, Carlson et al., 2012). Like the first golden gate reaction, Esp3I creates unique overhangs, allowing directional cloning. The reactions were assembled according to Table II-14 and the mixture was digested and ligated according to protocol (see Table II-15).

Table II-14: Golden Gate reaction II assembly

Component	Amount
pFUS_A and pFUS_B containing the arrays	150ng each
Last repeat plasmid (pLR vector)	150ng
RCIscript_GoldyTALEN vector	75ng
Esp3I (Thermo Fisher Scientific)	10U
T4 DNA ligase (NEB)	2000U
T4 DNA ligase buffer 10x (NEB)	1x
H$_2$O	Up to 20µl

Table II-15: Restriction-ligation cycling reaction II

Temperature	Duration	
37°C	5min	10 cycles
16°C	10min	
37°C	15min	
80°C	5min	

Subsequently, bacteria (*E. coli* Top10) were transformed with 1µl reaction mix and plated on LA containing Ampicillin (100µg/ml), X-gal (20µg/ml), and IPTG (100µM). The next day, transformants negatively selected for β-galactosidase expression and check for the correct construct by PCR. Colony

PCR was assembled with P37 and P44 and a bit of the colony (instead DNA) according to Table II-7 a run according to Table II-8 (55°C annealing and 3min extension). Correct transformants show a smear and a laddering of bands, with the strongest band at approximately 3kb. The correct colonies were expanded and plasmid DNA was extracted with NucleoSpin® Plasmid. Finally, the plasmid was sequenced using P44 and P45. Since the repetitive nature of the RVDs causes trouble in sequence alignments, the aa sequence was used to check the correctness of the clone.

2.2.4.2. Promoter conversion and transcription of TALENs

The RCIscript_GoldyTALEN scaffold harbors a T3 promoter suitable for *in vitro* transcription (Bedell et al., 2012; Carlson et al., 2012). Therefore, the respective TALEN plasmids were linearized using SacI (NEB) restriction enzyme according to Table II-11. The transcription reaction was performed according to mMESSAGE mMACHINE® T3 Transcription Kit (Ambion) and the resulting capped RNA was aliquoted and frozen at -80°C until use.

However, the T3 transcription kit yields capped RNA that is not 100% translatable. To increase *in vivo* translation I used a transcription kit that prevents reverse capping of RNA. Therefore, the initial T3 promoter GoldyTALEN scaffold was replaced with a T7 promoter. First, an amplicon was generated with a T3 to T7 conversion primer (reverse primer) P80 and P79 according to Table II-9 and Table II-10 (57°C anneal and 10sec extension) from RCIscrip_GoldyTALEN template. Then the short fragment was cloned into the respective TALEN scaffolds by digestion with AflIII (NEB) and HindIII (NEB) and subsequent ligation (see Table II-11 for digest and chapter 2.2.3.4 for ligation). Bacteria (*E. coli* Top10) were transformed with the ligation mixture and plated on LA containing appropriate antibiotics. Colonies were picked, expanded, prepped and the plasmids sequenced for T7 promoter insertion.

For the transcription of the T7 promoter TALENs, the plasmids were linearized using BstEII (NEB) and BsaI and the band (approximately 4kb) was purified by gel extraction using NucleoSpin Gel and PCR Clean-up kit (to get rid off a second T7 promoter located 3' of the construct). The DNA fragment was then used as a substrate for RNA transcription with the mMESSAGE

mMACHINE® T7 ULTRA Transcription Kit (Ambion). This transcription yields translatable orientated capped RNA that has been poly(A)-tailed in a second reaction step of the kit. The RNA was aliquoted and stored at -80°C until use.

2.2.5. Generation of transgenic lines

2.2.5.1. Cloning of constructs

Generally the reports were cloned downstream of a 4 times non-repetitive (4xnr) UAS (upstream activation sequence) to be driven by the Gal4 transcription factor (Akitake et al., 2011). Due to its reduced repetitive sequence the transgenic DNA is supposed to be less silenced in animals.

For efficient targeting of mRNA to ribosomes in the organisms, a short Kozak sequence was included in the constructs. The short Kozak sequence is located upstream of the translation beginning ATG and consists of the three nucleotides ACC. Although, the transgenic reporters worked fine, recent studies showed that the canonical Kozak sequence is not the most common one in zebrafish and therefore, different sequences could improve expression of transgenic reporters (Grzegorski et al., 2014).

Further, the transgenic constructs contain a SV40 (Simian virus 40) terminator sequence at the end of the coding sequence. The SV40 sequences acts as transcription terminator and poly-adenylator of mRNA (adding a polyA tail).

Finally, to facilitate trangenesis, all constructs were flanked by Tol2 transposable element, which are required for Tol2 transposase-dependent genome integration (Kawakami et al., 2000).

Cloning of the FR-mKate2 construct

The Folate receptor GPI-anchor signal - GFP fusion (FR-GFP) construct (pT25xUASFRGFP) was kindly provided by Chiara Zurzolo lab (Napoli, Italy) (Paladino et al., 2008) and served as template to generate a red fluorescent version of this apical marker. N- and F- terminal fragments of the FR construct were amplified with P1, P2, P3 and P4 from pT25xUASFRGFP. The coding region of mKate2, the third fragment, was amplified with P5 and P6 from

pmKate2-N (Evrogen). These three overlapping amplicons where then combined in a two-step PCR and subcloned into a transposable vector, generating pT2UASMCS_FRmKate2, which carries 5xUAS. The 5xUAS promoter of pT2UASMCS_FRmKate2 was then changed to a 4xnr UAS (4xUAS) promoter (Akitake et al., 2011). Therefore, pT2UASMCS_FRmKate2 and pUC57_4Xnr (a synthetic plasmid designed by Lukas Herwig and Yannick Blum) were digested with SphI (NEB) and BglII (NEB) and ligated to create pT2_4xUAS:FRmKate2. The construct was sequenced and checked against mutations.

Subcloning of the mCherry-zf-podocalyxin construct

A former lab member, Yannick Blum, did the mCherry zebrafish podocalyxin fusion construct. I took the construct and cloned it in front of the 4xUAS promoter described above. Therefore, I used his plasmid (pT2UASmCHERRYzfpdxl_cmlcEGFP) to cut out the coding sequence of mCherry-zfpdxl with BglII (NEB) and HpaI (NEB) and ligated it into the corresponding sites of pT2_4xUAS:FRmKate2. Sequencing confirmed the correctness of the generated plasmid pT2_4xUAS:mCHERRY-zfpdxl, which was later used for transgenesis.

Cloning of the EGFP-UCHD construct

The construct that contains the fusion between EGFP and the Utrophin calponin homology domain (UCHD) was a gift from the Bement lab (Burkel et al., 2007). The construct was amplified from pCS2+GFP-UCHD with P11 and P12 and the amplicon was used to replace the coding sequence of FR-mKate2 in pT2_4xUAS:FRmKate2. Therefore, the pT2_4xUAS:FRmKate2 plasmid and the EGFP-UCHD amplicon were digested with AgeI (NEB) and HpaI (NEB) and ligated, resulting in pT2_4xUAS:eGFP-UCHD. Finally, sequencing confirmed the correctness of the construct.

Cloning of the mRuby2-UCHD construct

For the far-red UCHD construct mRuby2 was amplified from pcDNA3-mRuby2 with P77 and P78. This amplicon was used to replace the EGFP coding sequence in pT2_4xUAS:eGFP-UCHD. The replacement was done by digesting amplicon and vector with NcoI (NEB) and subsequent ligation, which

generated pT2_4xUAS:mRuby2-UCHD. Constructs were then checked for integration of the mRuby2 in correct direction by restriction digestion (with DraI, NEB) and sequencing.

Cloning of the mClav-UCHD construct

To generate pT2_4xUAS:mClav-UCHD, the two plasmids pmClavGR2-NT and pT2_4xUAS:eGFP-UCHD were digested with AgeI (NEB) and BsrGI (NEB) and the respective fragments were ligated. The construct was sequenced to ensure correct sequence.

2.2.5.2. Transgenesis

The constructs were injected together with Tol2 transposase RNA into 1-cell stage eggs of Tg(*fli1ep:GFF*)[ubs3] or Tg(*fli1ep:GFF*)[ubs3](UAS:mRFP), as described in chapter 2.2.1.1. At 1dpf the embryos were dechorionated manually and screened for transient expression of the constructs. Embryos that expressed the constructs were raised to adulthood and crossed out to wt fish go check for germline transmission. The F1 offspring was then screened for expression and the ones with strongest and least mosaic expression were selected and raised to adulthood.
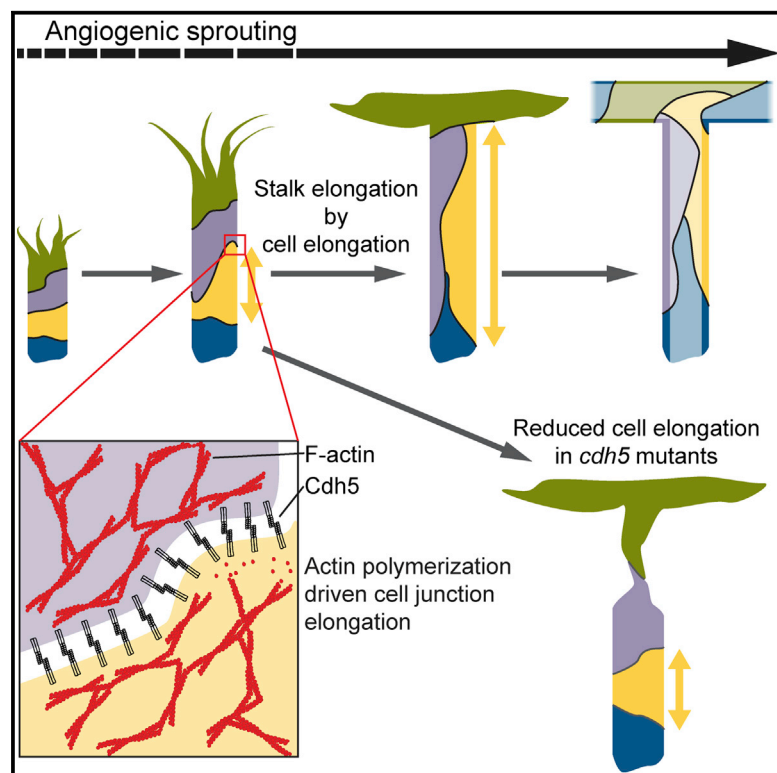
Chapter III

Results

3.1. First author publication

3.1.1. Sauteur, Krudewig, et al., 2014, Cell Reports

92

Cell Reports

Cdh5/VE-cadherin Promotes Endothelial Cell Interface Elongation via Cortical Actin Polymerization during Angiogenic Sprouting

Graphical Abstract

Authors

Loïc Sauteur, Alice Krudewig, ..., Markus Affolter, Heinz-Georg Belting

Correspondence

markus.affolter@unibas.ch (M.A.),
heinz-georg.belting@unibas.ch (H.-G.B.)

In Brief

Sauteur et al. have investigated the cell dynamics that occur during angiogenic stalk elongation. They show that endothelial cell elongation is driven by a transformation of junctional contacts from round to elliptic and that this transformation requires the adhesion molecule Cdh5 as well as actin polymerization.

Highlights

Angiogenic sprouting is driven by cell migration and cell elongation

Cell junctions undergo a circular to elliptic shape transformation

These junctional dynamics require Cdh5 and actin polymerization

CellPress

OPEN
ACCESS

Cell Reports

Report

Cdh5/VE-cadherin Promotes Endothelial Cell Interface Elongation via Cortical Actin Polymerization during Angiogenic Sprouting

Loïc Sauteur,[1,2] Alice Krudewig,[1,2] Lukas Herwig,[1] Nikolaus Ehrenfeuchter,[1] Anna Lenard,[1] Markus Affolter,[1,*] and Heinz-Georg Belting[1,*]
[1]Biozentrum der Universität Basel, Klingelbergstrasse 70, 4056 Basel, Switzerland
[2]Co-first author
*Correspondence: markus.affolter@unibas.ch (M.A.), heinz-georg.belting@unibas.ch (H.-G.B.)
http://dx.doi.org/10.1016/j.celrep.2014.09.024

SUMMARY

Organ morphogenesis requires the coordination of cell behaviors. Here, we have analyzed dynamic endothelial cell behaviors underlying sprouting angiogenesis in vivo. Two different mechanisms contribute to sprout outgrowth: tip cells show strong migratory behavior, whereas extension of the stalk is dependent upon cell elongation. To investigate the function of Cdh5 in sprout outgrowth, we generated null mutations in the zebrafish *cdh5* gene, and we found that junctional remodeling and cell elongation are impaired in mutant embryos. The defects are associated with a disorganization of the actin cytoskeleton and cannot be rescued by expression of a truncated version of Cdh5. Finally, the defects in junctional remodeling can be phenocopied by pharmacological inhibition of actin polymerization, but not by inhibiting actin-myosin contractility. Taken together, our results support a model in which Cdh5 organizes junctional and cortical actin cytoskeletons, as well as provides structural support for polymerizing F-actin cables during endothelial cell elongation.

INTRODUCTION

Organ morphogenesis requires dynamic cell behaviors, which are to a large extent based on junction-associated cell-cell interactions. Vascular endothelial cadherin (Cdh5/VE-cadherin) is the main constituent of endothelial adherens junctions. While the extracellular cadherin domains of Cdh5 engage in homophilic *cis*- and *trans*-interactions (Ahrens et al., 2003; Bibert et al., 2002), the C-terminal portion of the protein interacts with numerous proteins, most notably with β-catenin and plakoglobin, which couple the actin cytoskeleton to adherens junctions (Giannotta et al., 2013). In vitro studies have shown that Cdh5 plays a central role in many aspects of endothelial cell biology, such as regulation of cell adhesion, cell proliferation, cell survival, cell shape, cell motility, modulation of

signaling pathways, and transcriptional gene regulation (reviewed by Dejana and Vestweber, 2013; Harris and Nelson, 2010). Furthermore, recent studies have highlighted the potential of Cdh5 to sense, resist, and transmit mechanical forces (Conway et al., 2013; Gray et al., 2008; Huveneers et al., 2012; Liu et al., 2010; Tzima et al., 2005), suggesting that this aspect of Cdh5 function is essential for its control of endothelial cell behaviors such as proliferation, cell migration, and cell-shape changes. In vivo, Cdh5 function is best studied with respect to vascular permeability and leukocyte transmigration (reviewed by Dejana and Vestweber, 2013). The in vivo roles of Cdh5 in blood vessel morphogenesis are less well understood. On the one hand, full knockout of Cdh5 in mice leads to early embryonic lethality due to severe cardiovascular defects (Carmeliet et al., 1999; Gory-Fauré et al., 1999). Closer inspection of this mutant phenotype showed that, although blood vessels form, they are not maintained (Gory-Fauré et al., 1999). On the other hand, tamoxifen-induced loss of Cdh5 function in postnatal mice leads to a massive hypersprouting within the retinal vasculature (Gaengel et al., 2012). These observations, as well as a large number of other studies, suggest that during development Cdh5 is required to stabilize existing blood vessels as well as to attenuate extracellular proangiogenic signals (reviewed by Giannotta et al., 2013). In agreement with this view, *cdh5* knockdown in zebrafish leads to a hypersprouting phenotype, illustrated by supernumerous endothelial cell processes (Abraham et al., 2009; Montero-Balaguer et al., 2009). However, to fully understand the cell dynamics during blood vessel morphogenesis and the contribution of Cdh5 in this process, it is necessary to analyze cell behaviors at single-cell resolution in vivo.

Here, we describe the generation of targeted putative null mutations in the zebrafish *cdh5* gene and analyze its role during angiogenic sprouting. Live imaging and 3D quantification of junctional interfaces between endothelial cells show that junctional remodeling and stalk cell elongation require Cdh5 function. Loss of Cdh5 also leads to a disorganization of the actin cytoskeleton. Furthermore, expression of a truncated form of Cdh5 is not able to rescue the defects in junctional elongation in *cdh5* mutants. Finally, the defects in junctional remodeling can be phenocopied by pharmacological inhibition of actin polymerization, but not by inhibiting actin-myosin contractility. Taken

together, these findings support a cellular model for angiogenic spouting, in which Cdh5 promotes changes in cell shape by transmitting cytoskeletal forces, generated by actin polymerization, to drive concerted endothelial cell elongation.

RESULTS

Cdh5 Is Required for Segmental Artery Morphogenesis

To investigate the molecular mechanisms, which are involved in angiogenic cell-cell interactions during sprout outgrowth, we generated targeted mutations in the zebrafish *cdh5* gene and recovered two putative null alleles, *cdh5*[ubs8] and *cdh5*[ubs9] (for details, see Experimental Procedures and Figure S1).

Analysis of segmental arteries (SeAs) and the dorsal longitudinal anastomotic vessels (DLAVs) revealed that in contrast to wild-type, SeAs were disorganized with supernumerary filopodial extensions and frequently exhibited multiple contacts between neighboring SeAs in *cdh5*[ubs8] mutant embryos (Figure 1C′; Figure S1G″). Time-lapse analysis of SeA and DLAV formation confirmed these observations (Movie S1; Figures 1A–1C). Initial tip cell formation and dorsal extension of the SeA sprout was normal; however, tip cells failed to organize themselves into the DLAV. Furthermore, we observed that in about 34% (n = 18) of segments in *cdh5* mutants, the tip cells dissociated from the stalk, leaving the stalk cells in the proximity of the dorsal aorta (Figure 1C, red arrows).

The reduced motility of stalk cells in *cdh5* mutants was reflected by reduced motility of endothelial cell nuclei during sprout outgrowth (Figure S2). In wild-type siblings and *sih* morphant embryos, cell nuclei moved dorsally leading to a relatively even distribution of cell nuclei along the vascular axis (Figures S2A and S2B; Movie S2). In *cdh5* mutants (Figure S2C; Movie S2), the movement of tip cell nuclei appeared unchanged compared to wild-type and *sih* morphant vessels. However, and in sharp contrast to wild-type and *sih* morphants, *cdh5*[ubs8] stalk cell nuclei showed reduced dorsal movement and clustered near the dorsal aorta (Figure S2C, yellow and white arrows).

Cdh5 Is Specifically Required for Dynamic Stalk Cell Behavior

During angiogenesis the sprout is led by a tip cell, which is followed by stalk cells (reviewed by Siekmann et al., 2013). Therefore, the tip cell may exert a pulling force upon stalk cells, which may account for the stalling of stalk cells upon dissociation from tip cells in *cdh5* mutants. To test whether the loss of the tip cell phenocopies *cdh5* mutants, we ablated the tip cell by laser microsurgery during SeA sprouting (Figure 1D; Movie S3). Upon tip cell ablation, we did not observe retraction of the sprout, suggesting that the tip cell does not apply a major pulling force on the sprout and/or that the sprout contains an intrinsic stability, which maintains its integrity. Moreover, in ten out of 11 experiments, we found that tip cell ablated sprouts rapidly regenerated and established functional contact with the DLAV, which suggests that—in the absence of a tip cell—the stalk is able to quickly specify a new tip cell and thus maintains or reestablishes anteroposterior polarity to the stalk. Moreover, tip cell ablation did not phenocopy the *cdh5* mutant phenotype,

because mutant stalks did not regain sprouting activity upon tip cell dissociation. Taken together, our time-lapse and laser ablation studies indicate a stalk cell-specific role for Cdh5 during angiogenic sprouting.

Segmental Arteries Display Irregular Cellular Arrangements in *cdh5* Mutants

To analyze junctional remodeling during SeA formation we generated antibodies against zf-Esama (see Supplemental Experimental Procedures), which colocalizes with Zona Occludens-1 (Zo-1) in endothelial cells (Figures S3A–S3C). Immunofluorescent analysis showed that in early SeA sprouts endothelial cells are stacked upon each other connected by individual junctional rings (see Figures S3A and S3A′). During later stages of sprouting, the junctional pattern was transformed into distinct patterns, corresponding to different cellular architectures. In most cases, we observed formation of multicellular tubes, which are characterized by a longitudinal pattern of two (or more) junctions along the vascular axis (Figure S3A‴; Figure 2A) (Blum et al., 2008). In rare instances, we observed SeAs, in which endothelial cells maintain a ring-shaped junctional pattern, which are indicative of unicellular tubes containing a transcellular lumen (Figure 2A) (Herwig et al., 2011; Lenard et al., 2013).

In *cdh5* mutants, the endothelial cell junctions, decorated by Zo-1 or Esama, appeared quite normal during early stages of SeA formation (Figure S3B). At later time points (34 hpf), we noticed that junctions were frequently discontinuous in the dorsal region of the SeA axis and that the distances between longitudinal junctions appeared wider (Figure S3B‴; Figures 2A–2C). We used the distribution of Zo-1 protein to compare the frequencies of discontinuous junctions in wild-type, *sih* morphant, and *cdh5* mutant SeAs at 34 hpf (n = 66) (Figure 2D). In 53% of all wild-type SeAs, we found interrupted junctional patterns, consistent with local transcellular rather than multicellular tube formation. *sih* morphants did not display any significant increase in junctional gaps, whereas in 92% of *cdh5* mutants we found gaps in the junctional arrangements. Measurement of gap length (Figure 2E) also showed that the gaps are significantly bigger in *cdh5* mutants than in wild-type embryos (p < 0.005). These observations indicate that the cell rearrangements, which underlie multicellular tube formation, require Cdh5 function.

Cdh5-Deficient Junctions Are Defective in Cell Contact Elongation

Current models of junctional dynamics during epithelial morphogenesis are largely based on the contractile forces generated by the actin cytoskeleton and are exerted on cadherin-based adherens junctions (Lecuit et al., 2011; Maître and Heisenberg, 2013). Contraction forces within the actinmyosin ring tend to minimize the circumference of the junctional interface (Farhadifar et al., 2007; Maître et al., 2012). In a multicellular, flat epithelium, contraction forces within a junctional network collectively determine epithelial morphology at the level of cell shape and orientated cell division (Bosveld et al., 2012; Farhadifar et al., 2007; Kasza and Zallen, 2011). In our system of SeA outgrowth, we consider a cellular configuration in which cell contacts between two cells form isolated ring-shaped
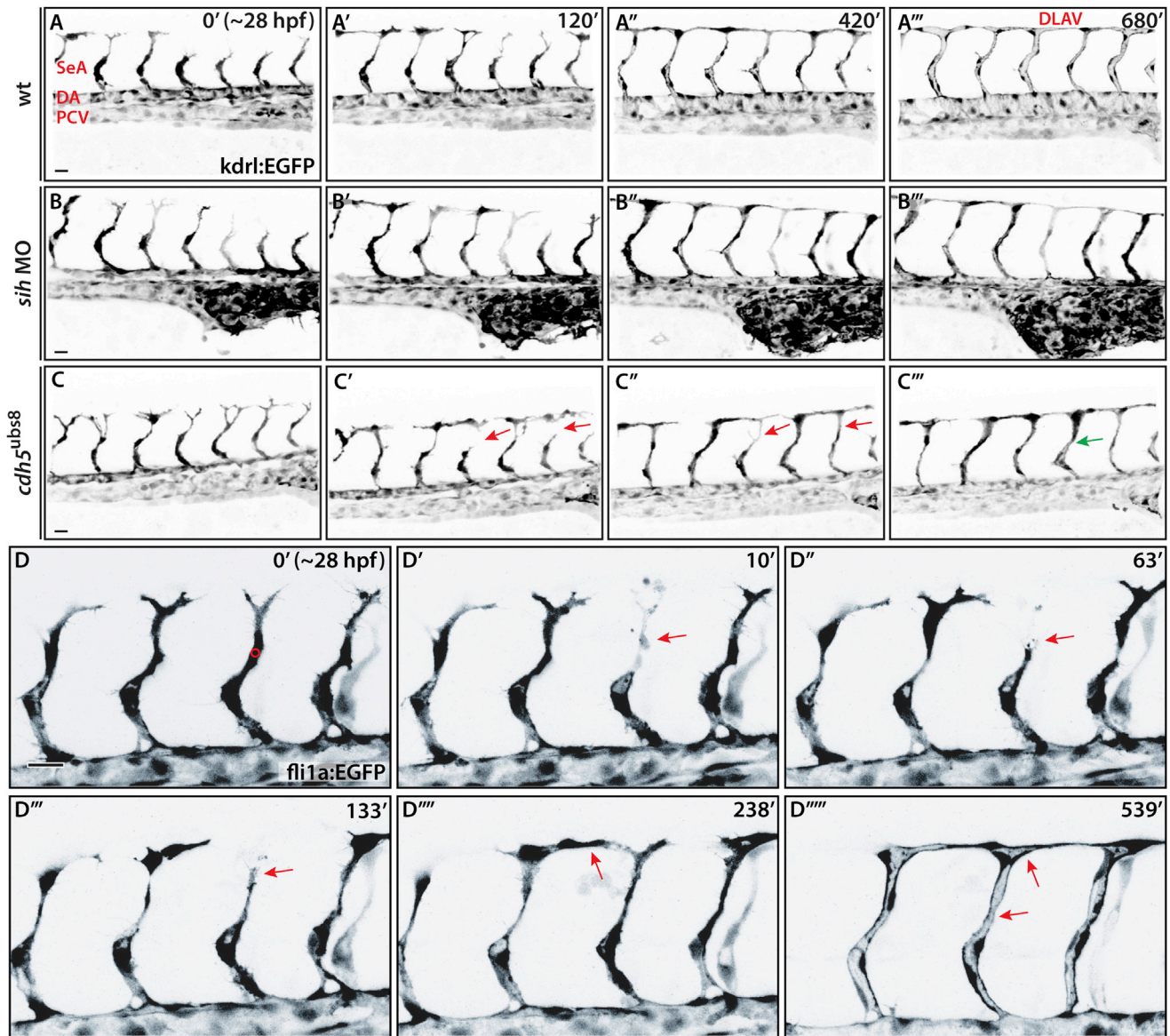
Figure 1. Cdh5 Is Required for Blood Vessel Integrity during Angiogenic Sprouting

(A–C) Confocal still pictures from time-lapse movies (starting around 28 hpf) showing lateral views (anterior to the left) of SeA morphogenesis in transgenic Tg(kdrl:EGFP)^s843 embryos in inversed contrast (Movie S1).

(A) In wild-type, SeAs sprout from the DA and fuse to neighboring vessels, which is followed by lumen formation.

(B) In sih morphants, SeA and DLAV form normally, indicating that blood flow is not required for SeA formation.

(C) Initial vessel sprouting in cdh5 mutant embryos is normal. However, endothelial cells disconnect in the dorsal region (arrows in C′). Stalk cells frequently reconnected to the DLAV; this was achieved by dorsal protrusions of ventrally localized cells rather than cell migration or cell movements (arrows in C′′). Mutant SeAs form discontinuous lumens (arrow in C′′′).

(D) Rapid recovery of sprouting behavior upon tip cell ablation. Confocal still pictures from time-lapse movie (Movie S3) showing lateral view (anterior to the left) of a tip cell ablated SeA in a transgenic Tg(fli1a:EGFP)^y1 embryo in inversed contrast. Segmental sprouts are shown 5 min prior to laser ablation in (D); the red circle demarcates the lasering region). After ablation, no retraction of the stalk cells is observed. Upon irradiation, the tip cell becomes apoptotic (arrow in D′), and former stalk cells start to extend protrusions and to migrate up dorsally (arrows in D′′ and D′′′). The new tip cell connects to neighbors and lumen is formed (arrows in D′′′′ and D′′′′′).

Scale bars, 20 μm; DA, dorsal aorta; DLAV, dorsal longitudinal anastomotic vessel; SeA, segmental artery; PCV, posterior cardinal vein.

junctions (in contrast to junctional networks, that form in continuous epithelial sheets). In this cellular configuration, cells are not exposed to deforming forces exerted from junctions between neighboring cells, and the junctional contraction forces will shape the cell junction into a perfect circle, as has been described in for 2-cell aggregates in zebrafish and MDCK cells
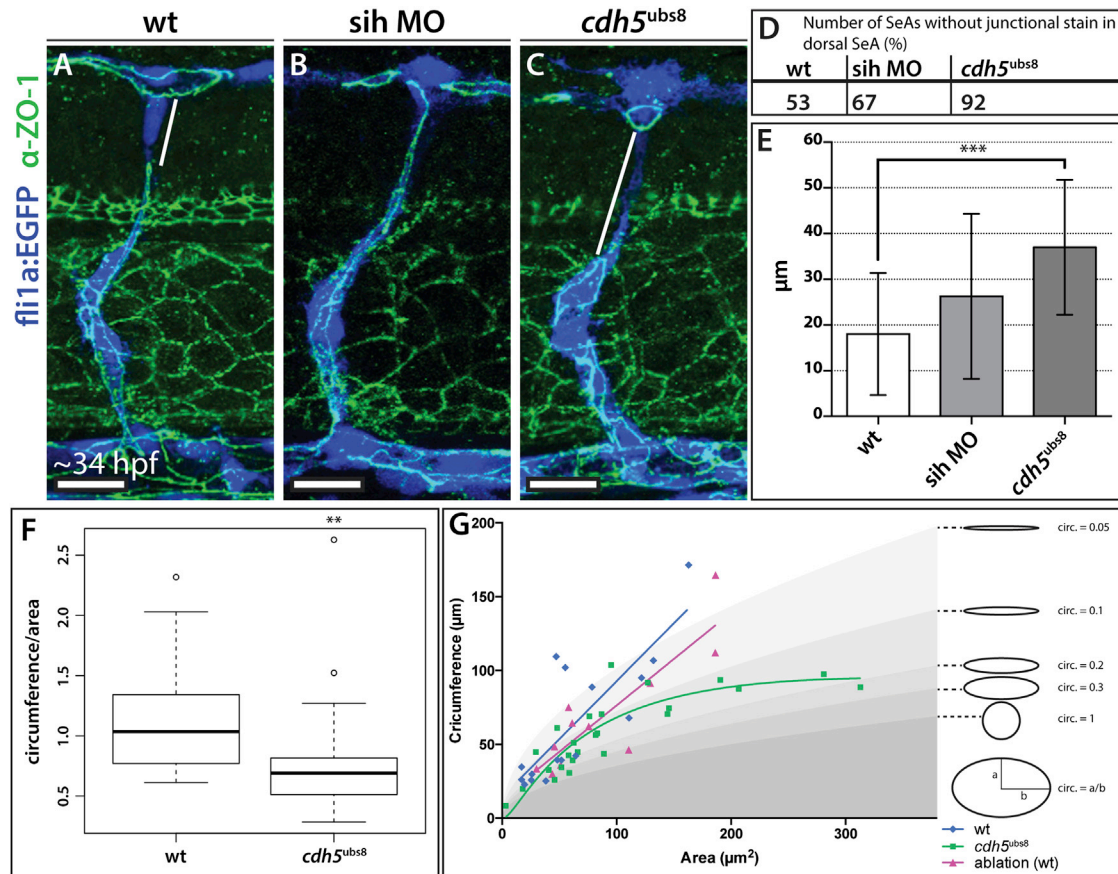
Figure 2. Cdh5 Is Required for Cell Rearrangements and Cell-Cell Interface Deformation during Sprout Outgrowth

(A–C) Lateral views of single SeAs in wild-type (A), *sih* morphant (B), and *cdh5* mutant (C) transgenic Tg(*fli1a:EGFP*)^{y1} (blue) embryos stained for Zo-1 (green) at around 34 hpf. In *cdh5* mutant embryos, the dorsal part of the SeA shows longer distances without any junctional Zo-1 staining (demarcated by the white lines in A and C), compared to wild-type and *sih* morphants.

(D) Quantification of SeAs without junctional Zo-1 in the dorsal region for wild-type (n = 40), *sih* morphants (n = 57), and *cdh5* mutants (n = 66). In contrast to wild-type and *sih* morphants, most *cdh5* mutant SeA lack junctions in the dorsal portion of the vessel.

(E) The length of the dorsal part of the SeA without Zo-1 was measured and found to be significantly longer in *cdh5* mutant embryos (p < 0.0001). Unpaired two-tailed t test; error bars indicate SD.

(F) A boxplot with whiskers (Tukey) of quantification of the quotient of circumference to area of cell-cell interfaces. A weighted t test (Welsh) reveals (p < 0.0019) that, in *cdh5* mutants, cell-cell interfaces are more circular than in wild-type.

(G) Plot showing circumference (μm) versus area (μm^2) of individual cell-cell interfaces. Wild-type (blue squares), *cdh5*^{ubs8} (green squares), and tip cell ablated wild-type cell-cell interfaces (purple triangles) and corresponding regressions. Gray-shaded zones show extrapolated ellipsoids with a schematic representation on the right hand side. The circularity (cir) is determined by the quotient of the two half-axes ("a" and "b") as depicted on the bottom right. With increasing surface, wild-type cell-cell interfaces become more elongated (cir < 0.1), whereas circularity of *cdh5*^{ubs8} interfaces remain close to 0.2. The cell-cell interfaces of tip cell ablated stalk cells show a similar distribution as wild-type (see Movie S4 for the workflow of the quantification process).

Scale bars, 20 μm; significance: **p < 0.01; ***p < 0.005.

(Ferrari et al., 2008; Maître et al., 2012). However, external forces may deform these cell junctions into more ellipsoid shapes. We therefore reasoned that the degree of circularity, which can be defined as the quotient of the two elliptical half-axes, can be used as an indirect measure to assess the relative deforming force that is applied on a junctional ring during angiogenic sprouting.

To calculate circumference and the surface area in three dimensions, we performed colocalization analysis and traced individual junctional rings (see Experimental Procedures for details) (Figures 2F and 2G; Figure S3D; Movie S4). We found that, on average, junctional rings in *cdh5* mutants were more circular than in wild-type siblings (Figure 2F). We further plotted individual junctional measurements of circumference/area onto a landscape depicting areas of relative circularity (Figure 2G). This plot showed a positive correlation between junctional area size and elliptical eccentricity in wild-type embryos: as stalk cells expanded their cell-cell interfaces these became more elliptic. *cdh5* mutant junctions did not show this shape transformation: although junctional rings increased their surface area to up to 300 μm^2, the circumference appeared to be limited to a threshold of approximately 100 μm. As a consequence, the degree of
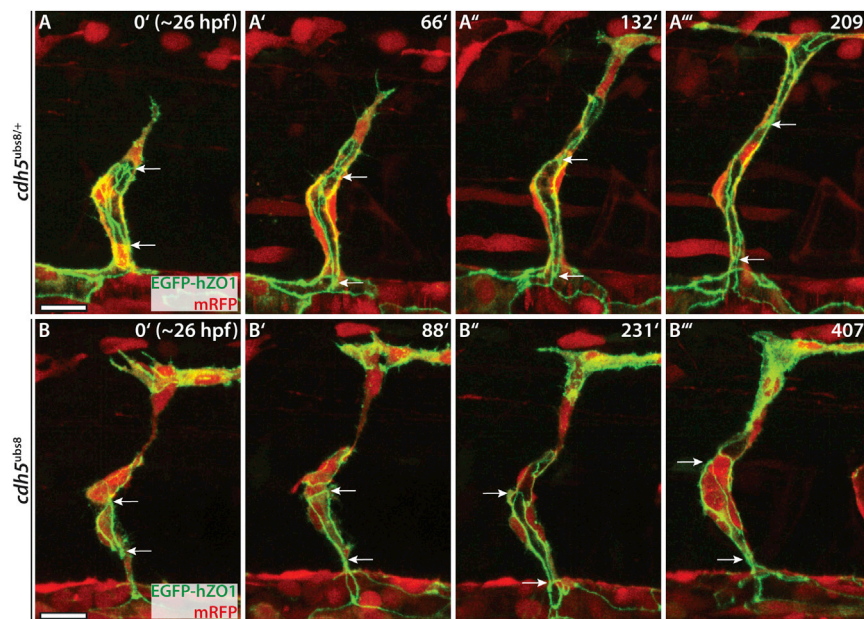
Figure 3. Cdh5 Is Required for Concerted Cell Elongation during Sprout Outgrowth

(A and B) Confocal still pictures from time-lapse movies (Movie S5; starting around 26 hpf) showing lateral views (anterior to left) of single SeAs of transgenic Tg(fli1ep:gal4ff)^{ubs3};(UAS:RFP); (UAS:EGFP-hsZo-1,cmlc:EGFP)^{ubs5} embryos.

(A) All cell-cell junctions of the angiogenic sprouts in a heterozygous cdh5$^{ubs8/+}$ embryo are labeled with EGFP-Zo-1 (green). Several ring-shaped cell-cell contacts have formed. These rings elongate while the sprout grows out, stretching over the whole length of the SeA.

(B) In cdh5 mutants the endothelial cells rearrange, but the junctional rings do not stretch to the most dorsal part of the stalk. Scale bars, 20 μm.

and 4B). Experiments in human umbilical vein endothelial cells (HUVECs) have previously shown that such protrusions coincide with the attachment sites of cortical actin cables (Huveneers e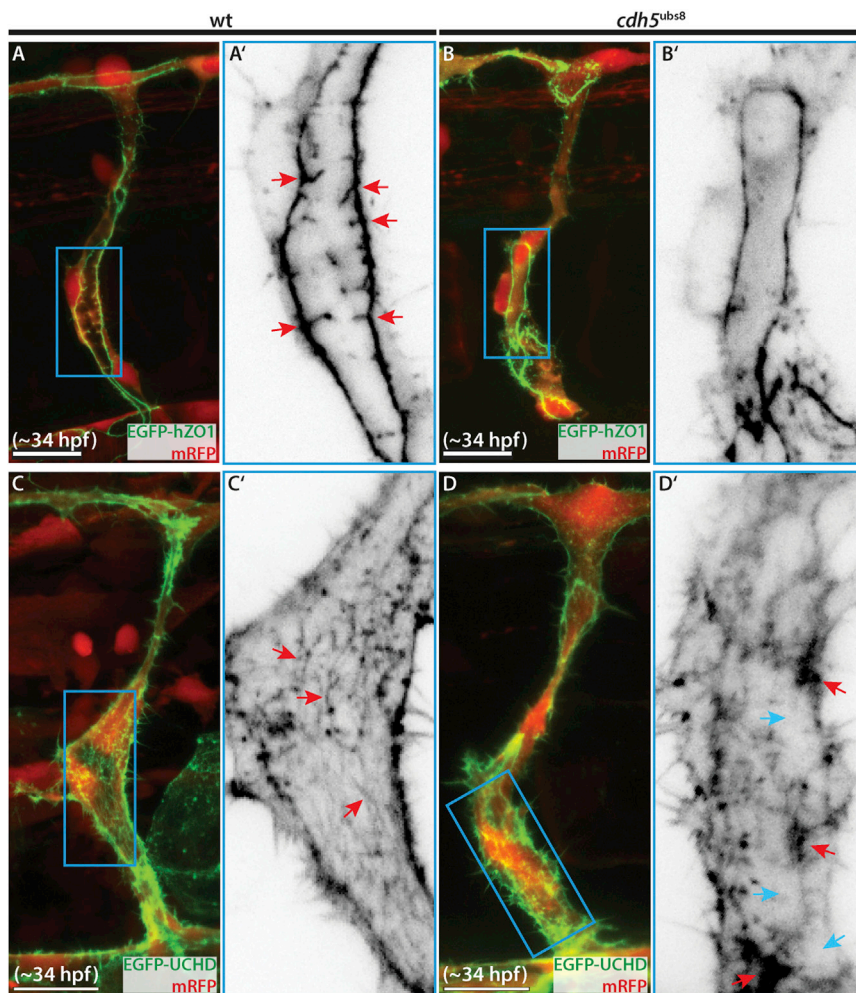t al., 2012; Millán et al., 2010). To address, whether the actin cytoskeleton is affected in cdh5 mutants, we generated a transgenic reporter, Tg(UAS:EGPF-UCHD)^{ubs18}, expressing EGFP tagged with the Utrophin Calponin Homology Domain (UCHD) of Utrophin (Burkel et al., 2007). In contrast to the regular meshwork of cortical actin fibers, which we observed during SeA outgrowth in wild-type, this pattern was disturbed in cdh5 mutants: instead, we found dense clusters of F-actin, as well as areas that seemed devoid of any actin cables (Figures 4C and 4D). Thus, loss of Cdh5 leads to a disorganization of the cortical actin cytoskeleton.

The C-terminal portion of Cdh5 is known to couple the actin cytoskeleton to adherens junctions. To test more directly whether the defects in endothelial cell elongation in cdh5 mutants can be attributed to the inability of the actin network to attach to Cdh5, we expressed a fluorescently tagged version of Cdh5, Tg(5xUAS:cdh5-EGFP)^{ubs12}, which lacks the β-catenin binding domain (Lenard et al., 2013). We followed junctional dynamics based on Cdh5-EGFP fluorescence in wild-type and cdh5 mutant sprouts and measured the longitudinal lengthening during the time course (see Table S1; Figure S4). When expressed in wild-type embryos, we observed extensive lengthening of endothelial cell junctions in agreement with our EGFP-Zo-1 experiments. By contrast, in cdh5 mutants expressing Cdh5-EGFP we observed no such junctional extension (five junctional rings examined). Instead, we observed moderate extensions as well as contractions. Taken together, these findings indicate that concerted endothelial cell elongation during SeA outgrowth requires anchoring of the actin cytoskeleton to endothelial junctions via Cdh5.

eccentricity decreased for large junctional rings. Taken together, these findings suggest that the deforming forces that underlie lengthening of endothelial cell junctions are reduced in cdh5 mutants. Because tip cells often dissociate from the stalk, we tested whether deforming forces depend on the presence of the tip cells. When we measured the junctional dimensions in sprouts, in which the tip cell had been removed by laser ablation (Figure S3C), we found that the junctions maintained normal shapes with respect to circumference and eccentricity (Figure 2G). We therefore conclude that the tip cell does not play a major role in junctional elongation.

Stalk Elongation Is Driven by Cell-Shape Changes

Because the above experiments strongly suggested a role for Cdh5 in the dynamic stalk cell behavior, we analyzed cell dynamics of SeA sprout outgrowth in transgenic fish expressing an EGFP-tagged Zo-1 reporter in endothelial cells. Time-lapse analysis revealed that during sprout outgrowth, cells in the stalk undergo substantial lengthening, reflected by an elongation of cell junctions concomitant with a longitudinal expansion of cell-cell surfaces, which is characteristic for the formation of multicellular vascular tubes (Figure 3A; Movie S5; Table S1). Therefore, sprout outgrowth is not only mediated by endothelial cell migration, but to a large extent accompanied by cell-shape changes, which elongate the nascent sprout. In cdh5 mutant SeAs, endothelial cells showed very little cell elongation along the axis of the forming vessel (Figure 3B; Movie S5).

Loss of Cdh5 Leads to Disorganization of the Cortical Actin Cytoskeleton

When we examined EGFP-Zo-1 distribution in sprouting SeA at high resolution in live embryos, we found that—in particular, during lumen formation—wild-type junctions formed protrusions that were oriented perpendicular to the cell junctions; in cdh5 mutant SeAs, we did not observe such protrusions (Figures 4A

F-Actin Polymerization Is Essential for Angiogenic Cell-Shape Changes

Because cell-shape changes appeared to be driven by cytoskeletal remodeling, we wanted to assess the involvement of actin fiber contraction and polymerization, respectively. When

OPEN ACCESS

CellPress

wt | **cdh5**^ubs8

Figure 4. Cdh5 Is Required to Link the Actin Cytoskeleton to Endothelial Cell Junctions

(A and B) Deconvolved images of lateral views (anterior to left) of single SeA of transgenic Tg(fli1ep:gal4ff)^ubs3;(UAS:RFP);(UAS:EGFP-hsZo-1,cmlc:EGFP)^ubs5 embryos around 34 hpf. (A) Within EGFP-Zo-1 rings (green) of wild-type embryos, we observed junctional spikes emerging from the junctions (arrow in A'), most pronounced during lumen formation processes (A' a close-up view of inset in (A) in inversed contrast). These spikes were not observed in cdh5 mutant SeA (B).

(C and D) Lateral views (anterior to left) of single SeA of transgenic Tg(fli1ep:gal4ff)^ubs3; (UAS:RFP); (UAS:EGFP-UCHD)^ubs18 embryos around 34 hpf. The actin cytoskeleton is visualized by F-actin binding domain of utrophin fused to EGFP (EGFP-UCHD). (C) In wild-type stalk cells, the cortical F-actin is oriented in the direction of the growth of the sprout (arrows in C'; C' a close-up view of inset in C in inversed contrast). (D) In cdh5 mutant stalk cells the actin cytoskeleton appears in punctate (red arrows in D') and areas that seem devoid of F-actin cables (blue arrows in D').

Scale bars, 20 μm; UCHD, utrophin calponin homology domain.

DISCUSSION

### Distinct Functions of Cdh5 during Vascular Morphogenesis

In this study, we have addressed the role of Cdh5 during angiogenic sprout outgrowth. Cdh5 has distinct functions during different stages of SeA formation. Cdh5 appears to be dispensable for early tip cell behavior, because we observed normal sprout formation in cdh5 mutants and that tip cells of mutants and wild-type siblings reached the dorsal neural tube simultaneously. However, and in agreement with our previous studies (Lenard et al., 2013), we observed that during DLAV formation, cdh5 mutant tip cells formed supernumerary contacts, suggesting defects in endothelial cell recognition.

During sprout outgrowth, tip cells frequently dissociate from the stalk. Upon losing contact, the stalk cells appeared arrested and showed very little motility. This cell behavior was different from wild-type sprouts in which the tip cell had been ablated; in this situation, the stalk cells quickly (within 30 min of tip cell ablation) reestablished sprouting behavior and formed a fully functional SeA. Although we do not yet know the molecular mechanism that allows this rapid recovery of sprouting behavior in wild-type sprouts, it may be speculated that it involves specification of a new endothelial tip cell from the distal stalk. Thus, it is possible that in the absence of Cdh5, sprout cells are not able to switch from stalk to tip cell character. Consistent with this view, knockdown of cdh5 prohibits endothelial cells of the subintestinal vessel from reinitiating

we treated wild-type embryos with blebbistatin, which inhibits actin-myosin contractions (Straight et al., 2003), we observed severe junctional defects (Figure 5B). However, these defects did not resemble the defects of cdh5 mutants. Instead, the junctions became extremely tortuous and often attained a concave curvature contrary to the overall convex curvatures observed in wild-type and cdh5 mutant SeAs. This result is in agreement with the view that actin contractility is primarily involved in generating contractile forces within junctional rings, rather than deforming forces, which would elongate the junctional ring.

In contrast, embryos treated with latrunculin B (latB), which inhibits actin polymerization (Morton et al., 2000), displayed SeAs with junctional gaps similar to those observed in cdh5 mutants (compare Figure 5C with Figures 2A–2C). Furthermore, quantification revealed that junctional rings attained rounder shapes consistent with defects in junction elongation (Figure 5D). Although lethality prevented us from using higher doses of latB, the defects we observed are in line with but milder than the cdh5 mutant phenotype, suggesting that actin polymerization rather than contraction is the primary mechanism of junction elongation (see Graphical Abstract).
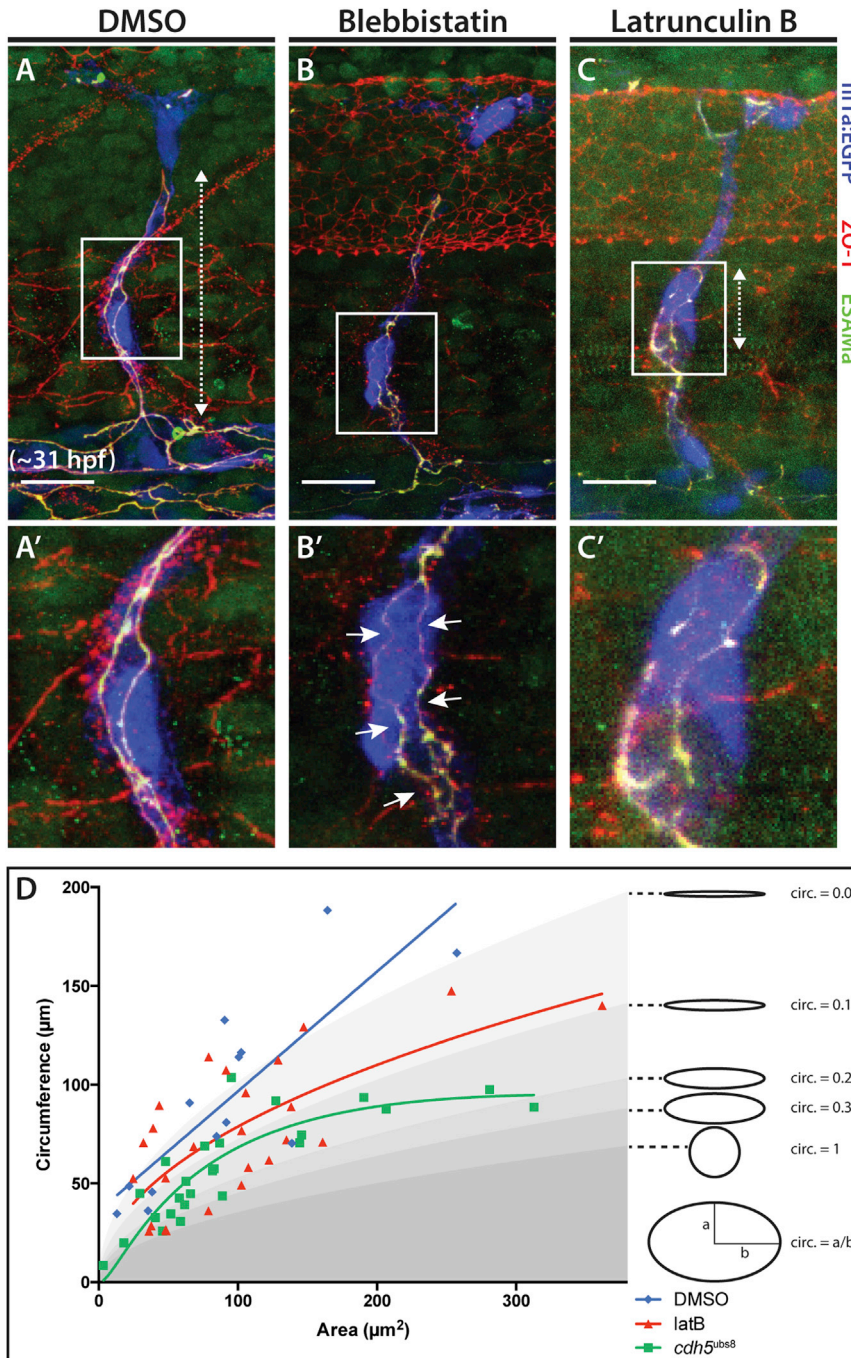
Figure 5. F-Actin Polymerization Is Essential for Angiogenic Cell-Shape Changes

(A–C) Immunofluorescent analysis Tg(fli1a:EGFP)^{y1} (blue) embryos at 30–32 hpf (anterior to the left) treated with inhibitors of cytoskeletal remodeling and stained for Zo-1 (red) and Esama (green).

(A) Control embryos (1% DMSO, 2 hr) show wild-type-like junctional ring elongation (dotted arrow in (A) (A′ a close-up view of inset in A).

(B) In blebbistatin-treated embryos, SeAs junctional patterns are tortuous and attain concave curvatures (arrows in B′).

(C) Treatment with latB reduces the stalk cells' ability to elongate (dotted arrow in C) and junctions have rounder shapes compared to control embryos.

(D) Plot showing circumference (μm) versus surface area (μm^2) of individual cell-cell interfaces. DMSO control (blue squares), 4 hr 0.15 μg/ml latrunculin B (red triangles) and for comparison cdh5^{ubs8} (green squares) and corresponding regressions. Gray-shaded zones show extrapolated ellipsoids with a schematic representation on the right-hand side. The circularity (cir) is determined by the quotient of the two half-axes ("a" and "b") as depicted on the bottom right. Alteration of F-actin polymerization dynamics with latB shows a decrease in junctional eccentricity, phenocopying cdh5 mutants.

Scale bars, 20 μm; Esama, endothelial cell-selective adhesion molecule a; latB, latrunculin B.

dent cell elongation as illustrated by the lengthening of endothelial cell junctions. Although cdh5 mutant endothelial cells are able to expand junctional rings, they do not transform these rings into elliptical shape.

The disorganization of the actin cytoskeleton in cdh5 mutants and our observation that junctional defects cannot be rescued by a Cdh5 isoform, which is unable to attach to the actin cytoskeleton, strongly suggest that the dynamic contact shape transformations are mediated by the interactions between Cdh5 and the actin cytoskeleton. Previous studies have shown that Cdh5 is an important mediator of endothelial cell shape and dynamic cell behavior (Chien et al., 2005; Nelson et al., 2004). In particular, our observations are in agreement with in vitro studies using allantoic explant cultures, which showed that endothelial migration per se does not require Cdh5; in contrast, blocking of Cdh5 function strongly interfered with dynamic cell rearrangements during sprout elongation (Perryn et al., 2008). In the same way, a recent study has demonstrated the importance of Cdh5 for angiogenic cell shuffling in ES-cell derived angiogenic sprouts and in the mouse retina (Bentley et al., 2014). Furthermore, these studies suggest that

angiogenic behavior upon xenotransplantation of tumor cells (Nicoli et al., 2007).

Cdh5 Interacts with F-Actin during Endothelial Cell Elongation

Sprout outgrowth is based on both cell migration and cell elongation. Although the tip cell is actively migrating, in wild-type embryos as well as in cdh5 mutants, we found that the extension at the level of the stalk is mainly driven by Cdh5 depen-

cell shuffling depends on differential adhesion between endothelial cells, which is mediated by different levels of Cdh5 at cell junctions. In the SeA of the zebrafish, we have not observed cell shuffling during sprout outgrowth. This may be attributed to the limited number of cells in the SeA sprout and/or to the short sprouting phase during SeA formation.

Endothelial Cell Elongation Is Dependent on Actin Polymerization

Recent in vitro studies on the mechanical forces, which drive contact expansion between two cells, have shown that contact initiation leads to circular junctions (Engl et al., 2014; Maître et al., 2012). These studies showed that contact expansion is mainly driven by cortical tension from the actin myosin cytoskeleton and that this tension is transmitted by E-cadherin. Moreover, the interaction between the actin cytoskeleton and cadherins was shown to be essential for contact formation, because expression of a truncated form of E-cadherin (deficient in actin binding) was not able to expand cell contacts (Maître et al., 2012).

The circular to elliptical junctional transformation appears to be a key feature of endothelial cells. One striking finding of our studies is that junctional remodeling in the SeA stalk appears to depend primarily on actin polymerization rather than contractility. Inhibition of actin polymerization phenocopied two aspects of loss of Cdh5 during SeA sprout outgrowth, namely, extensive junctional gaps and rounded junctional rings. Both defects illustrate the disability of endothelial cells to attain a paired configuration, which is a prerequisite for multicellular tube formation.

Recent experiments have explored the interplay between Cdh5 and actin polymerization during junctional remodeling of HUVECs (Abu Taha et al., 2014). This study showed that local loss of Cdh5 leads to the formation of so-called junction associated intermittent lamellipodia (JAIL) by the way of ARP2/3 recruitment and actin polymerization. Whether such lamellipodia are formed in the SeA remains to be determined. However, the similarity of the *cdh5* mutant and latB phenotypes suggests that such a mechanism may provide the deforming force, which underlies junction elongation during SeA outgrowth.

Taken together, our findings support a cellular model in which Cdh5 is specifically required in stalk cells to promote cell elongation by transmitting a deforming force on endothelial cell junctions. The disruption of the cortical actin network in *cdh5* mutants and the defects conferred by inhibition of actin polymerization suggest that junction elongation is driven by forces generated by actin polymerization and that Cdh5 serves as an anchor point to transmit these forces between cells. The deforming force, which elongates the junctional ring, may originate from different mechanisms. Although we do not rule out pulling forces generated by the tip cell or stalk cell/ECM interactions, our findings point to a third mechanism, in which local actin polymerization leads to the formation of lamellipodia, which exert the deforming force for junctional elongation.

EXPERIMENTAL PROCEDURES

Zebrafish Strains and Morpholinos

Zebrafish were maintained as previously described (Westerfield, 2000). All experiments were performed in accordance with federal guidelines and were approved by the Kantonales Veterinäramt of Kanton Basel-Stadt. Zebrafish lines were Tg(fli1a:EGFP)[y1] (Lawson and Weinstein, 2002), Tg(kdrl:EGFPnls)[ubs1] (Blum et al., 2008), Tg(kdrl:EGFP)[s843] (Jin et al., 2005), Tg(5xUAS:RFP) (Asakawa et al., 2008), Tg(fli1ep:gal4ff)[ubs3] and Tg(UAS:EGFP-hsZO-1,cmlc:EGFP)[ubs5] (Herwig et al., 2011), Tg(5xUAS:cdh5-EGFP)[ubs12] (Lenard et al., 2013), Tg(UAS:EGFP-UCHD)[ubs18] (this study), and cdh5[ubs8] and cdh5[ubs9] (this study). Morpholinos (GeneTools) used were as follows: *silent heart* (*sih/tnnt2*) 5′-CATGTTTGCTCTGATCTGAC ACGCA-3′ (Sehnert et al., 2002) and standard control 5′-CCTCTTACCTCAGT TACAATTTATA-3′.

Generation of Tg(UAS:EGFP-UCHD)[ubs18]

The 4xnrUAS promoter (Akitake et al., 2011) and the EGFP-UCHD (utrophin calponin homology domain) coding region (Burkel et al., 2007) were cloned into a Tol2 vector. The final pT24xnrUAS:EGFP-UCHD plasmid was coinjected with *tol2* mRNA into the Tg(fli1ep:gal4ff)[ubs3];(UAS:mRFP) embryos.

Pharmacological Treatment

To inhibit actin fiber contractions, we treated embryos with blebbistatin (Sigma-Aldrich) (Morton et al., 2000) from 28 to 30 hours postfertilization (hpf) in E3 medium containing 100 μM blebbistatin. To interfere with actin polymerization, we used sublethal concentrations latrunculin B (Merck Millipore), which still efficiently disrupt actin polymerization (Phng et al., 2013). Embryos were treated from 28 to 32 hpf in E3 medium containing 0.15 μg/ml latrunculin B. Embryos were fixed immediately after treatment for immunofluorescent analysis.

Immunofluorescence

Immunofluorescence was performed as previously described (Herwig et al., 2011). The following antibodies were used: rabbit anti-zf-Cdh5 1:200 (Blum et al., 2008), rabbit anti-Esama 1:200 (Lenard et al., 2013; this study), mouse anti-human-Zo-1 1:100 (Zymed), Alexa 568 goat anti-rabbit immunoglobulin G (IgG) 1:1,000, and Alexa 633 goat anti-mouse IgG 1:1,000 (both from Invitrogen).

Laser Microsurgery Experiments

Tip cell ablations were performed on an Olympus FV1000 confocal microscope using a 355 nm pulsed laser. Lasering was performed in a confocal plane, using a tornado movement of the laser at 65% power for three frames. Movies were recorded using a 30× silicone objective with a frame size of 640 × 640 pixels. z stacks were recorded with a step size of 0.8 μm every 7 min.

Laser ablations for immunostainings were performed on Leica DM6000b microscope equipped with a single-pulse laser (CryLaS FTSS 355-50). Lasering was performed using a 20× dry objective; the laser power was set to 86, with a speed of 2, specimen balance of 0, and an offset of 80. Tip cells were irradiated for less than 2 s. Specimen were fixed in 2% paraformaldehyde immediately after laser surgery.

Live Imaging

Time-lapse imaging was performed as previously described (Lenard et al., 2013). All movies were taken with a Leica SP5 confocal microscope using a 40 × water immersion objective (NA = 1.1) with a frame size of 512 × 512 pixels. Routinely, z stacks consisted of 80–100 slices with a step size of 0.8–1 μm. Stacks were taken every 8 or 10 min.

High-resolution imaging was performed a Leica SP5 microscope using a 63 × water immersion objective (NA = 1.2) using a vertical step size of 0.2 μm and subsequent Huygens deconvolution (SVI).

3D Measurement of Endothelial Cell Interfaces

To measure the shapes of cell junctions, Tg(kdrl:EGFPnls)[ubs1] embryos were stained for Zo-1 and Esama around 32 hpf and imaged as described above. In order to reconstruct the junctions in 3D, the Zo-1 and Esama signals were combined to build a colocalization channel using Imaris (Bitplane) software. The junctions were segmented from this channel using a semiautomated approach based on the filament module of Imaris. For further processing, tools for volumetric calculations were developed in Python. The junction area was derived by creating a tessellation from the junction's rim coordinates, using

those two points that are furthest from each other as start and end points. This leads to a lower bound estimate of the area inside the junctional rings by summing up the areas of the individual polygons resulting from the tessellation step. Additional parameters like length and diameter of the junctions were calculated as well.

The software developed is available as a Python package called "VolPy" (for Volumetric Python) (1). It makes use of the open-source packages "NumPy" (2) for numerical calculations and "matplotlib" (3) for graph plotting.

(1) https://github.com/imcf/imcf-toolbox/tree/master/lib/python2.7/volpy
(2) http://www.numpy.org/
(3) http://matplotlib.org/

SUPPLEMENTAL INFORMATION

Supplemental Information includes Supplemental Experimental Procedures, four figures, one table, and five movies and can be found with this article online at http://dx.doi.org/10.1016/j.celrep.2014.09.024.

AUTHOR CONTRIBUTIONS

M.A. and H.-G.B. conceived the project; L.S., A.K., L.H., and H.-G.B. designed and carried out experiments; H.-G.B. generated the *cdh5* mutants; A.K. performed immunofluorescent and time-lapse experiments; L.S. generated the Tg(UAS:UCHD-EGFP) fish line, analyzed the actin cytoskeleton, and performed junctional ring shape analysis; L.H. performed time-lapse experiments; N.F. developed "VolPy"; A.L. helped with imaging; and L.S. and H.-G.B. wrote the manuscript.

ACKNOWLEDGMENTS

REFERENCES

Abraham, S., Yeo, M., Montero-Balaguer, M., Paterson, H., Dejana, E., Marshall, C.J., and Mavria, G. (2009). VE-Cadherin-mediated cell-cell interaction suppresses sprouting via signaling to MLC2 phosphorylation. Curr. Biol. *19*, 668–674.

Abu Taha, A., Taha, M., Seebach, J., and Schnittler, H.-J. (2014). ARP2/3-mediated junction-associated lamellipodia control VE-cadherin-based cell junction dynamics and maintain monolayer integrity. Mol. Biol. Cell *25*, 245–256.

Ahrens, T., Lambert, M., Pertz, O., Sasaki, T., Schulthess, T., Mège, R.-M., Timpl, R., and Engel, J. (2003). Homoassociation of VE-cadherin follows a mechanism common to "classical" cadherins. J. Mol. Biol. *325*, 733–742.

Akitake, C.M., Macurak, M., Halpern, M.E., and Goll, M.G. (2011). Transgenerational analysis of transcriptional silencing in zebrafish. Dev. Biol. *352*, 191–201.

Asakawa, K., Suster, M.L., Mizusawa, K., Nagayoshi, S., Kotani, T., Urasaki, A., Kishimoto, Y., Hibi, M., and Kawakami, K. (2008). Genetic dissection of neural circuits by Tol2 transposon-mediated Gal4 gene and enhancer trapping in zebrafish. Proc. Natl. Acad. Sci. USA *105*, 1255–1260.

Bentley, K., Franco, C.A., Philippides, A., Blanco, R., Dierkes, M., Gebala, V., Stanchi, F., Jones, M., Aspalter, I.M., Cagna, G., et al. (2014). The role of differential VE-cadherin dynamics in cell rearrangement during angiogenesis. Nat. Cell Biol. *16*, 309–321.

Bibert, S., Jaquinod, M., Concord, E., Ebel, C., Hewat, E., Vanbelle, C., Legrand, P., Weidenhaupt, M., Vernet, T., and Gulino-Debrac, D. (2002). Synergy between extracellular modules of vascular endothelial cadherin promotes homotypic hexameric interactions. J. Biol. Chem. *277*, 12790–12801.

Blum, Y., Belting, H.-G., Ellertsdottir, E., Herwig, L., Lüders, F., and Affolter, M. (2008). Complex cell rearrangements during intersegmental vessel sprouting and vessel fusion in the zebrafish embryo. Dev. Biol. *316*, 312–322.

Bosveld, F., Bonnet, I., Guirao, B., Tlili, S., Wang, Z., Petitalot, A., Marchand, R., Bardet, P.-L., Marcq, P., Graner, F., and Bellaïche, Y. (2012). Mechanical control of morphogenesis by Fat/Dachsous/Four-jointed planar cell polarity pathway. Science *336*, 724–727.

Burkel, B.M., von Dassow, G., and Bement, W.M. (2007). Versatile fluorescent probes for actin filaments based on the actin-binding domain of utrophin. Cell Motil. Cytoskeleton *64*, 822–832.

Carmeliet, P., Lampugnani, M.G., Moons, L., Breviario, F., Compernolle, V., Bono, F., Balconi, G., Spagnuolo, R., Oosthuyse, B., Dewerchin, M., et al. (1999). Targeted deficiency or cytosolic truncation of the VE-cadherin gene in mice impairs VEGF-mediated endothelial survival and angiogenesis. Cell *98*, 147–157.

Chien, S., Li, S., Shiu, Y.-T., and Li, Y.-S. (2005). Molecular basis of mechanical modulation of endothelial cell migration. Front. Biosci. *10*, 1985–2000.

Conway, D.E., Breckenridge, M.T., Hinde, E., Gratton, E., Chen, C.S., and Schwartz, M.A. (2013). Fluid shear stress on endothelial cells modulates mechanical tension across VE-cadherin and PECAM-1. Curr. Biol. *23*, 1024–1030.

Dejana, E., and Vestweber, D. (2013). The role of VE-cadherin in vascular morphogenesis and permeability control. Prog. Mol. Biol. Transl. Sci. *116*, 119–144.

Engl, W., Arasi, B., Yap, L.L., Thiery, J.P., and Viasnoff, V. (2014). Actin dynamics modulate mechanosensitive immobilization of E-cadherin at adherens junctions. Nat. Cell Biol. *16*, 587–594.

Farhadifar, R., Röper, J.-C., Aigouy, B., Eaton, S., and Jülicher, F. (2007). The influence of cell mechanics, cell-cell interactions, and proliferation on epithelial packing. Curr. Biol. *17*, 2095–2104.

Ferrari, A., Veligodskiy, A., Berge, U., Lucas, M.S., and Kroschewski, R. (2008). ROCK-mediated contractility, tight junctions and channels contribute to the conversion of a preapical patch into apical surface during isochoric lumen initiation. J. Cell Sci. *121*, 3649–3663.

Gaengel, K., Niaudet, C., Hagikura, K., Laviña, B., Muhl, L., Hofmann, J.J., Ebarasi, L., Nyström, S., Rymo, S., Chen, L.L., et al. (2012). The sphingosine-1-phosphate receptor S1PR1 restricts sprouting angiogenesis by regulating the interplay between VE-cadherin and VEGFR2. Dev. Cell *23*, 587–599.

Giannotta, M., Trani, M., and Dejana, E. (2013). VE-cadherin and endothelial adherens junctions: active guardians of vascular integrity. Dev. Cell *26*, 441–454.

Gory-Fauré, S., Prandini, M.H., Pointu, H., Roullot, V., Pignot-Paintrand, I., Vernet, M., and Huber, P. (1999). Role of vascular endothelial-cadherin in vascular morphogenesis. Development *126*, 2093–2102.

Gray, D.S., Liu, W.F., Shen, C.J., Bhadriraju, K., Nelson, C.M., and Chen, C.S. (2008). Engineering amount of cell-cell contact demonstrates biphasic proliferative regulation through RhoA and the actin cytoskeleton. Exp. Cell Res. *314*, 2846–2854.

Harris, E.S., and Nelson, W.J. (2010). VE-cadherin: at the front, center, and sides of endothelial cell organization and function. Curr. Opin. Cell Biol. *22*, 651–658.

Herwig, L., Blum, Y., Krudewig, A., Ellertsdottir, E., Lenard, A., Belting, H.-G., and Affolter, M. (2011). Distinct cellular mechanisms of blood vessel fusion in the zebrafish embryo. Curr. Biol. *21*, 1942–1948.

Huveneers, S., Oldenburg, J., Spanjaard, E., van der Krogt, G., Grigoriev, I., Akhmanova, A., Rehmann, H., and de Rooij, J. (2012). Vinculin associates with endothelial VE-cadherin junctions to control force-dependent remodeling. J. Cell Biol. 196, 641–652.

Jin, S.-W., Beis, D., Mitchell, T., Chen, J.-N., and Stainier, D.Y.R. (2005). Cellular and molecular analyses of vascular tube and lumen formation in zebrafish. Development 132, 5199–5209.

Kasza, K.E., and Zallen, J.A. (2011). Dynamics and regulation of contractile actin-myosin networks in morphogenesis. Curr. Opin. Cell Biol. 23, 30–38.

Lawson, N.D., and Weinstein, B.M. (2002). In vivo imaging of embryonic vascular development using transgenic zebrafish. Dev. Biol. 248, 307–318.

Lecuit, T., Lenne, P.-F., and Munro, E. (2011). Force generation, transmission, and integration during cell and tissue morphogenesis. Annu. Rev. Cell Dev. Biol. 27, 157–184.

Lenard, A., Ellertsdottir, E., Herwig, L., Krudewig, A., Sauteur, L., Belting, H.-G., and Affolter, M. (2013). In vivo analysis reveals a highly stereotypic morphogenetic pathway of vascular anastomosis. Dev. Cell 25, 492–506.

Liu, Z., Tan, J.L., Cohen, D.M., Yang, M.T., Sniadecki, N.J., Ruiz, S.A., Nelson, C.M., and Chen, C.S. (2010). Mechanical tugging force regulates the size of cell-cell junctions. Proc. Natl. Acad. Sci. USA 107, 9944–9949.

Maître, J.-L., and Heisenberg, C.-P. (2013). Three functions of cadherins in cell adhesion. Curr. Biol. 23, R626–R633.

Maître, J.-L., Berthoumieux, H., Krens, S.F.G., Salbreux, G., Jülicher, F., Paluch, E., and Heisenberg, C.-P. (2012). Adhesion functions in cell sorting by mechanically coupling the cortices of adhering cells. Science 338, 253–256.

Millán, J., Cain, R.J., Reglero-Real, N., Bigarella, C., Marcos-Ramiro, B., Fernández-Martín, L., Correas, I., and Ridley, A.J. (2010). Adherens junctions connect stress fibres between adjacent endothelial cells. BMC Biol. 8, 11.

Montero-Balaguer, M., Swirsding, K., Orsenigo, F., Cotelli, F., Mione, M., and Dejana, E. (2009). Stable vascular connections and remodeling require full expression of VE-cadherin in zebrafish embryos. PLoS ONE 4, e5772.

Morton, W.M., Ayscough, K.R., and McLaughlin, P.J. (2000). Latrunculin alters the actin-monomer subunit interface to prevent polymerization. Nat. Cell Biol. 2, 376–378.

Nelson, C.M., Pirone, D.M., Tan, J.L., and Chen, C.S. (2004). Vascular endothelial-cadherin regulates cytoskeletal tension, cell spreading, and focal adhesions by stimulating RhoA. Mol. Biol. Cell 15, 2943–2953.

Nicoli, S., Ribatti, D., Cotelli, F., and Presta, M. (2007). Mammalian tumor xenografts induce neovascularization in zebrafish embryos. Cancer Res. 67, 2927–2931.

Perryn, E.D., Czirók, A., and Little, C.D. (2008). Vascular sprout formation entails tissue deformations and VE-cadherin-dependent cell-autonomous motility. Dev. Biol. 313, 545–555.

Phng, L.-K., Stanchi, F., and Gerhardt, H. (2013). Filopodia are dispensable for endothelial tip cell guidance. Development 140, 4031–4040.

Sehnert, A.J., Huq, A., Weinstein, B.M., Walker, C., Fishman, M., and Stainier, D.Y.R. (2002). Cardiac troponin T is essential in sarcomere assembly and cardiac contractility. Nat. Genet. 31, 106–110.

Siekmann, A.F., Affolter, M., and Belting, H.-G. (2013). The tip cell concept 10 years after: new players tune in for a common theme. Exp. Cell Res. 319, 1255–1263.

Straight, A.F., Cheung, A., Limouze, J., Chen, I., Westwood, N.J., Sellers, J.R., and Mitchison, T.J. (2003). Dissecting temporal and spatial control of cytokinesis with a myosin II Inhibitor. Science 299, 1743–1747.

Tzima, E., Irani-Tehrani, M., Kiosses, W.B., Dejana, E., Schultz, D.A., Engelhardt, B., Cao, G., DeLisser, H., and Schwartz, M.A. (2005). A mechanosensory complex that mediates the endothelial cell response to fluid shear stress. Nature 437, 426–431.

Westerfield, M. (2000). The Zebrafish Book: A Guide for the Laboratory Use of Zebrafish Danio rerio (Eugene, OR: University of Oregon Press).

Cell Reports

Supplemental Information for

Cdh5/VE-cadherin promotes cell interface elongation via cortical actin polymerization during angiogenic sprouting

Loïc Sauteur*, Alice Krudewig*, Lukas Herwig, Nikolaus Ehrenfeuchter, Anna Lenard, Markus Affolter[1] and Heinz-Georg Belting[1]
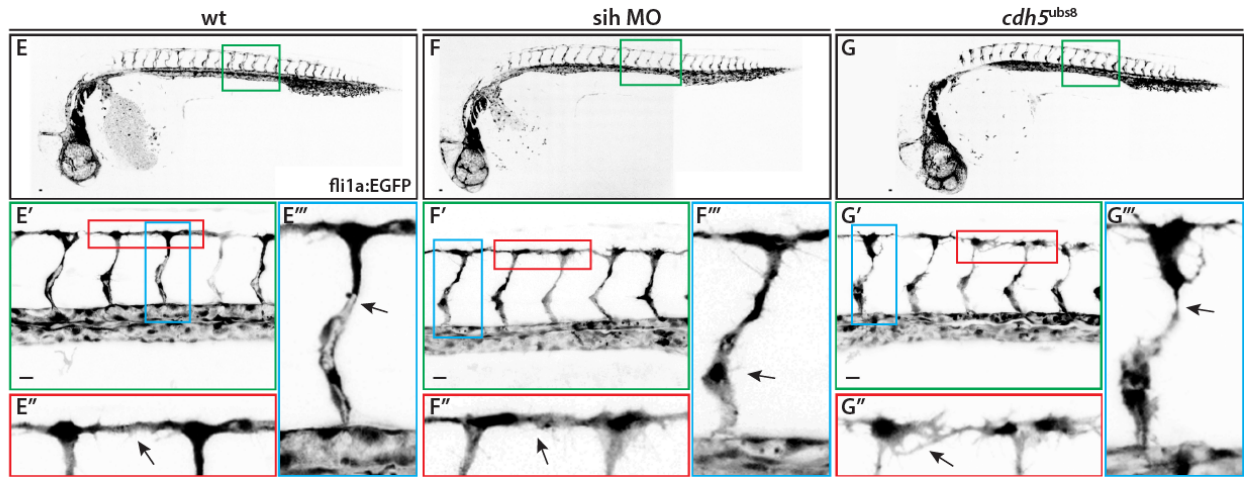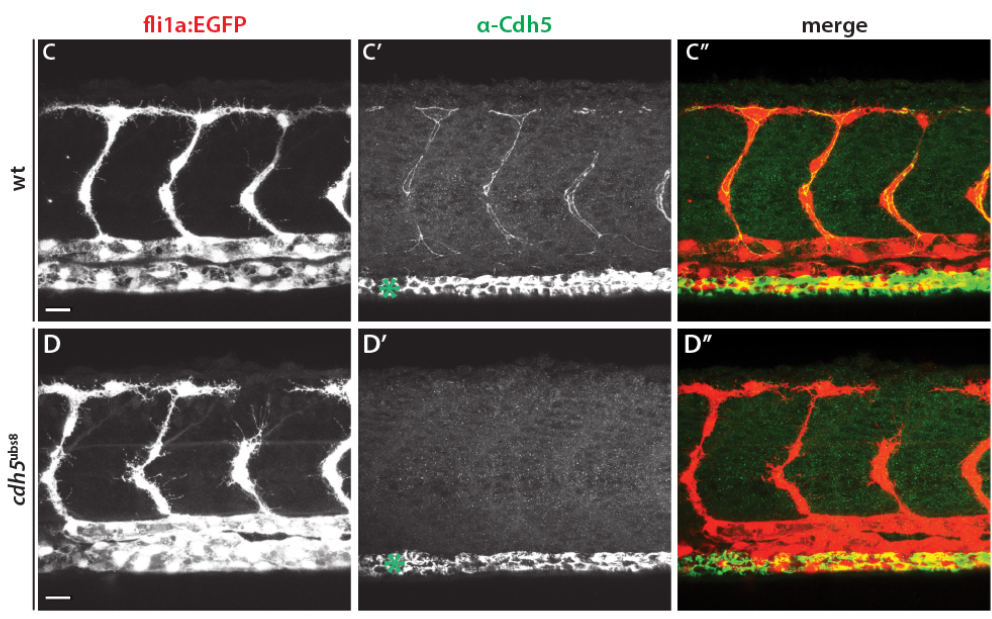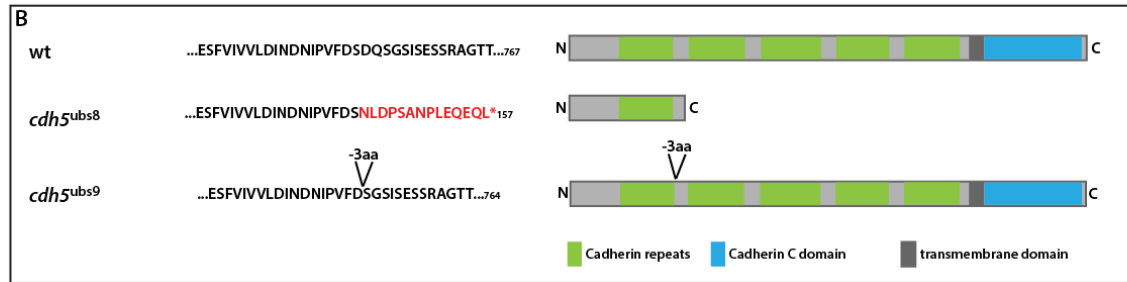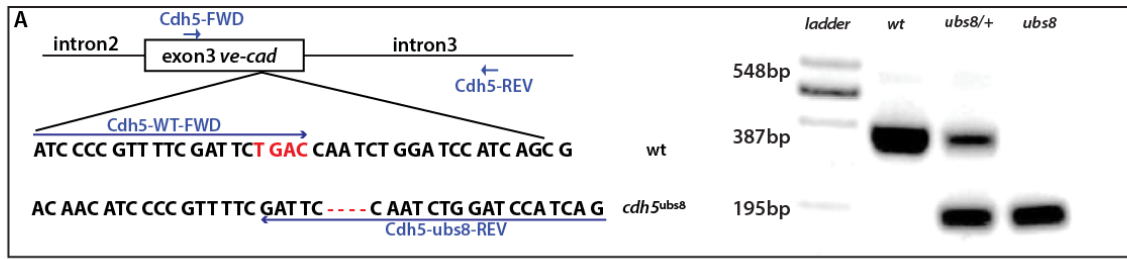
Biozentrum der Universität Basel, Klingelbergstrasse 70, CH-4056 Basel

* co-first authors
[1] corresponding authors

email: heinz-georg.belting@unibas.ch
            markus.affolter@unibas.ch

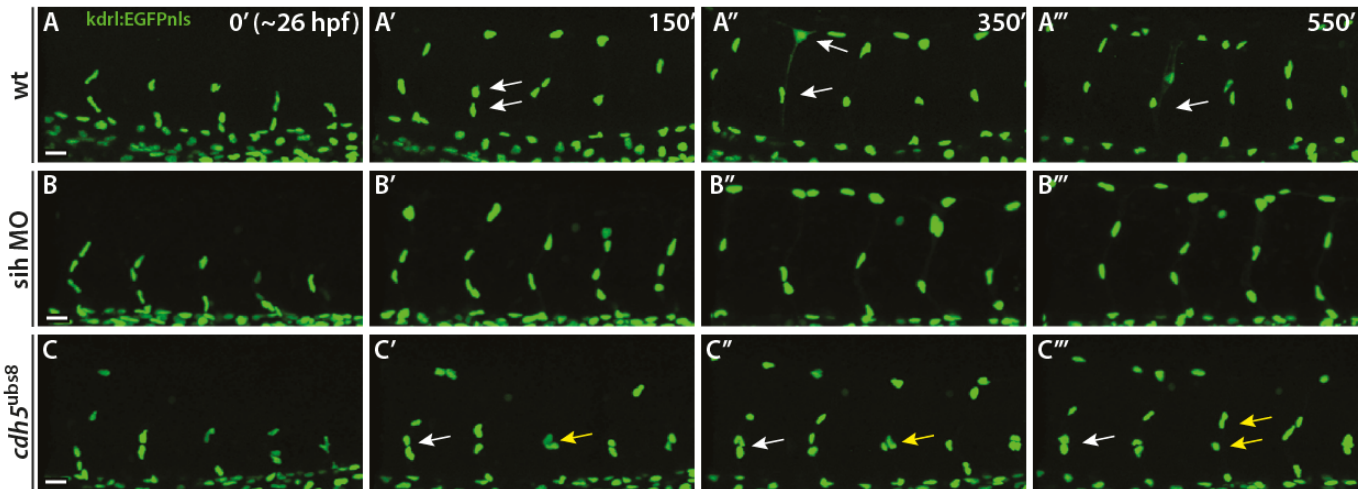# Figure S1

Figure S1 (Related to Figure 1). Characterization of the *cdh5*^{ubs8} and *cdh5*^{ubs9} mutant alleles.

(**A**) Schematic representation of the PCR strategy to screen for *cdh5* mutant embryos or fish. Allele specific PCR primers generate specific products as shown on the right hand side. (**B**) Schematic representation of two isolated mutant alleles, *cdh5*^{ubs8} and *cdh5*^{ubs9}. The wild-type amino acid sequence at the mutation site and schematic drawing of the *cdh5* gene product, with the 5 cadherin repeats (green), the transmembrane domain (dark gray) and the cytoplasmic domain (blue) are depicted. *cdh5*^{ubs8} carries a 4-base pair deletion in exon 3, this frameshift leads to a premature translational stop. *cdh5*^{ubs9} carries a 9 bp deletion leading to a deletion of 3 amino acids between cadherin repeat 1 and 2. (**C and D**) Immunofluorescent analysis of transgenic Tg(*fli1a:EGFP*)^{y1} embryos (anterior to left, 32 hpf) stained for Cdh5. Junctional localization of the Cdh5 as shown in wild-type embryos (**C**) is lost in *cdh5*^{ubs8} mutant embryos (**D**). The green asterisks in (**C'**) and (**D'**) indicate cross-reactivity of the Cdh5 antiserum in the pronephros. (**E to G**) Lateral views (anterior to left) of transgenic Tg(*fli1a:EGFP*)^{y1} embryos at 32 hpf in inversed contrast. (**E**) A wild-type embryo; (**E'**) is a close-up of the trunk of the green square in (**E**); (**E''**) is a close-up of the red square in (**E'**) showing neighboring tip cells establishing contact (**arrow in E''**); (**E'''**) is a close-up of the blue square in (**E'**) showing lumen formation in the SeA (**arrow in E'''**). (**F**) A *sih* morphant that has normal angiogenic behavior (**arrow in F''**) except for the lumen formation (**arrow in F'''**). (**G**) A *cdh5*^{ubs8} mutant embryo, which shows several angiogenic defects. During contact establishment between tip cells (**arrow in G''**), supernumerous contacts are made; in the stalk, weak tip cell – stalk cell connections (**arrow in G'''**) lead to detachments. Scale bars, 20µm; SeA, segmental artery.

Figure S2

Figure S2 (Related to Figure 1). Stalk cells cluster close to the DA in *cdh5* mutant SeAs.

(**A to C**) Confocal still pictures from time-lapse movies (**Movie S1**) showing lateral views (anterior to left) of transgenic Tg(*kdrl:EGFPnls*)^{ubs1} embryos expressing nuclear EGFP. After initial vessel outgrowth the nuclei are distributed regularly over the SeA and DLAV in wild-type embryos (**A**) and *sih* morphants (**B**). In *cdh5*^{ubs8} mutants (**C**) the nuclei accumulate in clusters close to the dorsal aorta (compare arrows in **C** and **A**). Scale bars, 20μm; DLAV, dorsal longitudinal anastomotic vessel; SeA, segmental artery.

Figure S3
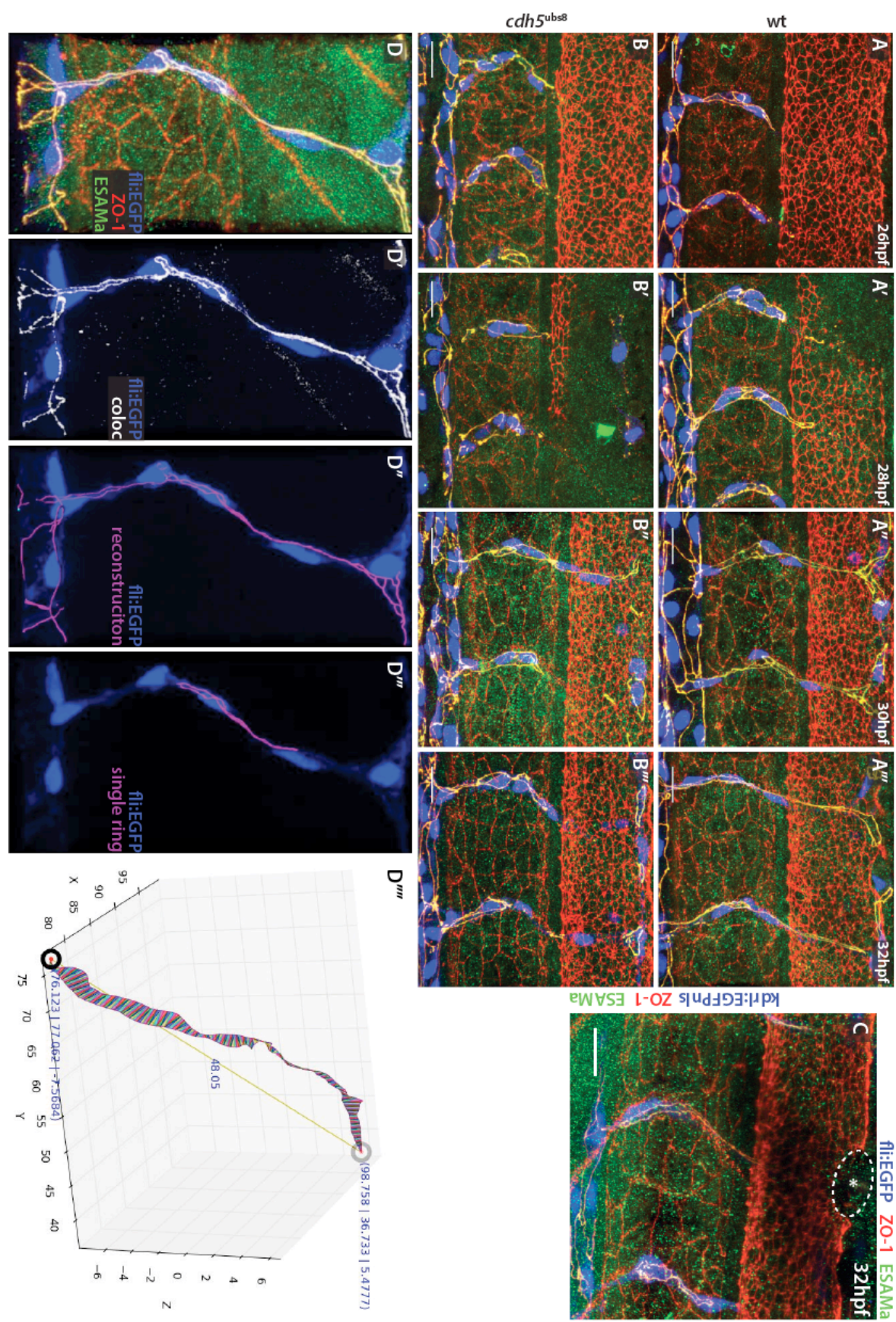
**Figure S3 (Related to Figure 2). Cdh5 is required for circular to elliptic transformation of junctional shapes.**

(**A and B**) Immunofluorescent analysis Tg(*kdrl:EGFPnls*)*[ubs1]* (blue) embryos stained for Zo-1 (red) and Esama (green). Zo-1 and Esama co-localize at endothelial cell junctions during SeA formation. In wild-type embryos cell junctions elongate during SeA outgrowth (**A**), whereas stalk cells of *cdh5* mutant embryos cluster close to the DA no junctional elongation is observed (**B**). (**C**) Example of a tip cell ablated wild-type Tg(*fli1a:EGFP*)*[y1]* (blue) embryo stained for Zo-1 (red) and Esama (green) around 32 hpf. The white asterisk and the white dotted circle demarcate the area of laser irradiation. (**D**) Procedure of junctional interface calculation **(Movie S4)**. Tg(*fli1a:EGFP*)*[y1]* (blue) embryo stained for Zo-1 (red) and Esama (green) around 32 hpf (**D**). The junctional signals were co-localized (**D'; white**) to reconstruct the junctions in 3D (**D''**; purple). Single reconstructed rings (**D'''**; purple) were selected for 3D shape quantification (**D''''**). In the reconstruction the coordinates of the two most distant points as well as their shortest distance are indicated. Surface area was calculated by tessellation (illustrated by colored polygons). The x-, y- and z-axes are indicated in µm. Scale bars, 20µm; DA, dorsal aorta; SeA, segmental artery; Zo-1, zona occludens 1; Esama, endothelial cell-selective adhesion molecule a.

Figure S4
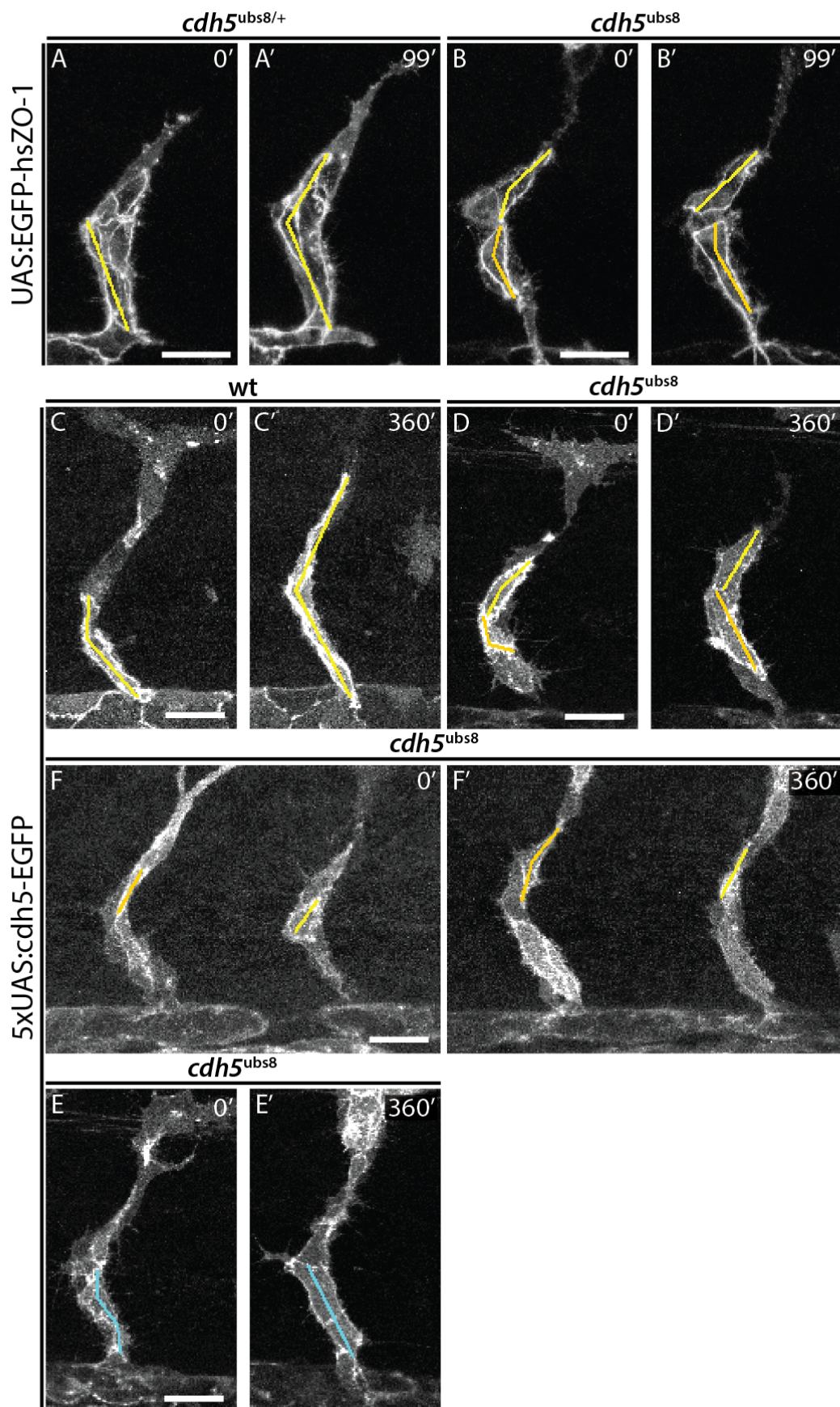
Figure S4 (Related to Figures 3 and 4). Junctional elongation requires actin-binding domain of Cdh5.

Confocal still pictures from time-lapse movies showing lateral views (anterior to left) of SeAs of transgenic Tg(*fli1ep:gal4ff*)^{ubs3};(*UAS:RFP*);(*UAS:EGFP-hsZO-1,cmlc:EGFP*)^{ubs5} (**A and B**) and Tg(*fli1ep:gal4ff*)^{ubs3};(*UAS:RFP*);(5x*UAS:cdh5-EGFP*)^{ubs12} (**C to F**) embryos. The longitudinal extent of junctional interfaces was measured at the beginning and end of the experiment. Individual measurements (**see Table S1**) are indicated in colored lines (yellow, orange or blue). Different colors were used to distinguish measurements taken within single embryos. Scale bars, 20µm; SeA, segmental artery.

Table S1

	genotype	L (t1)	L (t2)	ΔL (µm)
EGFP-hsZO-1	ubs8+/-	33.082	55.633	**22.55**
	ubs8-/-	24.883	24.124	**-0.76**
	ubs8-/-	22.179	27.974	**5.80**
cdh5-EGFP	ubs8+/+	39.647	80.867	**41.22**
	ubs8-/-	23.306	22.792	**-0.51**
	ubs8-/-	18.475	29.045	**10.57**
	ubs8-/-	30.172	33.547	**3.375**
	ubs8-/-	13.404	17.791	**4.39**
	ubs8-/-	16.673	27.642	**10.97**

Table S1 (Related to Figure S4). Junctional elongation requires the actin-binding domain of Cdh5.

Longitudinal junctional elongation monitored with EGFP-hsZO-1 or Cdh5-EGFP. Substantial junctional lengthening was observed in heterozygous *cdh5ubs8* embryos with EGFP-hsZO-1, while in mutant embryos the lengthening was negligible, reflecting the stalk's cells inability to elongate (corresponding pictures in **Figure S4A-B**). Expression of Cdh5-EGFP, that lacks the cytoplasmic domain and therefore also the actin binding domain, in wild-type embryos showed extensive lengthening of endothelial cell junctions (similar to those observed with EGFP-ZO-1 marker). By contrast, the construct could not rescue the defects observed in the *cdh5* mutant. Instead only moderate extensions, as well as contractions were observed (corresponding pictures in **Figure S4C-E**). L (t1):

longitudinal junctional length at time point 1 in µm; L (t2): longitudinal junctional length at time point 2 in µm; ΔL: difference in junctional length between time point 1 and 2 in µm.

Supplemental Movie legends

Movie S1 (Related to Figure 1). Cdh5 is required for blood vessel integrity during angiogenesis.

Time-lapse movie (starting around 28 hpf) showing lateral view (anterior to the left) of SeA morphogenesis in wild-type (**A; top**), *sih* morphant (**B; middle**) and *cdh5^ubs8* (**C; bottom**) transgenic Tg(*kdrl:EGFP*)^*s843* embryo in inversed contrast. At 32 hpf, when wild-type SeAs have established intersegmental contacts to form the DLAV, *cdh5* mutant SeAs appeared disorganized and with supernumerary filopodial extensions and frequently exhibited multiple contacts between neighboring SeAs. Initial tip cell formation and dorsal extension of SeA sprout was normal, however tip cells failed to organize themselves into the DLAV. Furthermore, tip cell dissociated from stalk in 34% of segments in *cdh5* mutant SeAs (n=18), leaving the stalk cell in the proximity of the dorsal aorta. Stalk cells frequently reconnected to the DLAV, which they achieved by dorsal protrusions rather than cell migration or cell movement. These defects in sprout outgrowth were not caused by disruption of blood circulation, because *sih* morphants, which lack blood flow, displayed normal SeA outgrowth.

Movie S2 (Related to Figure S2). Stalk cells cluster close to the DA in *cdh5* mutant SeAs.

Time-lapse movie (starting around 26 hpf) showing lateral view (anterior to the left) of a wild-type (**A; top**), *sih* morphant (**B; middle**) and *cdh5^ubs8* (**C; bottom**) transgenic Tg(*kdrl:EGFPnls*)^*ubs1* embryo during angiogenesis. In wild-type and *sih* morphant embryos cell nuclei (green) move dorsally and distribute over the SeA. In *cdh5^ubs8* mutant embryos the cell nuclei initially move dorsally, but remain close to the dorsal aorta.

Movie S3 (Related to Figure 1). Rapid recovery of sprouting behavior upon tip cell ablation.

Time-lapse movie (starting around 28 hpf) showing lateral view (anterior to the left) of a wild-type transgenic Tg(*fli1a:EGFP*)*[y1]* embryo during laser microsurgery. On the left hand side the fluorescent signal (EGFP) is shown and on the right hand side brightfield was recorded to visualize the embryos during the laser ablation. To record the lasering process only the focal plane was recorded (starting at 5 min). Application of the laser starts at 5 min and 5 seconds and lasts for 4 seconds (a hole appears at the lasering spot). Approximately 1 min after laser ablation whole stacks were recorded and the ablated tip cell undergoes apoptosis between 6 and 17 minutes. The stalk cells rapidly resume sprouting (around minute 31). Eventually a functional SeA is formed.

Movie S4 (Related to Figures 2 and S3). Junctional ring measurement procedure.

Animation of the junctional ring measurement procedure. Rotating 3D image of a SeA of a transgenic Tg(*kdrl:EGFPnls*)*[ubs1]* embryo stained for Esama and Zo-1 by immunofluorescence. First, the original confocal stack is shown; cell nuclei (EGFPnls):blue; Esama: green; Zo-1: red. For a more specific junctional signal, the green and red channels were co-localized (white). On the co-localization signal the junctions were reconstructed (purple).

A single junctional ring was selected and reconstructed in 3D for shape quantification (which is shown in the last part of the movie). The coordinates of the two most distant points as well as their shortest distance are indicated. Surface area was calculated by tessellation as illustrated by colored polygons. The x-, y- and z-axes are indicated in μm.

Movie S5 (Related to Figure 3). Cdh5 is required for concerted cell elongation during sprout outgrowth.

Time-lapse movie (starting around 26 hpf) showing a lateral view (anterior to the left) of a heterozygous $cdh5^{+/ubs8}$ (**A; top**) and homozygous $cdh5^{ubs8}$ (**B; bottom**) transgenic Tg(*fli1ep:gal4ff*)^{ubs3}; (*UAS:mRFP*); (*UAS:EGFP-hsZO-1,cmlc:EGFP*)^{ubs5} embryo during angiogenic sprouting. On the left hand side the red (mRFP) and the green (EGFP-ZO-1) are merged, on the right hand side only the EGFP-ZO-1 channel is shown. During wild-type sprout elongation, cell junctions (EGFP-ZO-1) stretch over the entire length of the SeA. This ring expansion represents stalk cells, which are elongating their cell bodies from bottom to top of the SeA, while in mutant embryos the cells do not elongate and the rings stay rather round.

Supplemental Experimental Procedures

Generation of anti-zf-Esama antibodies

2 different peptides derived from the intracellular domain of zf-Esama (XP_001339787) were synthesized, coupled to keyhole limpet hemocyanine and used to raise polyclonal anti-sera in rabbits using standard immunization procedures (Peptide Specialty Laboratory, Heidelberg, Germany). Peptide sequences: zf-Esama-pep1 (aa310-327): TSSYPRDAHNHHHYPHSD; zf-Esama-pep2 (aa355-380): LPGYNTNPAPTRGPFGPPSTNGGSQH. We tested specificity of the serum by morpholino injections against *Esama*, which abrogated all endothelial staining (details will be provided upon request). Weak cross-reactive labeling within the myotome and pronephros was maintained in *Esama* morphants.

Generation of *cdh5* mutant alleles

Zinc-finger nucleases (ZFN) were designed to target exon 3 of *cdh5* and generated by Sigma-Aldrich. Capped ZFN mRNA was injected into 1- to 2-cell stage embryos. G0 adults were crossed to Tg(*fli1*:EGFP)^{y1} fish and their progeny were screened for restriction polymorphisms in the ZFN target site (n=80 per G0 fish in pools of 5 embryos). A PCR product generated with *cdh5*-FWD1 (GAAGAGGCATTTAGGAACTG) and *cdh5*-REV1 (CTGCATATTATTCTAAATGCTGCC) primers was used to screen for loss of the Hpy188I site, which overlaps with the target site of the *cdh5* ZFN. F1 progeny of G0 adults were screened for germ line transmission and sequence analysis of F1 progeny revealed two mutant alleles, a 4-bp and a 9-bp deletion (*cdh5*^{ubs8} and *cdh5*^{ubs9}, respectively) at the ZFN target site (**Fig. S1B**).

For subsequent genotyping experiments we designed a codominant marker, comprising of two outside and two allele specific internal primers (**Fig. S1A**). Multiplex PCR including these primers generated allele-specific products for $cdh5^{wt}$ (387 bp) and for the $cdh5^{ubs8}$ mutant (195 bp).

Primer sequences are:

$cdh5$-FWD:　　　TTGGTGTAACTGACAATGGGG

$cdh5$-REV:　　　ACAGTCTTGGTGTTACCATTGGG

$cdh5$-WT-FWD:　ATCCCCGTTTTCGATTCTGAC

$cdh5$-ubs8-REV: CTGATGGATCCAGATTGGAATC

3.2. Contribution to publications

3.2.1. Lenard et al., 2013, Developmental Cell

Summary:

Lenard et al., describes cell behaviors during anastomosis in the cranial vasculature of zebrafish embryo (Lenard et al., 2013). Tip cells of angiogenic sprouts connect to other sprouts or pre-existing blood vessels, forming a branched vascular network. Cell recognition over single filopodial contacts precedes *de novo* apical polarization, apical membrane invagination and fusion of luminal compartments. Newly formed vessel branches initially form as unicellular tubes with transcellular lumen in blood pressure-dependent manner. Subsequent cell rearrangements, involving cell splitting, quickly transform these tubes from a unicellular to multicellular conformation. These cell rearrangements also occur in the absence of blood flow and formed luminal pockets are reminiscent of cord hollowing process.

Since a single contact is sufficient for ECs to anastomose, we investigated the role of VE-cad in this process. The absence of VE-cad increases the sprouting activity of EC, which also resulted in multiple contact points between two anastomosing ECs. This suggests roles for VE-cad in cell recognition, which could not be normalized by limiting VEGFR2 signaling. Furthermore, subsequent polarization defects were not observed in *ve-cad* mutant embryos.

My contribution:

I generated, tested and established the α-Esama antibody, which was essential for the analysis of the *ve-cad* mutant phenotype.

The full publication is appended in chapter A.1, page 190.

3.2.2. Santos et al., 2014, Nature Communications

Summary:

Santos et al. investigated the evolutionary occurrence of haplochromines (a species-rich group of cichlids) egg-spots on male fins that are involved in mating behaviors (Santos et al., 2014). They identified two paralogous genes, *fhl2a* and *fhl2b*, which are involved in pigmentation. *fhl2b* was associated with the formation of egg spots and harbors an evolutionary feature only present in the haplochromines group: a transposable element in the *cis*-regulatory region of the gene. This regulatory region further showed enhancer activities in transgenic zebrafish iridophores. Especially this type of pigment cells are found in egg-spot bearing fins and suggest gain of function during evolution of haplochromines.

My contribution:

I helped in the design and generation of the zebrafish transgenic lines and during the imaging process. Further, I contributed during the writing and reviewing process with comments.

3.2.3. Phng et al., 2015, Developmental Cell

Summary:

Phng et al. investigated the role of Formin-like 3 (Fmnl3) during lumen formation in zebrafish (Phng et al., 2015). As an actin nucleator, Fmnl3 acts as actin nucleator and elongation factor and localizes to filopodia and junctions in ECs. When Fmnl3 is knocked down during early ISV development, filopodial number and length are decreased, but does not affect morphogenesis. However, during ISV lumenogenesis, pharmacological inhibition of formin function or mosaic expression of a dominant-negative Fmnl3ΔC construct leads to the collapse of lumen. This indicates that formins are needed for F-actin polymerization and thus junctional integrity, which was further validated by EGFP-actin FRAP (fluorescence recovery after photobleaching) experiments. Furthermore, cell culture experiments showed that pharmacological inhibition of formins leads to the disassembly of linear junctions and even force-dependent intercellular gap formation. However, the weakening of junctional F-actin and the subsequent opening of junctions only happens if the actin is physically coupled to the cell junctions (through VE-cad). Thus, they observed a decrease in junctional organization in *ve-cad*[ubs8] mutants expressing VE-cadΔC-EGFP (UBS12) (VE-cad that lacks the cytoplasmic domain and thus cannot bind to actin), suggesting a decrease in junctional stability when VE-cad is not linked to F-actin. These findings suggest that Fmnl3 maintains F-actin stability at the junctions, which is important for lumenization and lumen stability. This study is one of the first ones to highlight the importance of formins at EC junctions.

My contribution:

I provided zebrafish embryos positive for the VE-cadΔC-EGFP (UBS12) reporter in VE-cad mutants (UBS8). Further, I critically commented on the manuscript during the writing and reviewing procedure.

3.2.4. Ittig et al., in preparation

Summary:

Ittig et al. propose a protein delivery tool based on a bacterial type III secretion system (T3SS). Ittig et al. hijacked the T3SS of *Yersinia enterocolitica* and demonstrate controllable and effective protein translocation into eukaryotic host cells. Furthermore, they validated their tool in living zebrafish embryos. Therefore, the tool offers new possibilities in medical applications for directed protein delivery.

My contribution:

I helped during the validation of the bacterial-based protein delivery system in zebrafish embryos. Bacterial suspensions that express either an apoptosis inducing or control protein were injected into hindbrains of zebrafish embryos. We quantified the induced apoptosis by staining and subsequent confocal imaging of the injected embryos.

Due to possible conflicts of interest only the abstract is appended in chapter A.4, page 229.

3.3. Additional results

3.3.1. Generation fish lines

3.3.1.1. Apical marker lines

Cell polarization during angiogenesis is thought to happen simultaneously with junctional maturation and is crucial for subsequent vessel lumenization. Therefore, the generation of transgenic zebrafish that express molecules that are tethered to the apical membrane would visualize the cell polarization processes. We chose two different proteins that are known to localize to apical membranes once cell polarity is established, namely Podocalyxin (Pdxl) and Folate receptor (FR).

Podocalyxin as an apical marker

We previously showed that endogenous Podocalyxin-like 2 (Pdxl2) is localized to the apical membrane by antibody staining (Herwig et al., 2011; Lenard et al., 2013). Yannick Blum, a former lab member, cloned a zebrafish Pdxl2 N-terminally tagged with mCherry. I exchanged the promoter to a four times non-repetitive UAS (4xUAS) (Akitake et al., 2011) and generated Tg(*4xUAS:mCherry-zfpdxl*). In this line, the reporter showed strong mosaicism and rather weak expression. Further, it sometimes showed puncta that seemed to be located apically (Figure III-1). However, the localization of the marker was not always easily associated with apical compartments (blue arrowheads in Figure III-1 A'' and B''). Often it looked like the fluorescent spots localized to cell junctions (blue arrowhead in Figure III-1 B''). For these reasons, the interpretation of this apical marker is tedious and unreliable. Therefore, also because of the weak expression, the line was not further characterized.
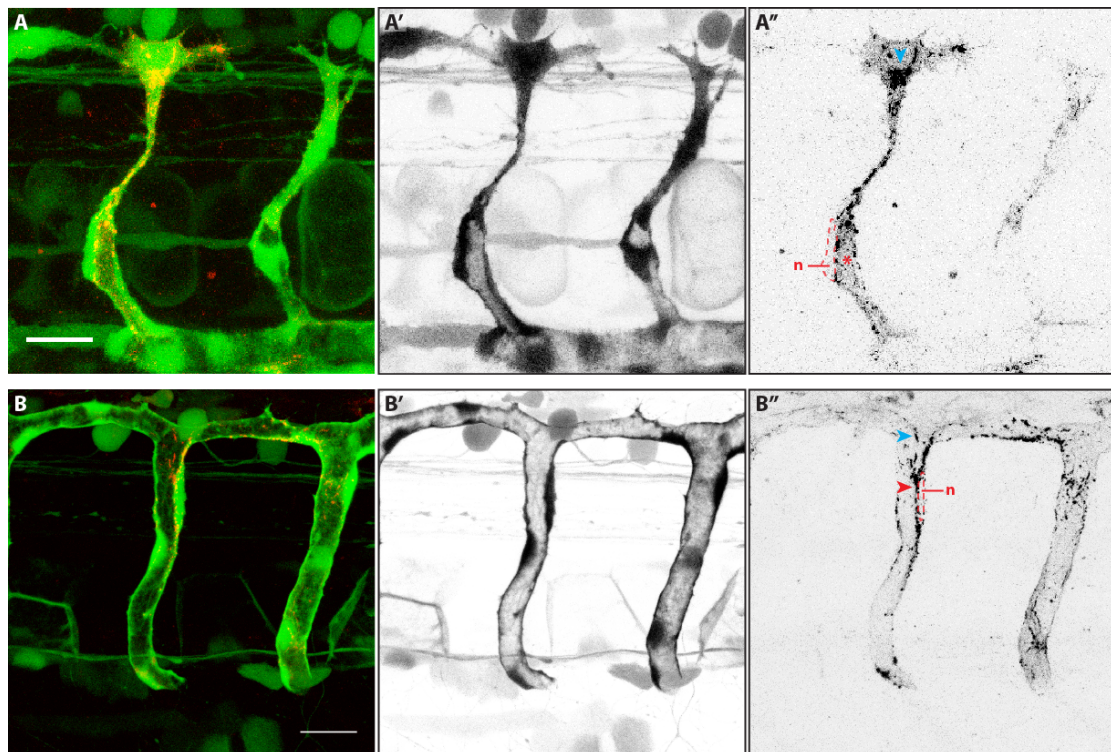
Figure III-1: The mCherry-zfpdxl marker seems to localize apically

Tg(*fli1ep:GFF*)[ubs3](*UAS:EGFP*)(*4xUAS:mCherry-zfpdxl*) embryos at 30hpf (A) and 48hpf (B). Merged channels on the left-hand side and cytoplasmic EGFP (green, A' and B') and pdxl-mCherry (red, A'' and B'') in inversed contrast. (**A**) Still pictures from movie **AMovie_1**. Partially luminized ISV shows compartments enriched with the apical Pdxl2 marker (red asterisk), just above the cell nucleus. However, the apical localization is not always apparent and localizes throughout the cell (blue arrowhead). (**B**) The red puncta seem to localize apically (red arrowhead), but also where junctions are expected (blue arrowhead). The red dotted line demarcates cell nuclei; scalebars, 20µm; n, nucleus.

FR-mKate2 an engineered apical marker

Folate receptors (FR) are secreted glycosylphosphatidylinositol (GPI) anchored proteins that are sorted to the apical membrane. Its GPI attachment signal sequence contains information for apical sorting. The GPI sorting signal of FR fused to GFP was shown to accumulate at apical membrane compartments in cultured cells (Paladino et al., 2008). To create an apical marker, we used the construct kindly provided by the Chiara Zurzolo lab (Napoli, Italy) (Paladino et al., 2008) and I exchanged the GFP sequence with the one of a red fluorescent protein (mKate2), which would allow the

simultaneous usage of green junctional marker lines (e.g. Zo-1-EGFP). The generated Tg(*4xUAS:FR-mKate2*)[ubs17] was first crossed to Tg(*fli1ep:GFF*)[ubs3](*UAS:EGFP*) fish to determine the marker's localization with respect to luminal compartments. The generated line showed little mosaicism (Figure III-2 A) and the fusion protein located to both (apical and basolateral) membranes. At first glance, the apical membrane seemed to be enriched with the marker (Figure III-2 B). However, inspection of single sections showed similar signals in both membrane compartments, especially evident around cell nuclei (Figure III-2 D'). Furthermore, strong patches of fluorescence aligned where junctions are expected, most evident in the DA (Figure III-2 A and B, and corresponding movies **AMovie_2** and **AMovie_3** respectively).

Since both membrane compartments are labeled, the FR-mKate2 marker is somewhat difficult to use as a cell polarization marker. Further characterization of the line is needed to understand the origin of the junction-like accumulation of the marker. One explanation for this could be the translocation of the marker from the basolateral to apical compartment, more of this will be discussed in chapter A.5.1 on page 230.

Figure III-2: FR-mKate2 labels membrane compartments

The GPI anchored mKate2 in Tg(*fliep:GFF*)[ubs3](*UAS:EGFP*)(*4xUAS:FR-mKate2*)[ubs17] embryos are located to the membranes and the junctions. Single channel for FR-mKate2 is shown in inversed contrast. (**A**) Is a still image from movie **AMovie_2** taken at approximately 30hpf (anterior to the left). The apical marker is expressed with little mosaicism and strong patches appear in a junction-like pattern (see blue arrowheads). (**B**) Still picture of movie **AMovie_3** at around 40hpf. The marker still localizes in strong junction-like patches, especially apparent in the DA (blue arrowheads in B'). The membrane surrounding the nucleus appears lighter in B', while the apical membrane is darker (red arrowheads). This apically enriched signal is due to superimposed membrane compartments (basal and apical). (**C and D**) An embryo around 48hpf with fully lumenized ISVs. (D) Is a single confocal plane in the region demarcated by the blue dotted box in (C). The apical and basal membranes surrounding a nucleus show similar intensities (red arrowheads in D'). Junctional patches (blue arrowheads in C') are still observed at this stage, and furthermore they do not lay the same plane as the apical membrane compartment shown in D'. Asterisk demarcates luminal compartment. Scalebar, 20µm; n, nucleus.

FR-mKate2
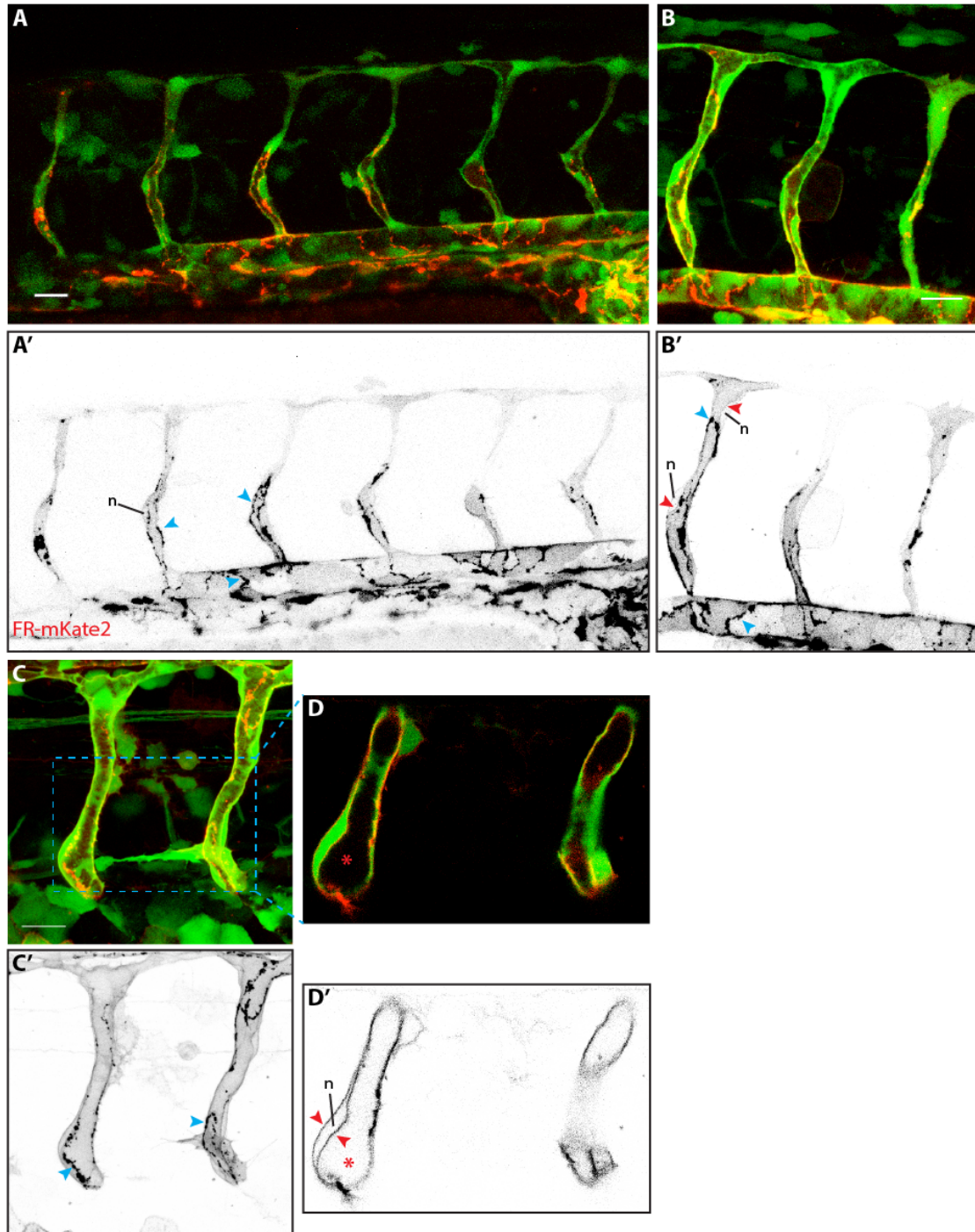
3.3.1.2.　　Actin cytoskeleton marker

Organ morphogenesis requires dynamic cell behaviors, including cell migration, adhesion and cell shape changes. All these activities are brought about by the cell's cytoskeleton and one of these cytoskeletal components is the actin one. Actin is well known to give a cell a given shape and regulate a cell's locomotion. Therefore, the visualization of the actin cytoskeleton leads to deeper understanding of processes underlying organ morphogenesis, including vascular morphogenesis.

A Life-act marker that visualizes cytoskeletal structures ineffectively

There are several life markers to visualize actin structures; one of the most commonly used ones is life-act (tagged with a fluorescent protein). Life-act is a 17aa peptide that binds F-actin without affecting actin dynamics (Riedl et al., 2008). I used the Tg(*UAS:lifeact-EGFP*) line (an unpublished transgenic line from Marina Mione's lab) together with the Tg(*fli1ep:GFF*)[ubs3] driver line and observed rather a cytoplasmic localization of the construct during early stages of development. At later stages an increase in junctional signal was observed (Figure III-3 B), indicating the construct's ability to bind to actin structures. However, high magnification images of CCV cells (which are flat, similar to cell culture) revealed single F-actin cables very poorly (Figure III-3 C).
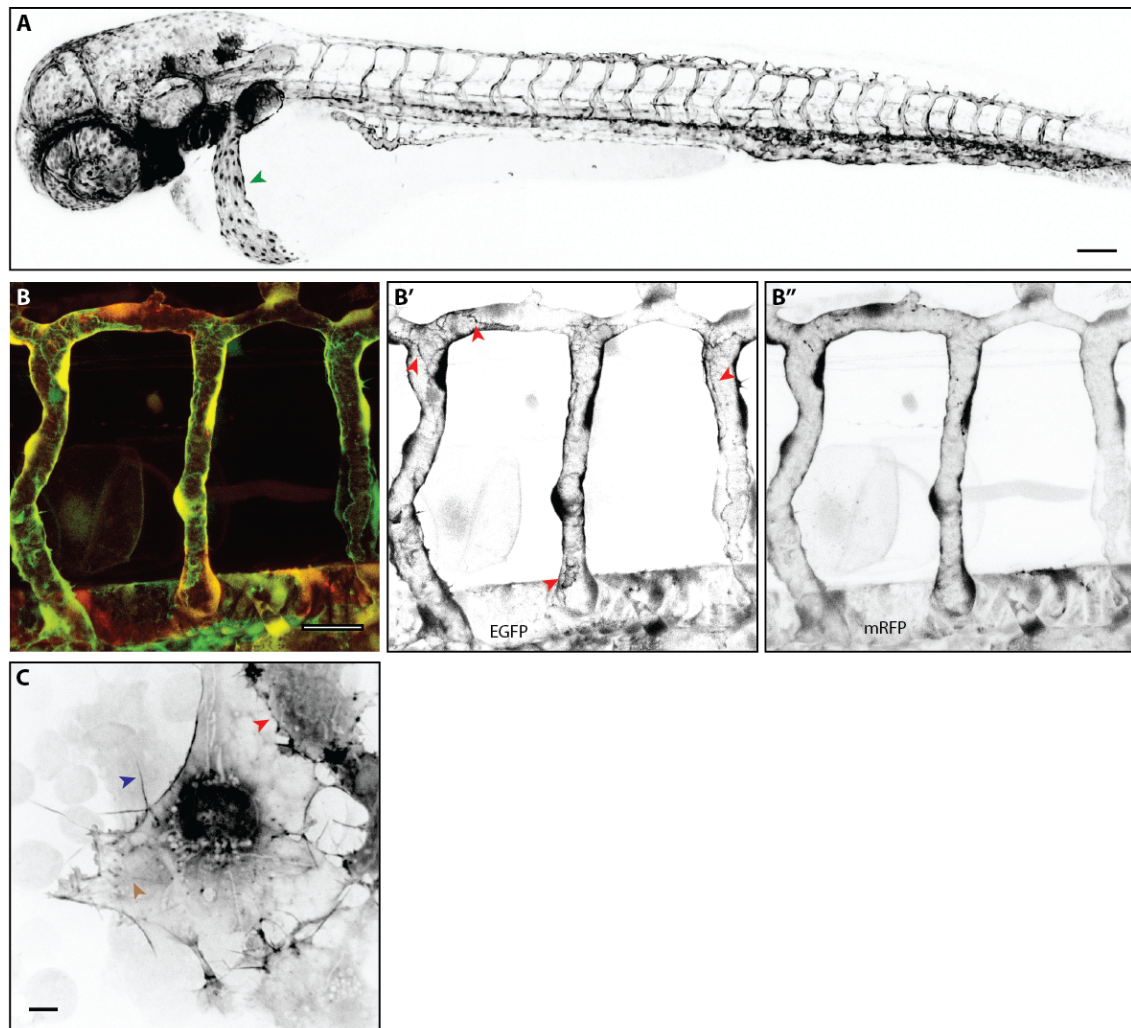
Figure III-3: Life-act-EGFP localizes poorly to F-actin

(**A**) Represented picture a Tg(fli1a:EGFP)y1 embryo. The green arrowhead points to the CCV. Scalebar, 100µm. (**B**) Lumenized ISVs of a Tg(*fli1ep:GFF*)[ubs3](*UAS:lifeact-EGFP*)(*UAS:mRFP*) embryo at 48hpf, anterior to the right. Life-act (green or in inversed contrast in B') is mainly cytoplasmic localized and looks similar to cytoplasmic mRFP (red or inversed contrast in B''). However, cell-cell junctions are weakly labeled (red arrowheads in B'). Scalebar, 20µm. (**C**) Endothelial cell of the CCV of a Tg(*fli1ep:GFF*)[ubs3](*UAS:lifeact-EGFP*) embryo. Distinct subcellular compartments are visible with high magnification in flat (cell culture-like) cells. The life-act construct localizes to junctions (red arrowhead), filopodia (blue arrowhead), and labels F-actin cables within the cell, however poorly (brown arrowhead). Scalebar, 5µm.

UCHD, a multipurpose actin marker

To better visualize the actin cytoskeleton, we decided to try another actin binder: based on the calponin homology domain of Utrophin (UCHD). Utrophin is best known as the non-muscular counterpart of dystrophin, which links the actin cytoskeleton via transmembrane proteins to the ECM. The UCHD based probes bind to F-actin, do not interfere with biological processes in the cells and furthermore, it can highlight actin dynamics (Burkel et al., 2007).

I generated three transgenic zebrafish lines expressing differently tagged human UCHD. Tg(*4xUAS:EGFP-UCHD*)[ubs18] embryos expressed the fusion protein mostly uniformly in the vasculature, when driven by Tg(*fli1ep:GFF*)[ubs3] (Figure III-4 A). However, amongst ECs of the same embryo, the reporter showed different expression levels (compare both ISV in Figure III-4 B'). The junctions were very nicely labeled with this transgenic marker, which reflects high actin content. Furthermore, high magnification imaging visualized the actin cytoskeleton very well, compared to the life-act marker (compare Figure III-4 C to Figure III-3 C). Usually around the nucleus, fluorescent spots were observed (Figure III-4 A and C), which might be accumulation of the construct due to overexpression. High magnification time-lapse imaging allowed the imaging of the dynamics of the cytoskeleton, predominantly seen during filopodial assembly (see movie **AMovie_4**).

Next to the green UCHD line, I also generated a red one. I initially fused the UCHD with mKate2, however, this fusion protein did not appear to localize properly. Similar observations have been made in other labs (Li-Kun Phng personal communication). Therefore, I fused the UCHD to mRuby2 fluorescent protein and the transient expression overlapped with the EGFP-UCHD localization (Figure III-5 A). Using this line, the junctional and cytoskeletal actin dynamics can be compared. As shown in Figure III-5 B the Zo-1 (green) marker overlaps with the red mRuby2-UCHD at the junctions. Even more, the UCHD marker is a very versatile cytoskeletal marker and visualizes many different structures (e.g. filopodia). Furthermore, it also marks differences in junctional actin content, when compared with Zo-1 (at the upper edge of the junctional ring in Figure III-5 B, green arrowhead). Junctional actin

is in constant turnover and therefore, differences in junctional actin content indirectly correlates with dynamics of junctional maturation.

Taken together, the UCHD cytoskeletal markers allow detailed analysis of EC cytoskeletal architectures. Although we can observe differences in actin dynamics with these markers, the cellular resolution is only provided by mosaic analysis. For this reason I generated also a photoconvertible version of the UCHD construct, by fusing it to mClav. The Tg(*4xUAS:mClav-UCHD*) seems to work *in vivo*, i.e. the localization of the marker is similar to the EGFP and mRuby2 versions and it also converts from green to red, when irradiated with UV light. However, I have not performed confocal imaging with this line yet.

Figure III-4: The UCHD reporter labels the actin cytoskeleton

Representative pictures of the vasculature of a Tg(*fli1ep:GFF*)[ubs3](*UAS:mRFP*)(*4xUAS:EGFP-UCHD*)[ubs18] embryo. On the left-hand side the merged channels and on the right-hand side, the EGFP-UCHD channel in inversed contrast. (**A**) Deconvolved confocal images of an embryo at around 32hpf. The reporter predominantly labels the junctions (red arrowhead), but also filopodial extension (blue arrowhead). Scalebar, 20µm. (**B**) Confocal images of a 48hpf old embryo. At this time point the ISVs have a patent lumen. The cytoskeletal marker nicely labels the cell-cell junctions (red arrowheads). Scalebar, 20µm. (**C**) Spinning disk confocal image of CCV cells at around 40hpf (Still picture from movie **AMovie_4**). The high magnification allows the visualization of actin filaments within the cell, which seem relatively stable. Strong signals are also observed at the cell periphery and junctions (brown and red arrowheads respectively). Time-lapse imaging also shows the dynamics of filopodia (blue arrowhead). The white asterisk in (C) demarcates a macrophage, which is passing by. Scalebar, 5µm.
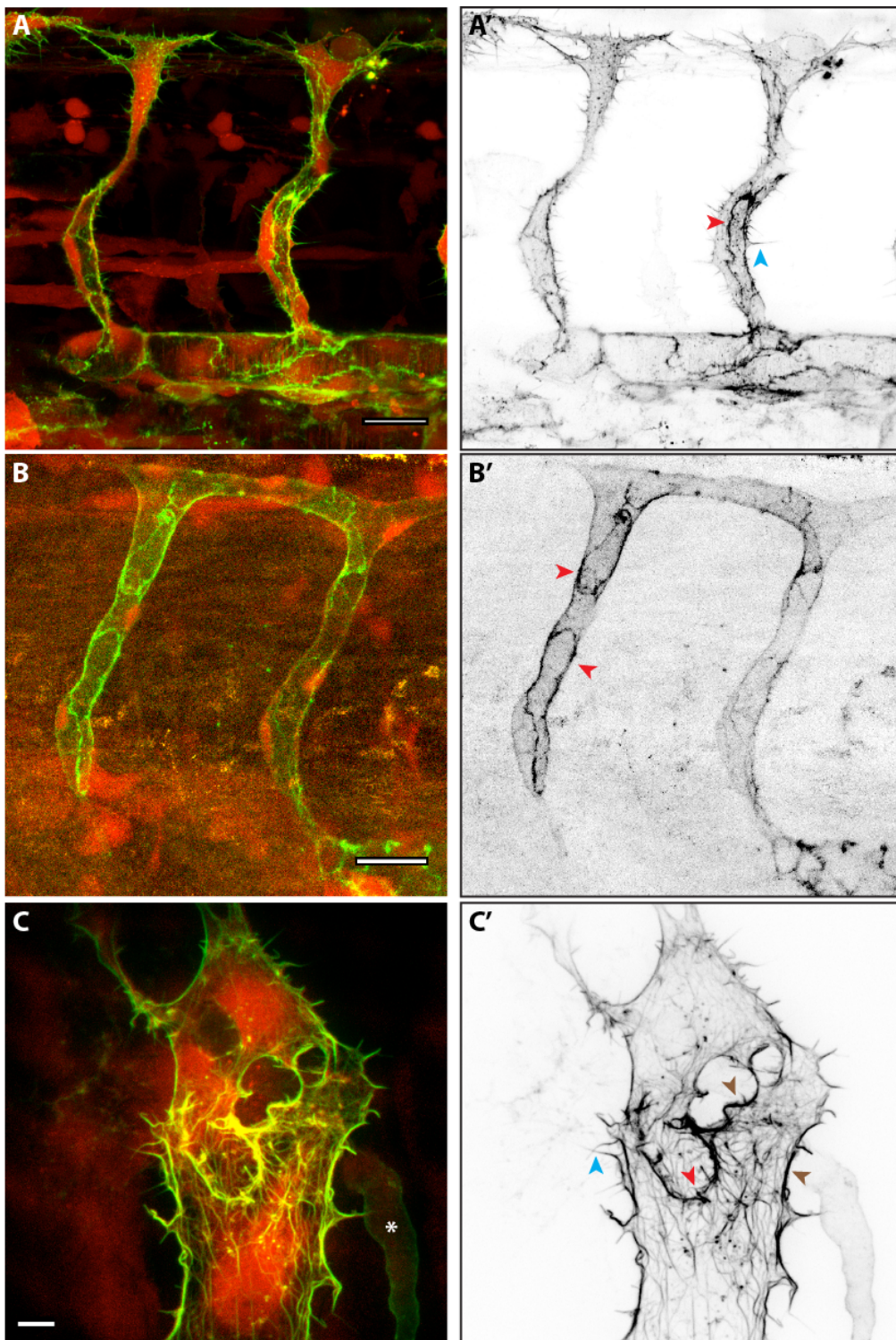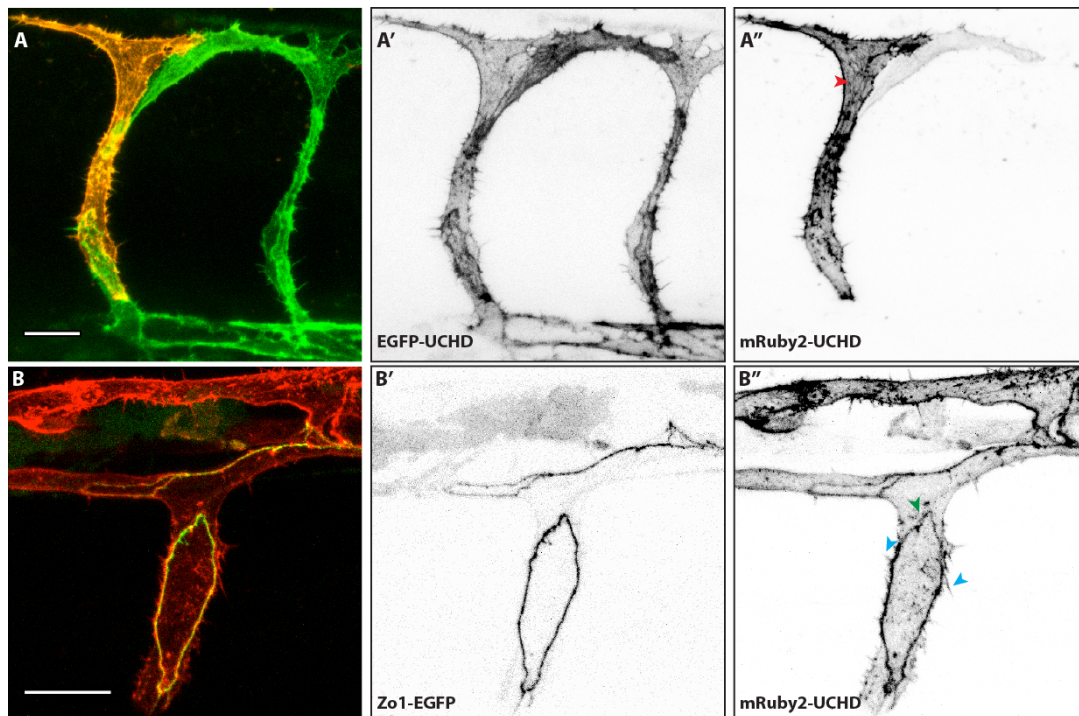
Figure III-5: The EGFP-UCHD and mRuby-UCHD markers colocalize

(**A**) Transient expression of 4xUAS:mRuby2-UCHD in Tg(*fli1ep:GFF*)[ubs3](*4xUAS:EGFP-UCHD*)[ubs18] embryo at around 34hpf. Single ECs express the red construct and the expression co-localizes with the EGFP-UCHD marker and single filaments are seen in the tip cells (red arrowhead). (A) Shows the merge of the green EGFP-UCHD (A', in inversed contrast) and the red mRuby2-UCHD (A'', in inversed contrast) channels. (**B**) Tg(*fli1ep:GFF*)[ubs3](*UAS:hsZo1-EGFP, cmlc:EGFP*)[ubs5](*4xUAS:mRuby2-UCHD*)[ubs20] embryo around 36hpf; (B) is the merge of the green Zo-1 (B') and the red mRuby2-UCHD (B''). The combination of the Zo-1 and the UCHD markers allows the differentiation of subcellular actin structures. Junctional actin and Zo-1 overlap, but mRuby2-UCHD visualizes also junctional spikes too (B'', blue arrowheads). Furthermore, junctional actin content seems to be lower at some sites of the ring than others (green arrowhead), which might represent differential junctional maturity. Scalebars; 20µm.

## 3.3.2. Analysis of angiogenic sprout outgrowth

During my PhD research I have thoroughly investigated the role of VE-cad during angiogenic sprout outgrowth (see Sauteur et al., 2014 in chapter 3.1.1). I found two morphogenetic processes that govern angiogenic sprouting. While tip cells have strong migratory behavior, stalk elongation is achieved by stalk cell elongation. In these processes, VE-cad is crucial to link the actin cytoskeleton at the cell-cell interface and so supports the adhesive properties of ECs. In the absence of VE-cad, tip and stalk cells detach occasionally from each other (observed in one third of the ISVs). After these detachments, the stalk cells of the *ve-cad* mutant sprout remained close to the DA for a long period. Furthermore, I found evidence for a role of VE-cad in angiogenic tip cell selection during sprout outgrowths. To analyze the role of tip cells during angiogenic sprouting, I ablated tip cells by laser irradiation, and observed that the stalk cells quickly redefine a new tip cell that leads the sprout, which was true for 10 out of 11 experiments (Sauteur et al., 2014).

Similarly, I performed tip cell ablation experiments also in the *ve-cad* mutant background. In 5 of 6 experiments, the stalk of *ve-cad* mutant ISVs recovered; however, the recovery happened significantly later (data not shown). While in wt conditions the sprout recovered within 2-5hr after tip cell ablation, *ve-cad*[ubs8] stalk cells remained close to the DA for over 10hr. Overall, tip cell ablated *ve-cad* mutant sprouts behave similar to mutant stalk cells, which have lost tip cell contact by cell detachment. Additionally, I observed that the stalk cells in the mutant extended long protrusions up to the DLAV, while the nucleus remained stationary. This seemed different to wt, where a recovering stalk cell extended filopodial protrusions and cell movement was accompanied by cell nucleus movement, which can be used as approximation for EC migration. These observations suggest that, in contrast to wt sprouts, *ve-cad* mutant sprouts are not able to functionally reestablish a tip cell.

3.3.2.1. VE-cad∆C exerts a dominant negative effect

Since cell elongation drives sprout extension, we considered that the same accounts for regenerating sprouts after tip cell ablation. To look at these dynamic processes, I performed live imaging of wt embryos transgenic for VE-

cadΔC-EGFP junctional marker. For these cell ablation experiments, I used a dissecting microscope and ablated with a 20x objective. To reduce tissue damage (surrounding the tip cell of interest), I used short and low laser pulses. Therefore, out of 5 embryos only 2 had ablated tip cells. Importantly, in both successful ablation experiments the DLAV formed (Figure III-6 B), which reflects little tissue damage. Surprisingly, the stalk did not regrow over the whole imaging session (>12hr) and the cells remained close to the DA. This is similar to the behavior of *ve-cad*[ubs8] mutant stalk cells. Despite of that, the stalk cells behaved normally, i.e. they divided (Figure III-6 B) and lumen formed into the partial sprout (Figure III-6 C). Therefore, the ectopic expression of the VE-cad construct that lacks the cytoplasmic domain (and thus cannot bind to actin) acts dominant negatively on the outgrowing sprout.
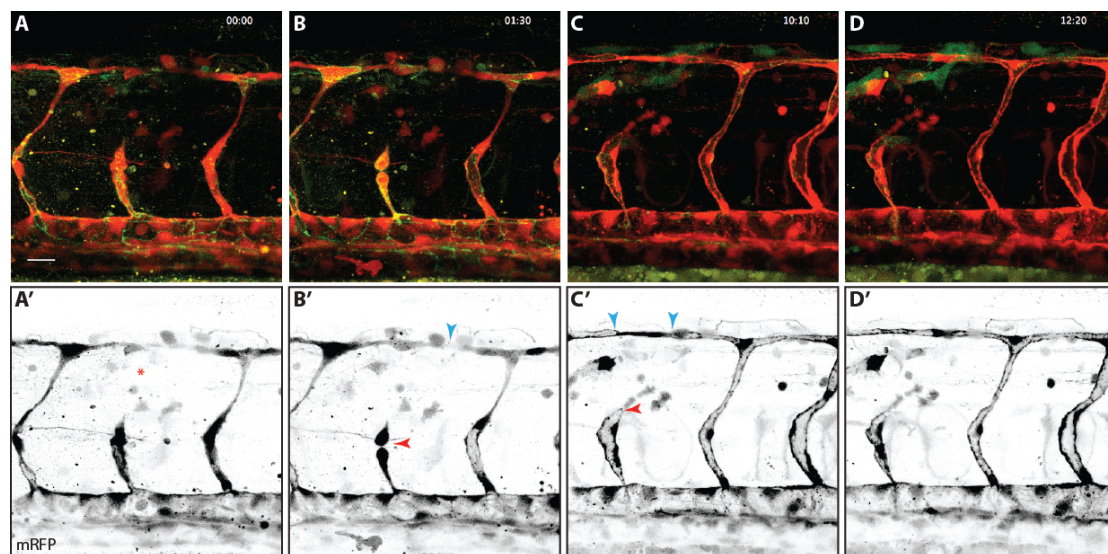
Figure III-6: Dominant negative effect of VE-cadΔC construct prevents sprout recovery

Stills from time laps movie **AMovie_5**. The tip cell of an ISV in a Tg(*fli1ep:GFF*)[ubs3](*UAS:mRFP*)(*UAS:VEcadΔC-EGFP*)[ubs12] embryo was ablated around 30hpf. The VE-cad-EGFP construct (green) lacks the cytoplasmic domain of VE-cad and the ectopic expression prevents the stalk from regenerating after tip cell ablation. (**A**) Confocal stack right after the tip cell ablation. (A') The red channel is shown separately in inversed contrast. The red asterisk demarcates where the ablated tip cell was. (**B-D**) At the level of the DLAV endothelial cells connect (blue arrowhead in B') over the ablation point and the vessel is perfused (blue arrowheads

in C'). The tip cell ablated stalk cells divide (red arrowhead in B') and lumenize (red arrowhead in C'), but does not regrow over the observation period (>12hr), indicating a possible dominant negative effect of the transgenic construct. Scalebar, 20µm.

Notch signaling in zebrafish angiogenic sprouts

After tip cell ablation in wt, the leftover stalk cells quickly redefine a new tip cell that guides the recovering sprout. This is a phenomenon that is not observed in the *ve-cad* mutant. Rather, stalk cells of *ve-cad* mutant embryos cluster close to the DA after detachment from the tip cell (or also after tip cell ablation). This suggests defects in redefining tip cell properties in *ve-cad* mutant stalk cells, which, during normal development, is defined by Notch signaling. To investigate possible defects of Notch signaling in the absence of VE-cad I imaged Tg(*tp1:venus-PEST*)[s940]BAC(*kdrl:mKate2-CAAX*)[ubs16], which should express destabilized Venus fluorescent protein as a response to Notch activation (in stalk cells). The red membrane marker was used to co-localize the vascular specific Venus signal. Unfortunately, the transgenic notch indicator line did not perform well; already in wt embryos I observed yellow signal (Venus) in tip cells (Figure III-7). Furthermore, the expression was sometimes observed in the whole angiogenic sprout or absent at all. The latter might be due to mosaic expression of the transgene and therefore, Notch signaling could not be assessed in living zebrafish.
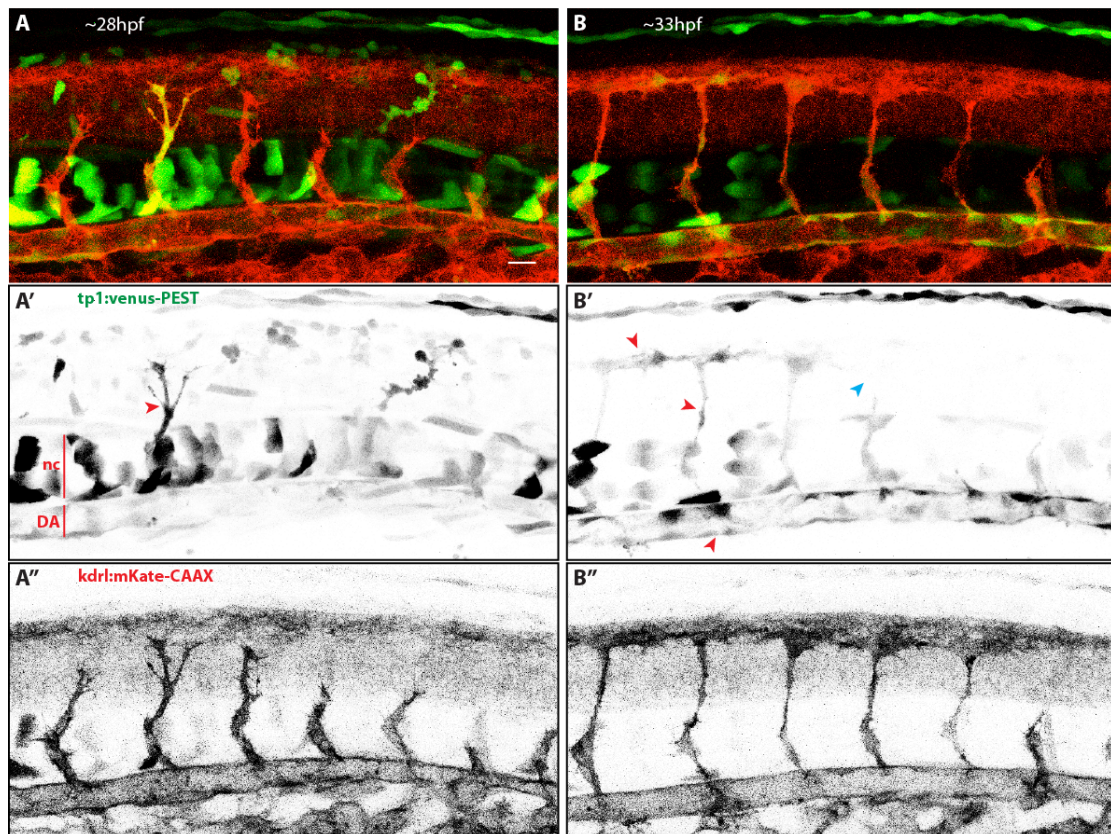
Figure III-7: Inconclusive Notch-indicator line

Two time points from movie **AMovie_6** of a Tg(*tp1:venus-PEST*)[s940]BAC(*kdrl:mKate2-CAAX*)[ubs16] embryo. Notch response (Venus) is shown in green or in inversed contrast (A' and B'). Endothelial specific Notch response co-localizes with the signal from the membrane reporter (mKate2-CAAX) in red or inversed contrast (A'' and B''). (**A**) At around 28hpf, Notch should be read in stalk cells, but strong signal is observed in a single tip cells (red arrowhead in A') and cells of the DA. However, no other angiogenic ECs seem to express Venus. (**B**) 5.5hr later (~33hpf) the Notch indicator is weakly expressed in most ECs of the zebrafish trunk (red arrowheads in B'), but also absent in single cells (a tip cell indicated by the blue arrowhead in B'). Scalebar, 20µm; nc, notochord; DA, dorsal aorta.

3.3.3.   Generation of α-Esama antibody

The generation of the zebrafish specific α-Esama antibody was done by Peptide Specialty Laboratory (Company in Heidelberg, Germany) and is briefly described in Sauteur et al., 2014. The company has run an antigenicity algorithm on the Esama protein sequence and found two sites in the intracellular domain of the protein with high scores. These two peptides, pep1 (aa310-237):   TSSYPRDAHNHHHYPHSD   and   pep2   (aa355-380): LPGYNTNPAPTRGPFGPPSTNGGSQH, were used to immunize two rabbits and one guinea pig. Importantly, the Esama protein sequence was derived from a genomic DNA sequence, which shows single nucleotide polymorphisms (SNPs) to sequenced cDNA clones. According to cDNA a SNP converts the underlined Threonine ("T") in pep2 to Asparagine ("N"), two amino acids that are somewhat similar (both are polar).

Furthermore, the chosen peptides were not conserved amongst the two zebrafish Esam paralogs. Therefore, the antibody was supposed to specifically recognize Esama but not Esamb. The specificity of the antibody to Esama was confirmed by MO knock down (see Figure III-10) and in the *esama* mutant background (see Figure III-15 D and E).

Testing of the sera

We were provided with sera of animals before and after immunization. The sera before immunization ("pre") did not show any staining on zebrafish embryos. The sera of all animals (guinea pig [gp], rabbit one [r1] and rabbit two [r2]) showed junctional specific staining, however both rabbit sera also showed unspecific staining (results are summarized in Table A- 1 in the appendix). The rabbit sera cross-reacted with the myotome (r1) or somitic tissue (r2) (Figure III-8).

Using r1 serum diluted 1:50 showed relatively high background that could be reduced by further diluting the serum to 1:200, (similarly gp signal was improved). Pre-absorbing the serum by incubation with zebrafish embryos further increased the specificity of the staining (compare Figure III-8 B to D). For further experiments, Esama was stained with pre-absorbed serum from r1 at a working dilution of 1:200.
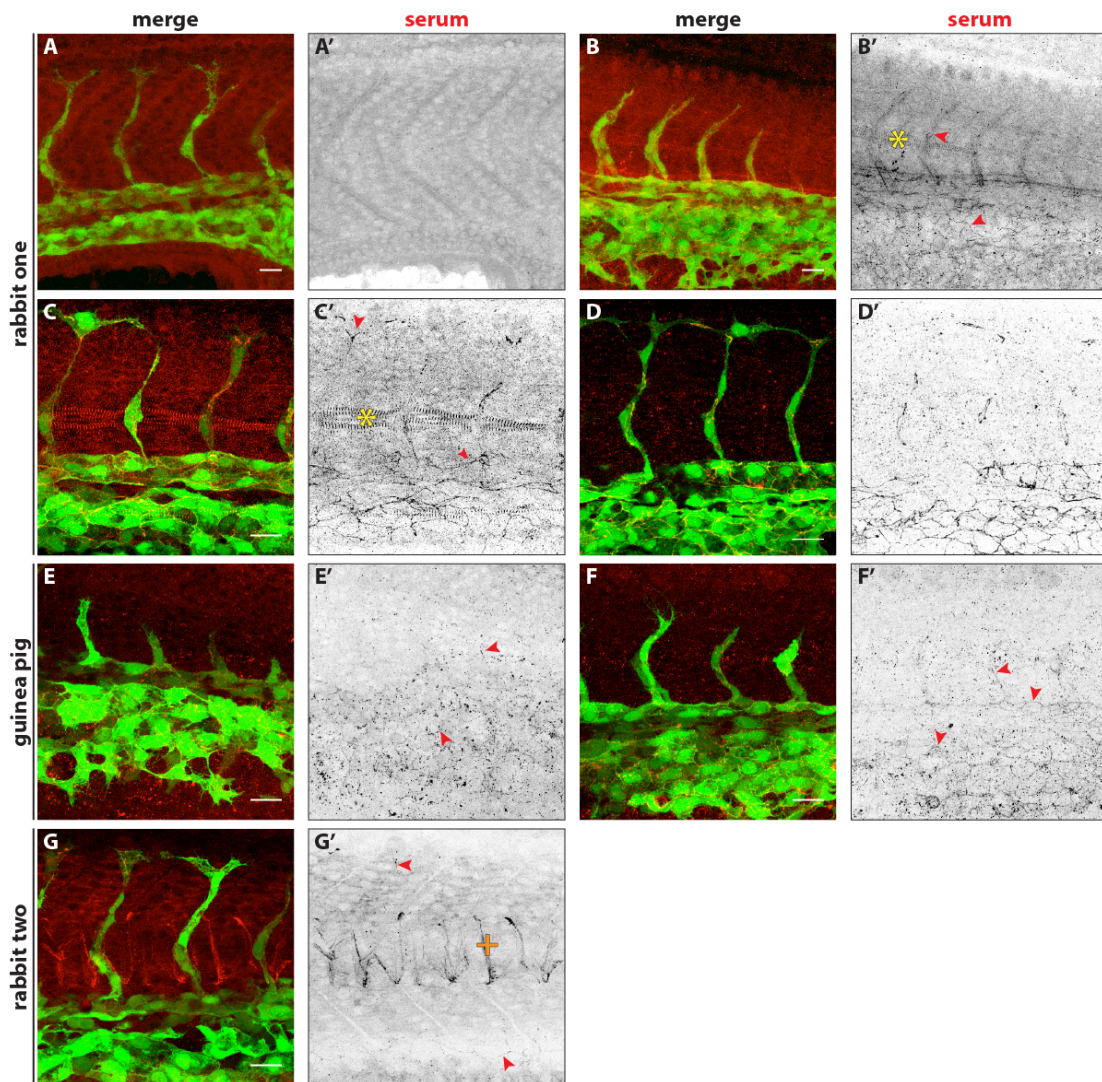
Figure III-8: Rabbit one serum shows best staining for Esama

Tg(*fli1a:EGFP*)^y1 (green) embryos stained for Esama (red or separately in inversed contrast) with antibodies raised in rabbits (A-D or G, r1 and r2 respectively) or guinea pig (E and F, gp). (**A**) r1 serum before immunization of the animal shows no staining (similar stainings were obtained for r2 and gp, data not shown). However, serum of the same animal (r1) after immunization (1:50 diluted) shows junctional staining (red arrowheads) and cross-reactivity to the myotome (yellow asterisks), but with relatively strong background (**B**). The background could be reduced by diluting the serum (1:200) (**C**) and the signal to noise ratio was further improved by pre-absorbing this antibody dilution (**D**). Guinea pig serum (in a 1:50 dilution) also stained junctions (**E**), although weaker than the corresponding r1 antibody dilution. The signal could be increased, in similar manner as for r1, by diluting 1:200 (**F**). (**G**) Some junctional staining was observed for sera derived from r2 (red arrowheads in G'). However, analysis of ISV junctions is complicated by the cross-reactivity of the serum with somitic tissue (orange plus). Scalebars, 20µm.

138

3.4. Esama and VE-cad participate in anastomosis

The formation of vascular networks by angiogenesis involves extensive interactions between ECs. To understand these endothelial cell-cell interactions, I am particularly interested in the molecular mechanisms by which ECs generate cell-type specific contacts. These mechanisms are best studied in the process of blood vessel anastomosis.

3.4.1. Esama and VE-cad act together during angiogenesis

Little is known how tip cells recognize each other specifically and efficiently. The regulators must be proteins on cell membranes, such as components of the junctional complexes. They act an in homotypic manner and therefore will confer cell-specific recognition. Recently we showed that VE-cad is important for effective contact formation between two tip cells (Lenard et al., 2013; Sauteur et al., 2014). Endothelial tip cells that lack VE-cad engage with multiple filopodial contacts during anastomosis (Lenard et al., 2013). Several of these filopodial contacts are expanded, whereas in wt, only one contact results in efficient recognition and contact expansion. Furthermore, anastomosis in VE-cad mutants is greatly delayed.

3.4.1.1.　　Esama, a candidate for vascular morphogenesis control

We reasoned that in addition to VE-cad, other junctional proteins are involved in contact formation and, similar to VE-cad, these proteins should be expressed in an EC specific manner. One such junctional protein is Claudin5b. However, Claudin5b seems not to be essential for vascular development and homozygous mutants are viable (Krudewig, 2012). Double mutants for *claudin5b* and *ve-cad* do not show a phenotype distinct from the *ve-cad* mutant either. Therefore, we chose to investigate the role of another endothelial restricted junctional component, Esam.

Endothelial restricted expression of Esama

The expression of *esam* is predominantly restricted to the endothelium in mice (Hirata Ki et al., 2001). Because of the teleost genome duplication, zebrafish harbor two copies (paralogs) of *esam*, namely *esama* (428aa encoded in 7 exons on chromosome 10) and *esamb* (436aa encoded in 7 exons on chromosome 15). Esama shows 32.7 and 30.9% identity and 47.3% and 47.1 similarity to human and mouse orthologs, respectively (Wong et al., 2009). The two zebrafish Esam paralogs share 53% identity in aa sequence and the two immunoglobin-loops are conserved. However, in contrast to Esama, the expression of Esamb has not been investigated in zebrafish yet.

In order to determine the expression pattern of *esamb*, I performed *in situ* hybridizations on 30hpf embryos. For comparison I included embryos hybridized for fli1a, which visualized the vasculature nicely, especially in the trunk and tail region (Figure III-9 A). The colorimetric reaction had to be drastically prolonged to visualize *esama* and *esamb*, which reflects the lower expression levels of these genes. Yet, the long incubation time also increased the background (for example in the head region). Nevertheless, *esama* showed endothelial-restricted expression (Figure III-9 B' and B'''). But I was not able to determine any cell-restricted expression pattern for *esamb*. It seems to be expressed throughout the trunk region, except maybe the notochord (Figure III-9 C'). Further experiments are needed to determine the exact expression pattern of *esamb*.

140
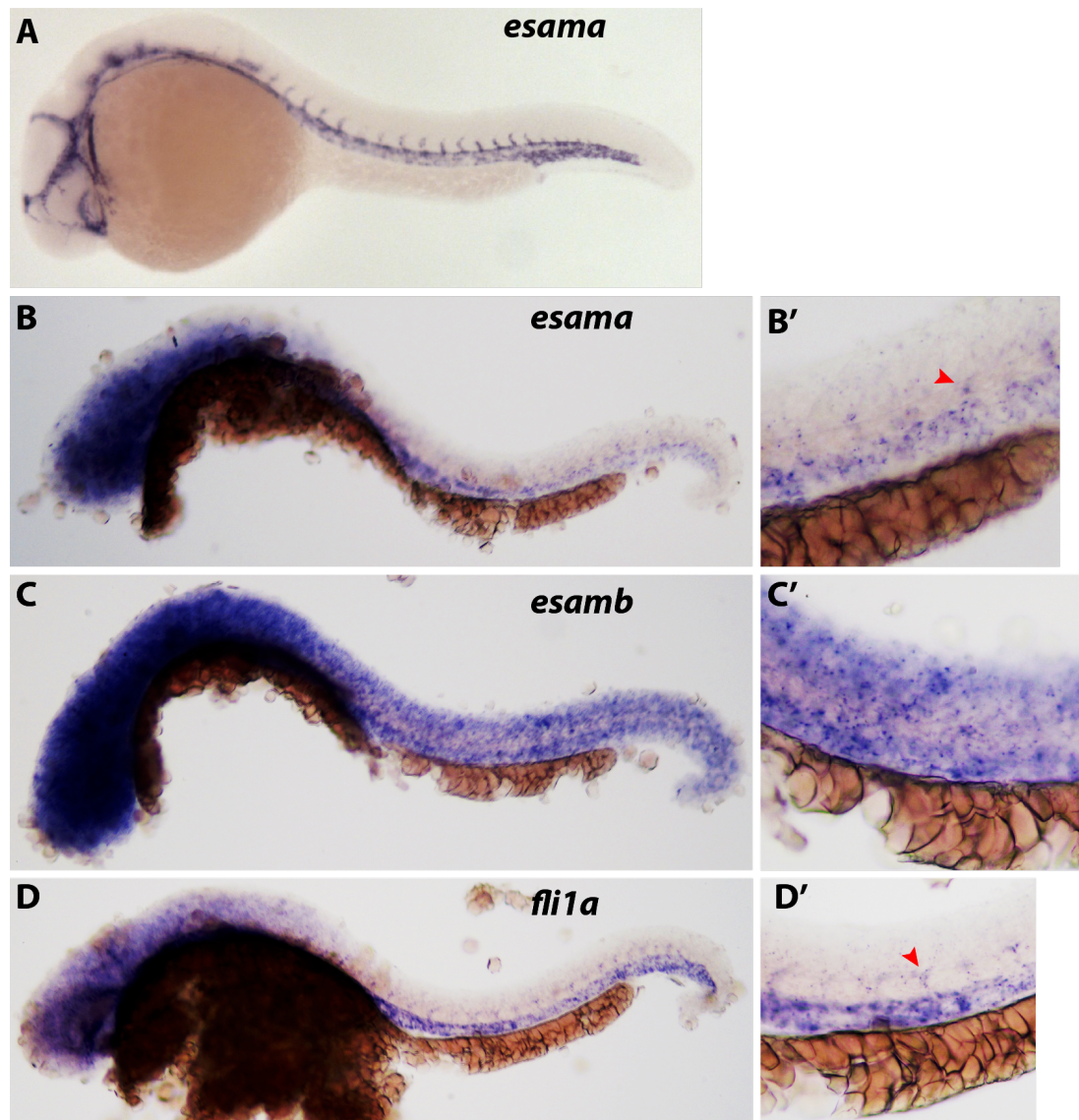
Figure III-9: Expression pattern of *esama* and *esamb*

(**A**) *in situ* hybridization of *esama* on 1 dpf embryo, performed by Thisse et al., 2008. The signal is visible throughout the vasculature. (**B-D**) Own *in situ* hybridization of *esama* (B), *esamb* (C) and *fli1a* (D) on wt 30 hpf embryos. All three embryos show high background in the head. The Right-hand side shows a higher magnification of the images on the left-hand side. (B) The expression pattern of *esama* is restricted to the endothelium. Red arrowheads indicate ISVs. (C) No cell selective expression pattern for *esamb* could be determined. It looks expressed everywhere, except the notochord. (D) Known endothelial specific expression pattern of *fli1a*, DA and PCV and ISV (red arrowhead) are well visible.

Knockdown of Esama suggest synergistic roles during vascular morphogenesis

Although its redundant role during angiogenesis, we assumed a synergistic role for Esama with other junctional proteins (e.g. VE-cad) during vascular morphogenesis, especially for cell-type specific interactions. Before taking the big leap into the generation of a mutant, we tested our hypothesis by MO knockdown.

I designed two MOs, one translation blocking MO (Esama-ATG) and a splice site blocking MO at the exon 2 – intron 2 boundary (Esama-E2I2) (for sequence information see materials chapter 2.1.6.1). Together with these two MO, I tested also a published MO preventing splicing at the intron 3 – exon 4 boundary (Esama-MO1) (O'Connor et al., 2009). All these MOs worked (data not shown) but I obtained the best and most consistent results with Esama-E2I2 MO. Using this MO, I confirmed specific *esama* KD by staining for the protein (compare Figure III-10 A and C) and furthermore, knocked down the gene in a dose dependent-manner (compare Figure III-10 B and C).
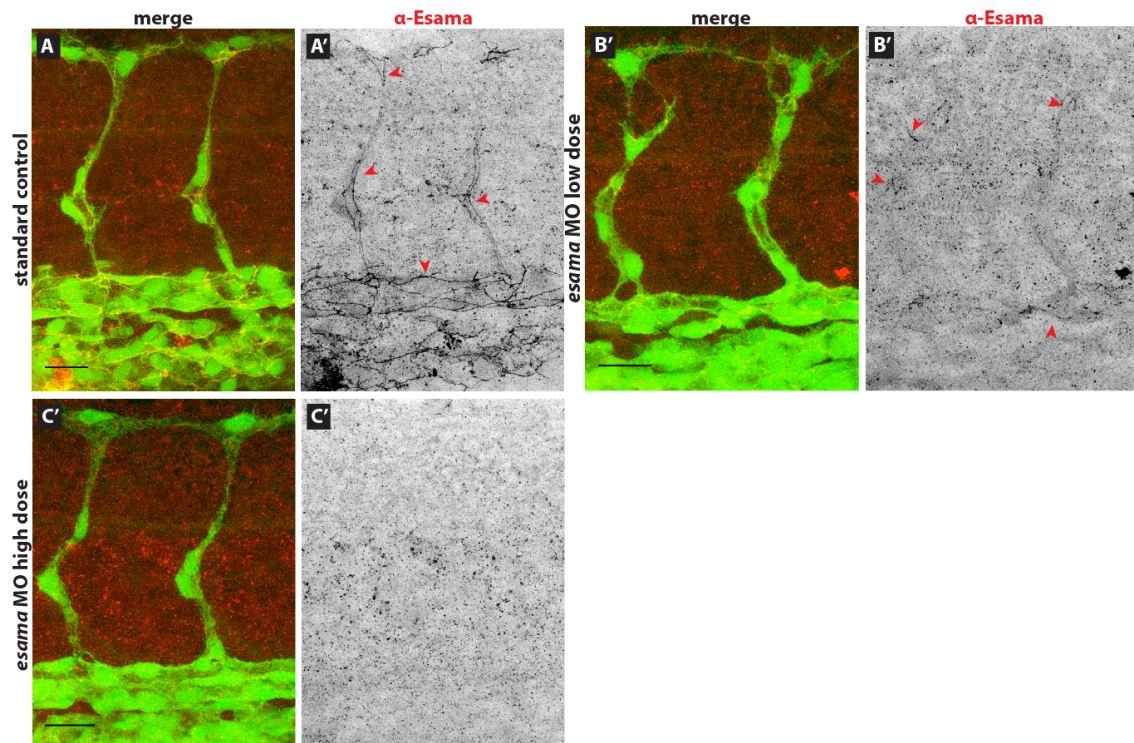

Figure III-10: *esama* knock down in a dose dependent-manner

Tg(*fli1a:EGFP*)^{y1} (green) embryos stained for Esama (red or separately in inversed contrast) at around 32hpf, anterior to the left. (**A**) Embryo injected with standard

control MO shows a nice junctional stain with the α-Esama antibody (red arrowheads in A'). (**B**) Very weak junctional staining is observed, when the embryos are injected with a small volume of Esama-E2I2 MO (red arrowheads in B'). (**C**) Higher concentration or bigger volume injection of Esama-E2I2 MO results in complete knockdown, and no junctional staining is observed. Scalebars, 20µm.

As expected embryos injected with an *esama* splice MO (Esama-E2I2) did not show any apparent vascular defects. The ISVs develop similarly to standard control MO injected embryos (compare Figure III-11 A with B). Because Esama has a redundant role during angiogenesis, we tested the possibility of synergistic roles with other junctional proteins. Therefore, we performed knock down experiments in the *ve-cad*^ubs8 mutant background. In the absence of VE-cad, endothelial tip cells engage in multiple contacts during anastomosis (Figure III-11 C), while in wt only one contact is needed. Furthermore, the loss of function of VE-cad reduces the adhesion between tip and stalk cells and causes them to detach from each other (not shown in Figure III-11 A) (Sauteur et al., 2014). When *esama* is knocked down in *ve-cad*^ubs8 mutants, the angiogenic processes were strongly perturbed. EC-EC adhesion was strongly reduced (many stalk and tip cells dissociate from each other), and anastomosis delayed (Figure III-11 D and see also movie **AMovie_7**). Essentially, the KD of *esama* in the *ve-cad* mutant showed a worsening phenotype than that observed in the *ve-cad* mutant itself.
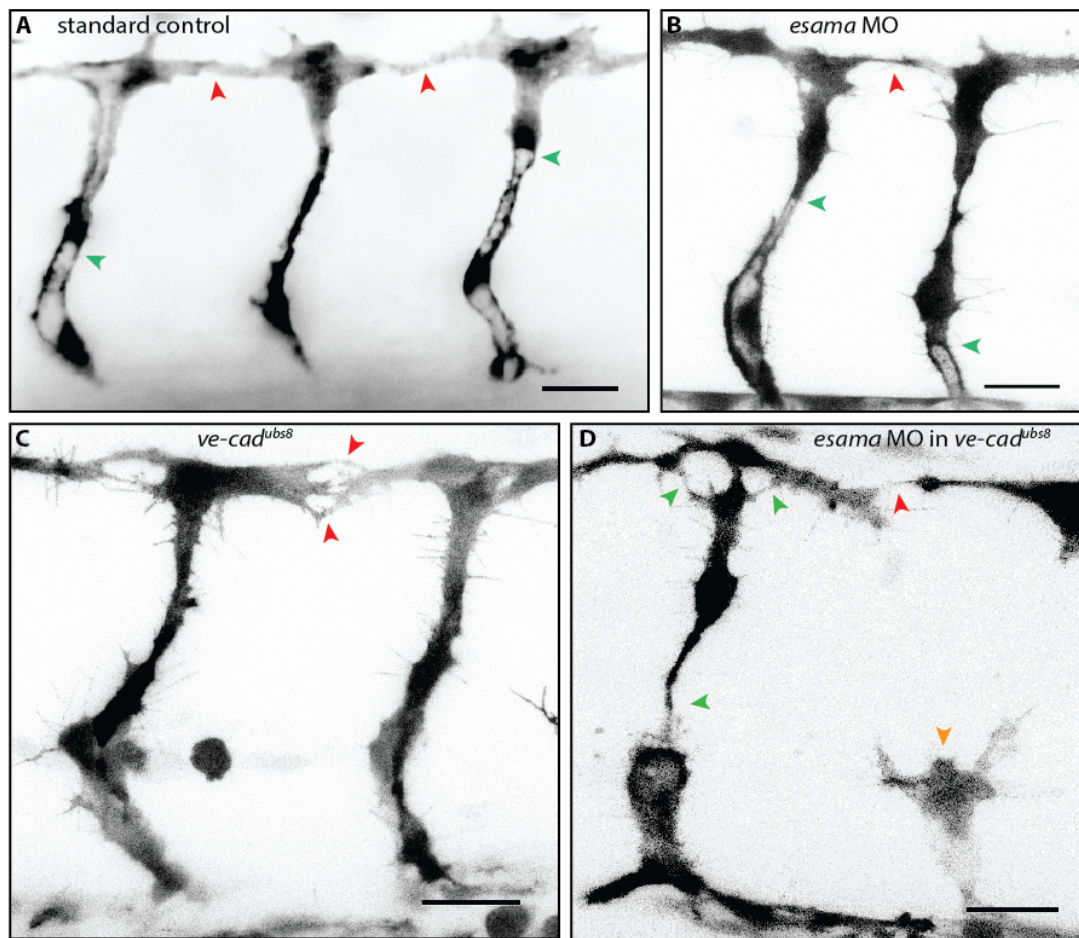
Figure III-11: *esama* knock down aggravates the *ve-cad* mutant phenotype

Tg(*fli1a:EGFP*)^{y1} embryos at around 32hpf, anterior to the left in inversed contrast. (**A**) Standard control MO injected embryo shows normal angiogenesis (including anastomosis, red arrowheads) and partially lumenized ISVs (green arrowheads). (**B**) Esama-E2I2 splice MO injected embryo shows similar vasculature as the control (red arrowhead for anastomosis and green arrowheads for lumenization). (**C**) A *ve-cad*^{ubs8} mutant tip cells engage in supernumerary anastomotic contacts (red arrowheads). (**D**) A *ve-cad*^{ubs8} mutant embryo injected with Esama-E2I2 MO shows enhanced *ve-cad* mutant phenotype in respect to defects in anastomosis (red arrowhead) and reduced tip to stalk cell adhesion (green arrowheads) and more tip and stalk cell detachments (orange arrowhead) (see also movie **AMovie_7**). Scale bars, 20µm.

3.4.1. Generation of *esama* mutant fish line

3.4.1.1. Mutagenesis of *esama*

The exaggerated anastomosis phenotype observed in *ve-cad* mutant embryos injected with *esama* MO supported our hypothesis that several junctional components are implicated in the regulation of the dynamic cell behaviors. However, because of the known limitations of the MO technology (Kok et al., 2015), I decided to generate a genetic loss of function mutation by using TALENs.

Choice of TALEN pairs

The first exon of *esama* encodes 5' UTR (untranslated region) and the start codon. Using the online tool described by Cermak et al., 2011 (see also methods, chapter 2.2.4), I found one TALEN target site in the first exon, one in the second exon and two in the third exon, each of those harboring a restriction site in the spacer region between the two TALEN binding sites (see Figure III-12), which facilitates later screening for mutations. And all these exons are still encoding the extracellular domain of the protein.
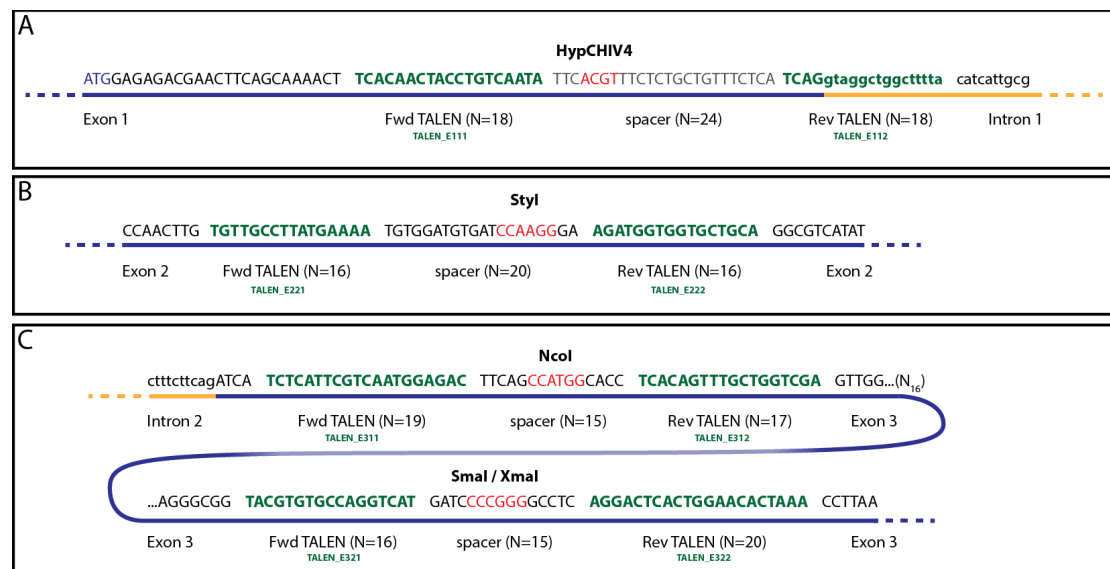
**Figure III-12: Targeting the *esama* locus, four possible TALEN pairs**

(**A**) *esama* exon 1 contains 5' UTR and the transcription starting ATG (blue). The reverse TALEN (E112) binding site overlaps with the exon – intron boundary and the forward TALEN (E111) bind 24bp upstream of E112. The spacer region between the

two TALEN binding sites contains a HypCHIV4 enzyme-cutting site. (**B**) In the middle of the second *esama* exon a StyI restriction site is flanked by two relatively short TALEN binding sequences (namely TALEN_E221 and TALEN_E222). (**C**) Within the third *esama* exon, two target sites were found. One spacer region containing an NcoI site is flanked by TALEN_E311 and TALEN_E312, while the other spacer region, containing a SmaI/XmaI site, is surrounded by TALEN_E321 and TALEN_E322. Nucleotides encoded in exons are in capitals and underlined in blue, intros are underlined in yellow, nucleotides bound by TALENs are green and restriction enzyme palindromes are red.

Injection and validation of TALEN pairs

The TALEN pairs were tested by directly injecting embryos with mRNA and embryos were grown until 2-4dpf. I performed PCR on genomic DNA to screen for appearance of restriction polymorphisms, because NHEJ should lead to the loss of the restriction site in TALEN mRNA injected embryos. For experimental details consult chapter 2.2.1.2, 2.2.3.3 and appendix A.6.

I did not observe any nuclease activity on *esama* exon 1, nor exon 3 (data not shown) with the respective TALEN pairs. For the nuclease pair in the second exon some mutagenic activity was observed, which I could increase, using an improved protocol (see methods in chapter 2.2.4.2). Examples of transiently mutagenized *esama* locus are shown in Figure III-13 A and B, and injected siblings were raised to adulthood (G0 fish).
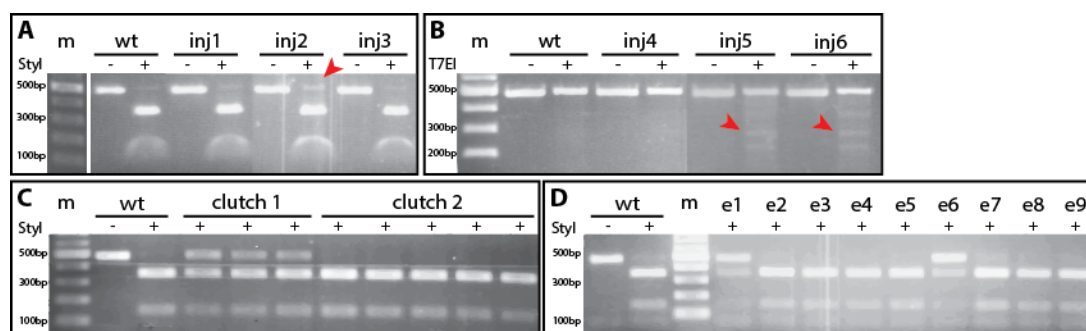
Figure III-13: Screening for mutations in the second *esama* exon

(**A and B**) Injected embryos were tested for TALEN induced mutations by restriction enzyme StyI (A) or by T7EI assay (B). (**A**) StyI degrades all wt products (from 482bp to 347bp and 135bp bands), while mutated restriction palindromes are not cut, which remain as uncut product, as seen for "inj2" (red arrowhead, compared to wt). (**B**) In

contrast, the T7EI assay only degrades heteroduplexed DNA (e.g. a wt plus a mutated DNA strand). While uninjected embryos (wt) products are not degraded, "inj5" and "inj6" shows multiple bands (see red arrowheads), which is an indication for DNA heteroduplexes and thus mutations. (**C and D**) Pooled (C) and single embryos (D) were tested (with StyI) for parental transmission of mutant alleles. (**C**) Embryos from single G0 fish were pooled (each well represents 7 embryos) and tested for loss of restriction polymorphism. In each well of "clutch 1" (offspring from a single G0 parent) an uncut wt band and two degraded bands appear, indicating that each pool contains at least one embryo with a mutated allele. "clutch 2" shows the same banding pattern as wt, thus no mutated alleles. (**D**) Single embryos, from a second outcross of the G0 fish that gave the "clutch 1" in (C), were tested for mutant alleles. Approximately a third of the offspring carried a mutant allele (as seen for e1 and e6). m, ladder; +, with enzyme; -, without enzyme; inj: injected embryo; wt, uninjected embryo.

3.4.1.2. Isolation of the *esama* mutant allele

Adult G0 fish that carried possible germline mutations in the *esama* gene were mated with wt zebrafish. To screen for germline transmission embryos of a clutch were pooled (7 embryos per tube) and tested for mutant *esama* alleles (as described above) (see Figure III-13 C). I tested more than 20 G0 fish for germline transmission and only one of those fish carried a mutation in the germline. The mutant allele of the founding G0 fish was propagated and the genotypes of the offspring were assessed by larval fin biopsies (see Figure III-13 D and methods chapter 2.2.1.2). Larvae carrying mutant allele (roughly a 25-37% of the offspring) were then raised to adulthood.

Genotyping the esama mutant

To sequence the mutant allele only, PCR product of single embryos carrying a mutation was digested with restriction enzyme StyI, the uncut product isolated and sent for sequencing. Interestingly, all the mutant alleles originating from the same G0 fish carried the same 10bp deletion (see Figure III-14).

The frameshift mutation leaves the first 37aa of the protein intact. Thereafter the protein sequence is altered and leads to a premature stop codon 33aa after the mutation (see Figure III-15 A). The mutant *esama* allele (UBS19) presumably produces a 70aa short peptide, which does not contain any known functional domains anymore and is therefore a putative null allele.

I designed a PCR strategy to identify wt versus UBS19 alleles in a single reaction (see methods 2.2.1.3 and Figure III-15 B and C).
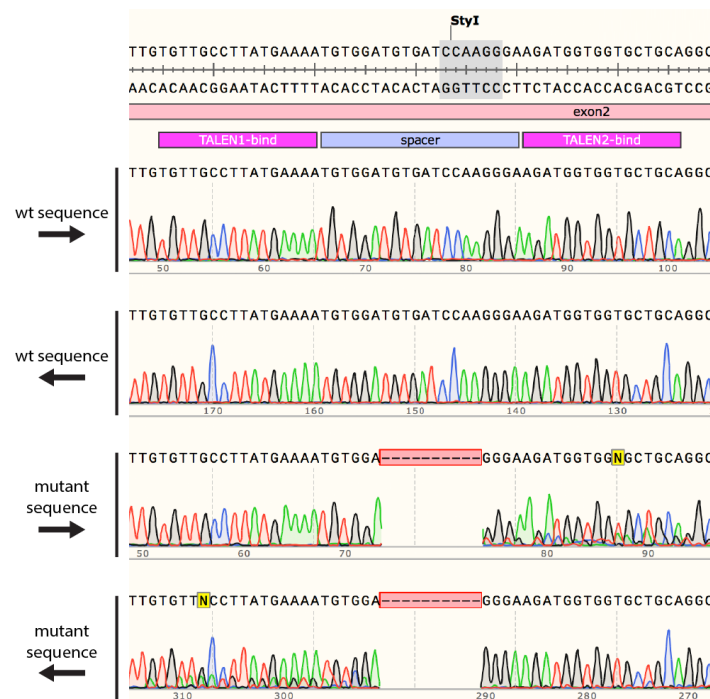
Figure III-14: Isolation of a 10bp deletion

Sequencing of mutant bands of different embryos yielded always the same mutant allele; a 10bp deletion. Top shows the genomic locus of *esama*, where the two TALENs bind in the second exon and the StyI restriction polymorphism (gray) in the spacer region. Below the sequencing alignment for wt embryos (forward and reverse). And below the forward and reverse sequence alignment of a single mutant embryo, which lacks 10bp in the spacer region.
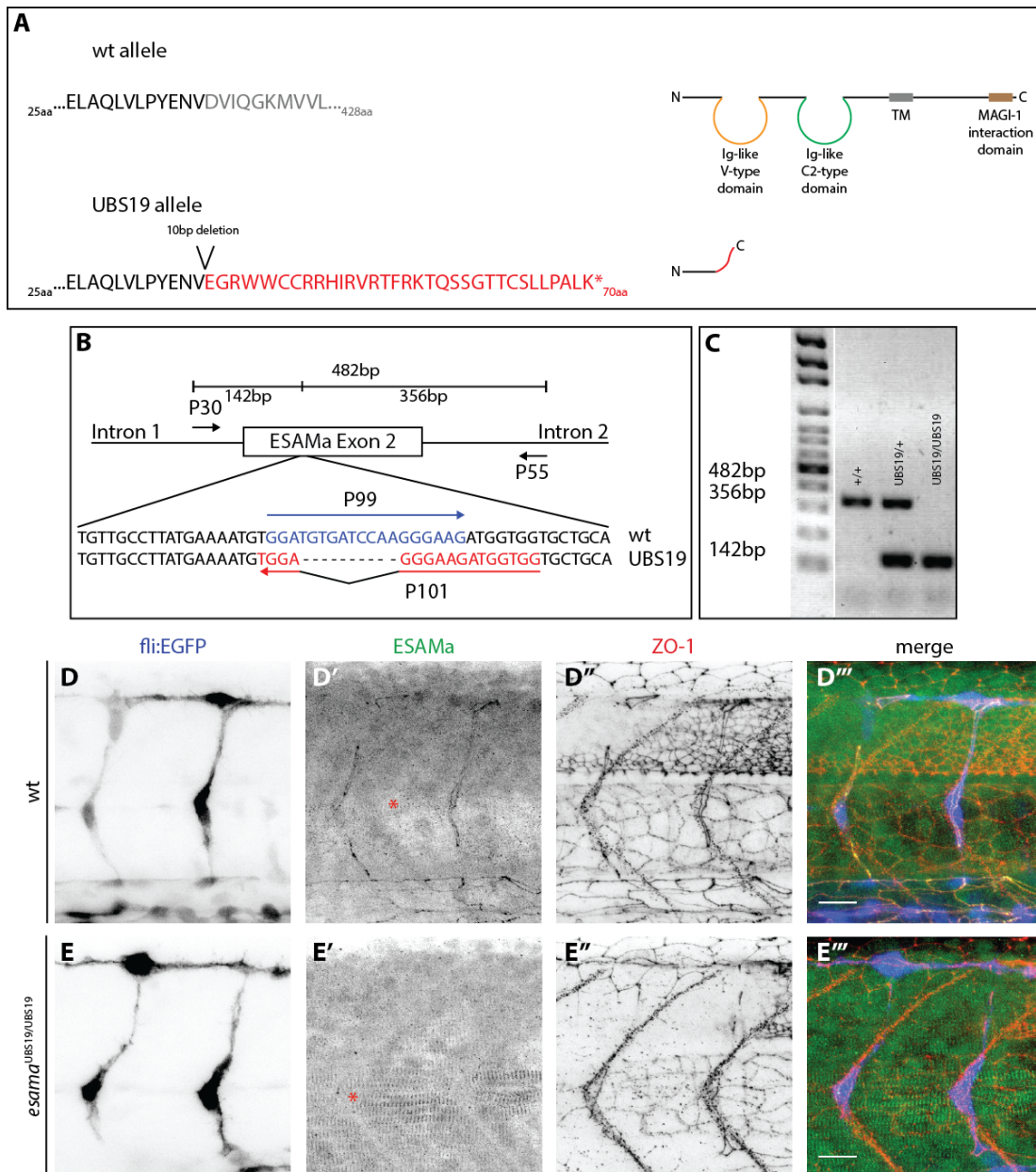
Figure III-15: The *esama* UBS19 mutant allele

(**A**) The 10bp mutation alters Esama's sequence after the first 37aa and leads to a premature stop after a total of 70aa. The corresponding wt aa sequence is indicated and schematic representations of the wt and mutant protein are shown on the right. (**B** and **C**) Genomic locus with primers used for genotyping PCR (B) and an example of band pattern produced by the different *esama* genotypes (C). The external primers (P30 and P55) flank exon 2 and amplify both, mutant and wt alleles. However, this band is not seen on the gel, because it is outcompeted by the smaller wt and UBS19 products. P99 is homologous to the wt sequence where the mutation is and produces a band of 356bp with P55. P101 is specific for the mutation and together with P30 generates a 142bp product. (**D and E**) Confocal stacks of wt (D) and UBS19 (E)

Tg(*fli:EGFP*)[y1] (blue) stained for Esama (green) and Zo-1 (red), single channels are shown in inversed contrast, anterior to the left. The architecture of ISV looks similar between wt and UBS19 (compare the EGFP channels D and E); there are no obvious angiogenic defects in the mutant. Furthermore, staining for Esama confirms the loss of protein in the mutant background (E'). Only antibody cross-reactivity with the myotome remains in the mutants (demarcated by red asterisk in E'). aa, amino acid; TM, transmembrane domain.

3.4.2. Esama is required for junctional continuity

I only recently isolated the *esama* mutant allele and the F1 generation of heterozygous mutants were born in May 2014. Therefore, the analysis of the mutant is preliminary and surprising findings suggest novel roles for Esama in junctional dynamics during angiogenesis.

3.4.2.1.   No morphological defects in the *esama* null mutant

The first generations (F1) of the fish heterozygous for UBS19 were incrossed to produce UBS19 homozygous fish. 20.56% (n=180) of the offspring was UBS19[hom], a bit lower than the expected 25%, however still in range of normal segregation.

In agreement with mouse data (Ishida et al., 2003), homozygous UBS19 fish were viable, fertile and did not show severe vascular defects (compare Figure III-15 D and E). Furthermore, the UBS19 fish were fertile and produce healthy offspring. Therefore, I did not investigate the *esama* null allele in more detail, since the major phenotype is more apparent in conjunction with the lack of VE-cad.

3.4.2.2.   Esama and VE-cad act synergistically during angiogenesis

For experiments in *esama* and *ve-cad* double mutants, the *ve-cad*[ubs8] allele was crossed to the *esama*[ubs19] mutant. Normal Mendelian distribution was expected, since the genes are located on different chromosomes (*ve-cad* on chromosome 7 and *esama* on chromosome 10).

In a next mating, double heterozygous fish for *esama* (*esama*[UBS19/+]) and *ve-cad* (*ve-cad*[UBS8/+]) were in-crossed and Mendelian 13.54% (~⅛, n=109) of

the offspring was UBS19[hom] and UBS8[het]. These fish were healthy and raised for later experiments in the double mutant background.

The phenotype of ve-cad dominates the double mutant phenotype

The macroscopic phenotype of the double mutant resembled the usual *ve-cad* mutant, which is at the early stages: lack of blood flow (usually sets on around 24hfp) and inflated CV (Figure III-16 C and D). And at later stages: heart edema (most obvious in embryos older than 2dpf, see Figure III-16 G and H) and lethality during late embryonic to larval development (around 5-6dpf), which is due to the lack of blood flow.
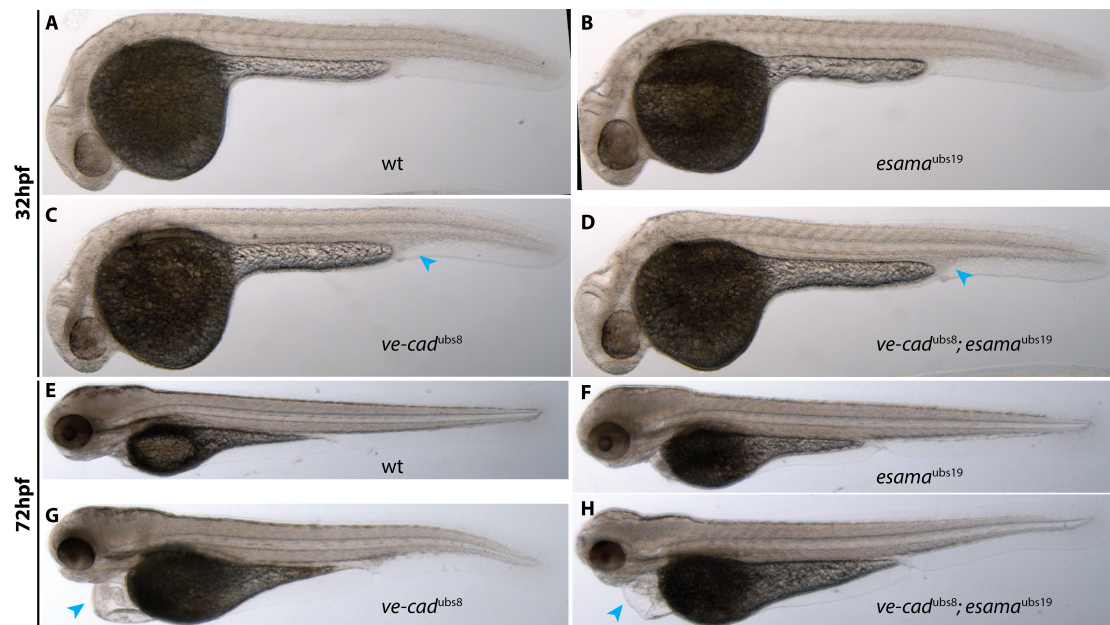
Figure III-16: The *esama* mutant looks phenotypically normal

Images of fixed embryos at 32hpf (A-D) and 72hpf (E-H). (**A-D**) At 32hpf *esama* mutant (B) embryos cannot be distinguished from wt (A) ones. Also *ve-cad* mutants (C) and the *esama* and *ve-cad* double mutant (D) look very similar to wt, however, the CV (blue arrowheads in C and D) is inflated. (**E-H**) wt (E) and *esama*[ubs19] mutant (F) embryos develop similarly. The most obvious phenotype of 3-day-old *ve-cad* mutant embryos (G) is the big edema (blue arrowheads in G and H), which develops similarly in the double mutant (H). This phenotype is caused by the heart pumping plasma into the heart chamber, due to the poorly sealed endothelium in the absence of VE-cad.

At low magnification the overall early vascular network (around 32hpf) in the *esama* mutant looked similar to wt (Figure III-17 A-D). At this stage the most prominent difference between wt and *ve-cad* mutants is an inflated CV, also apparent in the double mutant (red arrowheads in Figure III-17 C and D). In addition, ECs of CCV in the double mutant appeared loosely connected (blue arrowhead in Figure III-17 D), which might reflect reduced adhesion between these cells.

Later development of *ve-cad* and *esama; ve-cad* double mutants are characterized by growth developmental defects, such as growth retardation and pericardial edema (Figure III-17 E-H). These defects are typical of secondary defects due to general defects of the cardiovascular system and can, for example, also be observed in *silent heart* mutants.

For further analysis I focused on the cellular level during angiogenesis of ISVs.
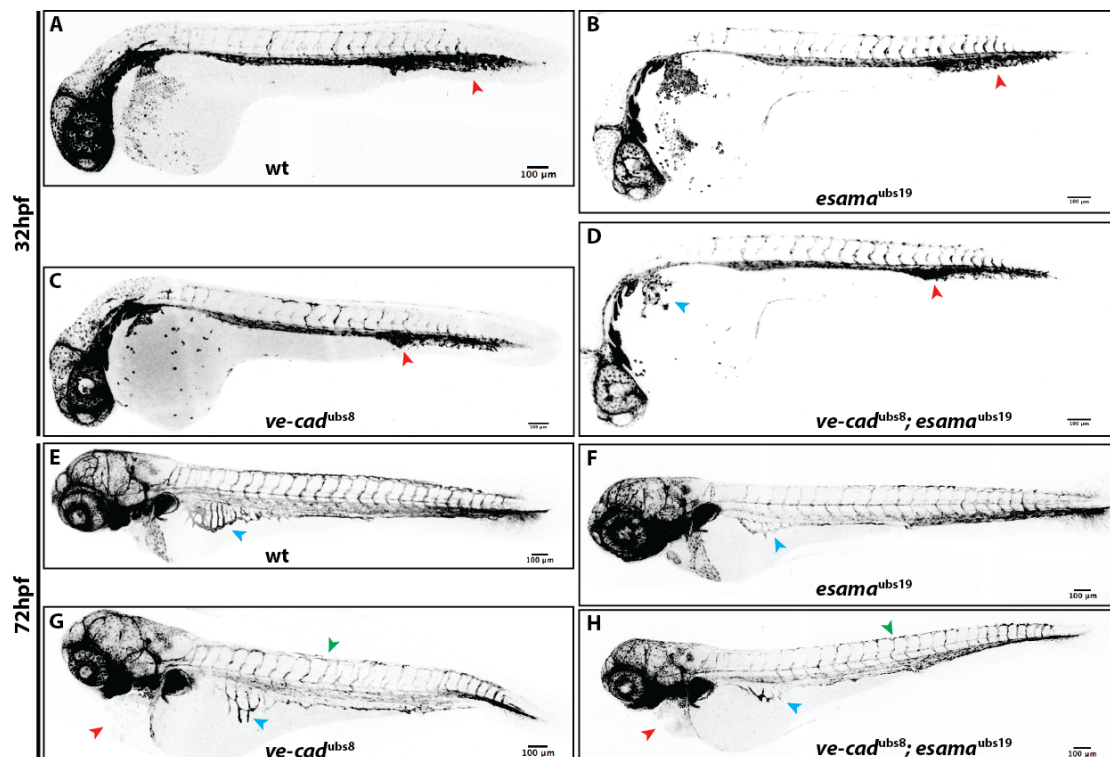
Figure III-17: Defects in vascular network formation in *ve-cad* and double mutant embryos

Confocal images of fixed Tg(*fli1a:EGFP*)[y1] embryos at 32hpf (A-D) and 72hpf (E-H) in inversed contrast. (**A-D**) The vascular networks of wt (A) and *esama*[ubs19] mutants look very similar with nice CV plexus (red arrowheads). The overall vascular network

of *ve-cad* (C) and double mutants (D) look very similar to the control. The only difference at this magnification is seen in the CV where the plexus seems to be less branched and the yolk extension proximal part is inflated (compare red arrowheads in C and D with A). In addition, the double mutant shows defects in CCV formation, where single EC can be seen (blue arrowhead in D). (**E-H**) wt (E) and *esama* (F) mutant embryos develop similarly. The DA is inflated, the CV plexus is branched and the subintestinal vessels (SIV) (blue arrowheads in E and F) and the CCV are formed. In the *ve-cad*[ubs8] (G) and the *ve-cad* and *esama* double mutant (H) the vasculature is underdeveloped to a similar degree. The CV plexus is poorly developed and the head vasculature is not as far as in wt embryos. Fewer head vessels formed, there are defects in DLAV formation (green arrowheads) and the SIV are poorly formed (blue arrowheads). The heart edema is very prominent (red arrowheads), while the CCV is not apparent. Scalebars, 100µm.

The lack of Esama in the ve-cad mutant severely impairs angiogenesis

For the analysis of the defects in vascular network formation I focused on angiogenic processes that occur in the trunk of zebrafish embryos, i.e. the outgrowth of segmental vessels (ISVs) that are, at the time point of observation, of arterial nature (SAs).

We previously showed that tip cell migration is unaffected by the lack of VE-cad. However, the stalk elongation is severely impaired in the absence of VE-cad, because stalk cells are unable to elongate properly. Moreover, stalk cells detach from the leading tip cell in a third of the ISVs (see (Sauteur et al., 2014) and chapters 3.1.1 and 3.3.2). In addition, anastomosis is delayed and tip to tip cell contact formation is disturbed (Lenard et al., 2013; Sauteur et al., 2014).

esama[ubs19] homozygous embryos were viable and vascular network formation occurred comparable to wt embryos (compare Figure III-18 A with B). However, the angiogenic defects of double mutants are clearly discernable from the *ve-cad*[ubs8] phenotype at cellular resolution. The most striking difference between *ve-cad*[ubs8] mutant embryos and the *ve-cad* and *esama* double mutant was the cell morphology of angiogenic ECs (especially tip cells, compare Figure III-18 C with D). ECs of the *ve-cad* mutant already have higher protrusive activity than wt. Double mutant ECs show even more cell

protrusions, which seemed not to be of filopodial origin. They rather appeared lamellipodia-like, thick cell extensions, very apparent also in tip cells (red and orange arrowheads in Figure III-18 D).

Next, cell-cell adhesion in the double mutant was greatly decreased compared to the *ve-cad*[ubs8] mutant. Tip and stalk cells detached from each other more frequently and anastomosis was consequently further delayed and ineffective (compare Figure III-19 B with C and see also movies **AMovie_10** and **AMovie_11**). The *ve-cad*[ubs8] mutant was able to recover to some extent and formed a vascular network, albeit without lumen (Figure III-19 B). The double mutant was not able to recover to the same extent as the *ve-cad* mutant (Figure III-19 C), and even the DLAV is poorly formed. Moreover, cell in the DLAV grew in an undirected fashion into somitic tissue (blue arrowhead in Figure III-19 C'''), suggesting defects in correct vascular network formation.

All together, the lack of Esama in the *ve-cad*[ubs8] mutant enhanced the anastomosis and cell adhesion defects observed in the *ve-cad* mutants. Moreover, the cell morphology in the double mutant background was perturbed, which resulted in multiple (big) cell and the cells seemed to grow in spatially less restricted manner.
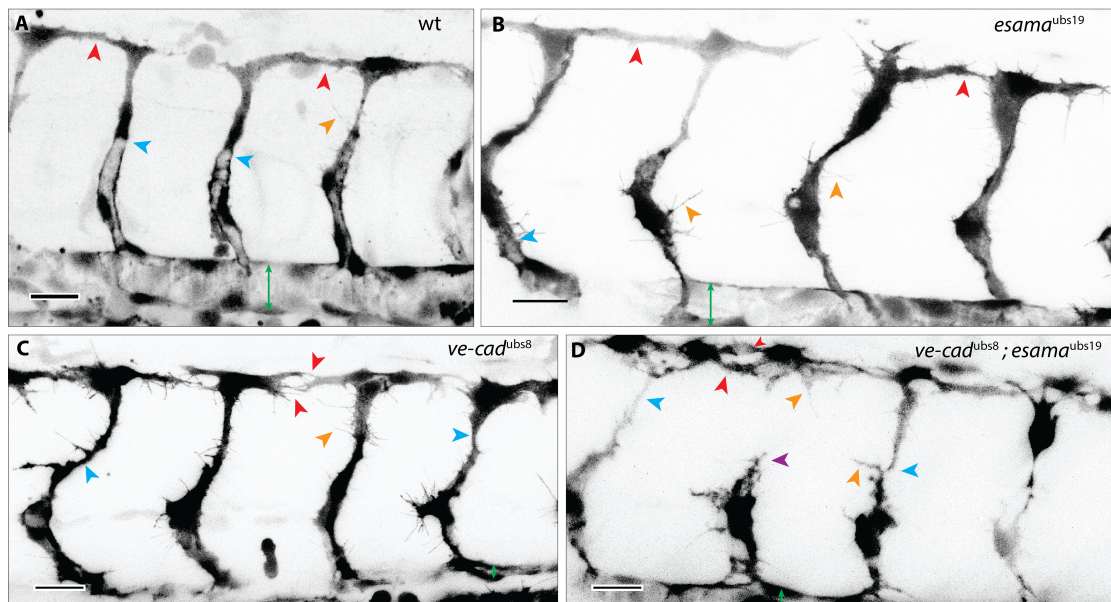

Figure III-18: Severely disturbed EC behavior in *ve-cad* and *esama* double mutants

Images of wt and mutant embryos at 32hpf in inversed contrast, anterior to the left.

(**A**) A wt Tg(*fli1ep:GFF*)^{ubs3}(*UAS:mRFP*) embryo (see movie **AMovie_8**) showing lumenized DA (green double-headed arrow) and partially lumenized ISVs (up to the blue arrowheads). The stalk cells that are not lumenized yet show little filopodial activity (orange arrowhead). At 32 hpf the tip cells grow laterally and start to anastomose (red arrowheads). (**B**) A still picture of Tg(*fli1a:EGFP*)^{y1} *esama*^{ubs19} mutant embryo taken from movie **AMovie_9**. Here, angiogenesis is comparable to the wt, with lumenized DA (green double-headed arrow) and partially lumenized ISVs (up to the blue arrowhead). Also the stalk cells that are not lumenized yet show some filopodial extensions (orange arrowheads) and the tip cells engage in homotypic interactions (red arrowheads). (**C**) In Tg(*fli1a:EGFP*)^{y1} *ve-cad*^{ubs8} mutant embryos the DA is collapsed (green double-headed arrow) and thus the ISVs are not being lumenized (see movie **AMovie_10**). Further, stalk cells have more filopodial activity (orange arrowhead) and they are loosely attached to their leading tip cell (blue arrowheads). Anastomosis is perturbed and the tip cells engage in multiple filopodial interactions (red arrowheads). (**D**) Similarly to the *ve-cad* mutant, the Tg(*fli1a:EGFP*)^{y1} *ve-cad* and *esama* double mutant has no blood flow and therefore the DA is also partially collapsed (green double-headed arrowhead) (see movie **AMovie_11**). However, in contrast to the *ve-cad* mutant, angiogenic ECs of the double mutant look different in their morphology. They extend lots of cell protrusions, that are however thicker than filopodia (orange arrowheads). The same accounts for anastomotic contacts, where cell contacts engage over a multiple of these thick cell protrusions (red arrowheads). Furthermore, cell-cell adhesion is greatly reduced and stalk cells are, similarly to the *ve-cad* mutant, attached to the tip cell over thin bridges (blue arrowheads), which often break and leave the stalk cells close to the DA (purple arrowhead). Scalebars, 20μm.
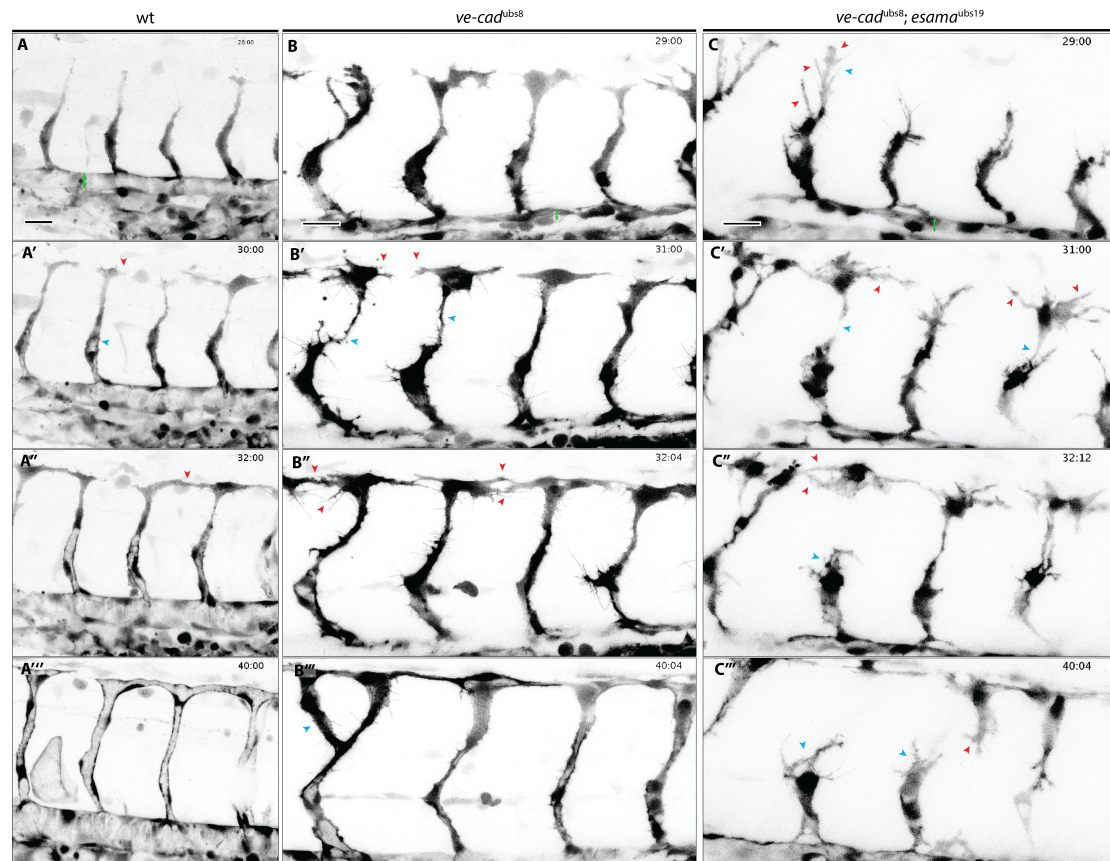
Figure III-19: Severe angiogenic defects in *ve-cad* and *esama* double mutants

Still pictures from time-lapse movies **AMovie_8** (A), **AMovie_10** (B) and **AMovie_11** (C) in inversed contrast, anterior to the left. (**A**) In wt Tg(*fli1ep:GFF*)ubs3(*UAS:mRFP*) embryos the DA is inflated (yellow double-headed arrow in A) and tip cells guide the sprout dorsally. Tip cells do extend their filopodia mainly straight up. While extending lumen is pushed into the trunk of the sprout (blue arrowhead in A'). Once tip cells reached the level of the dorsal neural tube, they grow laterally (filopodial extensions marked with a red arrowhead in A'). As angiogenesis proceeds, lumen is further expanded in the stalk and tip cells anastomose (red arrowhead in A''). Further cell rearrangements lead to a vascular network with patent lumen (A'''). (**B**) In Tg(*fli1a:EGFP*)y1 *ve-cad*ubs8 embryos, next to the lack of blood flow and the collapsed lumen in the DA (yellow double-headed arrow in B), angiogenesis is perturbed. Tip and stalk cells are weakly connected (blue arrowheads in B') and sometimes detach (not apparent in this movie). However, the tip cells, once up, extend filopodia laterally (red arrowheads in B'), but tip cell recognition is ineffective, which results in multiple contact points (red arrowheads in B''). While wt embryos established a functional network, the *ve-cad* mutant also established a network but without lumen (see B'''). Sometimes additional bifurcations form (see blue arrowhead in B'''). (**C**) In Tg(*fli1a:EGFP*)y1 *ve-cad*ubs8 *esama*ubs19 double mutant embryos, blood does not flow

due to the lack of VE-cad and the DA is collapsed (yellow double-headed arrow). While the tip cells migrate out, they extend cell protrusions that are occasionally thicker than filopodia (red versus blue arrowheads respectively in C). Tip and stalk cells are more loosely connected than in *ve-cad* mutants (blue arrowheads in C') and detach frequently (blue arrowheads in C'' and C'''). Tip cells, that try to contact each other, extend thick extensions (red arrowheads in C' and C''), however seem to fail to form proper contacts, even with multiple contact sites (red arrowheads in C''). At the time point where even the *ve-cad* mutant formed a network, the double mutant vascular network is still incomplete. Tip cells try to grow down to reconnect to stalk cells but grow in undirected fashion (red arrowhead in C''). Scalebars, 20µm.

Discontinuous junctions form in the absence of Esama

To investigate the distribution of other junctional components in the *esama* mutant, I performed α-Zo-1 antibody stainings on fixed embryos.

As described previously, the junctional pattern of wt showed very elongated rings in ISVs (see Figure III-20 A), which is concomitant with the extensive cell elongations in the stalk of the segmental sprouts. Furthermore, tip cell interactions during anastomosis resulted in quick deposition of junctional material at the contact site (seen as Zo-1 spots, demarcated by red arrowheads in Figure III-20 A). Also the *ve-cad*[ubs8] stalk cells showed junctional rings between each other, however, they were more circular and dorsal regions of ISVs were devoid of junctional staining (see Figure III-20 C). This reflects the inability of *ve-cad* mutant stalk cells to undergo the characteristic cell shape changes, which lead to sprout elongation.

The *esama* mutant embryos displayed elliptic junctional rings, comparable to those of wt. However, the detailed immunofluorescent analysis of junctional proteins revealed that these junctions were sometimes discontinuous, i.e. Zo-1 staining showed gaps within the rings (see blue arrowheads in Figure III-20 B''). Although the significance of this defect is not clear, it may suggest that in the absence of Esama, Zo-1 is not properly targeted to the junctions. Moreover, VE-cad did not seem to close the junctional gap either (data not shown), suggesting defects in assembly of junctions due to the absence of Esama. The junctional gaps became even bigger in the contemporaneous absence of VE-cad (red arrowheads Figure III-20 D''). Furthermore, in the

double mutant it is sometimes difficult to identify junctional rings in ISVs, because (i) Zo-1 also stains surrounding tissue, which makes endothelial specific staining more difficult to isolate and (ii) rings sometimes seemed to be absent at all where one would expect them (i.e. the gaps were actually longer than the Zo-1 stained stretches).

The junctional gaps in the *esama*[ubs19] mutant appeared to be reduced after further embryonic development (Zo-1 stainings of 2dpf embryos, data not shown). This suggests that these gaps only occurred transiently during angiogenesis and that vessel maturation also increases junctional continuity and/or maturity. However, further investigation and analysis will be needed to confirm these observations.

Another observation I made is the increase in cytoplasmic signal for Zo-1 in angiogenic ECs that lack Esama. This observation was mostly apparent within junctional rings, compare Figure III-20 B'' and D'' with Figure III-20 A'', but was not further investigated.

Taken together, the lack of Esama affects the organization or the recruitment of junctional components (e.g. VE-cad and Zo-1) and thus results in discontinuous junctional rings. When in addition also VE-cad is missing, the junctional gaps increase in length and the disorganization of junctional pattern becomes more apparent. This disorganization is in agreement with the reduced adhesion between angiogenic ECs.
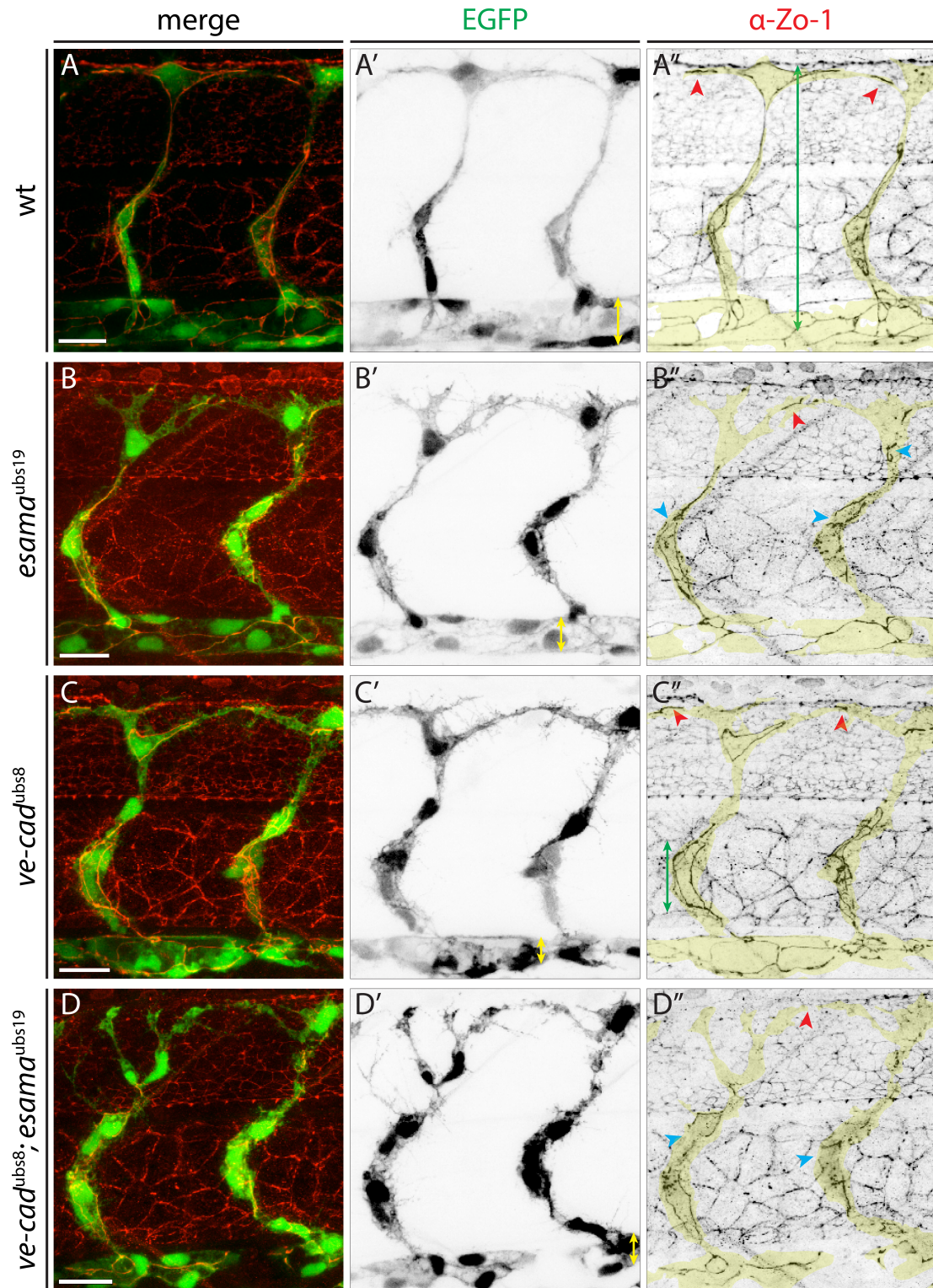
Figure III-20: Discontinuous junctions in the absence of Esama

Tg(*fli1a:EGFP*)[y1] (green) wt and mutant embryos fixed at 32hpf stained for α-Zo-1 (red), single channels in inversed contrast, anterior to the left. Cell bodies are overlaid in semi-transparent yellow in the Zo-1 channel. (**A**) wt embryos show junctional rings, that extend over the whole ISV axis (green double-headed arrow in A''). Anastomosis just began and junctional rings started to form (seen as lines, red

arrowheads in A''). (**B**) The junctional pattern of *esama*[ubs19] mutants is comparable to the one wt, with anastomotic contacts between tip cells (red arrowhead). However, at closer inspection, gaps in junctional rings in ISVs are apparent (blue arrowheads in B''), which indicate defects in the recruitment of Zo-1 to the junctions. (**C**) In *ve-cad*[ubs8] mutant embryos the junctional rings in ISVs are less elongated and appear more circular (demarcated by the green double-headed arrow). First anastomotic contacts can be observed (red arrowheads). (**D**) In the *ve-cad* and *esama* double mutant junctional gaps in rings are big (blue arrowheads in D''), e.g. the junction in the left ISV should be a single ring. Furthermore, the two tip cells seem to have overlapping cell extensions, but no Zo-1 staining is observed (red arrowhead in D''). Inflated or partially collapsed DA demarcated with a yellow double-headed arrow in the EGFP channel in A' and B' or C' and D' respectively. Scalebars, 20µm.

Further observations

In a next step in the analysis of the *esama*[ubs19] mutant embryos, I looked at apical polarization by staining embryos with Pdxl2, a process subsequent of junction formation. I do not include this preliminary data in my thesis but mention it briefly.

In wt embryos the apical staining is very weak and mostly found in membrane compartments enclosed by junctions. In agreement with previous studies, apical polarization in *ve-cad*[ubs8] mutant embryos seemed to occur similarly to wt (Lenard et al., 2013). There might be subtle differences in the intensity of the apical staining in *ve-cad* mutants but due to the weak staining quantification was not possible.

Junctional integrity is thought to be a prerequisite for proper apical-basal polarity. Therefore, the junctional discontinuities may interfere with segregation of apical and basal membrane components. However, when I examined the distribution of the apical marker Pdxl2 in *esama* mutants, the protein appeared to be properly localized, i.e. enclosed by a junctional ring. However, in the double mutant, Pdxl2 staining might also show more basolateral signal, i.e. weak staining throughout the cell body, suggesting defects in the segregation of apical determinants or in polarization. Further experiments are needed to validate these observations.

3.4.2.3.   Conclusions

Angiogenesis and anastomosis are dynamic processes, which rely on the extensive endothelial cell interaction that are mediated through endothelial specific adhesion molecules. In my PhD work, I have examined the consequence of the concomitant loss of VE-cad and Esama during these processes. My results suggest an important function of both proteins during angiogenic sprouting and anastomosis. While general angiogenic behavior of individual cells appears quite normal, cell-cell interactions that are required for vascular tube formation or blood vessel fusion are strongly compromised. These overall defects in endothelial specific contact formation result in a change of EC morphology and, rather than organizing themselves into continuous endothelium, ECs attain a morphology more typical for individual cells. At the molecular level, the defects in contact formation (and/or maintenance) are reflected by junctional discontinuity in angiogenic sprouts and also defects in the formation of "anastomotic rings".

Chapter IV

Discussion

4.1. VE-cadherin promotes endothelial cell elongation

A major focus of my thesis was to understand how ECs dynamically interact with each other during angiogenic sprouting and anastomosis. A key finding was that sprout extension is driven by EC elongation, which is concomitant with junction elongation. VE-cad appears to play a central role during this process.

I have investigated the role of junctional VE-cad, a protein expressed at the cell-cell interface, and this protein not only physically links cells of the same type but also controls a subset of morphogenetic cell behaviors. Angiogenic stalk elongation is mainly achieved by tip cell migration and stalk cell elongation. VE-cad-dependent actin cytoskeletal anchorage to the junction and actin polymerization is crucial to drive stalk cell elongation.

4.1.1. Cell elongation drives angiogenic sprout outgrowth

Previously studies showed that stalk cells of angiogenic sprouts overlap (Blum et al., 2008; Herwig et al., 2011). Our observations revealed that sprout extension is mainly driven by endothelial cell elongation, rather than the recruitment of new EC into the sprout or cell division. At the onset of angiogenesis, ECs of the stalk are piled upon each other. At this initial stage, the junctional interfaces are demarcated by relatively small circular rings. As the tip cell is migrating, the stalk cells rearrange and appear in a paired fashion, overlapping along the sprouting axis. We quantified these observations by three-dimensional (3D) measurement of junctional shapes. In contrast to the initial set up of the sprouts, later stages showed very elongated junctional shapes with a big perimeter and small area. Therefore stalk cells have an intrinsic capacity to change their cell shape and elongate a sprout.

164

4.1.1.1. VE-cadherin interacts with the actin cytoskeleton

During epithelial morphogenesis, individual cells of a cell layer are shaped in a honeycomb-like pattern. These cell shapes result from contraction forces exerted by every cell, which tries to minimize its apical surface and thus cell morphologies are regulated by the combination of the forces exerted by every individual cell and their adhesion to neighboring cells (Farhadifar et al., 2007) (see Figure IV-1 A). Furthermore, in cell duplets, cadherins are needed to couple the junctions to the actin cytoskeleton and the cytoskeletal tension is then driving cell-cell contact expansion (Maître et al., 2012) (see Figure IV-1 B). This illustrates the importance of cadherins in the intercellular connection of actin cytoskeletons that allow tensile forces to determine the cell shapes, not only of their own, but also of neighboring ones and finally of a whole epithelium.
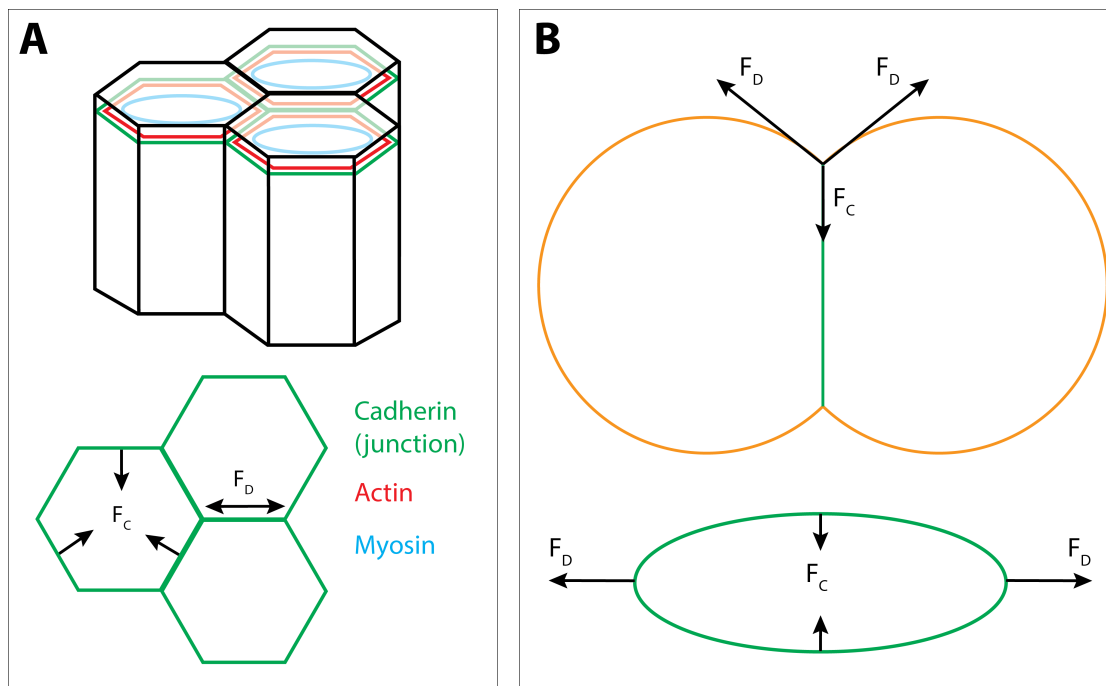
Figure IV-1: Forces that govern junctional shapes

(**A**) An epithelial cell sheet with a honeycomb-like pattern. The junctions in epithelial cells are located at the apical side of the cells and are lined by an actin-myosin ring. Each individual cell minimizes its apical side (a contractile force; F_C), which also will deform the junctional shape of the neighboring cell (a deforming force; F_D). After Farhadifar et al., 2007. (**B**) Forces that shape the cell-cell interface of a cell duplet need actin cytoskeleton anchored cadherins. The upper part shows the side view of

the cell duplet; the lower part shows the junctional ring made by the duplet. The junctional ring shape is given by the adhesive forces (not shown), the cortical contraction forces at the cell-cell interface (F_C) and the cortical deforming forces at the cell periphery (F_D). After Maître et al., 2012. Equal F_C and F_D will maintain circular ring shapes, but might still allow an increase or decrease in area. Imbalance in forces can transform a ring to an ellipse. F_C, contraction force; F_D, deforming force.

During angiogenesis, we do not look at a monolayer of cells, which forms a junctional network, but rather a small group of cells, which are connected by isolated junctional rings. In this condition, only two cells appear to determine the shape of the mutual surface and therefore control the cell rearrangements that deform this surface. We found that VE-cad deficient stalk cells still increase their mutual surface. However, as the junctional shape analysis showed, mutant cells do not transform the junctional interface into elongated elliptical shapes. Thus, VE-cad at endothelial junctions is involved in cell shape changes. Furthermore, VE-cad dependent attachment of the actin cytoskeleton to the junctions is a prerequisite; the rescue of *ve-cad* mutants with a VE-cad construct that lacks its cytoplasmic domain and thus cannot bind actin, did not rescue the phenotype. These findings are in agreement with models, where the remodeling of junctions also induce cytoskeletal rearrangements (Huveneers et al., 2012), and hence, in the *ve-cad* mutants, the actin cytoskeleton of stalk cells is disorganized and unable to drive cell-cell dependent shape transformations (Sauteur et al., 2014).

4.1.1.2.   VE-cadherin modulates actin dynamics

As mentioned above, contractile forces that minimize the apical surface of individual cells determine cell shapes in epithelial monolayers (reviewed by Lecuit et al., 2011).

To investigate the forces that drive stalk elongation, we performed pharmacological inhibition experiments during sprouting angiogenesis. When inhibiting contractile forces exerted by actin and myosin interactions, no reduction in junctional ring elongation was observed. However, the morphology of the rings attained local concave shapes. These observations appear logic, since contractile forces are supposed to minimize apical surfaces. However, the tortuous ring shapes after blebbistatin administration

imply roles of actin myosin interaction for local regulation of ring morphology. Nevertheless, junctional ring elongation seems not to depend on contractile forces. Therefore, other cytoskeletal forces must drive cell elongation.

We considered actin polymerization as another cytoskeletal component to induce cell shape changes. Chemical inhibition (by Latrunculin B, lat. B) of actin polymerization during wt angiogenesis showed a similar junctional phenotype as the one observed in *ve-cad*[ubs8]. We were not able to fully recapitulate the defects observed in *ve-cad* mutants by lat. B administration, presumably because we used low doses of lat. B to prevent cell migration defects or even lethality (Phng et al., 2013). However, a slightly higher concentration of lat. B seemed to further reduce junctional elongation (data not shown).

These findings suggest that VE-cad regulates local actin polymerization dynamics that drive cell elongation. Since VE-cad is known to interact with small GTPases, VE-cad might locally modify cytoskeletal dynamics to drive cell elongation. The subcellular localization of this actin polymerization remains to be determined. However, different possibilities are plausible: actin polymerization might be required (i) at the longitudinal junction, to reinforce, stabilize and elongate the junction or (ii) at the edges of the cell junctions to enlarge the cell-cell interface.

Local VE-cadherin and actin turnover increase cell-cell interface

Computational models suggest that local VE-cad turnover at junctions, and thus differential adhesion, enables stalk cells to overtake leading tip cells (Bentley et al., 2014). This indicates that certain VE-cad dynamics enable stalk cells to attain stronger migratory behaviors. Cell migration, on the other hand, depends on lamellipodia formation and actin polymerization at the leading edge (reviewed by Michaelis, 2014).

Our pharmacological inhibition experiments with lat. B, do not interfere with tip cell migration (also described by Phng et al., 2013). However, it could locally interfere with stalk cell protrusive activity. The junctional elongation has to involve an increase of the interface of two ECs, which should be archived by the generation of new VE-cad adhesion sites through cortical protrusions.

This notion is supported by observations we have recently made when studying anastomosis (Lenard et al., 2013). During contact formation, junctional rings labeled by ectopic VE-cad-EGFP construct, fluctuated in their linear thickness. These were most prominent at the edge of the junctional rings, where new adhesion sites form (see Figure IV-2 A). The local "spreading" of the junctions has been described in subconfluent cell cultures, where local turnover of VE-cad drives the formation of new adhesion sites (JAIL; junction-associated intermittent lamellipodia) (Abu Taha et al., 2014). JAILs contain dynamic actin networks (marked by ARP2/3), which ensure the continuity of a cell layer by preventing gap formation. They have been described in cell culture but their biological relevance is not clear. Our observations suggest that JAILs may play a fundamental role in dynamic EC movements during sprouting and anastomosis of blood vessels. Moreover, JAIL may be a mechanism, which ensures the formation of continuous endothelia and the integrity of blood vessels.

In our study, we mainly marked the junctions with Zo-1 and with this marker we did not observe the junctional dynamics that were observed with the VE-cadΔC-EGFP marker (i.e. possible JAILs as seen in Figure IV-2 A). This is an indication that JAILs are dynamic junctional intermediates, which have not recruited all junctional components yet. On the other hand, when imaging the EGFP-UCHD fish, I observed also local expansion of the junctions (Figure IV-2 B). With this transgenic line, it could therefore be possible to observe the formation of branched actin networks that locally enlarge the cell-cell interface, hence to follow JAILs *in vivo*.

Taken together, JAILs are VE-cad-based adhesion sites, which are marked by a branched actin network with high actin polymerization rates. Our observation that enlarged junctions predominantly are observed at the cell poles could therefore represent a JAIL-based mechanism for junctional elongation. Moreover, these adhesion sites could provide a VE-cad-based location for the deforming forces, which elongate circular junctional shapes into elliptic ones (see Figure IV-1 and Figure IV-3). Eventually, EC elongation via JAIL can be seen as cell migration on EC substrates.

Further validation will be needed to confirm that cell elongation is based on JAIL formation and the photoconvertible cytoskeletal marker line

[Tg(*4xUAS:mClav-UCHD*)] will be useful for cellular resolution of JAIL formation.
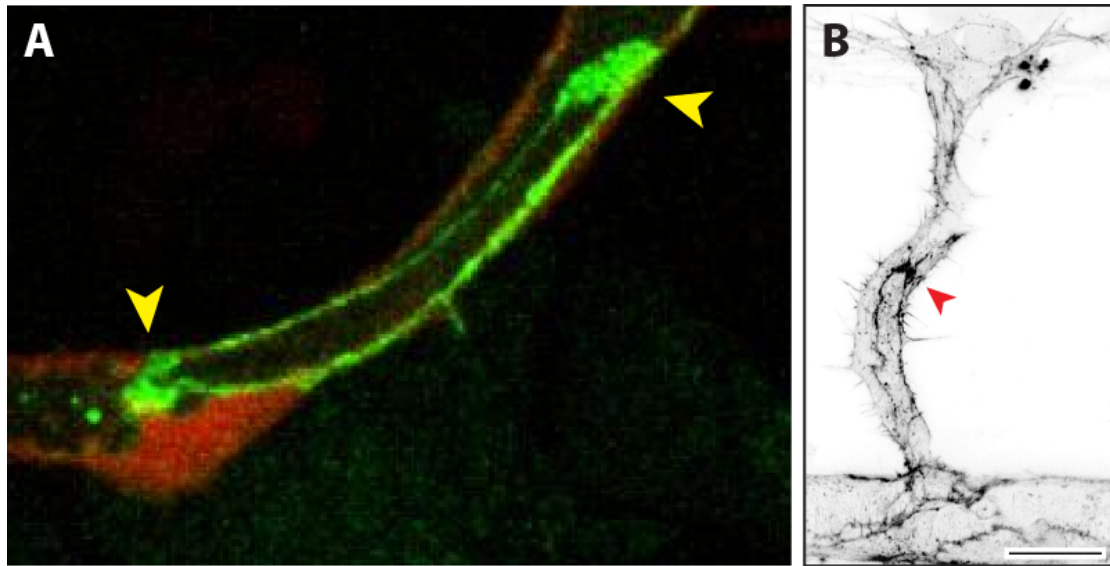
Figure IV-2: JAIL at junctional edges

(**A**) Still image from a supplemental movie taken by Lenard et al., showing the development of the posterior caudal cerebral vein in a Tg(*fli1ep:GFF*)[ubs3](*UAS:mRFP*)(*UAS:VEcadΔC-EGFP*)[ubs12] embryo. In this specific frame we see an isolated junctional ring marked with VE-cadΔC-EGFP (green) and the edges of the ring are widened VE-cad patches (yellow arrowheads) that could possibly represent JAILs. Taken from (Lenard et al., 2013) (supplemental movie 5). (**B**) A Tg(*fli1ep:GFF*)[ubs3](*4xUAS:EGFP-UCHD*)[ubs18] embryo at around 31hpf, anterior to the left. The UCHD channel is shown in inversed contrast. In the more ventral part of the ISV a junctional ring is seen and the actin cytoskeleton at the dorsal edge of the ring is enlarged (red arrowhead), indicating possible JAIL formation. Scalebar, 20µm.

ECM and cell-cell interactions

We consider here cell migration not on ECM substrates but on other EC. However, cell migration is best described on ECM substrates, where leading edges anchor to substrates by focal adhesion sites in an integrin-dependent manner.

While tip cell migration is a perfect example of ECM-based migration, ECs also secrete ECM components, which are later needed for vessel stabilization. Furthermore, Notch signaling (via Notch4) has been involved in

EC to ECM adhesion (Leong et al., 2002). Although the importance of stalk cell and ECM interaction during angiogenic sprouting is not understood, we did not investigate the role of stalk cell-ECM interactions, aspects that should not be neglected during angiogenic sprouting.

Such interactions might be important to stabilize the stalk during angiogenic sprouting. Stalk extension might be a combination of different adhesive factors and communication between EC-EC and EC-ECM adhesion sites might represent a more detailed model for angiogenic sprout extension.

An example of crosstalk between ECM and junctions is given during apical polarization processes. Once new junctions form between cells, Pdxl is translocated from the cell periphery to the newly formed junction (Bryant et al., 2010). This translocation depends on signaling from ECM adhesion sites in an integrin-dependent manner (Bryant et al., 2014). Here, *de novo* formation of junctions leads to signaling at cell-ECM adhesion sites via an ill-known mechanism. Therefore, ECM and junctions are in communication and might not only control apical polarization processes but also other activities such as, in our case, cell elongation.

4.1.1.3. Endothelial cells are highly dynamic during sprout outgrowth

When we ablated endothelial tip cells, we found that wt stalk cells quickly react to this new condition and redefine a new tip cell. This reflects the high plasticity and competitive nature of angiogenic EC for tip cell position (Jakobsson et al., 2010).

When I performed tip cell ablation experiments in *ve-cad* mutant embryos, I did not observe the respecification of a new tip cell. The remaining stalk cells rather clustered close to the DA, a situation very similar to *ve-cad* mutants, when stalk cells detach from tip cells. Eventually, after several hours in this condition, stalk cells would extend very long protrusions up to the DLAV and connect, essentially reproducing the *ve-cad* mutant phenotype.

These protrusions of the *ve-cad* mutant stalk cells are different to normal tip cell behavior. Tip cells usually migrate concurrent with their cell nucleus. In *ve-cad* mutant stalk cells (after ablation or after tip cell detachment), the protrusive activity was not accompanied by nuclear movements. There are

several potential causes for this detachment phenotype. First, as discussed below, the inability to form a new tip cell may reflect signaling defects downstream of VEGF or Notch. Alternatively, the lack of migration may be caused directly by aberrant EC adhesion or motility.

Bentley and colleagues have recently described a connection between VE-cad, cell motility and Notch signaling. Here, fluctuations in Notch signaling correlate with differential VE-cad dynamics and cell protrusive activity (Bentley et al., 2014). The authors further showed, that Notch signaling reduces VE-cad turnover and therefore EC mobility. This effect is observed in stalk cells, which interact directly with tip cells. Conversely, treatment with Notch inhibitor augments VE-cad turnover (and thus cell protrusive activity). Dynamic regulation of Notch signaling levels is also likely to be involved in the rearrangement and cell shape deformation of stalk cells. In agreement with this view, VE-cad turnover has been shown to regulate the dynamics of lamellipodia (JAIL) (Abu Taha et al., 2014), which may be the underlying structures that drive EC elongation.

While low levels of VE-cad can promote cell protrusions, it remains unclear what happens in the complete absence of VE-cad. Several studies showed that VE-cad physically interacts with VEGFR2 (Carmeliet et al., 1999), but can also alter cellular responses to VEGF signals (Carmeliet et al., 1999; Gavard and Gutkind, 2006; Lampugnani et al., 2002). My cell ablation experiments suggest a role for VE-cad in the maintenance of EC plasticity with respect to VEGF regulated Notch signaling; and maybe minute levels of VE-cad are required to maintain this signaling activity. *ve-cad* mutant stalk cells, after cell detachments or tip cell ablation, retain stalk cell characteristics (with little protrusive activity) for longer times. This is maybe because they lack the VE-cad component, which integrates into VEGF and Notch signaling. Eventually, these molecular interactions could not only regulate the stalk cell's protrusive activity but also their migratory behavior (i.e. cell movement accompanied by nuclear movement).

Uncoupling the adhesive and actin anchorage functions of VE-cadherin

Many advances in the understanding of biological processes have been facilitated by the use of dominant negative proteins. In zebrafish, these tools are limited.

The Tg(*fli1ep:GFF*)[ubs3](*UAS:VE-cadΔC-EGFP*)[ubs12] line is viable and angiogenesis appears normal, in spite of the Gal4 dependent overexpression of the construct. However, ectopic expression of the VE-cadΔC construct during tip cell ablation experiments phenocopied the *ve-cad* mutant phenotype. This indicates that this construct might act in a dominant negative manner. This transgene could provide a tool to investigate the adhesive functions of VE-cad independently of its intracellular functions (e.g. attaching to the cytoskeleton or signaling) *in vivo*. How the ectopic expression of the construct leads to the observed phenotype remains to be determined. These experiments reveal new roles of VE-cad in cell signaling during angiogenesis, rather than just linking the junctions to the actin cytoskeleton.

The increase of VE-cadΔC at the junctions could recruit more VE-PTP, which switches the ECs to a more quiescent state. Furthermore, the lack of the cytoplasmic domain could alter the cytoskeletal dynamics and also cell signaling (through e.g. β-catenin). Differential adhesion during sprouting was associated with tip cell position competition of sprouting cells (Bentley et al., 2014). The differences in adhesion in this model could also be induced by Notch or/and Wnt signaling, yet all these explanations are purely speculative and would need more molecular analysis. Unfortunately, I was not able to investigate Notch signaling during angiogenesis, since the transgenic marker (Tg(*tp1:venus-PEST*)[s940]) was expressed in a very mosaic manner and even in tip cells, where it should not have been.

Therefore, other methods are needed to assess signaling during angiogenesis in zebrafish, like *in situ* hybridization or antibody staining for tip cell markers (e.g. Dll4 or p-ERK). However, other transgenic Notch indicator lines would be very useful for the visualization of cell signaling dynamics.

172

4.1.2. Concluding remarks and outlook

Angiogenic sprout elongation is achieved by extensive stalk cell elongation and VE-cad is important for this process. Our studies showed that during these processes, VE-cad interacts with and orchestrates the actin cytoskeleton. VE-cad is essential for coupling the actin cytoskeleton to the junctions and this function is needed to drive extensive stalk cell elongation. We propose a model, whereby VE-cad locally regulates actin polymerization, which is needed for cell elongation. Yet, we do not know exactly where the polymerization occurs, but our observations suggest that it happens at the dorsal and/or ventral edges of the stalk cells, where lamellipodia-like structures (so called JAIL) form. Our hypothesis is that local turnover of VE-cad promotes JAIL formation at the cell edges, which provides a pulling force on the cells. This pulling drives cell-cell contact expansion (and cell elongation) during angiogenic sprouting and ultimately is a mechanism of cell migration on EC substrate (i.e. another stalk cell) (see Figure IV-3). This EC-based cell migration represents a general mechanism for stalk cell elongation but also anastomotic contact expansion.

4.1.2.1. Future directions

Although we suggest that VE-cad controls local actin polymerization, we lack firm evidence of the subcellular localization of this polymerization. To investigate the origin of the actin polymerization, we will use the VE-cadΔC-EGFP line to validate possible locations for JAILs occurrence. Moreover, by combining junctional marker (i.e. Zo-1-EGFP) with cytoskeletal marker (i.e. mRuby2-UCHD) we will be able to observe the formation of JAIL in real-time.
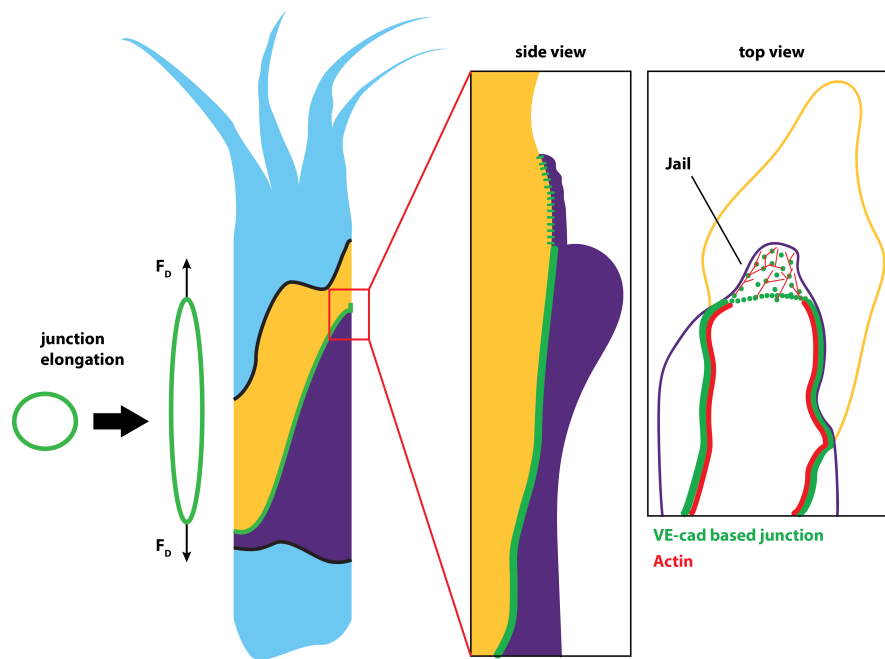
**Figure IV-3: JAIL promotes cell-cell dependent stalk cell elongation**
During angiogenic sprouting the cell-cell interface between stalk cells have circular junctional shapes. As the sprout grows out, the stalk elongates and deforming forces transformed junctions from circular to very elliptic shapes (left-hand side). VE-cad is crucial for these shape transformations and accomplishes this cell elongation by forming new adhesion plaques at the leading edge of the stalk cell (green VE-cad-based adhesion spots in the side view). These adhesion plaques occur after local VE-cad turnover at junctions, which allow local lamellipodium formation (or JAIL), which are marked by a branched actin network and expand the mutual cell-cell interface. Green lines and spots, VE-cad-based junctions; red lines, F-actin; F_D, deforming force.

Our studies have, however, just scratched the surface and have opened new directions to investigate the role of VE-cad in the control of cell behaviors.

We have shown that VE-cad is needed for stalk cell shape changes that do not appear to result from pulling forces exerted by the tip cell, but rather are of a stalk cell intrinsic nature. Yet, we do not know how strong the junctional tensile forces are and to elucidate this question, we plan to perform several experiments. One such experiment is to obtain direct information of tensile forces within junctional rings, by cutting the junctions with a micro-laser ablation system. Using zebrafish lines with marked junctions (e.g. Zo-1-EGFP

174

or VE-cadΔC-EGFP), I have cut junctions in embryos and observed recoil in these structures. Cutting junctions at different locations presumably shows different recoil speeds and hence will indicate differences in tensile forces. Furthermore, this technique could also show differences in junctional tensions between angiogenic and mature junctions, which would also give indications to the importance of forces that govern the morphogenetic processes during angiogenesis and mature vascular tubes.

Another method to measure these tensile forces is the use of transgenic tension sensing modules. In collaboration with the group of Benjamin Hogan, and based on a construct made by the group of Martin Schwartz (Conway et al., 2013), we obtained a zebrafish line that expresses a VE-cad construct capable to sense forces. This VE-cad construct harbors a FRET (fluorescence resonance energy transfer) module between the p120-catenin and the β-catenin binding site (Figure IV-4). When the actin cytoskeleton binds to VE-cad, through α-catenin and β-catenin, it can exert pulling forces on the junctions. In a resting phase (no pulling force), the fluorescent proteins of the FRET module are close enough to allow energy transmission after excitation of the blue fluorescent protein, resulting in emission of yellow light. However, when cytoskeletal forces stretch the FRET module, no signal will be released. With this line, we could therefore assess the relative subcellular forces, which reside within a junctional ring in real-time and also in whole blood vessels.
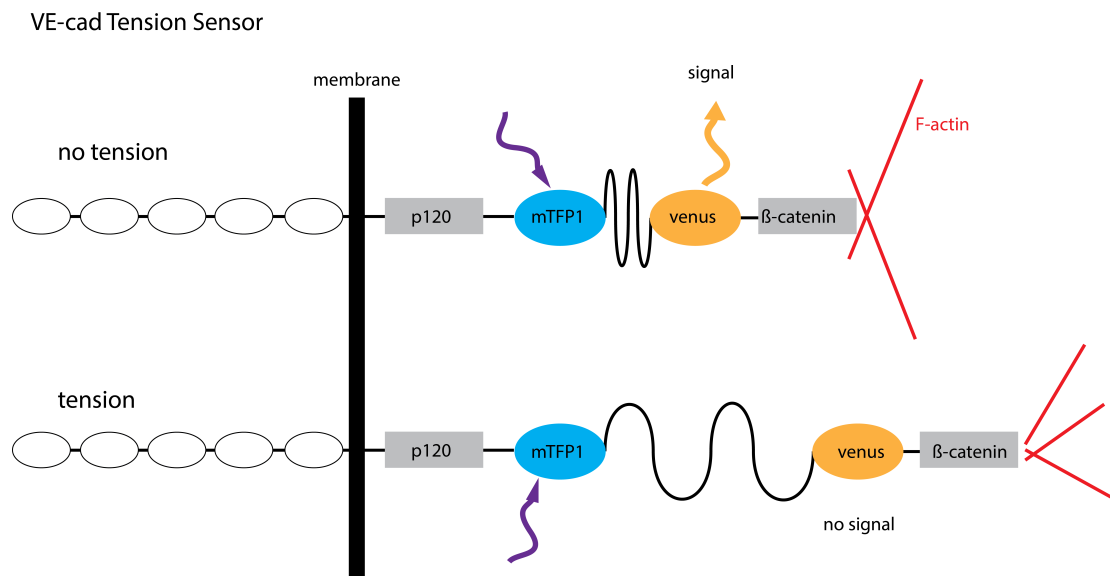
Figure IV-4: VE-cad tension sensor module

Engineered VE-cad that contains a tension-sensing module between the cytoplasmic p120-catenin- and β-catenin-binding site. In case of no tension, the blue (mTFP1) and yellow (Venus) florescent parts are close enough to allow transmission of energy (FRET) from mTFP1 to Venus after excitation of the mTFP1 protein. When the actin cytoskeleton exerts pulling forces on VE-cad by binding through β-catenin on VE-cad, the mTFP1 and Venus are pulled from each other, preventing FRET and signal form Venus. FRET, fluorescence resonance energy transfer.

4.2. The role of Esama during angiogenesis

Even though we have thoroughly investigated the role of VE-cad during vascular morphogenesis, the absence of this protein does not abrogate basic network formation of the endothelium. Therefore, we reasoned that other junctional molecules participate in these processes. We started to look into the role of another junctional restricted adhesion molecule in zebrafish embryos: Esama. We assume that such cell-type specific molecules have roles during angiogenesis and therefore, enable tissue specific morphogenetic processes and cell-cell interactions.

I generated a zebrafish mutant for endothelial-restricted *esama* using TALEN technology. And until now, I could show that Esama participates in vascular morphogenesis. However, it has mostly redundant roles during angiogenesis; *esama* mutant zebrafish are viable and fertile and show only subtle angiogenic defects (junctional discontinuities), which do not seem to affect angiogenesis *per se*. In the *esama* and *ve-cad* double mutant the junctional gaps increase in size. Moreover, the phenotypes observed in the *ve-cad* mutant, with regard to cell adhesion, protrusive activity and cell-type specific recognition, are worsen in the double mutant. Therefore, the double mutant will be a valuable tool to investigate cell behaviors and genetic components that are important for angiogenic morphogenesis.

4.2.1. Spatially and temporally restricted expression of Esama

The teleost group of fish harbors duplications of many genes, and conserved paralogs sometimes make the analysis of isolated genes tedious. Therefore, it is important to define possible synergistic roles of paralogs. The paralog of Esama is Esamb and virtually nothing is known about it.

I was not able to determine the exact expression pattern of Esamb, albeit around 32hpf, the paralogs seem not to be expressed in a tissue specific manner. Looking at published expression patterns of Esama, shows that it is

expressed early on (during somitogenesis) in the vasculature and the heart (Thisse et al., 2008). From then on, it remains expressed in the whole vasculature, especially nice around 24hpf, when ISV started to sprout. However, thereafter, the expression seems to be reduced and around 3-5dpf it remains strongly expressed in the head (Thisse et al., 2008; Wong et al., 2009).

The exact purpose of this timed expression pattern remains elusive, and has not been considered, nor observed in mouse. In zebrafish around 3dpf I still observed Esama with immunohistochemistry, but due to the experimental setup I could not quantify if the protein levels decreased (data not shown). However, this indicates that *esama* might be expressed during angiogenic sprouting in a spatial and temporal restricted manner or dosage and thus implicate an angiogenic specific role for Esama. Similarly, during nephrogenesis TJ proteins are expressed in temporal and spatial restricted patterns, which is crucial for the kidney's development and functions (McKee et al., 2014). Therefore, the controlled expression of junctional components seems to have important functions during development of different organs. Along this line, stainings for Claudin5b in the zebrafish vasculature showed that before sprouting, the DA is well stained; however, during ISV angiogenesis, protein levels are reduced (H.-G. Belting personal communication). Again, temporally controlled expression of junctional components seem to have important roles during development. Thus, temporal restriction of Esama expression might facilitate process such as anastomosis or sprout outgrowth. And maybe *esamb* is also expressed in the zebrafish vasculature, however, not simultaneously with *esama*.

4.2.2. Low efficiency mutagenesis of *esama*

Low mutagenic efficiency of TALEN for *esama* was already observed transiently in embryos, even upon the improvement of the mRNA transcription. Therefore, I had to screen a lot of offspring to isolate a mutant allele, although I used the same TALEN scaffolds as described by Bedell et al., where they mutated the *ve-cad* locus and observed already transiently high mutation rates, even recapitulating the *ve-cad* mutant phenotype (Bedell et al., 2012).

There might be several explanations for the low efficiency on my target gene; one is the DNA state of the target. CpG islands methylation is very prominent in vertebrate genomes (~70%) and methylation of cytosine was shown to prevent recognition of the respective RVD. Therefore, methylation of my target sequences would reduce the TALENs' affinity. Unfortunately, there are no resources for DNA methylation in the zebrafish genome to check for possible methylation states in the *esama* locus. Furthermore, repressed or tightly packed DNA could sterically reduce the accessibility of target sites.

4.2.3. Synergistic roles of VE-cad and Esama during angiogenesis

Even though Esama has a redundant role with VE-cad during angiogenesis, it does contribute during this process, which is most apparent when both proteins are absent. While the major phenotype is caused by the lack of VE-cad, the simultaneous absence of Esama enhances the defects of *ve-cad* mutants. Similarly to *ve-cad* mutant embryos, the double mutant seems not to show any vasculogenic defects, i.e. the DA and PCV form properly. Angiogenic ECs of double mutant embryos have very reduced adhesion and thus many stalk and tip cells detach from each other. This is also seen during anastomosis, in which cell-specific recognition is greatly decreased.

4.2.3.1.   VE-cad and Esama deficiency alters cell protrusive activity

Binding of VEGFA to VEGFR2 in ECs results in their activation and the cells attain a migratory potential and protrusive activity, which facilitates EC migration. The protrusive activity has to be regulated, which is important for EC quiescence and vessel maturation. While the protrusive activity of stalk cells is reduced by downregulation of VEGFR2 via lateral inhibition through Notch signaling, the absence of VE-cad in ECs increases protrusive activity (Abraham et al., 2009). Furthermore, when tip cells engage in a homotypic manner in anastomosis, VE-cad and VEGFR2 interaction is supposed to reduce their activity, leading to more quiescent phenotypes (Lampugnani, 2006). However, reducing VEGFR2 activity in VE-cad deficient cells did not reduce protrusive activity of ECs during anastomosis (Lenard et al., 2013). Therefore, VE-cad homotypic interaction seems to induce cell intrinsic mechanisms for a cells protrusive activity.

Also during sprouting of ISV in zebrafish, the absence of VE-cad leads to more protrusions in ECs. This phenotype is even more prominent in the simultaneous absence of Esama. The overall protrusive activity of ECs in the double mutant was shifted to thicker protrusions, which looked like lamellipodia. Therefore, the proper formation of endothelial cell junctions seems to regulate the protrusive activity of ECs. The exact molecular interactions that regulate these processes need to be determined. However, the absence of these molecules suggests regulation of the actin cytoskeleton via small GTPases.

Inhibition of VE-cad or Rho-kinase shows similar phenotypes with respect to sprouting, suggesting that protrusive activities are VEGF-driven and Rac1-dependent (Abraham et al., 2009). Therefore, VE-cad appears to regulate the cell's actin cytoskeleton from the junctions. My results suggest that the lack of several junctional components (i.e. VE-cad and Esam) leads to a disorganization of the actin cytoskeleton, which affects general cell behaviors.

4.2.3.2.   The absence of Esama reduces junctional continuity

Esam has roles during pathological angiogenesis but the role during physiological processes is redundant (Ishida et al., 2003). Little remains known about the roles of Esam in vascular development and all studies to date have investigated the role of the protein at a systemic level. The overall morphology of blood vessels appears normal in the absence of Esam; however, and since Esam is a junctional component, the studies neglected obviously the effects on cell junctions themselves.

Due to the high homology of Esam proteins in zebrafish, mouse and human, the loss of functions have similar phenotypes amongst species. Therefore, the vascular network of *esama* mutant zebrafish has no aberrant phenotypes and fish are viable and fertile. However, on closer inspection, subtle defects can be observed. The junctional architecture in *esama* mutant angiogenic sprouts showed small gaps in the continuity of junctional rings that enclose EC interfaces. Although I have just started to look into these aspects of the mutant, it looks like a specific phenotype affects the whole junctional architecture.

Zo-1 is mainly known to interact with TJ components, such as JAMs, but also VE-cad can recruit it to the junctions (Dejana, 2004), while Esam was shown not to interact with Zo-1 (Wegmann et al., 2004). The gaps observed by staining with Zo-1 could result from defects in the recruitment of Zo-1 to the junctions, and thus would imply to date unknown interactions between Esam and Zo-1. However, VE-cad seemed to be distributed similarly to Zo-1. This suggests that Esama is needed to ensure proper maturation of junctions and argues against physical interactions between Zo-1 and Esama.

These junctional gaps, however, seem to occur only transiently during angiogenesis. At later stages, when the network has formed and blood flows through the vessels, the gaps seemed not apparent anymore (data not shown). This suggests that during the development of sprouts, other junctional components (e.g. VE-cad) compensate for the loss of Esama.

The molecular pathways that lead to Esama-dependent junctional maturation remain to be determined. Possible players could include MAGI1, a multipurpose protein that binds to Esam (Wegmann et al., 2004). MAGI1 could act in different ways: (i) in a signaling point of view increase the

transcription of other junctional components, as VE-cad and β-catenin do for Claudin5 (Taddei et al., 2008), or (ii) regulate cytoskeletal dynamics. The latter point looks attractive, because in this way Esama would indirectly regulate cytoskeletal dynamics throughout the junctional ring. Esama-dependent increase in junctional actin would therefore facilitate homophilic VE-cad interactions at respective junctions, and thus decrease gap formation observed in Esama's absence. Furthermore, the lamellipodia-like cell extensions suggest a disregulation of cell cytoskeleton, which could be accounted for the lack of Esama.

Loss of VE-cad function in esama mutants increases junctional gaps

In *ve-cad* mutants, junctional rings of angiogenic sprouts do form, although their dynamics are altered. In these continuous rings, Esama and Zo-1 are distributed throughout the ring. This suggests that other junctional components ensure that junctions are formed properly. In the absence of both, VE-cad and Esama, only small stretches of junctions form. This suggests that homotypic cell interactions still occur in the absence of these proteins; however, junctions do not form properly. The big gaps further suggest that in the absence of VE-cad, Esama is crucial for the formation of junctions and their maturation to complete junctional rings. Here again, Esama seems to support the recruitment of junctional and cytoskeletal components.

4.2.3.3. Esama contributes to cell-type specific recognition and cell-cell adhesion

Both Nectins and Cadherins are involved in initial contact formation between cells. While Nectin interactions are more versatile, Cadherin interactions occur only in a homotypic manner and thus allow cell-type specific recognition. However, it remains controversial which protein initiates cell contact formation (Miyoshi and Takai, 2008). In epithelial cells, inhibition of E-cadherin homotypic interactions (by Ca^{2+} depletion) abrogates cell interactions and leads to cell rounding, despite the presence of other junctional components (Ebnet, 2008). Nevertheless, the ability of homotypic interactions of junctional components is supposed to confer cell-type specific adhesion and recognition (Dejana, 2004).

182

In zebrafish embryos that lack VE-cad, the EC's adhesive properties are reduced. As discussed before, stalk cells detach form leading tip cells, which can be explained by reduced adhesion in the absence of VE-cad. Furthermore, during anastomosis, several filopodial extensions engage in homotypic interactions and a number of them expand and merge (Lenard et al., 2013). In wt embryos, a single contact is sufficient for cell type specific recognition. Therefore, the lack of VE-cad seems to prevent signaling from contact sites for proper contact formation.

When additional junctional components are knocked out (i.e. VE-cad and Esama), EC adhesion is greatly decreased, which results in frequent cell detachments. In *ve-cad* and *esama* double mutants, contact formation seems to occur; however, cell recognition is further perturbed and several and big mutual surfaces are required for adhesive engagement. Progression of contact formation does not seem to lead to the combination of multiple contact sites as seen in *ve-cad* mutant embryos. Rather, the combinatorial lack of Esama and VE-cad seems to result in the maintenance of multiple contact points over big cell extensions. This suggests that poorly-formed junctions are unable to signal contact formation and ineffectively remodel the junctions to single mutual surfaces.

4.2.3.4.   Esama might be involved in apical polarization

Cell membrane invagination and the joining of luminal compartments drive blood vessel lumenization in zebrafish. Apical membrane fusion events combine different luminal pockets, thus apical polarization occurs before lumen generation. Anastomosis quickly recruits apical marker Pdxl2 at the cell-cell interface (Lenard et al., 2013). Here, Pdxl2 is supposed to separate the apical membranes in the luminal compartment (Strilić et al., 2010). This happens after EC engage with each other, and therefore the formation of junctions precedes apical polarization. TJ components (e.g. JAMs) recruit polarity determinants, such as Par3 and aPKC to junctions, where further molecules aggregate and are supposed to drive apical polarization (Ebnet et al., 2003). Recent studies identified molecular pathways that induce the translocation of Pdxl from the cell periphery to the apical compartments (Bryant et al., 2014). Here, integrin-dependent signaling inhibits RhoA-

dependent regulation of Pdxl at the cell periphery, which leads to PKC-dependent dissociation of NHERF-1 from Pdxl. Pdxl is then endocytosed and associated with NHERF-2, which are then targeted to AMIS. Arrived at the apical membrane, NHERF-1 is re-associated with Pdxl.

Esam as a TJ component could be involved in apical polarization more directly. Although Esam seems not to be involved directly in Par3 recruitment to the junctions (Ebnet et al., 2003), it could be involved in the targeting of apical determinants. Esam was shown to interact with NHERF-1 (Stalker et al., 2009) and thus could help to associate Pdxl with apical compartments after translocation from the cell periphery. Therefore, more detailed analysis of apical polarization is needed to investigate the role of Esam during these processes.

Staining zebrafish tissues with Pdxl2 localizes the protein to apical compartments enclosed by junctions. This also happens in the absence of VE-cad, suggesting that the polarity complex forms also in its absence. If the same accounts for *esama* mutants this needs further validation. However, when VE-cad and Esama are knocked out simultaneously, Pdxl2 seems to stain the whole cell membrane. Junctional discontinuities could account for the diffusion of Pdxl through membrane compartments. Furthermore, the formation of small junctional stretches raises the possibility that also the apical polarization complex is targeted to these junctions in the double mutant.

4.2.4. Concluding remarks

The preliminary analysis of *esama* and *ve-cad*; *esama* double mutant zebrafish embryo demonstrates an important role for Esama during vascular morphogenesis. Although the predominant phenotypes of the double mutant can be contributed to the lack of VE-cad, the simultaneous lack of Esama strongly enhances these defects. This suggests that the two proteins have overlapping roles in controlling angiogenic cell behaviors. Although angiogenic ECs of the double mutant appear relatively normal in respect to sprouting activity, the cell-cell interactions, which are needed for collective cell migration and cell-type specific recognition, are severely impaired. These

defects prevent ECs to form a proper endothelium, but rather retain a mesenchymal-like morphology. The morphological defects are reflected by discontinuities in stalk cell junctions and defects in the formation of anastomotic cell-cell junctions.

Taken together, the formation of proper cell-cell junctions appears to be crucial in the regulation of cell behaviors that are required for most, if not all, aspects of angiogenesis.

4.3. Acknowledgements

Thanks to Mami, Papa, Nilia, Mutti, Vatti, Grand-papa, Ruth, Ralph, Elisha, Naim, Resli, Ilaria, Debi, Patric, Alexander, Anna, Markus, Henry, Dimi, Vahap, Charles, Emmanuel, Alexandru, Stefan, Daniel, Oguz, Kumu, Shinya, Mario, Martin, Amanda, Ilkka, Helen, Niels, Etienne, Alessandra, Lukas, Yannick, Alice, Ania, Fisun, Michi, Elín, Magda, Rebecca, Anthony Percival-Smith, Gerhard Christophori, Andrea Banfi, Oliver Biehlmaier, Alexia Ferrand, Nikolaus Eherenfeuchter, Scott Loynton, Wolf Heusermann, Stefan Terjung, Bernadette Bruno, Gina Evora, Karin Mauro, Vaclav Mandak, Simon Ittig, Emília Santos, Walter Salzburger, Li-Kun Phng, Gerhard Holger, Benjamin Hogan, Anne Lagendijk and all I forgot to mention.

Appendix

A.1.　　Lenard A., et al. 2013

In Vivo Analysis Reveals a Highly Stereotypic Morphogenetic Pathway of Vascular Anastomosis

Anna Lenard,[1] Elin Ellertsdottir,[1] Lukas Herwig,[1] Alice Krudewig,[1] Loïc Sauteur,[1] Heinz-Georg Belting,[1,*] and Markus Affolter[1,*]
[1]Biozentrum der Universität Basel, Klingelbergstrasse 50/70, CH-4056 Basel, Switzerland
*Correspondence: heinz-georg.belting@unibas.ch (H.-G.B.), markus.affolter@unibas.ch (M.A.)
http://dx.doi.org/10.1016/j.devcel.2013.05.010

SUMMARY

Organ formation and growth requires cells to organize into properly patterned three-dimensional architectures. Network formation within the vertebrate vascular system is driven by fusion events between nascent sprouts or between sprouts and pre-existing blood vessels. Here, we describe the cellular activities that occur during blood vessel anastomosis in the cranial vasculature of the zebrafish embryo. We show that the early steps of the fusion process involve endothelial cell recognition, de novo polarization of endothelial cells, and apical membrane invagination and fusion. These processes generate a unicellular tube, which is then transformed into a multicellular tube via cell rearrangements and cell splitting. This stereotypic series of morphogenetic events is typical for anastomosis in perfused sprouts. Vascular endothelial-cadherin plays an important role early in the anastomosis process and is required for filopodial tip cell interactions and efficient formation of a single contact site.

INTRODUCTION

The vasculature of vertebrate species is indispensable for the distribution of oxygen, nutrients, metabolites, and blood cells to and from all organs of the body. The interconnected network of vascular tubes develops to a large extent during embryogenesis (Risau and Flamme, 1995). To maintain its vital function during embryonic growth and organogenesis, the vascular system undergoes extensive remodeling and expansion. Sprouting angiogenesis is thought to be the main process used to vascularize previously avascular tissues or areas (Carmeliet and Jain, 2011; Gerhardt et al., 2003; Herbert and Stainier, 2011). To form new vascular loops, angiogenic sprouts emerge from parental vessels and eventually fuse with another sprout or a pre-existing blood vessel, a process called anastomosis (Adams and Alitalo, 2007; Isogai et al., 2003; Wacker and Gerhardt, 2011).

Little is known about blood vessel anastomosis at the morphological and at the molecular level. Vascular fusion has not been studied extensively in cell culture, and in vivo studies have been held back by the difficulty to image developing blood vessels in mice.

We have previously analyzed the fusion of segmental arteries (SAs) during zebrafish trunk development (Herwig et al., 2011). These studies showed how distinct cellular mechanisms, such as cell polarization and cell shape changes, contribute to SA fusion and DLAV (dorsal longitudinal anastomotic vessel) formation. Surprisingly, we found that after the first contact formation, endothelial cells (ECs) can use two alternative mechanisms to connect luminal compartments of fusing sprouts and form a perfused vessel. These include unicellular tube formation through membrane invagination or cell rearrangements that lead to multicellular tubes. In the SAs, these two mechanisms occur with similar frequency, which raised the question as to how they are controlled and regulated. It is not clear to what extent the fusion events in the DLAV reveal the cellular activities underlying this process during later stages, when blood flow in the embryo is fully established. In addition, vessel sprouts often fuse to perfused vessels, a process that involves a single sprout. Whether this altered cellular configuration uses similar mechanisms to establish functional connections is not known. Furthermore, molecular components important for distinct events during the fusion process have not been identified thus far.

Here, we have performed high-resolution time-lapse analysis on cranial blood vessels in the zebrafish to reveal the morphogenetic mechanisms that underlie anastomosis of perfused sprouts and vessels. Using fluorescent reporters, labeling different cell compartments, we are able to define a multistep process, which operates consistently in the different blood vessels examined. The sequence of events is controlled by blood flow, ensuring that unicellular tube formation precedes cell rearrangements. Furthermore, we find that vascular endothelial (VE)-cadherin is essential for coordinating the early steps of the anastomosis process but is not required for the initial tip cell polarization upon contact.

RESULTS

Formation of the Palatocerebral Artery in the Zebrafish Cranial Vasculature

The palatocerebral artery (PLA) is one of the first cranial vessels that form via angiogenesis in the head of a developing zebrafish embryo (Figure 1A). It is a unique vessel that extends rostrally along the base of the forebrain (Isogai et al., 2001) and connects the two cranial divisions of the internal carotid artery (CrDI) vessels that encircle the optic capsules on both sides of the embryo head. At ~36 hpf, sprouts of the PLA vessel (PLA and PLA′, Figure 1B) start to grow ventrally from the CrDIs on both sides of the embryo head. The sprouts
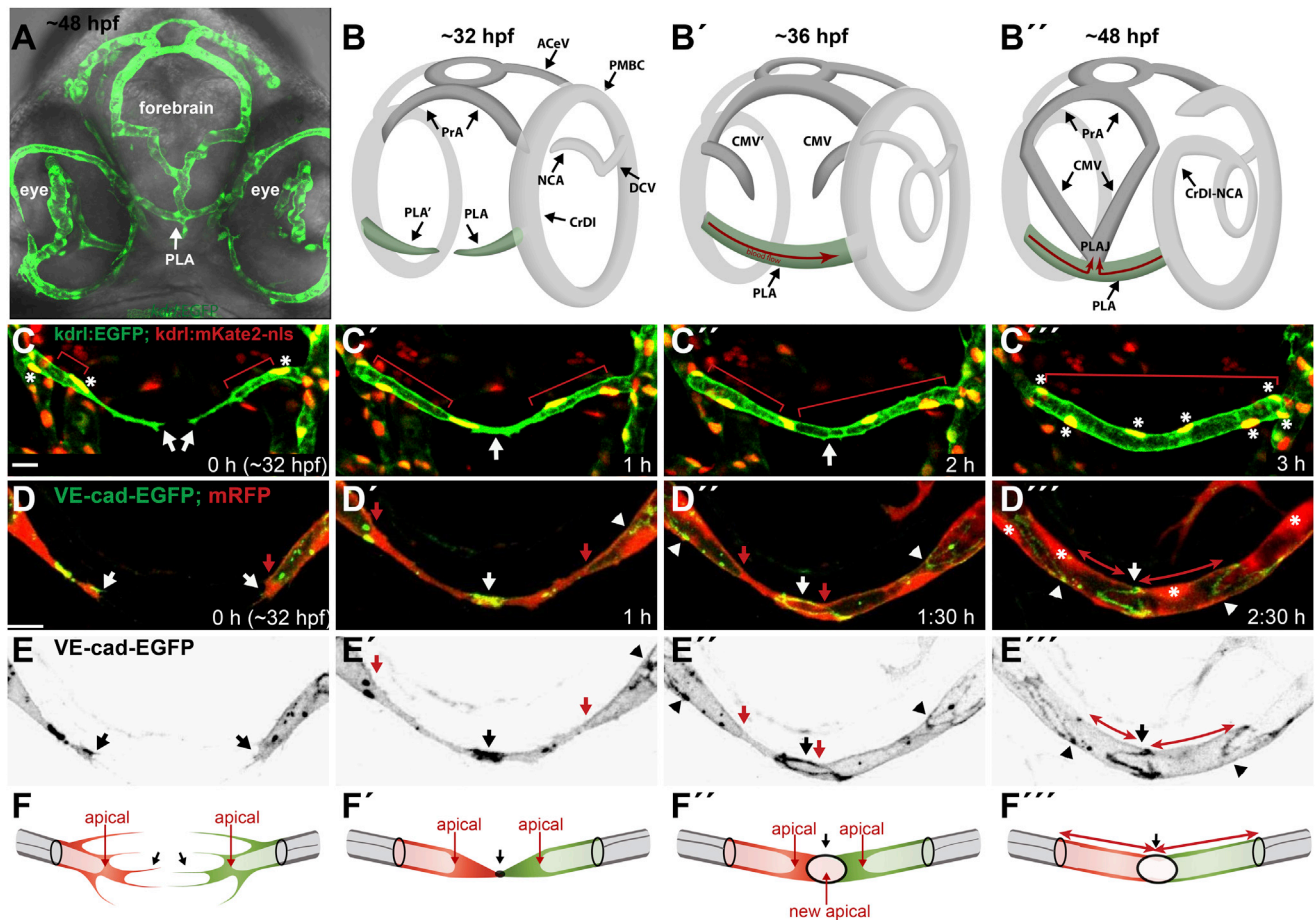
Figure 1. Palatocerebral Artery Forms through Fusion of Two Lumenized Angiogenic Sprouts

(A) Front view of a zebrafish Tg(*kdrl*:EGFP)[s843] embryo head at ~48 hpf. Blood vessels (green) together with bright-field image show the location of PLA within the head tissue (arrow).

(B) Schematic representation of PLA development (green) in the head vasculature from 32 to 48 hpf. PLA, palatocerebral artery; PLAJ, junction of the palato-cerebral arteries; CrDI, cranial division of the internal carotid artery; DCV, dorsal ciliary vein; PrA, prosencephalic artery; PMBC, primordial midbrain channel; ACeV, anterior (rostral) cerebral vein; CMV, communicating vessel; NCA, nasal ciliary artery.

(C) Still pictures of a time-lapse movie showing formation of the PLA in a transgenic embryo Tg(*kdrl*:EGFP)[s843];(*kdrl*:mKate-nls)[ubs13]. Endothelial cell cytoplasm is green and the nuclei are yellow (*). The PLA sprouts (C, arrows) extend from the CrDI and grow toward each other. Red bars mark the lumen length. The sprouts contact each other and anastomose (white arrow) to form a lumenized vessel that consists of five to six cells.

(D) Still pictures of a time-lapse movie showing the formation of the PLA in a transgenic embryo Tg(*fliep*:GFP)[ubs3],(UAS:mRFP),(UAS:VE-cadherinΔC-EGFP)[ubs12]. Cell-cell junctions are shown in green and cell cytoplasm in red. PLA sprouts (D, white arrows) are led by single tip cells connected to the stalk by a ring-shaped junction (D′–D‴, white arrowheads). Red arrows show the lumen margin in each sprout. Upon contact of the sprouts, a spot of VE-cadherin-EGFP appears (D′, white arrow). The spot elongates into a ring-shaped junction (D″, D‴, white arrow), and lumen is pushed through the junction for vessel perfusion (D″ and D‴ red arrows). An asterisk marks the endothelial nuclei.

(E) VE-cadherin-EGFP only (black), corresponding to stills in (D).

(F) A cellular model of PLA fusion. Time points correspond to the images shown above. Red and green cells are tip cells; stalk cells are gray. Black arrows show the sprouts (F) and the contact formation (F′–F″). Red arrows show the luminal/apical membrane (F–F″) or transcellular lumen (F‴).

See also Figure S1 and Movie S1. Scale bars, 20 μm.

meet centrally and establish a connection. The vessel is perfused at ~40 hpf, and blood flow is present in one direction (Figure 1B′). Subsequently, the communicating vessel (CMV) and CMV′ sprout ventrally from the prosencephalic arteries (PrA and PrA′) and connect to the center of the PLA, making up the PLA junction (PLAJ) (Figure 1B″). After this connection is made, blood flow is redirected and blood cells start to move from both parts of the PLA toward the centrally situated PLAJ and upward to the CMVs.

To gain insights into cellular aspects of PLA formation, we performed high-resolution four-dimensional (4D) confocal imaging using transgenic zebrafish lines with endothelial-specific cytoplasmic EGFP and nuclear mKate2 expression (Tg(*kdrl*:EGFP)[s843];(*kdrl*:mKate-nls)[ubs13]). We found that each of the PLA sprouts consisted of two to three endothelial cells. The sprouts moved toward each other and finally connected in a process called vessel fusion or anastomosis. The newly formed vessel was subsequently lumenized and soon after blood flow

started (Figure 1C). Because cytoplasmic EGFP expression is uniform in all endothelial cells, it was not possible to resolve individual cell shapes and cell behavior within the developing blood vessel with these analyses.

De Novo Cell Polarization Initiates the Formation of the PLA

To describe the process in greater detail, we used in vivo visualization of cell-cell junctions in order to follow individual cells of the developing PLA during contact formation and anastomosis. We used a previously generated transgenic line Tg(fliep:GFF)[ubs3];(UAS:mRFP);(UAS:EGFP-ZO-1)[ubs5], that expresses and localizes ZO-1 (Zona occludens 1) tagged with EGFP to endothelial cell junctions, referred to as EGFP-ZO-1. This transgene shows mosaic expression convenient for single-cell analyses. Additionally, we generated a transgenic line expressing the vascular-specific adhesion molecule VE-cadherin, in which the cytoplasmic domain was replaced by EGFP (Tg(UAS:VE-cadherinΔC-EGFP)[ubs12]). In this line, referred to as VE-cadherin-EGFP, the fusion protein was expressed in most of the endothelial cells. In both lines, the cell-cell junctions of ECs are visualized with EGFP, and the cell bodies are marked by the presence of cytoplasmic monomeric red fluorescent protein (mRFP).

In multiple time-lapse analyses with VE-cadherin-EGFP (n = 20), we observed that in each PLA sprout, a single tip cell was leading the front of the sprout and was connected to the following stalk cells by a ring-shaped junction (Figures 1D and 1E). Upon contact of two tip cells from opposing sprouts, a spot of VE-cadherin-EGFP appeared at the contact site (n = 20), demonstrating the de novo deposition of junctional material in the basal membrane (Figure 1D'). This spot was subsequently transformed into a ring as the cells expanded their contact surface (Figures 1D/E'–D/E'''; Movie S1 available online). During the fusion process, cell membranes within the ring of VE-cadherin-EGFP were of apical character, as shown by the presence of Podocalyxin-like 2 (Pdxl2), a marker for apical membrane, in immunostaining experiments (Figure S1B). Interestingly, each tip cell had two apical membrane compartments at this stage: one at the new contact site and one facing the lumen, where the cell was connected to the following stalk cells (Figures 1F'' and S1A–S1C).

Lumen Formation in the PLA

The formation of a new contact and apical polarization was followed by lumen perfusion. The PLA forms at ~36 hpf when the developing embryo has already established heartbeat and blood flow. We observed that the outgrowing sprouts were already lumenized, in many cases almost to the very tip, thus including parts of the tip cells (n = 20). The lumen extended from the parental CrDI vessel, between the stalk cells of the sprout, beyond the ring-like junctional connection into the tip cell, causing its luminal/apical membrane to invaginate toward the end of the sprout (Figures 1D and 1E), generating a dead-ended tube. Apical membrane invagination into the tip cell was confirmed by immunostaining with Pdxl2 (Figures S1A–S4C). After tip cell contact formation, the lumen extended toward the new contact site and eventually pushed through the newly formed junctional ring, suggesting that the perfusion of a new

vessel involved further tip cell membrane invagination and finally apical membrane fusion within the tip cell, leading to the formation of a unicellular tube with continuous transcellular lumen (Figures 1D, 1E, and 1F''', n = 20).

We confirmed the presence of transcellular lumen in the newly anastomosed PLA vessel with antibody staining, which showed a continuous apical membrane within single tip cells (Figure S1D). Furthermore, we observed that blood cells traveled through single lumenized endothelial cells in live embryos (data not shown).

To confirm the initial events in PLA fusion, we also performed single-cell live imaging analyses using the junctional marker EGFP-ZO-1 (n = 2), which is expressed in a mosaic fashion. In the particular experiment shown, only a single tip cell was labeled with the fluorescent junctional marker. We were able to follow the formation of a new junction spot that later transformed into a ring-like structure, as well as the formation of the transcellular lumen, demonstrating that, during the fusion process, an individual tip cell formed a unicellular tube connected on both sides to neighboring cells with junctional rings (Figures 2A and 2B; Movie S2).

Because membrane invagination appeared to be an important cellular aspect of vessel fusion, we generated a transgenic line expressing a membrane tagged version of mKate2 red fluorescent protein in endothelial cells (TgBAC(kdrl:mKate2-CAAX)[ubs16]). In these embryos, the fluorescent protein localized to endothelial cell membranes and allowed distinguishing the apical and the basal cell membrane with the use of high-resolution confocal imaging (Figure S1F). After a new contact was established, the apical membrane of each PLA sprout tip cell invaginated toward the contact site to finally reach the other, newly formed apical membrane of the same cell (Figures 2C, 2D, and 2G; Movie S3A). This process lead to the connection of the two luminal/apical compartments of each tip cell into a single, continuous one, resulting in lumen perfusion in both tip cells (n = 13).

Additionally, we performed angiography experiments by injecting fluorescein-labeled 500 kDa dextran (FITC-Dextran, Molecular Probes) into the vascular system. In these experiments, all open vessels connected to the flow were filled with the fluorescent dye (Figure 2C, green). The sprouting PLA filled up with dextran, up to the point to which membrane invagination had proceeded (Figure 2C, red arrows). This showed that the lumen forming in each sprout was continuous and connected to the existing vascular network. As the vessel perfused, the lumens from both sprouts connected and the vessel opened up, allowing the dextran to flow through.

The initial perfused lumen was not always stable. In ~40% (n = 13) of the time-lapse experiments we performed with the membrane marker, we observed that the lumen temporarily collapsed and inflated again. This involved dynamic rearrangements of the apical membrane, which in certain cases formed large spherical compartments no longer connected to the perfused lumen (Figures 2E and 2F). These membrane compartments were always filled with dextran, showing that they originated from the previous luminal membrane. Eventually, the sphere reconnected with the neighboring luminal compartment, forming again a continuous luminal space (Figures 2E and 2F''''; Movie S3B).
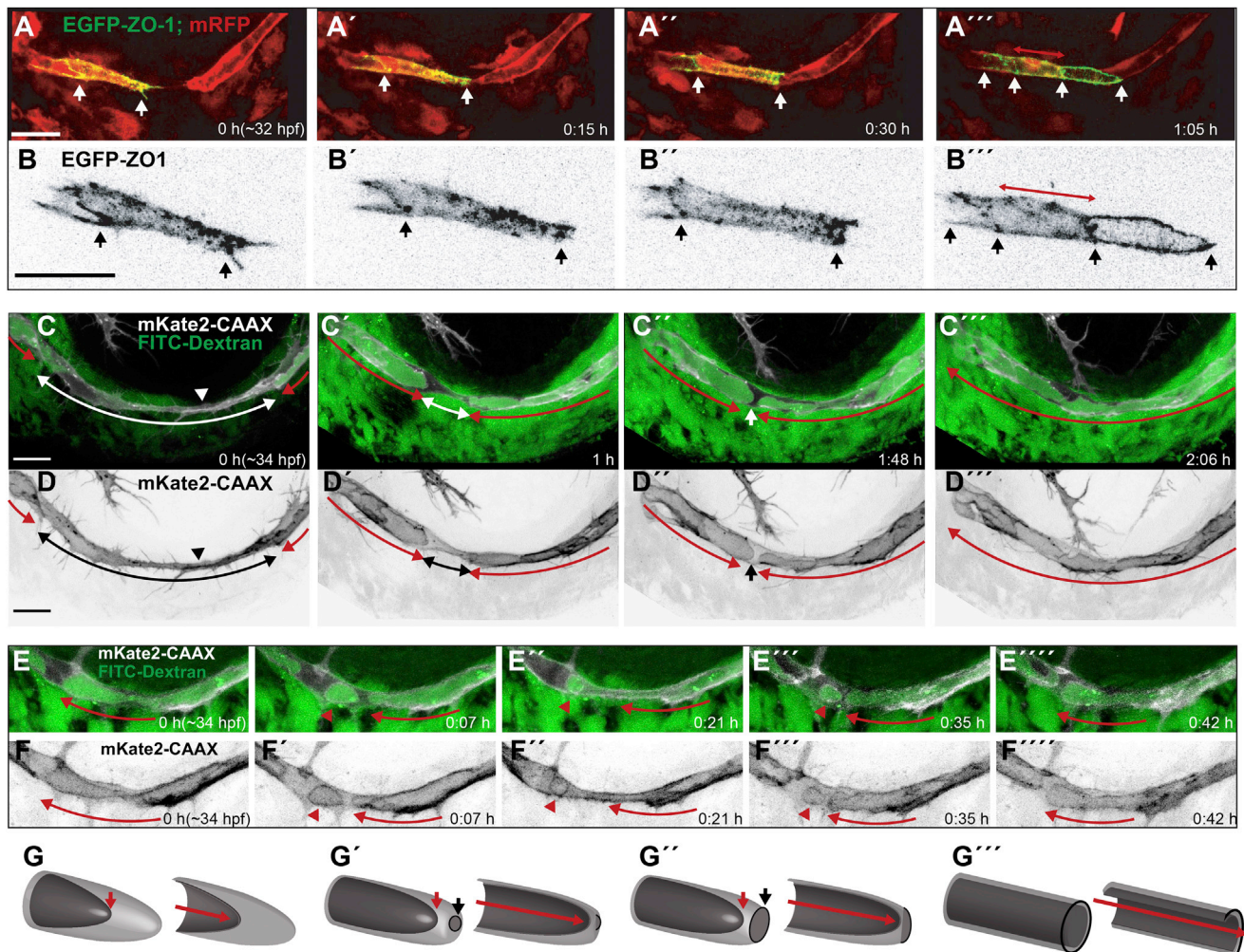
Figure 2. Lumen Formation in the PLA

(A and B) Still pictures of a time-lapse movie showing contact and lumen formation in a transgenic embryo Tg(*fliep*:GFF)[ubs3],(UAS:mRFP),(UAS:EGFP-ZO-1)[ubs5]. One of the tip cells is labeled with EGFP-ZO-1 (green). ECs cytoplasm is red. White arrows point the ends of the labeled cell (A–A″) and the edges of EGFP-ZO-1 rings (A‴) when the cell becomes a unicellular tube with transcellular lumen (A‴, red arrow). (B) shows the EGFP-ZO-1 labeled cell alone, enlarged 2× (black).

(C and D) Still pictures of a time-lapse movie showing lumen formation in the PLA in a transgenic embryo TgBAC(*kdrl*:mKate-CAAX)[ubs16] injected with FITC-dextran. After the tip cell contact is established, the luminal/apical membrane (red arrows) invaginates toward the contact site (C, D, arrowheads). White/black arrows shows the nonlumenized cell parts. Dextran (green) reaches the end of the luminal membrane, showing that the lumen is connected to the circulation. The membrane invagination advances from both sides (red arrows) until the two lumens are only separated by a small part of the cell body (C″/D″ white/black arrows). Perfusion of the lumen involves membrane fusion and connects the two lumens allowing the dextran to flow through.

(E and F) Still pictures of a time-lapse movie showing possible apical membrane rearrangements after initial lumen perfusion. A fully formed lumen (red arrow marks continuous lumen) partially collapses leading to separation of an apical membrane compartment in the form of a large sphere filled with Dextran (red arrowheads). The sphere can be maintained for a certain time (E″ and E‴), and finally it reconnects with the neighboring luminal compartment.

(G) A 3D model of a tip cell undergoing transcellular lumen formation through cell membrane invagination. The basal membrane is light gray; the apical/luminal membrane is dark gray. Red arrows point out the lumen end and the lumen length (in the cross section models). Black arrows show the new contact formation site, with junctions marked in black and new apical membrane in dark gray within.

Scale bars, 20 μm. See also Figures S1 and S2 and Movies S2 and S3.

Transformation of the PLA into a Multicellular Tube

The above experiments demonstrate that the initial lumen formed during PLA fusion involves cell membrane invagination and results in a transcellular lumen within the two participating tip cells, which form unicellular tubes. However, using antibody staining and live imaging of junctional proteins, we observed that the PLA had a clear multicellular architecture at later stages (~48 hpf) (Figure S1E). This suggests that the initial unicellular conformation, present right after fusion, is transient and that endothelial cells engage in a series of dynamic cell rearrangements within the existing vessel to finally form a multicellular tube.

Unexpected Cell Splitting during Tube Remodeling

In order to understand the cellular events during the transition of a unicellular tube to a multicellular tube, we followed tube
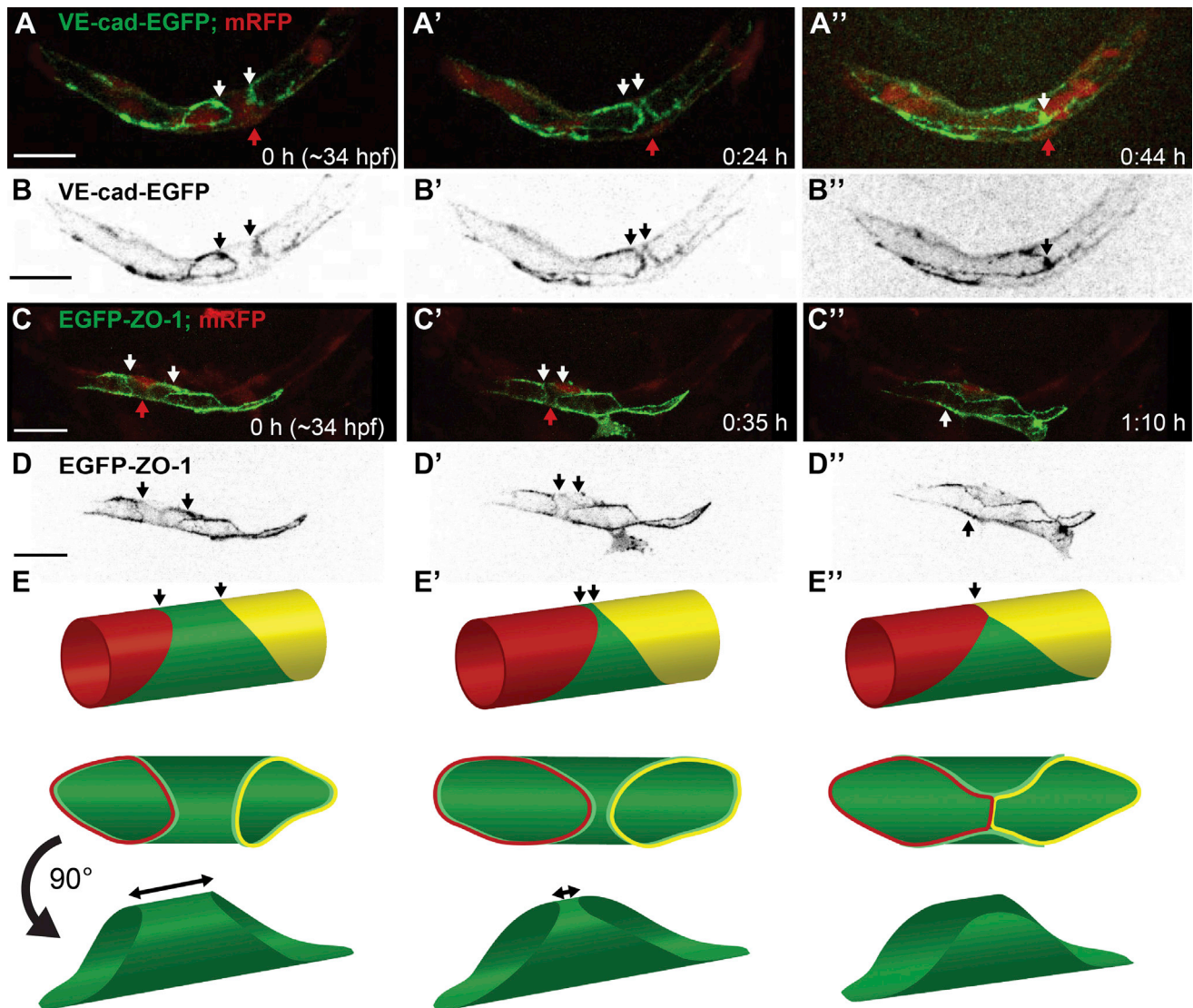
Figure 3. Formation of a Multicellular Tube through Cell Rearrangements

(A and B) Still pictures of a time-lapse movie showing PLA formation in a transgenic embryo Tg(*fliep*:GFF)[ubs3],(UAS:mRFP),(UAS:VE-cadherinΔC-EGFP)[ubs12]. Cell-cell junctions are marked in green and cell cytoplasm in red. One of the cells is a unicellular tube (A, red arrow) connected to the neighboring cells by ring shaped junctions (A and B, white/black arrows). A blood cell is visible within the lumen. With time the junctional rings move closer together meaning the neighboring cells migrate toward each other (A′, white arrows). Finally the rings meet making a new connection visible as a line of junctions (A″, white arrow). At this time point several blood cells go through the vessel. (B) shows VE-cadherin-EGFP alone (black).

(C and D) Still pictures of a time-lapse movie showing cell rearrangements in a transgenic embryo Tg(*fliep*:GFF) [ubs3],(UAS:mRFP),(UAS:EGFP-ZO-1)[ubs5]. The images show time points corresponding to (A), with only a single cell marked with EGFP-ZO-1 (C, green; D, black) and the endothelial cell cytoplasm in red. The cell (C, red arrow) is connected to the neighboring cells by ring shaped junctions. The cell body narrows on one side of the tube as the junctional rings move closer together (white arrows point the narrowing cell side). Finally, the cell splits on one side changing from unicellular tube into a flat cell, a part of the multicellular tube with one continuous junctional ring (white arrow).

(E) A cellular model of unicellular to multicellular tube transformation. The middle cell (green) is initially a unicellular tube (E). The neighboring cells (red, yellow) move closer together making the green cell narrow on one side of the tube (E′). Finally the green cell splits on one side of the tube to allow the red and yellow cells to meet and establish a new connection (E″, arrow).

Scale bars, 20 μm. See also Figure S2 and Movies S2 and S4.

remodeling using both fluorescent proteins marking the cell-cell junctions, EGFP-ZO-1 and VE-cadherin-EGFP (Figure 3; Movies S2 and S4). The initial new PLA vessel consisted of two cells with transcellular lumen connected to each other by a junctional ring and connected to the following cells by rings and/or lines of junc-

tions (Figures 1D‴, 1E‴, and 1F‴). In time-lapse experiments, we observed that the rings connecting the unicellular tube to its neighbors moved toward each other on one side of the vessel (Figures 3A–3D′, n = 22), meaning that the neighboring cells approached each other. Finally, the junctional rings touched and
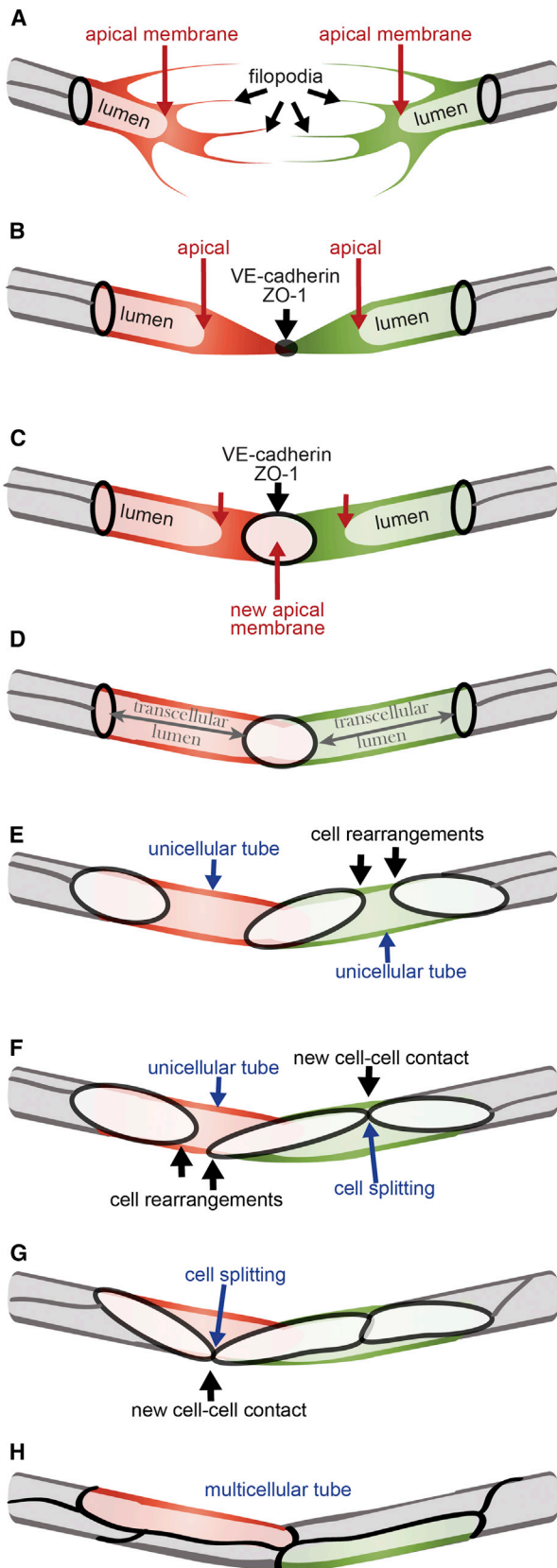
Figure 4. A Multistep Process Underlies Vessel Anastomosis

(A) In the first step, tip cells contact each other via filopodial extensions.

(B) Such contacts result in the formation of stable cell connections, manifested by the colocalization of VE-cadherin and ZO-1 at specific sites.

(C) At these sites of contacts, apical membrane is inserted, manifested by the localization of Podocalyxin-like 2.

(D) Concomitantly, filopodial activity of tip cells is dramatically reduced. While the luminal pocket generated by tip cell polarization and apical membrane insertion is slowly enlarged, the apical membranes that connect the tip cells to their corresponding stalk cells are invaginating rapidly due to blood plasma pressure, and eventually connect to the de novo generated luminal pocket. These initial steps in the anastomosis process thus lead to a vessel in which the two tip cells have a transcellular lumen.

(E–H) In a subsequent step (E), tip cells rearrange such that they eventually connect up to adjacent stalk cells (F) and form cell interactions (G). During these steps, the initial unicellular tip cells change shape through a cell-splitting event. As a result of this multistep process, a perfused multicellular vessel is generated (H). This vessel carries no obvious sign showing that it has been generated by a fusion process.

extended their contact area, thereby forming a new line of junctions (Figures 3A″ and 3B″). This means that a new connection was made between cells within the vessel, which were initially separated by a single cell making up the unicellular tube. At the same time, the cell forming this unicellular tube had to split on one side of the tube to allow the other cells to contact each other. This process was seen very clearly in the single-cell labeling experiments, in which only the "splitting cell" was labeled with the EGFP-ZO-1 marker (Figures 3C and 3D; Movie S2). The borders of the cell moved closer together, thereby narrowing the cell body on one side of the tube and eventually forming a very thin cytoplasmic bridge (Figure 3C′). This bridge was subsequently broken and the cell membranes reconnected in a different configuration, perpendicular to the previous one (Figures 3C″ and 3D″). At that point, the cell no longer had a transcellular lumen but adopted a U-shape with a single, large ring of junctions and became part of a multicellular tube with an extracellular lumen (Figures 3C″ and 3D″). As mentioned before, both tip cells can form unicellular tubes after the fusion is completed. Both of them also undergo "cell splitting," usually one after the other. As they are in contact with each other, they directly participate in the splitting of one another, temporarily taking the role of a "neighboring cell." Using live imaging and transgenic lines, we thus defined a multistep process underlying the formation of the PLA (model in Figure 4).

The PCeV Forms through Similar Cell Rearrangement and Cell-Splitting Events

To verify whether the described cellular processes also underlie fusion of larger vessel sprouts at later embryonic stages, we looked at the posterior (caudal) cerebral vein (PCeV), which forms in the dorsolateral region of the embryo head and connects the dorsal longitudinal vein (DLV) to the primary head sinus (PHS) on both sides of the brain (Figures 5A–5D). The vessel fuses between 2.5 and 3 dpf and is relatively large. The sprouts coming from the DLV and the PHS were wide and multicellular, but, like in the case of the PLA, were led by single tip cells (Figure 5A′, Movie S5, n = 4). The tip cells were partially lumenized through membrane invagination and extended long filopodia (Movie S5). A new spot of VE-cadherin-EGFP accumulated upon contact of the filopodia and subsequently elaborated into
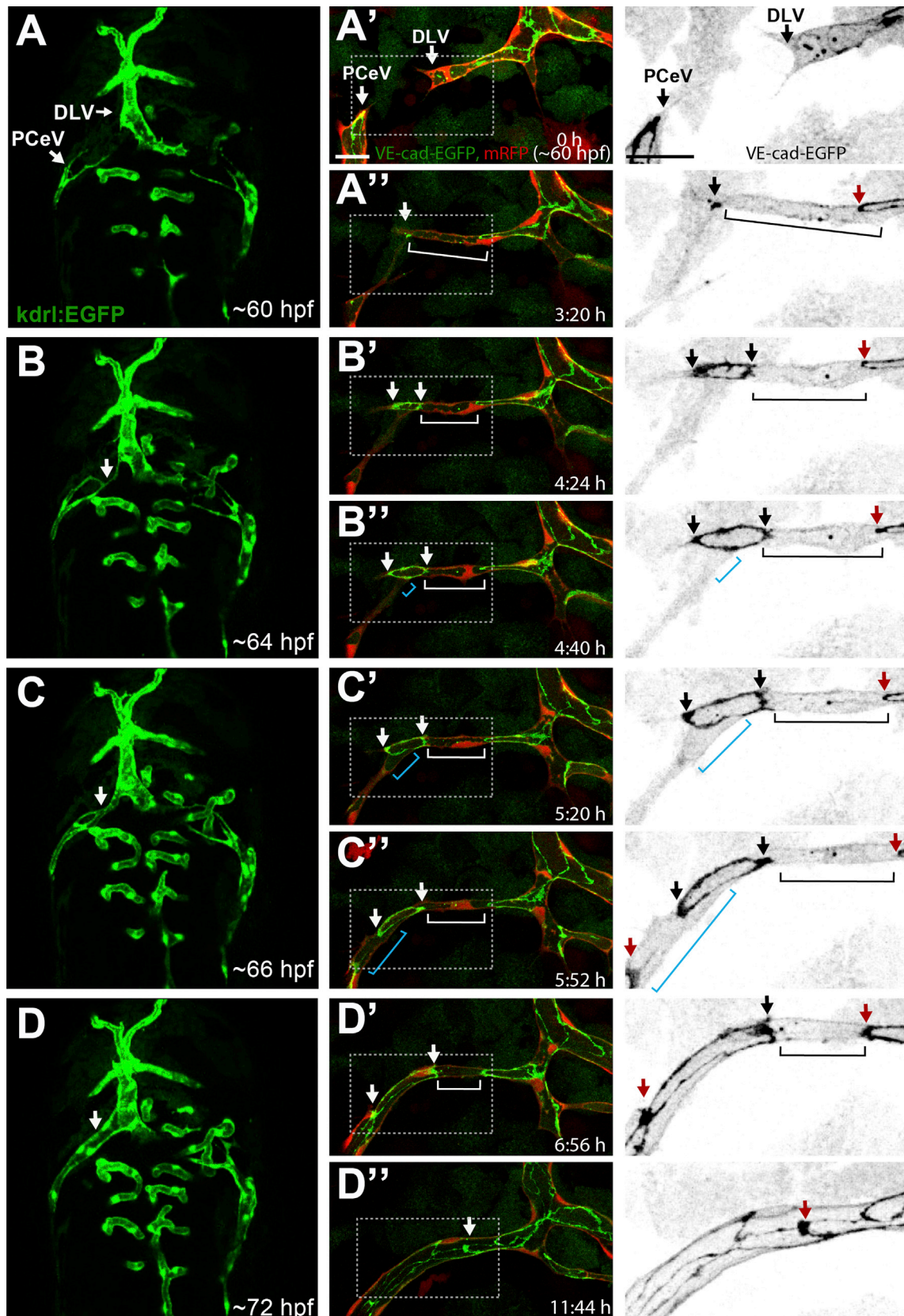
a ring-like structure (Figures 5A″–5B″). An initial transcellular lumen was formed in both tip cells (Figures 5B″–5C″) and further cellular rearrangements, virtually identical to those observed in the PLA, transformed the perfused vessel into a multicellular tube (Figures 5D′ and 5D″). Thus, the multistep process we describe during PLA formation, including transcellular lumen formation and cell splitting, appears to be a common feature of lumenized vessel anastomosis in the zebrafish.

Fusion of CMV to PLA Reveals Common Features of Vascular Anastomosis Events

Many vessels in a developing embryo are formed through fusion of two sprouts growing out of existing vessels, similar to the PLA or the PCeV. However, connections also form through fusion of a sprout to an existing, lumenized vessel, leading to a vascular junction with three or more branches. Such a situation is seen in the formation of the PLAJ, which connects the two CMVs to the PLA (Figure 1B″). The CMV sprouted ventrally toward the PLA (Figure 6A, Movie S6, n = 7), which was at that time already a lumenized, multicellular vessel. The leading tip cell of the CMV connected to the PLA via filopodia, leading to the accumulation of VE-cadherin-EGFP (Figure 6B). This first contact was made to the basal membrane of a cell within the PLA. The junctional spot rapidly elaborated into a ring, which eventually moved and connected to existing junctions within the PLA (Figure 6C). The newly formed apical membrane of the CMV tip cell invaginated into the sprout leading to transcellular lumen formation in this cell, from the PLA up toward the stalk of the sprout (Figures 6C–6G). The initial unicellular tube was eventually transformed into a multicellular tube through dynamic cell rearrangements, similar to the ones observed in PLA and PCeV (data not shown, model in Figure 6I). Even though the shape of the CMV-PLA connection is more complex than the one of the previously described vessels, we still observed the same cellular mechanisms, following the multistep fusion model adapted to this different vascular arrangement. Thus, the same cellular events connect either two sprouts or a single sprout with an existing patent vessel.

Together, this suggests that the multistep process described here is conserved and can be considered a general mode for lumenized blood vessel sprout anastomosis in the zebrafish.

Transcellular Lumen Formation Is Highly Influenced by Blood Flow

All of the analyzed cranial vessels form in the presence of blood flow in the neighboring and parental branches. As described before, the presence of blood plasma pressure in the sprouts appears to be important for the initial lumen formation by providing force for membrane invagination. Therefore, we asked whether the presence of this force is necessary, and, if so, which steps of the fusion process are most dependent on the presence of blood pressure. To characterize embryos that do not have any blood flow, we performed knockdown experiments using a morpholino that targets cardiac troponin T2a (tnnt2a) and causes the silent heart phenotype, in VE-cadherin-EGFP expressing fish (n = 5). The initial steps of PLA fusion occurred normally; the sprouts grew out, and upon contact, a junctional spot containing VE-cadherin was established and subsequently transformed into a ring (Figures S2A–S2C). The membrane within the junctional ring was apically polarized, as shown by Pdxl2 staining (Figure S2H). However, due to the lack of plasma pressure, no transcellular lumen was formed, and no apical staining was present outside of membrane compartments defined by junctional rings and lines, confirming that membrane invagination did not take place (Figures S2G and S2H). Despite the lack of a transcellular lumen, the cells within the vessel rearranged. After tip cell contact formation, neighboring cells from both sides moved toward each other and established new connections, transforming the vessel into a multicellular cord with continuous lines of junctions (Figures S2D–S2F) and continuous apical staining (data not shown), showing that cell polarization is independent of the presence of blood flow. Due to the lack of pressure and the resulting failure to generate unicellular tubes, the cell rearrangements did not result in cell splitting.

To investigate in more detail the role of blood flow in the initial steps of blood vessel fusion, we performed experiments using a high dose of tricaine methanesulphonate (4× tricaine), which resulted in significant decrease in the heartbeat and caused a collapse of vascular lumens in developing vessels. The PLA development was imaged before, during, and after 4× tricaine treatment in embryos with VE-cadherin-EGFP labeled junctions (n = 13, Figure S2; Movie S7). The heartbeat was inhibited at different stages of PLA fusion to assess the importance of blood pressure for particular steps. In all experiments analyzed, the PLA fusion continued upon lumen collapse, similar to the process observed in silent heart embryos completely lacking blood flow; the cells formed contacts and rearranged, but no unicellular tubes formed. After removal of tricaine, the heartbeat increased immediately and the lumens were reinflated. From that point on, the fusion process continued following the regular, pressure-dependent mode. In cases in which a new contact had just formed, lumen inflation was followed by unicellular tube formation in the tip cells (Figure S2I; Movie S7, embryo 1). In those cases, in which the cells had completed the cell rearrangements before tricaine removal, the lumen inflated immediately throughout the multicellular PLA (Figure S2J; Movie S7, embryo 2).

Figure 5. PCeV Forms through Cell Rearrangement and Cell-Splitting Events

Still pictures of a time-lapse movie showing the formation of the PCeV (posterior (caudal) cerebral vein).

(A)–(D) show a dorsal view (anterior up) of the head vasculature (green) at 60–72 hpf of a Tg(kdrl:EGFP)[s843] zebrafish embryo. The fusing PCeV and DLV (dorsal longitudinal vein) are marked with white arrows.

(A′)–(D″) show close-up of the PCeV fusion at time points corresponding to (A)–(D) of a transgenic embryo Tg(fliep:GFF)[ubs3],(UAS:mRFP),(UAS:VE-cadherinΔC-EGFP)[ubs12]. Right panel shows a close-up of VE-cadherin-EGFP alone (black).

Two lumenized sprouts approach each other led by single tip cells (A′, white arrows). A spot of VE-cadherin-EGFP is visible upon contact (A‴, white arrow). The spot becomes a ring as the cell contact surface expands (B′ and B″, white/black arrows show ring edges). Transcellular lumen forms in both tip cells (B′–C″, white and blue bars). When the lumen is perfused, the new junctional ring approaches junctions of following cells and contacts them (C′ and D″, red arrows), indicating cell rearrangements that transform the vessel into a multicellular tube.

Scale bars, 20 μm. See also Movie S5.
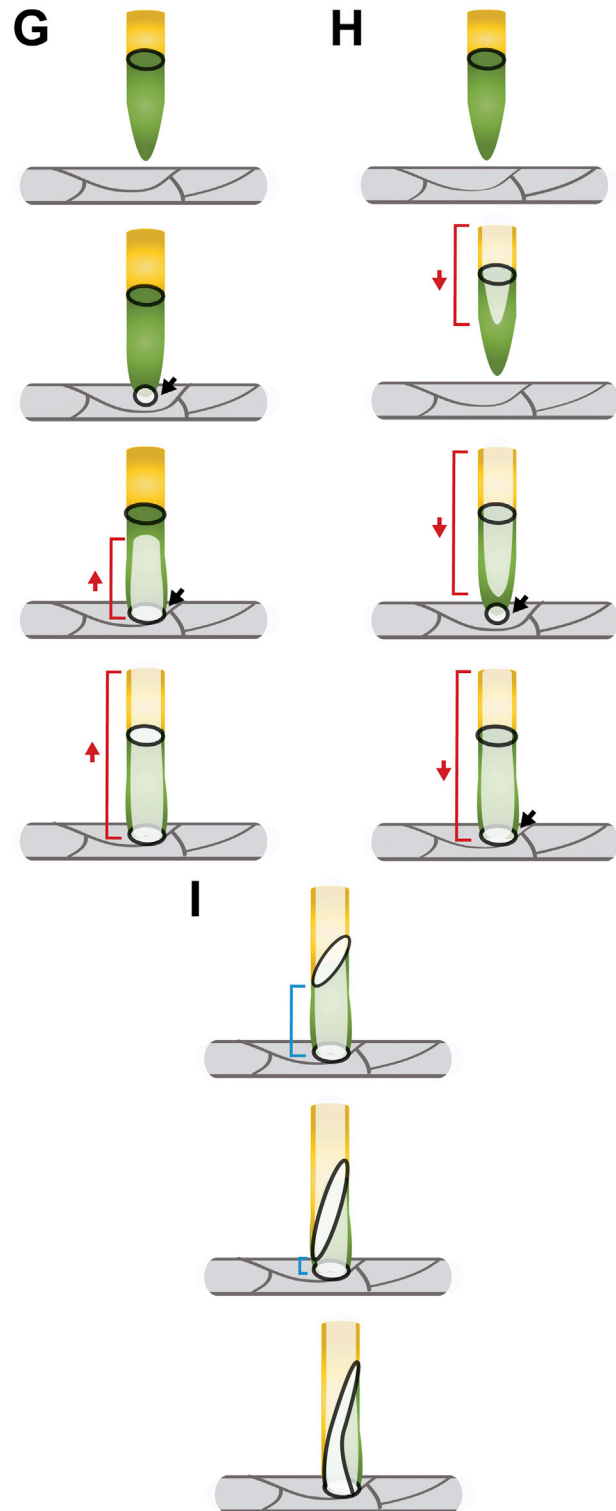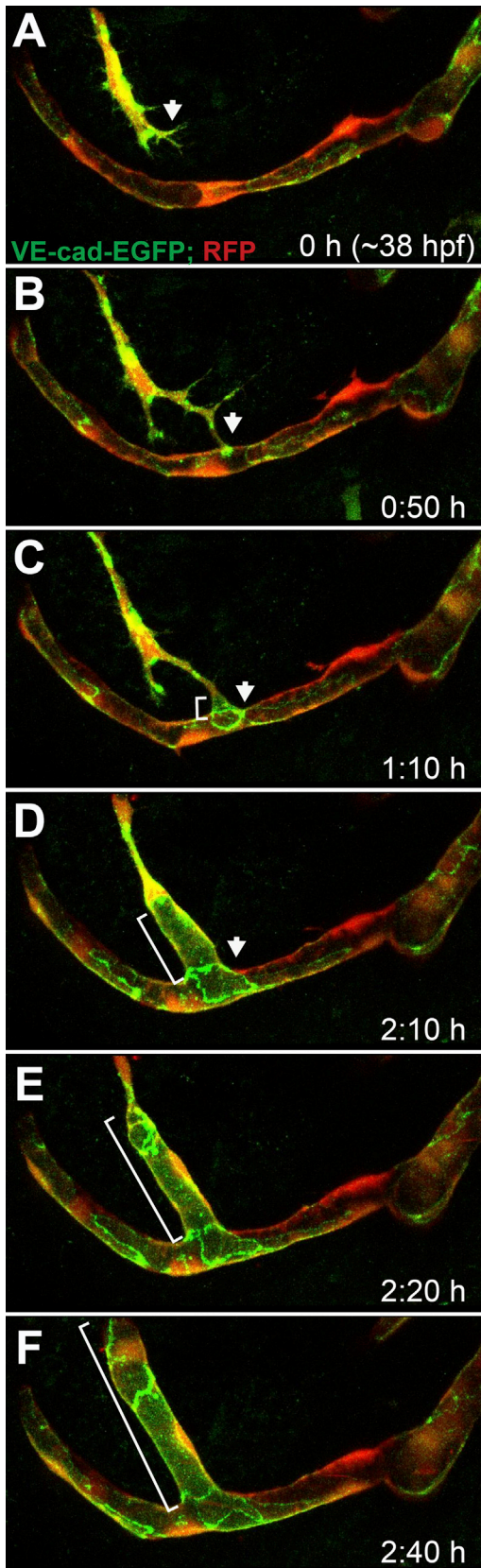
(legend on next page)

Therefore, we conclude that blood pressure is crucial for transcellular lumen formation through cell membrane invagination but is not necessary for cellular rearrangements to take place within an existing vessel. Cell splitting does not occur in the absence of blood flow as it requires a cell to first take the shape of a unicellular tube, and such tubes are only generated and maintained in the presence of blood plasma pressure.

VE-Cadherin Is Necessary for Single Contact Formation during Vessel Fusion

The proper establishment of a junctional connection is essential for the formation of new vessels and is one of the first steps of the vessel fusion model we propose. It was previously reported that the zebrafish VE-cadherin plays an important role in stabilizing novel vascular sprouts; reduction of VE-cadherin expression with a morpholino results in a lack of correct connections (Montero-Balaguer et al., 2009; Wang et al., 2010).

We used zinc finger nucleases to generate deletions in the *ve-cadherin* gene and isolated a null mutation (*ubs8*), which produces a truncated, nonfunctional protein (see Experimental Procedures). This mutation allowed us to investigate the role of VE-cadherin in the proposed multistep fusion process we described above. We analyzed PLA anastomosis in wild-type (n = 5) and *ve-cadherin*[ubs8/ubs8] (n = 7) embryos, using single-cell photoconversion experiments to differentially visualize the connecting sprouts in a transgenic zebrafish line expressing Eos2 photoconvertible protein in ECs (Tg(*kdrl*:tdEos2)[ubs15]). We additionally used *silent heart* embryos (n = 4, Figure S3) as a control, because the *VE-cadherin* mutants do not develop proper blood flow due to severe heart defects.

In both wild-type and *ve-cadherin*[ubs8/ubs8] embryos, tip cells displayed numerous filopodia and migrated toward each other in a similar fashion (Figures 7A and 7B; Figure S3C; Movie S8). However, while wild-type tip cells upon contact withdrew supernumerary filopodia and rapidly extended their initial single contact surface, the *ve-cadherin* mutant tip cells did not show such a behavior. In contrast, they continued sprouting activity long after the opposing cells had met and kept on extending additional filopodia, which resulted in the formation of several short connections instead of expanding the existing ones (Figures 7A and 7B; Movie S8). As a consequence, the tip cell contact surface expanded slower in the mutant embryos compared to the controls (Figure S3F). In 50% of the mutant movies (n = 7), we observed additional cells in the sprout showing tip cell behavior, which contributed to the increased number of contact points between the opposing sprouts.

In order to analyze the initial fusion events with greater detail, we imaged the process using high time resolution (recording every 15–30 s, n = 9), which allowed the observation of the dynamic filopodial activity during contact formation of PLA sprouts. We analyzed tip cell behavior using either photoconversion experiments (Tg(*kdrl*:tdEos2)[ubs15]) or visualization of the cell membrane marker described above (TgBAC(*kdrl*:mKate2-CAAX)[ubs16]). We found that filopodial activity was high before tip cell contact, both in wild-type and in *ve-cadherin*[ubs8/ubs8] embryos (Figures 7C, 7D, and S3D; Movie S9). While wild-type tip cells quickly established contact, mutant tip cells failed to recognize each other and took much longer to form a contact. Additionally, they continued sprouting and migration after the first contact was made, forming several connections over a large area that resulted in independent contact sites and holes within the contact surface.

Surprisingly, antibody staining analyses showed that ZO-1 and ESAM-a (endothelial cell-selective adhesion molecule a) were localized to the multiple contact points between the two connecting sprouts, demonstrating that tip cell interaction/recognition occurred in the absence of VE-cadherin (Figures 7E, S3A, and S3B). In many cases, apical membrane accumulated within these contact areas, as evidenced by the presence of Pdxl2 (Figure S3E). Consistent with the live imaging data, multiple contacts were formed and maintained, suggesting that the VE-cadherin protein is necessary for the generation of a single polarization event between interacting tip cells.

To observe the dynamics of the junctional contact formation in the mutant, we analyzed *ve-cadherin*[ubs8/ubs8] embryos expressing EGFP-ZO-1 (Figures 7F and 7G; Movie S10). Similar to the wild-type analyses (Movie S2), we observed a single labeled tip cell during the PLA formation. The sprouting tip cell expressed EGFP-ZO-1 uniformly at the membrane and, upon contact with the other tip cell, deposited the junctional protein at the contact site. However, the tip cell failed to properly form a single junctional ring; the connection was changing shape and the ring seemed to collapse, break, and split over time. The tip cell continued its sprouting activity and established a new connection a bit further up the other sprout, resulting in a new junctional spot. This process was repeated, and in total three contact sites were observed (Figures 7F″–7G‴). These sites eventually merged into a single one as the cells kept on moving over each other. These observations of the dynamic junctional rearrangements are in line with the other live imaging data and explain the disturbed junctional patterns observed in the antibody staining experiments.

VE-cadherin was shown to interact with VEGF Receptor 2 (VEGFR2) and *ve-cadherin* mutant cells show increased activity of this receptor (Abraham et al., 2009; Lampugnani et al., 2006). To analyze whether the phenotype we observed was related to the increased response of ECs to VEGF signaling, we used low doses of VEGFR2 inhibitor SU5416 in *ve-cadherin* mutant and

Figure 6. Fusion of a CMV Sprout to an Existing PLA Vessel
(A–F) Still pictures of a time-lapse movie showing fusion of CMV to PLA in a transgenic embryo Tg(*fliep*:GFF)[ubs3],(UAS:mRFP),(UAS:VE-cadherinΔC-EGFP)[ubs12]. CMV (communicating vessel) sprouts ventrally toward the PLA (A, arrow). The leading tip cell connects to the PLA on the cell body of one of the ECs making a spot of junctions (B, arrow). The newly formed ring connects to an existing junctional line on the PLA (C, arrow) and transcellular lumen forms in the CMV tip cell from the PLA upward (C, white bar). The lumen extends through the whole sprout (E and F, white bar).
(G) A cellular model of the CMV-PLA fusion. The CMV tip cell is green, followed by a yellow stalk. The PLA is bright gray with dark gray junctions. CMV makes a new junctional connection to the PLA (black ring, arrow). Lumen (bright green, red bar) is pushed through the tip cell and inflates up the sprout.
(H) A model of an alternative lumen formation process, where the CMV is lumenized from the CMV sprout toward the PLA (follow the red bars).
(I) Blue bars mark the cellular/junctional rearrangements leading to transformation of the CMV into a multicellular tube.
See also Movie S6. Scale bars, 20 μm.
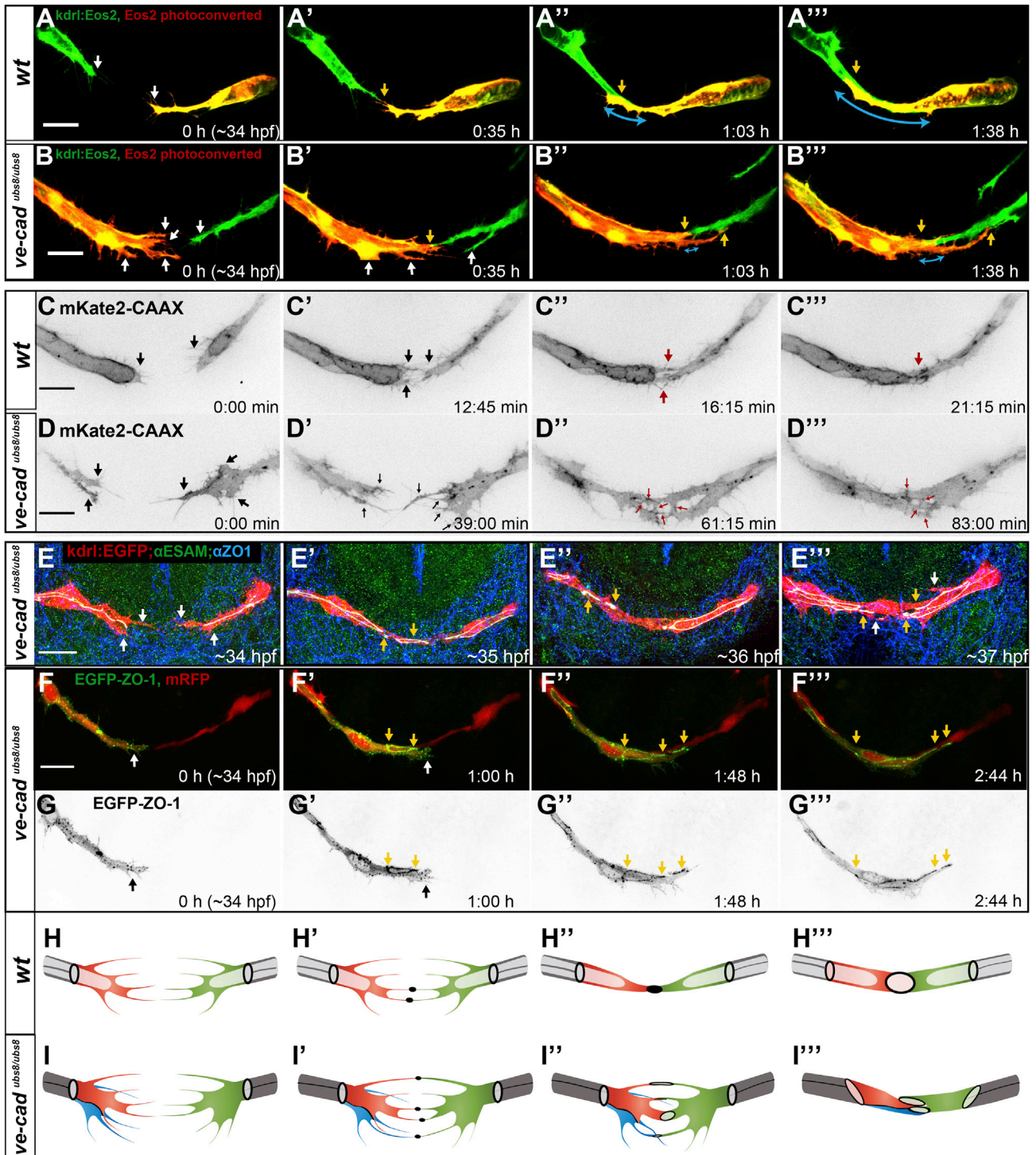
Figure 7. VE-Cadherin^{ubs8/ubs8} Embryos Show Defects in the Initial Steps of the Fusion Process

(A and B) Still pictures of a time-lapse movie showing development of the PLA in a transgenic line *ve-cad*^{ubs8/ubs8};Tg(*kdrl*:tdEos2)^{ubs15}; of a wild-type embryo (A) and a *ve-cadherin*^{ubs8/ubs8} embryo (B). White arrows point at cell extensions, single on each sprout in the wild-type (WT) embryo (A) and multiple in *ve-cadherin*^{ubs8/ubs8} mutant (B). Upon contact formation, the WT sprouts have one contact point (A′, yellow arrow) and do not form additional extensions, as the contact surface elaborates (A″ and A‴, yellow arrows point at the sprout end, blue arrows show the length of the contact surface). The *ve-cadherin*^{ubs8/ubs8} sprouts form multiple extensions (B′–B‴, white arrows) and multiple contact points form between the sprouts (yellow arrows). The continuous contact surface of the sprouts expands slowly (blue arrows).

(C and D) Still pictures of spinning disc time-lapse movies showing development of the PLA in transgenic line TgBAC(*kdrl*:mKate2-CAAX)^{ubs16} of wild-type (C) and VE-cadherin mutant (*ve-cad*^{ubs8/ubs8}) (D) embryos. Black arrows point at sprouting cell extensions, single or double in WT (C and C′) and multiple in

(legend continued on next page)

wild-type embryos and studied the fusion process. The lowest SU5416 dose used (0.1 μM) was sufficient to inhibit migration of WT sprouts for several hours but did not affect migration of mutant sprouts, suggesting that higher amounts of VEGFR2 might be present on VE-cadherin deficient ECs. However, this dose did not change the fusion phenotype of the *ve-cadherin* mutant embryos and the cells still produced supernumerous extensions and cell-cell recognition was disturbed (Movie S11). Higher SU5416 doses (0.5–2 μM) inhibited mutant sprout migration for several hours and delayed fusion; however, the cell behavior phenotype was also not rescued under these conditions.

These results demonstrate that VE-cadherin plays a central role in coordinating the anastomosis process at the early steps but appears to be dispensable for its initiation, suggesting that at least one other molecule is involved in this step of new vessel formation. In vessels lacking VE-cadherin, cells do not seem to recognize that contact formation has already occurred and continue angiogenic activity instead of proceeding to the next steps of the anastomosis process. This altered cell behavior results in multiple contact sites present over small areas of the cells that do adhere and polarize, but fail to form a continuous contact surface (Figures 7H and 7I, model).

DISCUSSION

In this study, we have analyzed how vessel sprouts anastomose in different vascular beds. We found that vessel anastomosis is brought about by a highly stereotypic multistep process, independent of whether new connections are made in an end-to-end fashion, involving the interaction of two tip cells, or in an end-to-side fashion, when the tip cell of a nascent sprout engages with an EC of an existing, lumenized vessel.

Initial Steps of Fusion Initiate Cell Polarization

During end-to-end anastomosis, nearby sprouts establish contact through filopodia of their respective tip cells. This initial contact quickly results in the establishment of a circular cell junction between the two tip cells. The cell membranes within these junctional rings are apically polarized, thus enclosing a luminal pocket, which will eventually be incorporated in the patent vessel. This process is consistently observed and has previously been reported for the SAs (Herwig et al., 2011). During anastomosis between the CMV and the PLA, a single tip cell from the

CMV contacts an EC within the PLA, which is a fully patent and blood-carrying vessel at this stage. CMV tip cell filopodia contact the "target vessel" on the basal side of the EC; these initial contact lead to junctional ring formation, indicating that the basal side of "resting" EC within a blood vessel can also be repolarized and undergo anastomosis.

Initial contacts between filopodia are thought to be mediated through cell-type-specific cell adhesion molecules (reviewed in Dejana, 2004; Xu and Cleaver, 2011). We have generated a loss-of-function mutation in the *ve-cadherin* gene in zebrafish and characterized homozygous *ve-cadherin* mutant embryos to explore the role of this vascular-specific protein during fusion of the PLA. In wild-type embryos, filopodia display a highly coordinated behavior; we observed that tip cells initially interact via one or more filopodial contacts. However, once the first contact has been firmly established and adherens junctions (AJ) components have been deposited at the site, the supernumerous filopodial contacts either resolved or merged with the primary contact site. In *ve-cadherin* mutants, tip cells do not "respond to" or "sense" these initial contacts, and thus several filopodial contacts are maintained, leading to several AJ deposit sites.

Previous studies have shown that VE-cadherin is required for the maintenance of endothelial quiescence (Dejana and Giampietro, 2012). Reduction of VE-cadherin in cell culture or zebrafish embryos leads to hypersprouting of ECs, and it has been suggested that this phenotype may be caused by an overactivation of VEGF-R2 signaling (Abraham et al., 2009; Lampugnani et al., 2006). Our observations on endothelia cell behavior during PLA fusion in *ve-cadherin* mutants are consistent with these studies; we also observed that tip cells form additional extensions even after tip cell contact formation. However, our timelapse analyses suggest that the primary defect in *ve-cadherin* mutants resides in the failure of proper cell-cell recognition between VE-cadherin deficient ECs, because experiments with limiting amounts of VEGFR2 inhibitor did not result in normalization of the tip cell phenotype.

Cell culture experiments and in vivo studies on the formation of the dorsal aorta in mice have indicated an essential role VE-cadherin for apical polarization and lumen formation (Lampugnani et al., 2010; Strilić et al., 2009). Surprisingly, we have not observed defects in apical polarization in the absence of VE-cadherin. These results suggest that additional cell surface proteins are involved in AJ protein deposition and repolarization of

---

ve-cadherin[ubs8/ubs8] vessels (D and D'). Red arrows point at cell-cell contacts. These contacts resolve into a continuous contact surface in wild-type (C''–C''''), whereas in the mutant they persist over time resulting in a noncontinuous contact surface (D'' and D''').

(E) Antibody staining of fusion steps corresponding to images in (A). *Ve-cad*[ubs8/ubs8];Tg(*kdrl*:EGFP)[s843] embryos (red) and anti-ZO-1 (blue) and anti-ESAM (green) antibodies were used. Junctions within vessels are visible where signals overlap (white). White arrows mark cell extensions (E). Yellow arrows mark the contact points where junctional proteins are deposited (E'–E'').

(F and G) Still pictures of a time-lapse movie showing contact formation in a transgenic embryo *ve-cadherin*[ubs8/ubs8];Tg(*fliep*:GFF)[ubs3];(UAS:mRFP);(UAS:EGFP-ZO-1). EGFP-ZO-1 (green in F; black in G) is expressed in only one tip cell. Cell bodies are red (F). Upon contact of the tip cells a junctional ring forms (F' and G', yellow arrows), but the cell forms new extensions (white arrow) that form additional contacts with the other sprout (F'' and F''', yellow arrows).

(H and I) Cellular models of initial steps of the fusion process in wild-type (H) and *ve-cadherin*[ubs8/ubs8] vessels (I). Initially, both sprouts form multiple extensions, which in the wild-type are limited to one to two per tip cell (H and H') and in the mutant often reach three to five (I and I'). Multiple cells can be present at the leading tip of the mutant sprout (I, red and blue cell) increasing the number of the observed extensions. When the filopodia touch, a contact is established with deposition of new junctional material in the wild-type (H', black dots) as well as the mutant sprouts (I', black dots). In the mutant, more contact spots are present. As the contact formation proceeds, the wild-type sprouts merge all the contact sites into one to form a continuous contact surface (H'' and H'''), whereas the mutant sprouts fail to merge all the contact sites resulting in multiple and disturbed junctional connections.

See also Figure S3 and Movies S8, S9, and S10. Scale bars, 20 μm.

the basal membrane upon filopodial tip cell contacts. These proteins remain to be identified.

Fusion of Two Apical Surfaces Connects Two Lumens

Upon the de novo formation of AJ and apical membrane insertion at the contact site, each tip cell is situated between two lumens, a distal one at the contact site and a proximal one at the base of the sprout. To connect the two lumens, the luminal membrane at the proximal site invaginates under the force exerted by blood plasma pressure and fuses to the distal cell membrane. This role for a mechanical force in vascular lumen formation is a striking parallel to the recently described requirement for a hydrodynamic force in canal cell lumen formation in *C. elegans* (Khan et al., 2013). It will be most interesting to identify the molecules that connect forces to membrane extension.

Cell Rearrangements Lead to Cell Splitting and Conversion of a Unicellular Tube into a Multicellular Tube

When blood vessels anastomose in a perfused surrounding, we find that the tip cell is invariably converted into a seamless tube containing a transcellular lumen. Within a short time window of less than 3 hr, this seamless tube is converted into a multicellular one. In vivo studies, in particular in quail embryos, have shown that ECs are quite motile and move considerable distances within the endothelium (Sato et al., 2010). Also in zebrafish, we have observed that ECs can switch positions between different segmental vessels (Blum et al., 2008). Thus, dynamic cell rearrangements within the endothelium appear to represent very common EC behavior in vivo. While it may be easy for ECs to move within multicellular tubes, seamless tubes do not have continuous cell junctions along their axes that facilitate cell movements. However, we find that ECs located adjacent to the seamless tube converge toward each other, thereby imposing drastic cell shape changes onto the intervening cell, which eventually results in cell splitting and in the generation of a multicellular tube with longitudinal junctions. From this perspective, it appears that the conversion of unicellular tubes into multicellular tubes is driven by intrinsic motile EC behavior and one would thus expect to find these conversions in most cases of anastomosis, which is indeed the case.

In order for cells to resolve the unicellular configuration, the former tip cell is split along one side of the tube, as neighboring cells close in on each other and physically interact. To our knowledge, this is the first time that such cell behavior has been observed to be an intrinsic step in a morphogenetic process. Splitting of the cell, in this context, may be best described as a change of cell shape from a ring to a u-shaped surface, which is mediated by an opening and immediate resealing of the cell membrane. This step may be reminiscent of the final steps of cytokinesis (abscission) during mitotic cell division (reviewed in Chen et al., 2012a; Fededa and Gerlich, 2012). Alternatively, splitting of the cell membrane may result in small lesions that are sealed by a general membrane healing process (Draeger et al., 2011; Roostalu and Strähle, 2012).

Blood Flow Is a Regulator of Anastomosis

The morphogenetic pathway we have described takes place in the presence of blood flow. Similarly, it has been described that, during angiogenesis in the postnatal mouse retina, the tip cell is in contact with the lumen as the sprout is growing out (Gerhardt et al., 2003). Blood flow has been implicated in many aspect of vascular remodeling, including blood vessel outgrowth and pruning (Bussmann et al., 2011; Chen et al., 2012b; Culver and Dickinson, 2010; Nicoli et al., 2010). We have investigated the role of blood flow during anastomosis of PLA and found that membrane invagination and consequently transcellular lumen formation does not occur in the absence of blood pressure. However, ECs are still motile, forming a vascular cord with luminal pockets, which subsequently converge into a continuous, noninflated lumen by further cell rearrangements. This "cord hollowing" mechanism is the same as the one we have observed during anastomosis of SAs that are not exposed to blood pressure if they fuse prior to the onset of blood flow in the zebrafish embryo (Herwig et al., 2011).

Future work will be directed toward understanding the molecular mechanisms that underlie and coordinate these complex cell behaviors during anastomosis. Recent studies in the MDCK system have shown that Synaptotagmin-like proteins control the formation of a single membrane domain in epithelial cells via the spatiotemporal organization of vectorial apical transport (Gálvez-Santisteban et al., 2012). Previous studies on cell polarization and lumen formation in MDCK and in ECs have also shown important roles for many intracellular proteins, for example, the Par3/Par6/aPKC complex, Rasip1 (Xu et al., 2011), CCM1 (Lampugnani et al., 2010), and the exocyst complex (Bryant et al., 2010) in initial polarization and subsequent apical membrane formation and lumen generation. It will be interesting to investigate the role of these proteins during contact formation and de novo polarization of ECs in vascular fusion events in vivo.

EXPERIMENTAL PROCEDURES

Generation of the *ve-cadherin*$^{ubs8/ubs8}$ Mutant Zebrafish

A *ve-cadherin* null mutation was isolated using zinc finger nucleases (Sigma), generating a stop codon in the first extracellular domain of the protein. Generation and characterization of the mutant fish will be described elsewhere in more detail. Beside the vasculature, the overall morphology of the mutant embryos is identical to wild-type within the time of our analyses (0–48 hpf).

Immunofluorescence and Imaging

Antibody staining was performed as described previously (Blum et al., 2008; Herwig et al., 2011). Images were taken with Leica TCS SP5 confocal microscope using a 63× glycerol immersion objective or a 40× water immersion objective. Images were analyzed using Imaris (Bitplane) and Image J software (http://imagej.nih.gov/ij/).

In Vivo Time-Lapse Analysis

Transgenic embryos selected for presence of fluorescence were anaesthetized in 1× tricaine (0.08%) and mounted in a 35 mm glass-bottom Petri dish (0.17 mm, MatTek), using 0.7% low melting agarose (Sigma) containing 0.08% tricaine and 0.003% 1-phenyl-2-thiourea (PTU; Sigma-Aldrich). Leica TCS SP5 confocal microscope was used for time-lapse analyses. Images were taken using following objectives: 20× air, 40× water, and 63× glycerol immersion. Single-cell photoconversion was performed as described before (Herwig et al., 2011). High time resolution analyses were performed using a 3i spinning disc microscope and 63× oil immersion objective or Leica TCS SP5 confocal microscope with resonance scanner. All images are maximal z-stack projections.

Microangiography

Fluorescein labeled 500 kDa Dextran (Molecular Probes) was injected into the sinus venosus of mounted embryos using glass needles (Biomedical Instruments) with tip opening of 10 μm and beveled tip.

Morpholino Injections

One to two cell-stage embryos were injected with 4 ng of antisense morpholino oligonucleotide targeting the start codon region of the cardiac Troponin T2a (5′-CATGTTTGCTCTGATCTGACACGCA-3′). The morpholino causes complete loss of heartbeat (Sehnert et al., 2002). The analyzed embryos were selected based on this criterion.

Heart Arrest using Tricaine Methanesulphonate

Embryos were mounted in agarose for live imaging, covered with 1× tricaine (0.08%) in egg water and imaged for 1–2 hr. The water was replaced with 4× tricaine in egg water, which strongly reduced heartbeat and completely inhibited blood circulation. After 5–6 hr of imaging the water was replaced again with 1× tricaine, bringing back heartbeat and blood flow.

SU5416 Treatment

DMSO stock solution (2 mM) of VEGFR2 inhibitor SU5416 (Sigma) was diluted in both agarose and egg water covering imaged embryos to the final concentration specified in the results (0.1–2 μM).

Fish Maintenance and Stocks

Zebrafish were maintained at standard conditions (Westerfield, 2000). Embryos were staged by hours postfertilization (hpf) at 28.5°C (Kimmel et al., 1995). The following zebrafish lines were used in this study: wild-type fish (AB/EK and EK/TL), Tg(kdrl:EGFP)^{S843} (Jin et al., 2005), Tg(UAS:EGFP-ZO1-cmlc:EGFP)$^{ubs5-7}$ (Herwig et al., 2011), Tg(UAS:RFP) and Tg(fli1ep:GAL4FF)$^{ubs2-4}$ (Totong et al., 2011; Zygmunt et al., 2011), TgBAC(kdrl:mKate2-CAAX)^{ubs16} this study, Tg(kdrl:tdEos2)^{ubs15} this study, Tg(kdrl:mKate2-3NLS)^{ubs13} this study, and TG(UAS:VE-cadherinΔC-EGFP)^{ubs12} this study. Details on plasmids and transgenic line generation can be found in the Supplemental Information.

SUPPLEMENTAL INFORMATION

Supplemental Information includes Supplemental Experimental Procedures, three figures, and 11 movies and can be found with this article online at http://dx.doi.org/10.1016/j.devcel.2013.05.010.

REFERENCES

Abraham, S., Yeo, M., Montero-Balaguer, M., Paterson, H., Dejana, E., Marshall, C.J., and Mavria, G. (2009). VE-Cadherin-mediated cell-cell interaction suppresses sprouting via signaling to MLC2 phosphorylation. Curr. Biol. 19, 668–674.

Adams, R.H., and Alitalo, K. (2007). Molecular regulation of angiogenesis and lymphangiogenesis. Nat. Rev. Mol. Cell Biol. 8, 464–478.

Blum, Y., Belting, H.G., Ellertsdottir, E., Herwig, L., Lüders, F., and Affolter, M. (2008). Complex cell rearrangements during intersegmental vessel sprouting and vessel fusion in the zebrafish embryo. Dev. Biol. 316, 312–322.

Bryant, D.M., Datta, A., Rodríguez-Fraticelli, A.E., Peränen, J., Martín-Belmonte, F., and Mostov, K.E. (2010). A molecular network for de novo generation of the apical surface and lumen. Nat. Cell Biol. 12, 1035–1045.

Bussmann, J., Wolfe, S.A., and Siekmann, A.F. (2011). Arterial-venous network formation during brain vascularization involves hemodynamic regulation of chemokine signaling. Development 138, 1717–1726.

Carmeliet, P., and Jain, R.K. (2011). Molecular mechanisms and clinical applications of angiogenesis. Nature 473, 298–307.

Chen, C.T., Hehnly, H., and Doxsey, S.J. (2012a). Orchestrating vesicle transport, ESCRTs and kinase surveillance during abscission. Nat. Rev. Mol. Cell Biol. 13, 483–488.

Chen, Q., Jiang, L., Li, C., Hu, D., Bu, J.W., Cai, D., and Du, J.L. (2012b). Haemodynamics-driven developmental pruning of brain vasculature in zebrafish. PLoS Biol. 10, e1001374.

Culver, J.C., and Dickinson, M.E. (2010). The effects of hemodynamic force on embryonic development. Microcirculation 17, 164–178.

Dejana, E. (2004). Endothelial cell-cell junctions: happy together. Nat. Rev. Mol. Cell Biol. 5, 261–270.

Dejana, E., and Giampietro, C. (2012). Vascular endothelial-cadherin and vascular stability. Curr. Opin. Hematol. 19, 218–223.

Draeger, A., Monastyrskaya, K., and Babiychuk, E.B. (2011). Plasma membrane repair and cellular damage control: the annexin survival kit. Biochem. Pharmacol. 81, 703–712.

Fededa, J.P., and Gerlich, D.W. (2012). Molecular control of animal cell cytokinesis. Nat. Cell Biol. 14, 440–447.

Gálvez-Santisteban, M., Rodriguez-Fraticelli, A.E., Bryant, D.M., Vergarajauregui, S., Yasuda, T., Bañón-Rodríguez, I., Bernascone, I., Datta, A., Spivak, N., Young, K., et al. (2012). Synaptotagmin-like proteins control the formation of a single apical membrane domain in epithelial cells. Nat. Cell Biol. 14, 838–849.

Gerhardt, H., Golding, M., Fruttiger, M., Ruhrberg, C., Lundkvist, A., Abramsson, A., Jeltsch, M., Mitchell, C., Alitalo, K., Shima, D., and Betsholtz, C. (2003). VEGF guides angiogenic sprouting utilizing endothelial tip cell filopodia. J. Cell Biol. 161, 1163–1177.

Herbert, S.P., and Stainier, D.Y. (2011). Molecular control of endothelial cell behaviour during blood vessel morphogenesis. Nat. Rev. Mol. Cell Biol. 12, 551–564.

Herwig, L., Blum, Y., Krudewig, A., Ellertsdottir, E., Lenard, A., Belting, H.G., and Affolter, M. (2011). Distinct cellular mechanisms of blood vessel fusion in the zebrafish embryo. Curr. Biol. 21, 1942–1948.

Isogai, S., Horiguchi, M., and Weinstein, B.M. (2001). The vascular anatomy of the developing zebrafish: an atlas of embryonic and early larval development. Dev. Biol. 230, 278–301.

Isogai, S., Lawson, N.D., Torrealday, S., Horiguchi, M., and Weinstein, B.M. (2003). Angiogenic network formation in the developing vertebrate trunk. Development 130, 5281–5290.

Jin, S.W., Beis, D., Mitchell, T., Chen, J.N., and Stainier, D.Y. (2005). Cellular and molecular analyses of vascular tube and lumen formation in zebrafish. Development 132, 5199–5209.

Khan, L.A., Zhang, H., Abraham, N., Sun, L., Fleming, J.T., Buechner, M., Hall, D.H., and Gobel, V. (2013). Intracellular lumen extension requires ERM-1-dependent apical membrane expansion and AQP-8-mediated flux. Nat. Cell Biol. 15, 143–156.

Kimmel, C.B., Ballard, W.W., Kimmel, S.R., Ullmann, B., and Schilling, T.F. (1995). Stages of embryonic development of the zebrafish. Dev. Dyn. 203, 253–310.

Lampugnani, M.G., Orsenigo, F., Gagliani, M.C., Tacchetti, C., and Dejana, E. (2006). Vascular endothelial cadherin controls VEGFR-2 internalization and signaling from intracellular compartments. J. Cell Biol. *174*, 593–604.

Lampugnani, M.G., Orsenigo, F., Rudini, N., Maddaluno, L., Boulday, G., Chapon, F., and Dejana, E. (2010). CCM1 regulates vascular-lumen organization by inducing endothelial polarity. J. Cell Sci. *123*, 1073–1080.

Montero-Balaguer, M., Swirsding, K., Orsenigo, F., Cotelli, F., Mione, M., and Dejana, E. (2009). Stable vascular connections and remodeling require full expression of VE-cadherin in zebrafish embryos. PLoS ONE *4*, e5772.

Nicoli, S., Standley, C., Walker, P., Hurlstone, A., Fogarty, K.E., and Lawson, N.D. (2010). MicroRNA-mediated integration of haemodynamics and Vegf signalling during angiogenesis. Nature *464*, 1196–1200.

Risau, W., and Flamme, I. (1995). Vasculogenesis. Annu. Rev. Cell Dev. Biol. *11*, 73–91.

Roostalu, U., and Strähle, U. (2012). In vivo imaging of molecular interactions at damaged sarcolemma. Dev. Cell *22*, 515–529.

Sato, Y., Poynter, G., Huss, D., Filla, M.B., Czirok, A., Rongish, B.J., Little, C.D., Fraser, S.E., and Lansford, R. (2010). Dynamic analysis of vascular morphogenesis using transgenic quail embryos. PLoS ONE *5*, e12674.

Sehnert, A.J., Huq, A., Weinstein, B.M., Walker, C., Fishman, M., and Stainier, D.Y. (2002). Cardiac troponin T is essential in sarcomere assembly and cardiac contractility. Nat. Genet. *31*, 106–110.

Strilić, B., Kucera, T., Eglinger, J., Hughes, M.R., McNagny, K.M., Tsukita, S., Dejana, E., Ferrara, N., and Lammert, E. (2009). The molecular basis of vascular lumen formation in the developing mouse aorta. Dev. Cell *17*, 505–515.

Totong, R., Schell, T., Lescroart, F., Ryckebüsch, L., Lin, Y.F., Zygmunt, T., Herwig, L., Krudewig, A., Gershoony, D., Belting, H.G., et al. (2011). The novel transmembrane protein Tmem2 is essential for coordination of myocardial and endocardial morphogenesis. Development *138*, 4199–4205.

Wacker, A., and Gerhardt, H. (2011). Endothelial development taking shape. Curr. Opin. Cell Biol. *23*, 676–685.

Wang, Y., Kaiser, M.S., Larson, J.D., Nasevicius, A., Clark, K.J., Wadman, S.A., Roberg-Perez, S.E., Ekker, S.C., Hackett, P.B., McGrail, M., and Essner, J.J. (2010). Moesin1 and Ve-cadherin are required in endothelial cells during in vivo tubulogenesis. Development *137*, 3119–3128.

Westerfield, M. (2000). The Zebrafish Book: A Guide for the Laboratory Use of Zebrafish *Danio rerio* (Eugene, OR: University of Oregon Press).

Xu, K., and Cleaver, O. (2011). Tubulogenesis during blood vessel formation. Semin. Cell Dev. Biol. *22*, 993–1004.

Xu, K., Sacharidou, A., Fu, S., Chong, D.C., Skaug, B., Chen, Z.J., Davis, G.E., and Cleaver, O. (2011). Blood vessel tubulogenesis requires Rasip1 regulation of GTPase signaling. Dev. Cell *20*, 526–539.

Zygmunt, T., Gay, C.M., Blondelle, J., Singh, M.K., Flaherty, K.M., Means, P.C., Herwig, L., Krudewig, A., Belting, H.G., Affolter, M., et al. (2011). Semaphorin-PlexinD1 signaling limits angiogenic potential via the VEGF decoy receptor sFlt1. Dev. Cell *21*, 301–314.

A.2. Santos E., et al. 2014

The evolution of cichlid fish egg-spots is linked with a *cis*-regulatory change

M. Emília Santos[1,†], Ingo Braasch[2], Nicolas Boileau[1], Britta S. Meyer[1,†], Loïc Sauteur[3], Astrid Böhne[1], Heinz-Georg Belting[3], Markus Affolter[3] & Walter Salzburger[1]

The origin of novel phenotypic characters is a key component in organismal diversification; yet, the mechanisms underlying the emergence of such evolutionary novelties are largely unknown. Here we examine the origin of egg-spots, an evolutionary innovation of the most species-rich group of cichlids, the haplochromines, where these conspicuous male fin colour markings are involved in mating. Applying a combination of RNAseq, comparative genomics and functional experiments, we identify two novel pigmentation genes, *fhl2a* and *fhl2b*, and show that especially the more rapidly evolving b-paralog is associated with egg-spot formation. We further find that egg-spot bearing haplochromines, but not other cichlids, feature a transposable element in the *cis*-regulatory region of *fhl2b*. Using transgenic zebrafish, we finally demonstrate that this region shows specific enhancer activities in iridophores, a type of pigment cells found in egg-spots, suggesting that a *cis*-regulatory change is causally linked to the gain of expression in egg-spot bearing haplochromines.

[1] Zoological Institute, University of Basel, Basel 4051, Switzerland. [2] Institute of Neuroscience, University of Oregon, Eugene, Oregon 97403-1254, USA. [3] Biozentrum, University of Basel, Basel 4056, Switzerland. † Present address: Institut de Génomique Fonctionnelle de Lyon, Ecole Normale Supérieure, CNRS UMR 5242, 46 Allée d'Italie, 69364 Lyon Cedex 07, France (M.E.S.); Evolutionary Ecology of Marine Fishes, GEOMAR Helmholtz Centre for Ocean Research Kiel, Düsternbrooker Weg 20, 24105 Kiel, Germany (B.S.M.). Correspondence and requests for materials should be addressed to M.E.S. (email: emilia.p.santos@gmail.com) or to W.S. (email: walter.salzburger@unibas.ch).

The *de novo* evolution of complex phenotypic traits poses a challenge to evolutionary biology[1–5]. While selection explains adaptation and speciation in an adequate manner[6], it is more difficult to conceive how selection would trigger the origin of evolutionary novelties such as insect wings, feathers, tetrapod limbs, flowers, the mammalian placenta, beetle horns or butterfly eye-spots[1,4,5,7,8]. The emergence of evolutionary innovations, that is, lineage-restricted traits linked to qualitatively new functions, involves the origin of new developmental modules that are responsible for the identity of these novel characters[4,5]. Most of the available evidence suggests that new developmental programs emerge largely through co-option of pre-existing regulatory gene networks via changes in their regulation and deployment ('old genes playing new tricks'[5]). Uncovering the mechanisms of how these developmental modules are co-opted or newly evolved is one of the primary goals of evo-devo research[2,3,5,7,8].

Anal fin egg-spots are an evolutionary innovation in the so-called 'haplochromines'[9] (Fig. 1a and Supplementary Fig. 1), the most species-rich group of cichlid fishes, best known for their spectacular adaptive radiations in the East African lakes Victoria and Malawi[10,11]. Adult males of ∼1,500 cichlid species feature this pigmentation trait in the form of conspicuously coloured circular markings[9,11,12]. Haplochromine egg-spots vary substantially in colour, shape, number and arrangement between species (Fig. 1b), and even within species a certain degree of variation is observed. In some species, also females show egg-spots, which are then much less pronounced and colourful. The

function of egg-spots has been implicated with the mating behaviour of the female-mouthbrooding haplochromines[12,13]. Immediately upon spawning, a haplochromine female gathers up her eggs into the mouth; the male then presents his egg-spots to which the female responds by snatching and bringing her mouth close to the male's genital opening; upon discharging sperm, the eggs become fertilized inside the female's mouth (Fig. 1c). The mother subsequently broods and carries her progeny in the oral cavities for several weeks after fertilization.

Here we are interested in the molecular basis of the anal fin egg-spots of haplochromine cichlids. The main advantages of the cichlid egg-spot system are that (i) the evolutionary innovation of interest emerged just a few million years ago and hence is recent compared with most other evolutionary novelties studied so far[9,10,14]; (ii) the phylogenetic context in which the novel trait evolved is known and living sister clades to the lineage featuring the novelty still exist[9,15,16]; and (iii) the genomes of two outgroup species lacking the trait and of three derived species featuring the trait are available. This allows us to study early events involved in the origin of an evolutionary innovation in an assemblage of phenotypically diverse, yet closely related and genetically similar species[14]. Using RNAseq, we identify two novel candidate pigmentation genes, the a- and b-paralogs of the four and a half LIM domain protein 2 (*fhl2*) gene, and show that both genes, but especially the more rapidly evolving b-copy, are associated with the formation of egg-spots. We then find that egg-spot bearing haplochromines—but not an egg-spot-less ancestral haplochromine and not the representatives from more basal
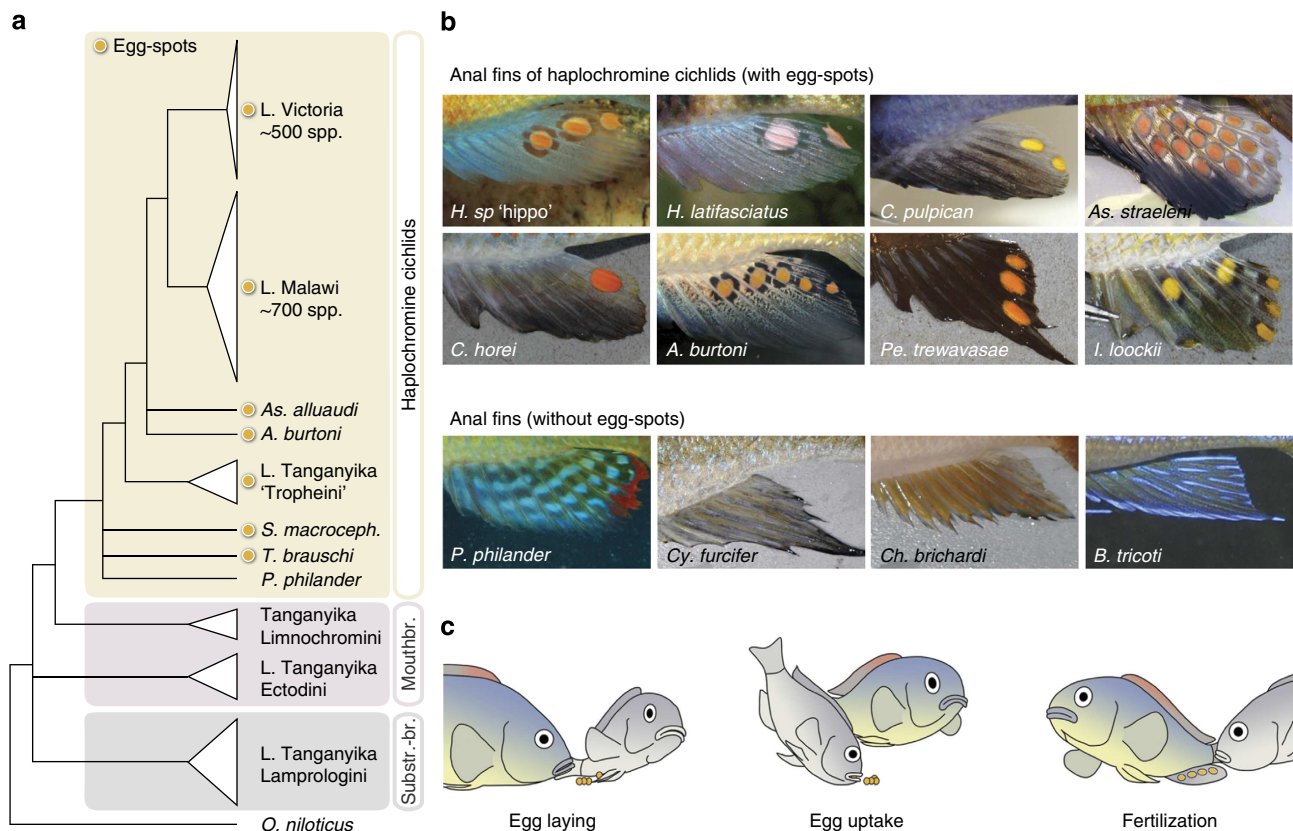
Figure 1 | The egg-spots of haplochromine cichlids. (**a**) Phylogeny of the East African cichlid fishes based on a new multimarker data set. The haplochromines are the most species-rich and derived group of cichlids in East Africa. One of the common features of haplochromines is the presence of egg-spots on the anal fin of males. Note that one of the ancestral lineages, represented here by *P. philander*, does not show this characteristic trait[9,33]. Substr-br, substrate brooders; mouthbr, mouthbrooders; spp.: species. (**b**) Examples of male anal fin patterns in East African cichlids. Haplochromine egg-spots (upper panel) vary in size, shape, number and colouration. Non-haplochromines and basal haplochromine *P. philander* (lower panel) do not show this trait. (**c**) A typical mating cycle of haplochromine cichlids.

cichlid lineages—exhibit a transposable element insertion in close proximity to the transcription initiation site of *fhl2b*. A functional assay with transgenic zebrafish reveals that only a haplochromine-derived genetic construct featuring the SINE (short interspersed repetitive element) insertion drove expression in a special type of pigment cells, iridophores. Together, our data suggest that a *cis*-regulatory change (probably in the form of a SINE insertion) is responsible for the gain of expression of *fhl2b* in iridophores, contributing to the evolution of egg-spots in haplochromine cichlids.

Results

fhl2 paralogs: novel candidates for egg-spot morphogenesis. As a first step, we performed an Illumina-based comparative transcriptomic experiment (RNAseq) between male (with egg-spots) and female (without egg-spots) anal fins in the haplochromine cichlid *Astatotilapia burtoni*. Two of the most differentially expressed genes according to RNAseq were the a- and b-paralogs of *fhl2* (~ 4 log$_2$-fold and ~ 5 log$_2$-fold differences, respectively; see Supplementary Table 2). These paralogs result from the teleost genome duplication[17] (Supplementary Fig. 2). The four and a half LIM domain protein 2 (Fhl2) is known as a transcriptional co-activator of the androgen receptor and the *Wnt*-signalling pathway[18,19]; Fhl2 plays a role in cell-fate determination and pattern formation, in the organization of the cytoskeleton, in cell adhesion, cell motility and signal transduction; furthermore, it regulates the development of heart, bone and musculature in vertebrates[20,21].

Expression of fhl2a and fhl2b is egg-spot specific. To confirm the results obtained by RNAseq, we performed quantitative real-time PCR (qPCR) experiments (Fig. 2a), this time also comparing egg-spot versus non-egg-spot tissue within male anal fins. In addition, we tested another haplochromine species, *Cynotilapia pulpican*, with a different egg-spot arrangement to exclude positional effects of gene expression on the anal fin. In both species, the two duplicates of *fhl2* were overexpressed in egg-spots (*A. burtoni*: *fhl2a*: $t_5 = 10.77$, $P = 0.0001$; *fhl2b*: $t_5 = 4.362$, $P = 0.0073$; *C. pulpican*: *fhl2a*: $t_4 = 5.031$, $P = 0.0073$; *fhl2b*: $t_4 = 9.154$, $P = 0.0008$). We then tested the expression of both *fhl2* paralogs in the four main developmental stages of egg-spot formation in *A. burtoni*[22] and compared it with other candidate pigmentation genes (including the previously identified xanthophore marker *csf1ra*, the melanophore marker *mitfa* and the iridophore marker *pnp4a*). We found that the expression of both *fhl2* paralogs increases substantially throughout anal fin and egg-spot development, and both genes showed higher expression levels compared with the other pigmentation genes (Fig. 2b); *fhl2b* shows the highest increase in expression exactly when egg-spots begin to form. Furthermore, we corroborate that the expression
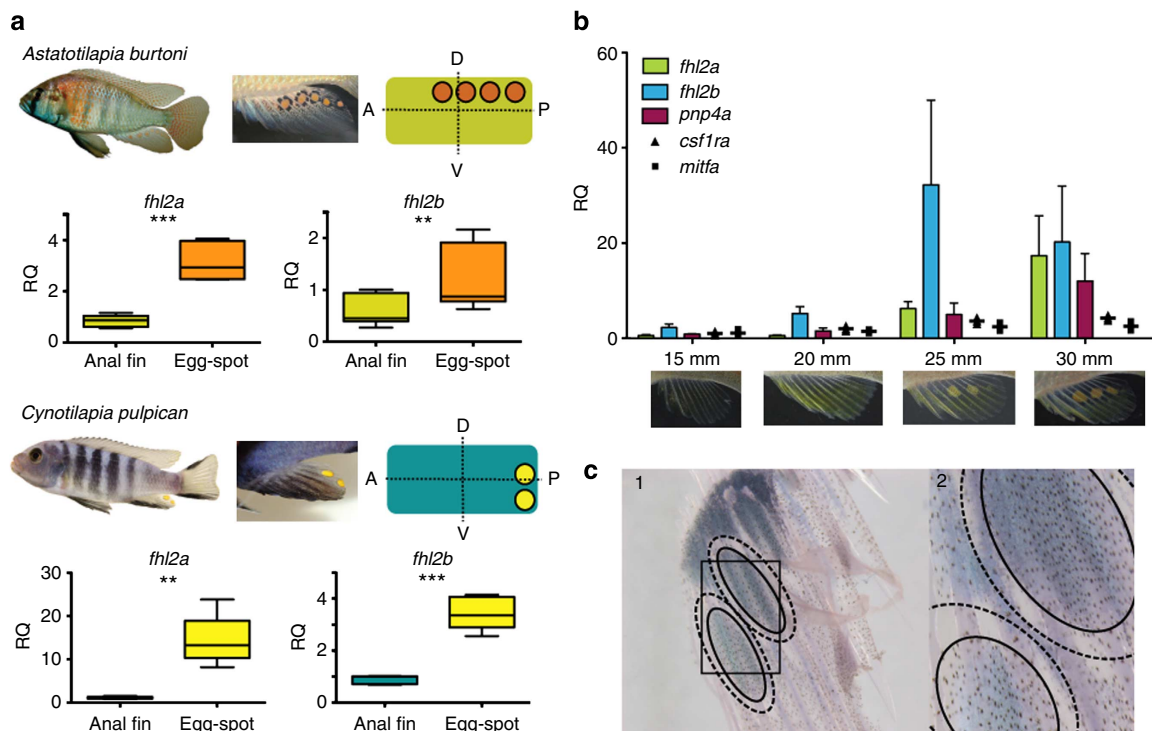
Figure 2 | The role of fhl2a and fhl2b in egg-spot formation. (a) qPCR experiments reveal that both genes are overexpressed in egg-spot compared with adjacent anal fin tissue in the haplochromine cichlids *A. burtoni* and *C. pulpican* (**P < 0.01; ***P < 0.001; RQ, relative quantity). Images of male fishes of the two species, their anal fins and a scheme showing the distribution of egg-spots are provided. **(b)** Expression profiles of *fhl2a* and *fhl2b* during the ontogenetic development of egg-spots in *A. burtoni* (note that egg-spots are absent in juveniles and only form when males become sexually mature; see ref. 22 for further details). The values on the *x* axis represent fish standard length in millimetres (three replicates per developmental stage were used). The error bars represent the s.e.m. *fhl2b* shows the largest increase in expression overall and its expression profile mimics the formation of egg-spots. Three other pigmentation genes (*pnp4a*, *csf1ra* and *mitfa*) were included for comparative reasons. *csf1ra* and *mitfa* show a much smaller increase in gene expression during egg-spot development than *fhl2a* and especially *fhl2b*, while *pnp4a* shows a constant increase in gene expression throughout the development of egg-spots. **(c)** RNA *in situ* hybridization experiments revealed that both *fhl2* paralogs (results only shown for *fhl2b*) are primarily expressed in the colourful inner circle of haplochromine egg-spots (defined by the solid line) and not in the transparent outer ring (defined by the dashed line). Expression was also observed in the proximal fin region, which also contains pigment cells. Panel 2 is a close-up from the region defined by the square in panel 1.

domain of both *fhl2a* and *fhl2b* matches the conspicuously coloured inner circle of egg-spots with RNA *in situ* hybridization (see Fig. 2c for results on *fhl2b*).

fhl2a and fhl2b evolved under purifying selection. In general, phenotypic differences can arise via mutations affecting the function of proteins or via changes in gene regulation[5]. Therefore, we examined coding sequence evolution in the two *fhl2* paralogs to test for positive selection and potential change of function in a phylogenetically representative set of 26 East African cichlids. We found that the two *fhl2* genes are highly conserved in cichlids, with few amino-acid differences between species and an average genetic divergence (0.4% in *fhl2a* and 0.7% in *fhl2b*) that lies below the transcriptome-wide average of 0.95% (ref. 23). None of the observed amino-acid changes was correlated with the egg-spot phenotype (Supplementary Table 7).

Greater functional specialization of fhl2b in haplochromines. Usually, after a gene duplication event, the duplicates go through a period of relaxed selection, during which one of the two copies can diversify and acquire new functions[24]. We found that the b-copy of *fhl2* shows an elevated rate of molecular evolution compared with its paralog (*fhl2a*), which more closely resembles the ancestral sequence (Fig. 3a). An additional series of qPCR experiments in 12 tissues revealed that, in cichlids, *fhl2a* is primarily expressed in heart, bony structures and muscles, whereas *fhl2b* is highly expressed in the eye, and further in skin and the egg-spots of haplochromines (Fig. 3b,c). This is different to the gene expression profiles in medaka, where both duplicates are highly expressed in heart, skin and eye tissues; and in zebrafish, where the two paralogs are primarily expressed in heart, eye and (pharyngeal) jaw tissues, with *fhl2a* showing rather low levels of gene expression (Supplementary Figs 3 and 4). When compared with the other teleost fishes examined here, our results suggest that the haplochromine *fhl2a* retained most of the previously described functions, whereas the more rapidly evolving *fhl2b* obtained new expression patterns. Together, the gene expression profile and the pattern of sequence evolution make *fhl2b* a prime candidate gene for the morphogenesis of haplochromine egg-spots.

fhl2b shows an AFC-SINE insertion in species with egg-spot. Since there were no changes in the coding regions of *fhl2a* and *fhl2b* that are specific to the egg-spot bearing haplochromines, we shifted our focus towards the analysis of putative regulatory elements, exploring the recently available genomes of five East African cichlids (including the egg-spot bearing haplochromines *A. burtoni*, *Pu. nyererei*, *Metriaclima zebra* and the egg-spot-less non-haplochromines *Neolamprologus brichardi* and *Oreochromis niloticus*). The non-coding region of *fhl2a* shows homology with other teleosts (*Oryzias latipes*, *Takifugu rubripes*, *Tetraodon nigroviridis* and *Gasterosteus aculeatus*) and we identified four conserved non-coding elements (CNEs) in all species examined (Supplementary Fig. 5a). These CNEs might thus represent conserved regulatory regions responsible for ancestral conserved functions of *fhl2a* in teleosts. We might be missing cichlid-specific regulatory regions in important upstream regions although, as our capacity to detect lineage-specific enhancers is limited owing to the small sample size for each lineage and the high background conservation level present in cichlids.

Concerning *fhl2b*, we did not find any CNE that is shared by cichlids and other teleosts (Supplementary Fig. 5b). Strikingly, however, we found a major difference that is shared by the three egg-spot bearing haplochromines: the presence of a transposable element upstream of *fhl2b*. Specifically, we identified a SINE

belonging to the cichlid-specific AFC-SINEs (African cichlid family of SINEs[25]), which inserted ~800-bp upstream of the transcriptional start site of *fhl2b* (Supplementary Fig. 6). To confirm that this insertion is associated with the egg-spot phenotype, we sequenced the upstream region of *fhl2b* in 19 cichlid species. The insertion was indeed present in nine additional, egg-spot bearing haplochromine species, yet absent in all 10 non-haplochromines examined (Supplementary Table 8). Importantly, we found that one haplochromine species lacks the AFC-SINE element, namely *P. philander*. This species belongs to one of the basal lineage of haplochromines (Fig. 1a), which is characterized by the absence of egg-spots (Fig. 1b). This suggests that the AFC-SINE upstream of *fhl2b* is not characteristic to the entire haplochromine clade, but to those that feature egg-spots, thus linking the SINE insertion to the origin of this evolutionary innovation.

Haplochromine fhl2b regulatory region drives iridophore expression. A long-standing hypothesis proposes that ubiquitous genomic repeat elements are potential regulators of transcription, and could thereby generate evolutionary variations and novelties[26,27]. SINEs are known for their capability of 'transcriptional rewiring', that is, to change the expression patterns of genes by bringing along new regulatory sequences when inserted in close proximity to a gene's transcriptional initiation site[7,28]. In order to test whether the insertion of an AFC-SINE close to *fhl2b* functions as an enhancer of gene expression, we aimed for a functional experiment. We were particularly interested to find out whether there were changes in enhancer activity between AFC-SINE-positive haplochromines and other cichlids lacking both the insertion and the egg-spot phenotype. To this end, we designed reporter constructs containing the upstream region of *fhl2b* (~2 kb upstream to intron 1) of three cichlid species linked to the coding region of green fluorescent protein (GFP), and injected these constructs into zebrafish (*Danio rerio*) embryos to generate transgenic lines. We switched to the zebrafish system here, as no functioning transgenesis was available for haplochromine cichlids at the time the study was performed (owing to the small number of eggs per clutch associated with the characteristic female-mouthbrooding behaviour). The three constructs were derived from *A. burtoni* (haplochromine with egg-spots, AFC-SINE⁺), *P. philander* (haplochromine without egg-spots, AFC-SINE⁻) and *N. sexfasciatus* (lamprologine, AFC-SINE⁻), respectively (Fig. 4a).

We were able to produce stable transgenic zebrafish lines for each of the three constructs to examine the expression of GFP. Importantly, we found striking differences in expression between the *A. burtoni* construct and the two constructs lacking the AFC-SINE. Of the three reporter lines, only the AFC-SINE⁺ showed GFP expression in iridophores, a silvery-reflective type of pigment cells (Fig. 4b,c and Supplementary Fig. 7). This experiment demonstrates the presence of novel enhancer activities in the regulatory region of *fhl2b* in derived haplochromines and strongly suggests that these came along with the SINE insertion.

Iridophores and egg-spot development. The egg-spot phenotype has previously been associated with pigment cells containing pteridines (xanthophores)[16,22], whereas our new results indicate an auxiliary role of iridophores in egg-spot formation. We thus re-evaluated the adult egg-spot phenotype by removing the pteridine pigments of the xanthophores (Fig. 4e). We indeed found that *A. burtoni* egg-spots show a high density of iridophores, which is further corroborated by the increase in gene expression of the iridophore marker *pnp4a* during egg-spot
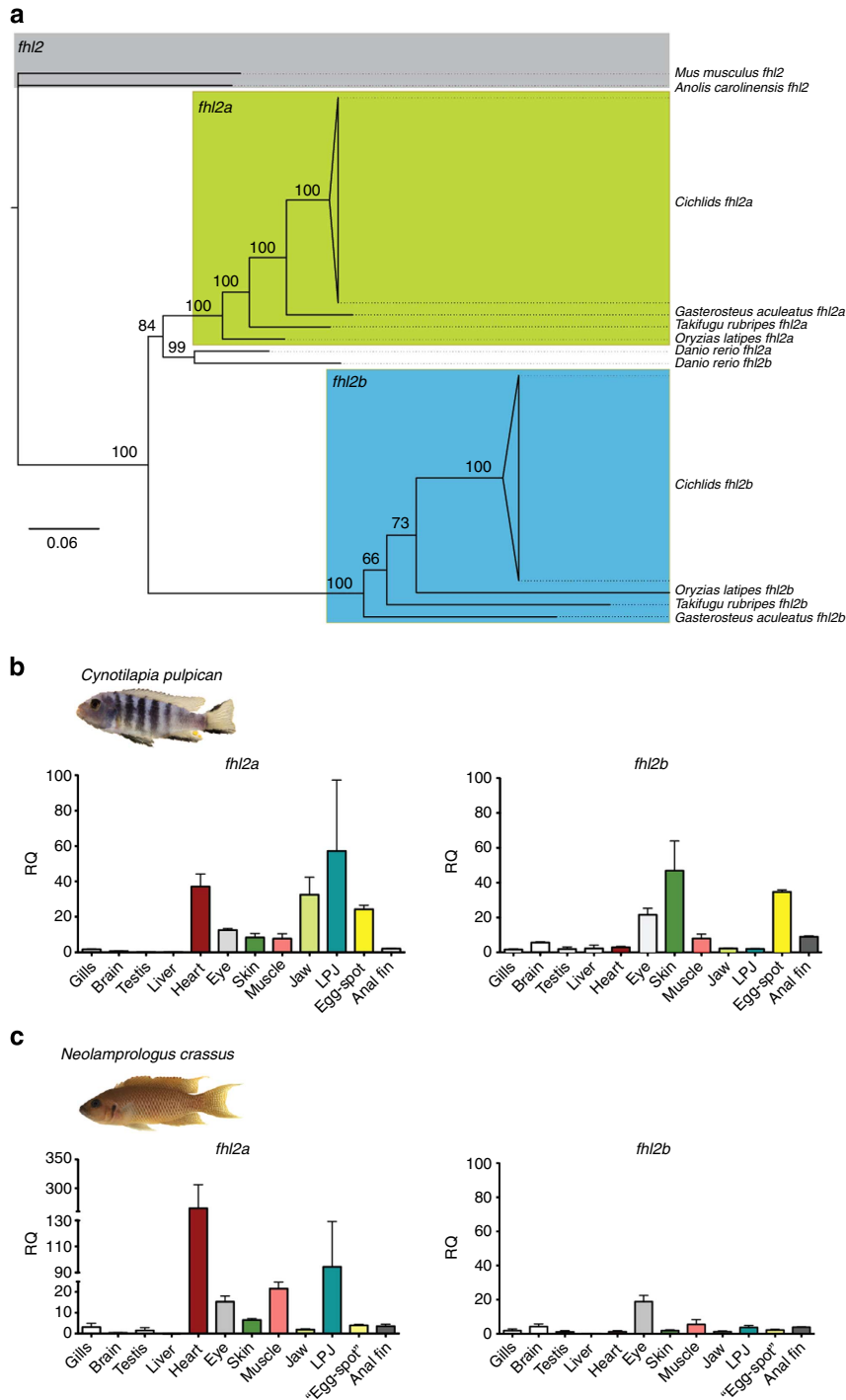
Figure 3 | Gene tree of the two *fhl2* paralogs and expression profiling in East African cichlid fishes. (**a**) Bayesian inference phylogeny of the orthology and paralogy relationships between cichlids, other teleosts (*O. latipes*, *D. rerio*, *Ta. rubripes* and *G. aculeatus*) and tetrapods (*Anolis carolinensis* and *Mus musculus*) *fhl2* sequences. This gene tree is important for generating functional hypotheses about both duplicates, and to infer the ancestral state of the *fhl2* gene before duplication. Our phylogeny indicates that *fhl2a* is more similar to the ancestral state, while *fhl2b* is apparently evolving faster in teleosts. Values at the tree nodes represent posterior probabilities. In Supplementary Fig. 2, we present a synteny analysis supporting the origin of teleost *fhl2* duplicates in the teleost genome duplication. (**b**) Relative quantity (RQ) of *fhl2a* and *fhl2b* gene expression in 12 tissues (three replicates per tissue) in *C. pulpican*, an egg-spot bearing haplochromine from Lake Malawi. The error bars represent the s.e.m. (**c**) RQ of *fhl2a* and *fhl2b* gene expression in 12 tissues in *N. crassus*, a substrate spawning lamprologine that has no egg-spots. In both species, gill tissue was used as reference; in *N. crassus*, 'egg-spots' corresponds to the fin region where haplochromines would show the egg-spot trait. In *C. pulpican* (**b**), *fhl2a* is highly expressed in heart, in pigmented tissues (eye, skin and egg-spot) and in craniofacial traits (oral jaw and lower pharyngeal jaw); *fhl2b* is mainly expressed in the pigmented tissues. *N. crassus* (**c**) shows a similar expression patterns for *fhl2a* and *fhl2b*, with the difference that *fhl2a* does not show high expression levels in jaw tissues, and *fhl2b* is not highly expressed in skin and fin tissue. These results suggest that *fhl2b* shows a higher functional specialization, and that it might be involved in the morphogenesis of sexually dimorphic traits such as pigmented traits including egg-spots. LPJ, lower pharyngeal jaw bone.
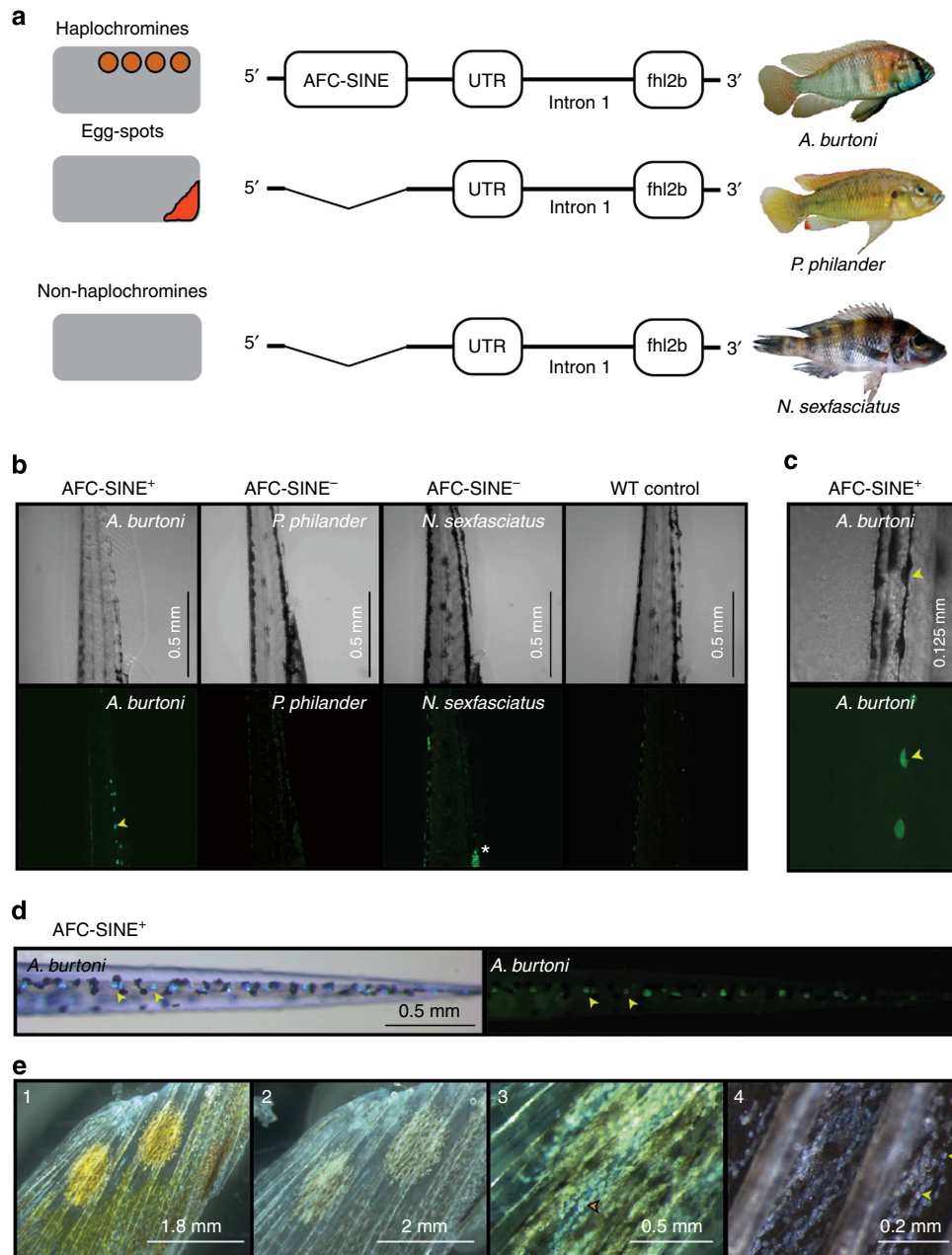
Figure 4 | The molecular basis of egg-spot formation. (**a**) The egg-spot bearing haplochromines feature an AFC-SINE insertion in close proximity to the transcriptional start site of *fhl2b*, which is absent in the ancestral and egg-spot-less genus *Pseudocrenilabrus* and in all non-haplochromines. The sequences from the three species shown here were the ones used to engineer the reporter constructs, where the *fhl2b* coding sequence was substituted by GFP. (**b**) In transgenic zebrafish, only the AFC-SINE$^+$ construct showed GFP expression in the iridophores, a type of pigment cells (one of them is indicated by a yellow arrow). The upper panel depicts bright-field images of 3-day-old zebrafish embryo trunks; the lower panel shows the respective embryos under ultraviolet light. The green signal in the AFC-SINE negative *N. sexfasciatus* line (marked with an asterisk) is auto-fluorescence from the yolk extension. (**c**) Higher magnification image from *A. burtoni* AFC-SINE$^+$ reporter construct driving GFP expression in the iridophores. Orientation in **b**,**c**: bottom: anterior, top: posterior. (**d**) Top-down view of a trunk of a 3-day-old AFC-SINE-positive zebrafish embryo. The left panel depicts a bright-field image where the iridophores of the dorsal stripe are illuminated by the incident light (yellow arrows). The right panel depicts GFP expression of the same embryo. The GFP signal co-localizes with iridophores. (**e**) Cellular basis of egg-spots: this series of images shows that egg-spots are made up of xanthophores, iridophores and scattered melanophores. Image 1 shows an *A. burtoni* fin with two egg-spots. Image 2 shows the same fin without pteridine pigments (xanthophores are not visible anymore). Images 3 and 4 are higher magnification images of the egg-spots without pteridine under slightly different light conditions confirming that egg-spots have a high density of iridophores (examples of this cell type are highlighted with arrows). UTR, untranslated region.

formation (Fig. 2b). With the exception of the proximal region of the anal fin, the number of iridophores is greatly reduced in the fin tissue surrounding egg-spots (Supplementary Fig. 8a). Interestingly, this proximal region is the only area of the anal fin besides the egg-spots where we observed *fhl2* expression with

RNA *in situ* hybridization (see Fig. 2c for *fhl2b*), once more linking *fhl2* expression with iridophores (and less so with xanthophores, which are very rare in this region). In the non-haplochromine *N. crassus*, which features a yellow anal fin pattern containing xanthophores, we did not find iridophores in

the xanthophore-rich region (Supplementary Fig. 9), suggesting that the xanthophore/iridophore pattern is unique to haplochromine egg-spots. Importantly, we also observed that iridophores appear early in the newly forming egg-spot of haplochromines, that is, before the first xanthophores start to aggregate (Supplementary Fig. 8b).

In zebrafish, stripe development is initiated by iridophores, which serve as morphological landmarks for stripe orientation in that they attract further pigment cells such as xanthophores by expressing the *csf1* ligand gene[29,30]. Interestingly, it has previously been shown that a gene encoding a Csf1 receptor known for its role in xanthophore development in zebrafish, *csf1ra*, is expressed in haplochromine egg-spots[16]. We thus examined the expression of the ligand *csf1b* and show that its relative level of gene expression doubles during egg-spot development, and that this increase coincides with the emergence of the phenotype (Supplementary Fig. 10). This leads us to suggest that a similar pigment cell type interaction mechanism might be involved in egg-spot patterning as the one described for zebrafish[29,30]. The specific mode of action of fin patterning in haplochromine cichlids, and how Fhl2b interacts with the Csf1/Csf1r system, remains to be studied in the future.

Contribution of *fhl2a* in egg-spot formation. The role of the more conserved and functionally constrained a-paralog of *fhl2* in egg-spot development cannot be dismissed. Its temporally shifted increase in gene expression compared with *fhl2b* (Fig. 2b) suggests that *fhl2a* most likely acts as a more downstream factor involved in pigment pattern formation. We were nevertheless interested in uncovering the regulatory region responsive for this expression pattern. The first intron of *fhl2a* shows two CNEs that are common across percomorph fish (Supplementary Fig. 5). Using the same strategy as described above, we generated a transgenic zebrafish line containing exon 1 and intron 1 of *A. burtoni* linked to GFP. This construct drove expression in heart in zebrafish embryos, which is consistent with the reported function of *fhl2a* in tetrapods[20], whereas there was no indication of a pigment cell related function for this reporter construct (Supplementary Fig. 7e). An alignment between the genomic regions of the two *fhl2* paralogs shows that there were no CNEs in common and generally very little homology between them, suggesting that the regulation of the expression of *fhl2a* in egg-spots might proceed in a different way (Supplementary Fig. 11).

Discussion

In this study, we were interested in the genetic and developmental basis of egg-spots, an evolutionary innovation of the most species-rich group of cichlids, the haplochromines, where these conspicuous colour markings on the anal fins of males play an important role in mating[11–13] (Fig. 1).

We first performed a comparative RNAseq experiment that led to the identification of two novel candidate pigmentation genes, the a- and b-paralogs of the four and a half LIM domain protein 2 (*fhl2*) gene. We then confirmed, with qPCR and RNA *in situ* hybridization, that the expression domain of both duplicates indeed matches the conspicuously coloured inner circle of egg-spots (Fig. 2). Especially the more rapidly evolving b-copy of *fhl2* emerged as strong candidate gene for egg-spot development, as its expression profile mimics the formation of egg-spots (Figs 2b and 3). Interestingly, we found that the egg-spot bearing haplochromines, but not other cichlids, feature a transposable element in the *cis*-regulatory region of *fhl2b*. Finally, making use of transgenic zebrafish, we could show that a *cis*-regulatory change in *fhl2b* in the ancestor of the egg-spot bearing haplochromine cichlids (most likely in the form of the AFC-SINE insertion)

resulted in a gain of expression in iridophores, a special type of pigment cells found in egg-spots (Fig. 4). This in turn might have led to changes in iridophore cell behaviour and to novel interactions with pigmentation genes (*csf1b*, *csf1ra* and *pnp4a*), thereby contributing to the formation of egg-spots on male anal fins. The specific mode of action of the SINE insertion, and how the *fhl2b* locus interacts with these other pigmentation genes remains elusive at present. Addressing these questions would require functional studies in haplochromines, which are, however, hampered by the specific mechanisms involved in the trait complex of interest (mouthbrooding makes it notoriously difficult to obtain enough eggs—in a controlled manner—to make such experiments feasible).

Our results are also suggestive of an important role of the a-copy of *fhl2* in cichlid evolution. With our qPCR experiments, we provide strong evidence that *fhl2a* is involved in jaw tissue in zebrafish (Supplementary Fig. 3) and, importantly, in the pharyngeal jaw apparatus of cichlids (Fig. 3b,c), another putative evolutionary innovation of this group. The pharyngeal jaw apparatus is a second set of jaws in the pharynx of cichlids that is functionally decoupled from the oral jaws and primarily used to process food[11,12,15]. Interestingly, *fhl2a* has previously been implicated in the evolution of fleshy lips in cichlids[31], which is yet another ecologically relevant trait. From a developmental perspective, the main tissues underlying these traits—the cranio-facial cartilage (the jaw apparatus) and pigment cells (egg-spots)—have the same origin, the neural crest, which itself is considered an evolutionary key innovation of vertebrates[32]. It thus seems that the function of *fhl2* in cichlids may have been split into (a) an ecologically important, that is, naturally selected, scope of duties, and (b) a role in colouration and pigmentation more likely to be targeted by sexual selection.

Taken together, our study permits us to propose the following hypothesis for the origin of cichlid egg-spots: In one of the early, already female-mouthbrooding, haplochromines the insertion of a transposable element of the AFC-SINE family in the *cis*-regulatory region of *fhl2b*, and its associated recruitment to the iridophore pigment cell pathway, mediated the evolution of egg-spots on the anal fins—possibly from the so-called *perfleckmuster* common to many cichlids[16]. The conspicuous anal fin spots were fancied by haplochromine females, which—just like many other cichlids and also the ancestral and egg-spot-less haplochromine genus *Pseudocrenilabrus*—have an innate bias for yellow/orange/red spots that resemble carotenoid-rich prey items[33], leading to the fixation of the novel trait. In today's haplochromines, egg-spots seem to have a much broader range of functions related to sexual selection[34].

Most of the currently studied evolutionary innovations comprise relatively ancient traits (for example, flowers, feathers, tetrapod limb, insect wings and mammalian placenta), thereby making it difficult to scrutinize their genetic and developmental basis. Here we explored a recently evolved novelty, the anal fin egg-spots of male haplochromine cichlids. We uncovered a regulatory change in close proximity to the transcriptional start site of a novel iridophore gene that likely contributes to the molecular basis of the origin of egg-spots in the most rapidly diversifying clade of vertebrates. This, once more, illustrates the importance of changes in *cis*-regulatory regions in morphological evolution[2].

Methods

issued by the cantonal veterinary office Basel). Individuals of all other specimens were collected in the southern region of Lake Tanganyika (Zambia) under the permission of the Lake Tanganyika Unit, Department of Fisheries, Republic of Zambia, and processed in the field following our standard operating procedure[15]. Tissues for RNA extraction were stored in RNAlater (Ambion, USA), and tissues for genomic DNA extraction were stored in ethanol and shipped to the University of Basel.

RNA and DNA extractions. Isolation of RNA was performed according to the TRIzol protocol (Invitrogen, USA) after incubating the dissected tissues in 750 µl of TRIzol at 4 °C overnight or, alternatively, for 8–16 h (in order to increase the RNA yield after long-term storage). The tissues were then homogenized with a Bead-Beater (FastPrep-24; MP Biomedicals, France). Subsequent DNase treatment was performed with DNA-Free kit (Ambion). RNA quantity and quality was determined with a NanoDrop 1000 spectrophotometer (Thermo Scientific, USA). cDNA was produced using the High Capacity RNA-to-cDNA kit (Applied Biosystems, USA). Genomic DNA was extracted using a high salt extraction method (modified from ref. 35).

Phylogenetic analyses. DNA extraction of 18 specimens of East African cichlid fishes was conducted as described above. For the amplification of nine nuclear markers (*rag, gapdhs, s7, bmp4, ednrb1, mitfa, tyr, hag* and *csfr1*), we used the primer sets published in ref. 36. The sequences of *M. zebra, O. niloticus* and *N. brichardi* were extracted from the respective genome assemblies (http://www.broadinstitute.org/models/tilapia). The data for *Astatoreochromis alluaudi, Thoracochromis brauschi* and *Serranochromis macrocephalus* were collected with Sanger sequencing following the method described in ref. 36, all other data were generated by amplicon sequencing with 454 GS FLX system at Microsynth, Switzerland, following the manufacturer's protocols[37,38]. Sequences were quality filtered using PRINSEQ (length: 150 bp minimum; low quality: mean ≥ 15; read duplicates)[39] and assembled with Burrows-Wheeler Aligner, Smith-Waterman alignment (BWA-SW) followed by visual inspection and consensus sequence generation in Geneious 6.1.6 (ref. 40). As a tenth marker, we included mitochondrial NADH dehydrogenase subunit 2 (ND2) sequences available on GenBank (see Supplementary Table 1 for accession numbers). Since the *ednrb1* gene sequence is not available in the *N. brichardi* genome assembly, we used the gene sequence from its sister species, *N. pulcher*, instead.

Sequences were aligned with MAFFT[41] and the most appropriate substitution model of molecular evolution for each marker was determined with JMODELTEST v2.1.3 (ref. 42) and BIC[43]. The partitioned data set (5,051 bp) was then subjected to phylogenetic inference in MRBAYES v3.2.1 (ref. 44) and GARLI v2.0 (ref. 45). MRBAYES was run for 10,000,000 generations with two runs and four chains in parallel and a burn-in of 25%, GARLI was run 50 times followed by a bootstrap analysis with 500 replicates. SUMTREES v3.3.1 of the DENDROPY package v3.12.0 (ref. 46) was used to summarize over the replicates and to map bootstrap values to the ML topology.

Differential gene expression analysis using RNAseq. We used a transcriptomic approach (RNAseq) to identify genes differentially expressed between male and female anal fins of *A. burtoni*. Library construction and sequencing of RNA extracted from three male and three female anal fins (at the developmental stage of 30 mm; Fig. 2) was performed at the Department of Biosystems Science and Engineering, University of Basel and ETH Zurich. The samples were sequenced on an Illumina Genome Analyzer IIx. Each sample was sequenced in one lane and with a read length of 76 bp.

The reads were then aligned to an embryonic *A. burtoni* reference transcriptome assembled by Broad Institute (http://www.broadinstitute.org/models/tilapia). This transcriptome is not annotated and each transcript has a nomenclature where the first term codes for the parent contig and the third term codes for alternatively spliced transcripts (CompX_cX_seqX). The reference transcriptome was indexed using NOVOINDEX (www.novocraft.com) with default parameters. Using NOVOALIGN (www.novocraft.com), the RNAseq reads were mapped against the reference transcriptome with a maximum alignment (*t*) score of 30, a minimum of good-quality base pair per read (*l*) of 25 and a successive trimming factor (*s*) of 5. Reads that did not match these criteria were discarded. Since the reference transcriptome has multiple transcripts/isoforms belonging to the same gene, all read alignment locations were reported (rALL). The mapping results were reported (o) in SAM format. The output SAM file was then transformed into BAM format, sorted, indexed and converted to count files (number of reads per transcript) using SAMTOOLS version 0.1.18 (ref. 47). The count files were subsequently concatenated into a single data set—count table—and analysed with the R package EDGER[48] in order to test for significant differences in gene expression between male and female anal fins. The 10 most differentially expressed transcripts were identified by BLASTx[49] against GenBank's non-redundant database (Supplementary Table 2).

We selected two genes out of this list for in-depth analyses—*fhl2a* and *fhl2b*—for the following three reasons: (i) *fhl2b* was the gene showing the highest difference in expression between male and female anal fins; (ii) the difference in gene expression in its paralog, *fhl2a*, was also significantly high; and (iii) the

functional repertoire of the Fhl2 protein family indicates that these might be strong candidates for the morphogenesis of a secondary male colour trait.

Differential gene expression analysis using qPCR. The expression patterns of *fhl2a* and *fhl2b* were further characterized by means of qPCR in three species, *A. burtoni, C. pulpican* and *N. crassus*. The comparative cycle threshold method[50] was used to calculate differences in expression between the different samples using the ribosomal protein L7 (*rpl7*) and the ribosomal protein SA3 (*rpsa3*) as endogenous controls. All reactions had a final cDNA concentration of 1 ng µl^{-1} and a primer concentration of 200 mM. The reactions were run on a StepOnePlusTM Real-Time PCR system (Applied Biosystems) using the SYBR Green master mix (Roche, Switzerland) with an annealing temperature of 58 °C and following the manufacturer's protocols. Primers were designed with the software GenScript Real-Time PCR (Taqman) Primer Design available at https://www.genscript.com/ssl-bin/app/primer. All primers were designed to span over exons to avoid gDNA contamination (see Supplementary Table 3 for details). Primer efficiencies of the experimental primers (*fhl2a* and *fhl2b*) were comparable to the efficiency of the endogenous controls *rpl7* and *rpsa3*.

We conducted the following experiments: qPCR experiment 1: Egg-spots were separated from the anal fin tissue in six male *A. burtoni* and five male *C. pulpican*. Relative quantity values were calculated for each sample, and the differential expression between anal fin (reference) and egg-spot tissue was analysed with a paired *t*-test using GraphPad Prism version 5.0a for Mac OS X (www.graphpad.com). qPCR experiment 2: *fhl2a, fhl2b, csf1ra, mitfa, pnp4a* and *csf1b* expression was measured in RNA extracted from *A. burtoni* fins at four different developmental stages[22]. Here, *csf1ra* was included as xanthophore marker[16], *mitfa* and *pnp4a* as melanophore and iridophore markers[51], respectively, and *csf1b* because of its role in pigment pattern organization in zebrafish[29,30]. We used three biological replicates for each developmental stage, and each replicate consisted of a sample pool of three fins, except for the youngest stage at 15 mm, where we pooled five fins. The first developmental stage was used as reference tissue. qPCR experiment 3: *fhl2a* and *fhl2b* expression was measured in RNA extracted from different tissues from three males from *C. pulpican* and *N. crassus* (gills, liver, testis, brain, heart, eye, skin, muscle, oral jaw, pharyngeal jaw and egg-spot). Although *N. crassus* does not have egg-spots, we separated its anal fin into an area corresponding to egg-spots in haplochromines and a section corresponding to anal fin tissue (the 'egg-spot' region was defined according to the egg-spot positioning in *A. burtoni*). Expression was compared among tissues for each species using gills as reference tissue. The same experiment was performed for *D. rerio* and *O. latipes* (two teleost outgroups), using *ef1a* and *rpl13a* (ref. 52), as well as *rpl7* and *18sRNA* (ref. 53) as endogenous controls, respectively.

Cloning of *fhl2a* and *fhl2b* and RNA *in situ* hybridization. *A. burtoni fhl2a* and *fhl2b* coding fragments were amplified by PCR (for primer information, see Supplementary Table 3) using Phusion Master Mix with High Fidelity buffer (New England BioLabs, USA) following the manufacturer's guidelines. These fragments were cloned into pCR4-TOPO TA vector using the TOPO TA cloning kit (Invitrogen). Plasmid extractions were done with GenElute Plasmid Miniprep Kit (Sigma-Aldrich). RNA probes were synthetized with the DIG RNA labelling kit (SP6/T7) (Roche). The insertion and direction of the fragments was confirmed by Sanger sequencing using M13 primers (available with the cloning kit) and BigDye terminator reaction chemistry (Applied Biosystems) on an AB3130xl Genetic Analyzer (Applied Biosystems). *In situ* hybridization was performed in 12 fins from *A. burtoni* males, six for *fhl2a* and six for *fhl2b*. The protocol was executed as described in ref. 16, except for an intermediate proteinase *K* treatment (20 min at a final concentration of 15 µg ml^{-1}) and for the hybridization temperature (65 °C).

Synteny analysis of teleost *fhl2* paralogs. The Synteny Database (http://synteny-db.uoregon.edu[54]) was used to generate dotplots of the human *FHL2* gene (ENSG00000115641) region on chromosome Hsa2 and the genomes of medaka (Supplementary Fig. 2a) and zebrafish (Supplementary Fig. 2b). Double-conserved synteny between the human *FHL2* gene and the *fhl2a* and *fhl2b* paralogons in teleost genomes provide evidence that the teleost *fhl2* paralogs were generated during the teleost genome duplication.

***fhl2a/fhl2b* coding region sequencing and analysis.** We then used cDNA pools extracted from anal fin tissue to amplify and sequence the coding region of *fhl2a* and *fhl2b* in a phylogenetically representative set of 26 cichlid species (21 Tanganyikan species, three species from Lake Malawi and two species from the Lake Victoria basin). This taxon sampling included 14 species belonging to the haplochromines and 12 species belonging to other East African cichlid tribes not featuring the egg-spot trait (Supplementary Table 4). *fhl2a* and *fhl2b* coding regions were fully sequenced (from start to stop codon) in five individuals per species in order to evaluate the rate of molecular evolution among cichlids. For PCR amplification, we used Phusion Master Mix and cichlid-specific primers (for primer information, see Supplementary Table 3) designed with Primer3 (ref. 55). PCR products were visualized with electrophoresis in a 1.5% agarose gel using GelRed (Biotium, USA). In cases where multiple bands were present, we purified the correct size fragment from the gel using the GenElute Gel Extraction Kit (Sigma-

Aldrich). PCR products were enzymatically cleaned with ExoSAP-IT (Affymetrix, USA) and sequenced with BigDye 3.1 Ready reaction mix (Applied Biosystems)—after BigDye XTerminator purificaton (Applied Biosystems)—on an AB3130xl Genetic Analyzer. Sequences were corrected, trimmed and aligned manually in CODONCODE ALIGNER (CodonCode Corporation).

fhl2 phylogenetic analysis. *fhl2a* and *fhl2b* sequences from non-cichlid teleosts and *fhl2* sequences from tetrapods were retrieved from ENSEMBL[56] (species names, gene names and accession numbers are available in Supplementary Table 5). We then constructed gene trees based on these sequences and on a subset of the cichlid sequences obtained in the previous step (information available in Supplementary Table 4) in order to confirm the orthologous and paralogous relationships of both duplicates. Sequences were aligned with CLUSTALW2 (ref. 57) using default parameters. The most appropriate model of sequence evolution was determined with JMODELTEST as described above. Phylogenetic analyses were performed with MRBAYES (1 million generations; 25% burn-in).

Tests for positive selection in fhl2a and fhl2b. Using PAUP* 4.0b10 (ref. 58), we first compiled a maximum likelihood tree based on the mitochondrial *ND2* gene, including all species used for the positive selection analyses (see Supplementary Table 6 for species and GenBank accession numbers). We used the GTR + Γ model with base frequencies and substitution rate matrix estimated from the data (as suggested by JMODELTEST[42]). We then ran CODEML implemented in PAML version 4.4b to test for branch-specific adaptive evolution in *fhl2a* and *fhl2b* applying the branch-site model (free-ratios model with ω allowed to vary)[59,60]. The branch comparisons and results are shown in Supplementary Table 7.

Identification of CNEs. We then made use of the five available cichlid genomes[61] to identify CNEs that could explain the difference in expression of *fhl2a* and *fhl2b* between haplochromines and non-haplochromines (note that there are three haplochromine genomes available: *A. burtoni, Pu. nyererei, M. zebra*; and two genomes belonging to more ancestral cichlid lineages: *N. brichardi* and *Or. niloticus*). For this analysis, we also included the respective genomic regions of four other teleost species (*O. latipes, Ta. rubripes, Te. nigroviridis* and *G. aculeatus*). More specifically, we extracted the genomic scaffolds containing *fhl2a* and *fhl2b* from the available cichlid genomes using BLAST v. 2.2.25 and the BIOCONDUCTOR R package BIOSTRINGS[62] to extract 5–6 kb of sequence containing *fhl2a* and *fhl2b* from these scaffolds.

Comparative analyses of the *fhl2a* and *fhl2b* genomic regions were done with MVISTA (genome.lbl.gov/vista)[63] using the LAGAN alignment tool[64]; *A. burtoni* was used as a reference for the alignment. We applied the repeat masking option with *Ta. rubripes* (Fugu) as reference. CNEs were defined as any non-coding section longer than 100 bp that showed at least 70% sequence identity with *A. burtoni*.

Sequencing of the upstream region of fhl2b. In order to confirm whether the AFC-SINE insertion was specific to egg-spot bearing haplochromines, we amplified the genomic region upstream of the *fhl2b* open reading frame in 19 additional cichlid species (10 haplochromines and 9 non-haplochromines). PCR amplification was performed as described above. For sequencing, we used four different primers, the two used in the amplification reaction and two internal primers, one haplochromine specific and another non-haplochromine specific. For detailed information about species and primers, see Supplementary Table 8.

Alignment of AFC-SINES from the A. burtoni genome. SINE elements were identified using the SINE insertion sequence 5′ of the *fhl2b* gene of *A. burtoni* as query in a local BLASTn search[49] with default settings against the *A. burtoni* reference genome. Blast hits were retrieved using custom scripts and extended to a region of 200-bp upstream and downstream of the identified sequence. Sequences were aligned using MAFFT v. 6 (ref. 41) with default settings and allowing for adjustment of sequence direction according to the reference sequence. The alignment was loaded into CODONCODE ALIGNER for manual correction and end trimming. Sequences shorter than 50 bp were excluded from the alignment. The final alignment contained 407 sequences that were used to build the *A. burtoni* SINE consensus sequence using the consensus method implemented in CODONCODE ALIGNER with a percentage-based consensus and a cutoff of 25%. The AFC-SINE element in the *fhl2b* promoter region was compared with the consensus sequence and available full-length AFC-SINE elements of cichlids in order to determine whether it was an insertion or deletion in haplochromines (Supplementary Table 8).

Characterization of fhl2b upstream genomic region in cichlids. The *fhl2b* genomic regions of the five cichlid genomes (*A. burtoni, M. zebra, Pu. nyererei, N. brichardi*, and *O. niloticus*) were loaded into CODONCODE ALIGNER and assembled (large gap alignments settings, identity cutoff 70%). Assemblies were manually corrected. Transposable element sequences were identified using the Repeat Masking function of REPBASE UNIT (http://www.girinst.org/censor/index.php) against all sequence sources and the bl2seq function of BLASTn[49]. Supplementary Fig. 6 shows a scheme of the transposable element composition of this genomic region in several cichlid species.

CNEs construct cloning and injection in zebrafish. We designed three genetic constructs containing the AFC-SINE and intron 1 of *fhl2b* of three cichlid species (*A. burtoni, P. philander* and *N. sexfasciatus*) (Fig. 4) and one containing the 5′-untranslated region, exon 1 and intron 1 of *A. burtoni fhl2a*. The three fragments were amplified with PCR as described above (see Supplementary Table 3 for primer information). All fragments were cloned into a pCR8/GW/TOPO vector (Invitrogen) following the manufacturer's specifications. Sequence identity and direction of fragment insertion were confirmed via Sanger sequencing (as described above) using M13 primers. All plasmid extractions were performed with GenElute Plasmid Miniprep Kit (Sigma-Aldrich). We then recombined these fragments into the Zebrafish Enhancer Detection ZED vector[65] following the protocol specified in ref. 66. Recombination into the ZED plasmid was performed taking into consideration the original orientation of the *fhl2b* genomic region. The resulting ZED plasmids were then purified with the DNA clean and concentrator − 5 Kit (Zymo Research, USA). Injections were performed with 1 nl into one-/two-cell stage zebrafish (*D. rerio*) embryos (*A. burtoni* construct was injected in wild-type strains AB and ABxEK, *P. philander* and *N. sexfasciatus* constructs were injected in wild-type strain ABxEK) with 25 ng μl^{−1} plasmid and 35 ng μl^{−1} Tol2 transposase mRNA. By outcrossing to wild-type zebrafish, we created five F2 stable transgenic lines for the *A. burtoni* construct, two F1 stable transgenic lines for the *P. philander* construct, and finally one F1 stable transgenic line for the *N. sexfasciatus* construct. Fish were raised and kept according to standard procedures[67]. Zebrafish were imaged using a Leica point scanning confocal microscope SP5-II-matrix and Zeiss LSM5 Pascal confocal microscope.

Fixation and dehydration of cichlid fins. In order to determine the pigment cell composition of egg-spots (and especially whether they contain iridophores in addition to xanthophores), we dissected *A. burtoni* anal fins. To better understand the morphological differences between non-haplochromine and haplochromine fins, we further dissected three *N. crassus* anal fins. To visualize iridophores, we removed the pteridine pigments of the overlying xanthophores by fixating the fin in 4% paraformaldehyde–PBS for 1 h at room temperature and washing it in a series of methanol:PBS dilutions (25%, 50%, 75% and 100%). Pictures were taken after 6 days in 100% methanol at − 20 °C.

References

1. Pigliucci, M. What, if anything, is an evolutionary novelty? *Philos. Sci.* **75**, 887–898 (2008).
2. Carroll, S. B. Evo-devo and an expanding evolutionary synthesis: a genetic theory of morphological evolution. *Cell* **134**, 25–36 (2008).
3. Wagner, G. P. & Lynch, V. J. Evolutionary novelties. *Curr. Biol.* **20**, R48–R52 (2010).
4. Wagner, A. The molecular origins of evolutionary innovations. *Trends Genet.* **27**, 397–410 (2011).
5. Carroll, S. B., Grenier, J. K. & Weatherbee, S. D. *From DNA to Diversity: Molecular Genetics and the Evolution of Animal Design* (Blackwell Science, 2001).
6. Schluter, D. Evidence for ecological speciation and its alternative. *Science* **323**, 737–741 (2009).
7. Lynch, V. J., Leclerc, R. D., May, G. & Wagner, G. P. Transposon-mediated rewiring of gene regulatory networks contributed to the evolution of pregnancy in mammals. *Nat. Genet.* **43**, 1154–1159 (2011).
8. Beldade, P. & Brakefield, P. M. The genetics and evo-devo of butterfly wing patterns. *Nat. Rev. Genet.* **3**, 442–452 (2002).
9. Salzburger, W., Mack, T., Verheyen, E. & Meyer, A. Out of Tanganyika: genesis, explosive speciation, key-innovations and phylogeography of the haplochromine cichlid fishes. *BMC Evol. Biol.* **5**, 17 (2005).
10. Kocher, T. D. Adaptive evolution and explosive speciation: the cichlid fish model. *Nat. Rev. Genet.* **5**, 288–298 (2004).
11. Salzburger, W. The interaction of sexually and naturally selected traits in the adaptive radiation of cichlid fishes. *Mol. Ecol.* **18**, 169–185 (2009).
12. Fryer, G. & Iles, T. *The Cichlid Fishes of the Great Lakes of Africa: their Biology and Evolution* (Oliver & Boyd, 1972).
13. Wickler, W. 'Egg-dummies' as natural releasers in mouth-breeding cichlids. *Nature* **194**, 1092–1093 (1962).
14. Santos, M. E. & Salzburger, W. How cichlids diversify. *Science* **338**, 619–621 (2012).
15. Muschick, M., Indermaur, A. & Salzburger, W. Convergent evolution within an adaptive radiation of cichlid fishes. *Curr. Biol.* **22**, 2362–2368 (2012).
16. Salzburger, W., Braasch, I. & Meyer, A. Adaptive sequence evolution in a color gene involved in the formation of the characteristic egg-dummies of male haplochromine cichlid fishes. *BMC Biol.* **5**, 51 (2007).
17. Braasch, I. & Postlethwait, J. in *Polyploidy and Genome Evolution* (eds Soltis, D E. & Soltis, P. S.) 341–383 (Springer, 2012).

18. Müller, J. M. *et al.* FHL2, a novel tissue-specific coactivator of the androgen receptor. *EMBO J.* **19,** 359–369 (2000).

19. Brun, J. *et al.* The LIM-only protein FHL2 controls osteoblast mesenchymal cell differentiation through non-canonical Wnt signalling. *Bone* **50,** S76 (2012).

20. Johannessen, M., Møller, S., Hansen, T., Moens, U. & Van Ghelue, M. The multifunctional roles of the four-and-a-half-LIM only protein FHL2. *Cell. Mol. Life Sci.* **63,** 268–284 (2006).

21. Kadrmas, J. L. & Beckerle, M. C. The LIM domain: from the cytoskeleton to the nucleus. *Nat. Rev. Mol. Cell Biol.* **5,** 920–931 (2004).

22. Heule, C. & Salzburger, W. The ontogenetic development of egg-spots in the haplochromine cichlid fish Astatotilapia burtoni. *J. Fish Biol.* **78,** 1588–1593 (2011).

23. Baldo, L., Santos, M. E. & Salzburger, W. Comparative transcriptomics of Eastern African cichlid fishes shows signs of positive selection and a large contribution of untranslated regions to genetic diversity. *Genome Biol. Evol.* **3,** 443–455 (2011).

24. Lynch, M. & Conery, J. S. The evolutionary fate and consequences of duplicate genes. *Science* **290,** 1151–1155 (2000).

25. Takahashi, K., Terai, Y., Nishida, M. & Okada, N. A novel family of short interspersed repetitive elements (SINEs) from cichlids: the patterns of insertion of SINEs at orthologous loci support the proposed monophyly of four major groups of cichlid fishes in Lake Tanganyika. *Mol. Biol. Evol.* **15,** 391–407 (1998).

26. Britten, R. J. & Davidson, E. H. Gene regulation for higher cells: a theory. *Science* **165,** 349–357 (1969).

27. Britten, R. J. & Davidson, E. Repetitive and non-repetitive DNA sequences and a speculation on the origins of evolutionary novelty. *Q Rev. Biol.* **46,** 111–138 (1971).

28. Feschotte, C. Transposable elements and the evolution of regulatory networks. *Nat. Rev. Genet.* **9,** 397–405 (2008).

29. Frohnhöfer, H. G., Krauss, J., Maischein, H.-M. & Nüsslein-Volhard, C. Iridophores and their interactions with other chromatophores are required for stripe formation in zebrafish. *Development* **140,** 2997–3007 (2013).

30. Patterson, L. B. & Parichy, D. M. Interactions with iridophores and the tissue environment required for patterning melanophores and xanthophores during zebrafish adult pigment stripe formation. *PLoS Genet.* **9,** e1003561 (2013).

31. Manousaki, T. *et al.* Parsing parallel evolution: ecological divergence and differential gene expression in the adaptive radiations of thick-lipped Midas cichlid fishes from Nicaragua. *Mol. Ecol.* **22,** 650–669 (2013).

32. Shimeld, S. M. & Holland, P. W. Vertebrate innovations. *Proc. Natl Acad. Sci. USA* **97,** 4449–4452 (2000).

33. Egger, B., Klaefiger, Y., Theis, A. & Salzburger, W. A sensory bias has triggered the evolution of egg-spots in cichlid fishes. *PLoS ONE* **6,** e25601 (2011).

34. Theis, A., Salzburger, W. & Egger, B. The function of anal fin egg-spots in the cichlid fish Astatotilapia burtoni. *PLoS ONE* **7,** e29878 (2012).

35. Miller, S., Dykes, D. & Polesky, H. A simple salting out procedure for extracting DNA from human nucleated cells. *Nucleic Acids Res.* **16,** 1215 (1988).

36. Meyer, B. S. & Salzburger, W. A novel primer set for multilocus phylogenetic inference in East African cichlid fishes. *Mol. Ecol. Resour.* **12,** 1097–1104 (2012).

37. Margulies, M. *et al.* Genome sequencing in microfabricated high-density picolitre reactors. *Nature* **437,** 376–380 (2005).

38. Binladen, J. *et al.* The use of coded PCR primers enables high-throughput sequencing of multiple homolog amplification products by 454 parallel sequencing. *PLoS ONE* **2,** e197 (2007).

39. Schmieder, R. & Edwards, R. Quality control and preprocessing of metagenomic datasets. *Bioinformatics* **27,** 863–864 (2011).

40. Kearse, M. *et al.* Geneious Basic: an integrated and extendable desktop software platform for the organization and analysis of sequence data. *Bioinformatics* **28,** 1647–1649 (2012).

41. Katoh, K., Kuma, K., Toh, H. & Miyata, T. MAFFT version 5: improvement in accuracy of multiple sequence alignment. *Nucleic Acids Res.* **33,** 511–518 (2005).

42. Darriba, D., Taboada, G. L., Doallo, R. & Posada, D. jModelTest 2: more models, new heuristics and parallel computing. *Nat. Methods* **9,** 772 (2012).

43. Schwarz, G. Estimating the dimension of a model. *Ann. Stat.* **6,** 461–464 (1978).

44. Ronquist, F. *et al.* MrBayes 3.2: efficient Bayesian phylogenetic inference and model choice across a large model space. *Syst. Biol.* **61,** 539–542 (2012).

45. Zwickl, D. J. *Genetic Algorithm Approaches for the Phylogenetic Analysis of Large Biological Sequence Datasets Under the Maximum Likelihood Criterion* (University of Texas, 2006).

46. Sukumaran, J. & Holder, M. T. DendroPy: a Python library for phylogenetic computing. *Bioinformatics* **26,** 1569–1571 (2010).

47. Li, H. *et al.* The Sequence Alignment/Map format and SAMtools. *Bioinformatics* **25,** 2078–2079 (2009).

48. Robinson, M. D., McCarthy, D. J. & Smyth, G. K. edgeR: a Bioconductor package for differential expression analysis of digital gene expression data. *Bioinformatics* **26,** 139–140 (2010).

49. Altschul, F. S., Gish, W., Miller, W., Myers, W. E. & Lipman, J. D. Basic Local Alignment Search Tool. *J. Mol. Biol.* **215,** 403–410 (1990).

50. Pfaffl, M. W. A new mathematical model for relative quantification in real-time RT–PCR. *Nucleic Acids Res.* **29,** e45 (2001).

51. Curran, K. *et al.* Interplay between Foxd3 and Mitf regulates cell fate plasticity in the zebrafish neural crest. *Dev. Biol.* **344,** 107–118 (2010).

52. Tang, R., Dodd, A., Lai, D., McNabb, W. C. & Love, D. R. Validation of zebrafish (*Danio rerio*) reference genes for quantitative real-time RT–PCR normalization. *Acta. Biochim. Biophys. Sin.* **39,** 384–390 (2007).

53. Zhang, Z. & Hu, J. Development and validation of endogenous reference genes for expression profiling of medaka (*Oryzias latipes*) exposed to endocrine disrupting chemicals by quantitative real-time RT–PCR. *Toxicol. Sci.* **95,** 356–368 (2007).

54. Catchen, J. M., Conery, J. S. & Postlethwait, J. H. Automated identification of conserved synteny after whole-genome duplication. *Genome Res.* **19,** 1497–1505 (2009).

55. Rozen, S. & Skaletsky, H. Primer3 on the WWW for general users and for biologist programmers. *Methods Mol. Biol.* **132,** 365–386 (2000).

56. Flicek, P. *et al.* Ensembl 2012. *Nucleic Acids Res.* **40,** D84–D90 (2012).

57. Larkin, M. *et al.* Clustal W and Clustal X version 2.0. *Bioinformatics* **23,** 2947–2948 (2007).

58. Swofford, D. L. *PAUP*. Phylogenetic Analysis Using Parsimony (*and Other Methods)* (Sinauer, 2003).

59. Yang, Z. PAML 4: phylogenetic analysis by maximum likelihood. *Mol. Biol. Evol.* **24,** 1586–1591 (2007).

60. Nielsen, R. & Yang, Z. Likelihood models for detecting positively selected amino acid sites and applications to the HIV-1 envelope gene. *Genetics* **148,** 929–936 (1998).

61. Brawand, D. *et al.* The genomic substrate for adaptive radiation in Africa cichlid fish. *Nature* **513,** 375–381 (2014).

62. Pages, H., Aboyoun, P., Gentleman, R. & DebRoy, S. Biostrings: String objects representing biological sequences, and matching algorithms. R-package, http://www.bioconductor.org/packages/release/bioc/html/Biostrings.html.

63. Frazer, K. A., Pachter, L., Poliakov, A., Rubin, E. M. & Dubchak, I. VISTA: computational tools for comparative genomics. *Nucleic Acids Res.* **32,** W273–W279 (2004).

64. Brudno, M. *et al.* LAGAN and Multi-LAGAN: efficient tools for large-scale multiple alignment of genomic DNA. *Genome Res.* **13,** 721–731 (2003).

65. Bessa, J. *et al.* Zebrafish enhancer detection (ZED) vector: a new tool to facilitate transgenesis and the functional analysis of cis-regulatory regions in zebrafish. *Dev. Dyn.* **238,** 2409–2417 (2009).

66. Bessa, J. & Gómez-Skarmeta, J. L. Making reporter gene constructs to analyze cis-regulatory elements. *Mol. Methods Evol. Genet.* **772,** 397–408 (2011).

67. Westerfield, M. *The Zebrafish Book. A guide for the Laboratory Use of Zebrafish (Danio rerio)* (University of Oregon Press, 2000).

Author contributions

M.E.S., I.B. and W.S. designed the study; M.E.S and W.S. collected the samples; M.E.S. performed the RNAseq, gene expression, comparative genomics and zebrafish functional analysis; N.B. performed the sequencing of *fhl2* paralogs coding region and analysed its rates of evolution; B.S.M. collected the 454 sequence data; and B.S.M. and W.S. performed the phylogenetic analysis; A.B. performed the SINE consensus alignments and analysed the transposable element composition of *fhl2b* genomic region; I.B. performed the zebrafish functional assays of the *A. burtoni* construct and *fhl2* paralogs synteny

Additional information

A.3.   Phng L.-K., et al. 2015

Formin-Mediated Actin Polymerization at Endothelial Junctions Is Required for Vessel Lumen Formation and Stabilization

Li-Kun Phng,[1,6] Véronique Gebala,[2] Katie Bentley,[3] Andrew Philippides,[4] Andrin Wacker,[1] Thomas Mathivet,[1] Loïc Sauteur,[5] Fabio Stanchi,[1] Heinz-Georg Belting,[5] Markus Affolter,[5] and Holger Gerhardt[1,2,7,*]

[1]Vascular Patterning Laboratory, Vesalius Research Center, VIB, Department of Oncology, KU Leuven, Herestraat 49, 3000 Leuven, Belgium
[2]Vascular Biology Laboratory, London Research Institute, Cancer Research UK, London WC2A 3LY, UK
[3]Computational Biology Laboratory, Center for Vascular Biology Research, Beth Israel Deaconess Medical Center, Harvard Medical School, Boston, MA 02215, USA
[4]Centre for Computational Neuroscience and Robotics, Department of Informatics, University of Sussex, Brighton BN1 9QJ, UK
[5]Biozentrum der Universität Basel, Klingelbergstrasse 50/70, 4056 Basel, Switzerland
[6]Present address: Department of Cell Biology, National Cerebral and Cardiovascular Center Research Institute, Osaka 565-8565, Japan
[7]Present address: Integrative Vascular Biology Laboratory, Max-Delbrück-Center for Molecular Medicine (MDC), 13125 Berlin, Germany
*Correspondence: holger.gerhardt@mdc-berlin.de
http://dx.doi.org/10.1016/j.devcel.2014.11.017

SUMMARY

During blood vessel formation, endothelial cells (ECs) establish cell-cell junctions and rearrange to form multicellular tubes. Here, we show that during lumen formation, the actin nucleator and elongation factor, formin-like 3 (fmnl3), localizes to EC junctions, where filamentous actin (F-actin) cables assemble. Fluorescent actin reporters and fluorescence recovery after photobleaching experiments in zebrafish embryos identified a pool of dynamic F-actin with high turnover at EC junctions in vessels. Knockdown of fmnl3 expression, chemical inhibition of formin function, and expression of dominant-negative fmnl3 revealed that formin activity maintains a stable F-actin content at EC junctions by continual polymerization of F-actin cables. Reduced actin polymerization leads to destabilized endothelial junctions and consequently to failure in blood vessel lumenization and lumen instability. Our findings highlight the importance of formin activity in blood vessel morphogenesis.

INTRODUCTION

The establishment and maintenance of functional blood vessels is crucial during development. Vessel lumenization involves apical membrane invagination and cellular rearrangements (Axnick and Lammert, 2012; Herwig et al., 2011; Lenard et al., 2013). Molecules that regulate vessel lumenization include vascular endothelial (VE)-cadherin (Lampugnani et al., 2010; Montero-Balaguer et al., 2009; Strilić et al., 2009; Wang et al., 2010), CCM1 (Lampugnani et al., 2010), β1 integrin (Zovein et al., 2010), VE-phosphotyrosine phosphatase (VE-PTP) (Hayashi et al., 2013), podocalyxin (Strilić et al., 2009), Rasip1 (Xu et al., 2011), Moesin 1 (Strilić et al., 2009; Wang et al., 2010), PP2A

(Martin et al., 2013) and Amotl2 (Hultin et al., 2014). A common feature of these molecules is their ability to associate to or regulate the filamentous actin (F-actin) cytoskeleton. Thus, the actin cytoskeleton is an effector of lumen formation. However, how the actin cytoskeleton or which actin structure regulates vessel lumenization in vivo is unknown.

Formin proteins regulate both the actin and microtubule cytoskeleton and play important roles in cell division, cell migration, adherens junction formation, and development (Bartolini and Gundersen, 2010; DeWard et al., 2010). Fifteen mammalian formin proteins have been identified and include Diaphanous-related formin 1 to 3 (Dia 1–3) and formin-like protein 1 to 3 (fmnl 1–3). Formins are characterized by the presence of formin homology (FH) domains, FH1 and FH2, and contain a GTPase-binding domain regulated by Rho GTPases (Schönichen and Geyer, 2010). Formins act as actin nucleation and elongation factors to promote the assembly of linear actin filaments. The FH1 domain binds to the actin monomer-binding protein profilin, while the FH2 domains form homodimers that associate to F-actin barbed ends to initiate actin nucleation.

Fmnl3 is selectively expressed in endothelial cells (ECs) during zebrafish embryonic development, where it influences intersegmental vessel (ISV) formation (Hetheridge et al., 2012; Santos-Ledo et al., 2012). However, it is unclear how fmnl3 regulates angiogenesis. In this study, we demonstrate that fmnl3 regulates F-actin assembly at EC junctions to promote junction stability and vessel integrity.

RESULTS

Formin Activity Regulates Lumen Formation and Maintenance

Similar to human FMNL3 in cultured cells (Harris et al., 2010), we detected EGFP tagged zebrafish fmnl3 (fmnl3-EGFP) in endothelial filopodia during zebrafish ISV development (Figures S1A and S1B available online). Knockdown of fmnl3 expression using antisense morpholino (Hetheridge et al., 2012) resulted in a small
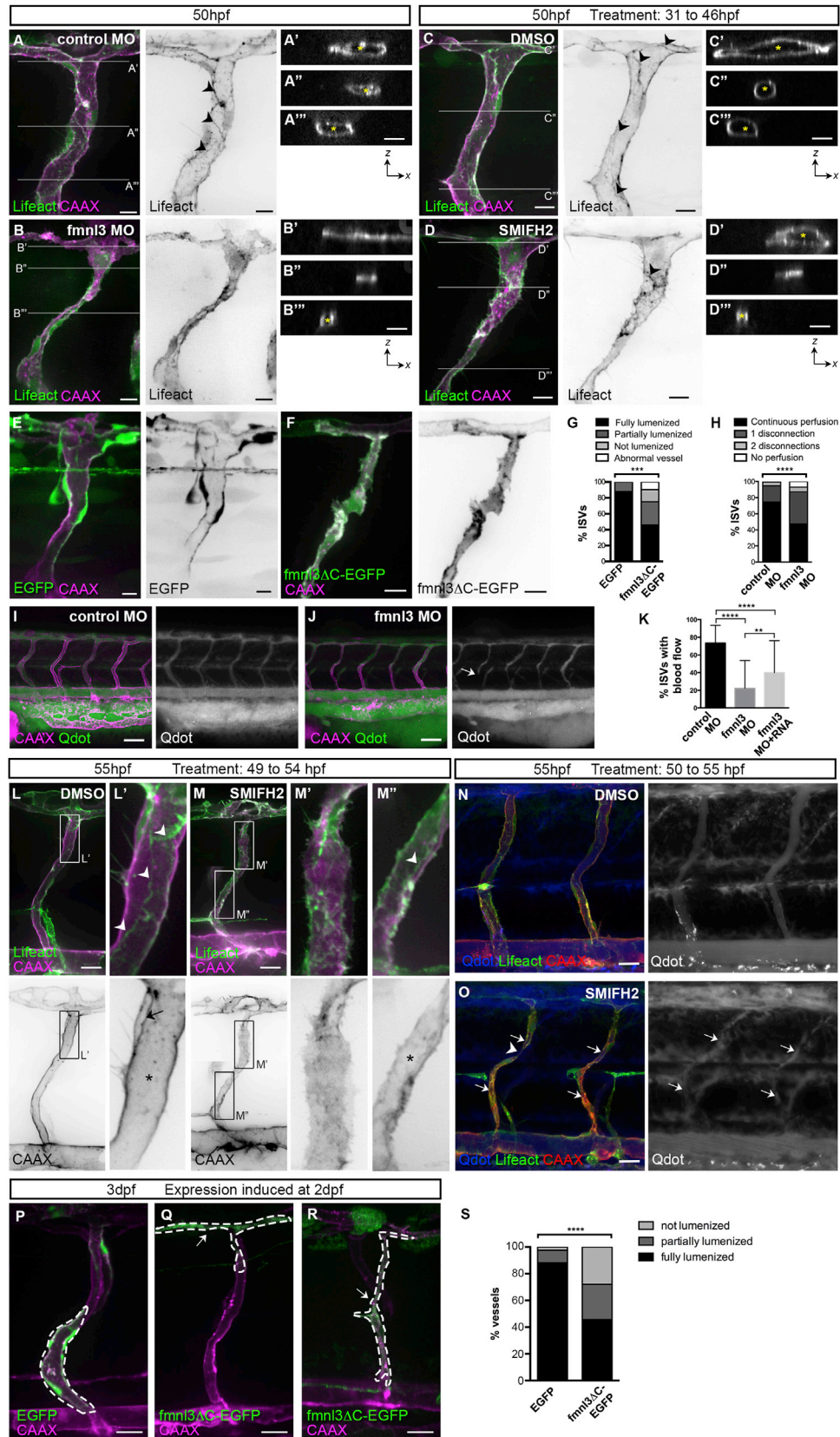
(legend on next page)

but significant decrease in endothelial filopodia number (p = 0.0013; Figures S1E–S1G) and length (p < 0.0001; Figures S1E, S1F, and S1H) during ISV formation. In contrast to a previous report (Hetheridge et al., 2012), the decrease in filopodia formation did not perturb ISV development (Figures S1I–S1K). However, fmnl3 knockdown prevented the formation of distinct dorsal and ventral veins in the caudal vein plexus (Figures S1L and S1M). The role of fmnl3 in the formation of this caudal vein plexus is covered in a separate paper in this issue of *Developmental Cell* (Wakayama et al., 2015).

Additionally, we discovered that formin inhibition perturbed lumen formation in the ISVs. Examination of 2 dpf fmnl3 morphants and embryos treated with SMIFH2, a broad-spectrum formin inhibitor (Rizvi et al., 2009), from 31 hpf, revealed poorly lumenized ISVs (Figures 1B and 1D) compared with control embryos (Figures 1A and 1C). ECs expressing a truncated form of fmnl3 lacking the catalytic C terminus FH1, FH2, and DAD domains (fmnl3ΔC) showed reduced linear F-actin cables at the cell cortex and a more relaxed morphology compared with control cells (Figure S1N). Quantification of ISVs with mosaic fmnl3ΔC expression revealed a decrease in the number of fully lumenized ISVs (p = 0.0002; Figures 1E–1G). Microangiography in 54–57 hpf embryos identified a significant decrease in the number of ISVs with continuous perfusion in fmnl3 morphants (p < 0.0001; Figures 1H–1J). Similarly, the flow of erythrocytes through ISVs was decreased in fmnl3 morphants (p < 0.0001; Figure 1K) and was partially rescued by overexpression of *fmnl3* mRNA (p < 0.0019; Figure 1K).

We next asked whether fmnl3 also controls lumen maintenance. In embryos treated with DMSO at 2 dpf, ISVs remained lumenized and displayed distinct longitudinal junctional F-actin cables (Figure 1L). In contrast, inhibition of formin activity using SMIFH2 for 4 to 5 hr resulted in a loss of continuous lumen within ISVs (Figure 1M). Injections of quantum dots into the blood flow of embryos at 50 hpf and immediate treatment with DMSO or SMIFH2 confirmed a loss of vessel functionality after formin inhibition. In control embryos, ISVs, dorsal longitudinal anastomotic vessels (DLAVs), the dorsal aorta (DA), and the posterior cardinal vein (PCV) were continuously perfused (Figure 1N). However, SMIFH2 treatment resulted in the trapping of quantum dots within segments of the ISVs (Figure 1O), demonstrating the disruption of previously formed lumen. Furthermore, SMIFH2

treatment led to cell disconnections within the ISVs (Figure 1O). To test the specific requirement of fmnl3 in lumen maintenance, we induced the expression of dominant-negative fmnl3ΔC specifically in ECs at 2 dpf using the mifepristone-inducible LexPR system (Emelyanov and Parinov, 2008). ISVs with mosaic expression of fmnl3ΔC revealed a decrease in the number of fully lumenized ISVs at 3 dpf compared with ISVs with mosaic EGFP expression (p < 0.0001; Figures 1P–1S).

In summary, these experiments demonstrate that formin activity regulates lumen formation and maintenance during angiogenesis.

Fmnl3 Does Not Regulate Microtubule Filament Assembly in ECs In Vivo

As fmnl3 was suggested to regulate microtubule alignment in angiogenic sprouts (Hetheridge et al., 2012), we asked whether potential microtubule defects contributed to lumen disruption. Coexpression of fmnl3-EGFP and mCherry-Doublecortin (DCX), a microtubule marker (Figure S2A), did not show colocalization of fmnl3 to microtubule filaments (Figure 2A). In 48–50 hpf *Tg(fli1ep:EGFP-DCX)* embryos injected with control morpholino (Figure 2B) or treated with DMSO (Figure 2D), ECs displayed long, thin microtubule filaments. In fmnl3 morphants (Figure 2C) and embryos treated for 2 hr with SMIFH2 (Figure 2E), microtubule filaments were still observed in ECs of unlumenized segments of ISVs. Interestingly, ISVs remained lumenized after 2 hr nocodazole treatment, although microtubule filaments were depleted (Figure 2F). These findings suggest that the microtubule cytoskeleton is not essential for lumen maintenance in the short term and that formins do not regulate vessel lumen integrity through the microtubule skeleton.

Formin Activity Maintains a Pool of Dynamic F-Actin at Endothelial Junctions

As blood vessels mature, ECs rearrange to form a multicellular tube. During this phase, fmnl3 translocates from the cytoplasm to junctions, where F-actin cables assemble (Figures 2G, S1C, and S1D). The colocalization of fmnl3 with junctional F-actin suggests a role of fmnl3 in promoting F-actin cable assembly at EC junctions. We next examined junctional F-actin in the DA and the PCV in more detail since junctions of ISVs disintegrate within 1 to 2 hr of SMIFH2 treatment (Figure 4G). Analysis of F-actin cables

---

Figure 1. Formin Activity Is Required for Vessel Lumen Formation and Maintenance

(A–D) *Tg(fli1ep:Lifeact-EGFP)*;*Tg(kdr-l:ras-Cherry)*[s916] embryos were injected with control or fmnl3 morpholino or treated with DMSO or 5 μM SMIFH2 from 31 to 46 hpf and examined at 50 hpf. The asterisk shows lumenized ISV, and arrowheads show junctional F-actin cables. Scale bars represent 10 μm.

(E–G) Mosaic expression of EGFP or fmnl3ΔC-EGFP in ISVs of *Tg(kdr-l:ras-Cherry)*[s916] embryos at 52 hpf. ISVs with EGFP or fmnl3ΔC-EGFP expression were phenotyped for lumen defects (G). EGFP, n = 41 ISVs, n = 16 embryos; fmnl3ΔC-EGFP, n = 52 ISVs, n = 27 embryos. Scale bars represent 10 μm.

(H–J) *Tg(kdr-l:ras-Cherry)*[s916] embryos were injected with quantum dots (Qdot) at 54–57 hpf. The arrow shows discontinuous perfusion. Control MO, n = 134 ISVs, n = 28 embryos; fmnl3 MO, n = 186 ISVs, n = 36 embryos. Scale bars represent 50 μm.

(K) Quantification of blood flow through ISVs. Control MO, n = 79 embryos; Fmnl3 MO, n = 87 embryos; Fmnl3 MO + 100pg *fmnl3* mRNA, n = 64 embryos. Data represent mean ± SD.

(L–O) Uninjected or Qdot-injected *Tg(fli1ep:Lifeact-EGFP)*;*Tg(kdr-l:ras-Cherry)*[s916] embryos were treated with DMSO or 10 μM SMIFH2 at 49–50 hpf and imaged 4–5 hr later. (L and M) Arrowheads show junctional F-actin cables. The arrow shows apical membrane, and the asterisk shows lumen. (O) Arrows show fragments of Qdot-filled vessels, and the arrowhead shows vessel disconnection. Scale bars represent 20 μm.

(P–S) Mosaic endothelial EGFP or fmnl3ΔC-EGFP expression (serrated lines) was induced in *Tg(kdr-l:ras-Cherry)*[s916] embryos at 2 dpf and examined at 71–77 hpf for lumen defects. Arrows show unlumenized vessel. EGFP, n = 42 ISVs, n = 16 embryos; fmnl3ΔC-EGFP, n = 57 ISVs, n = 33 embryos. Scale bars represent 20 μm.

See also Figure S1.
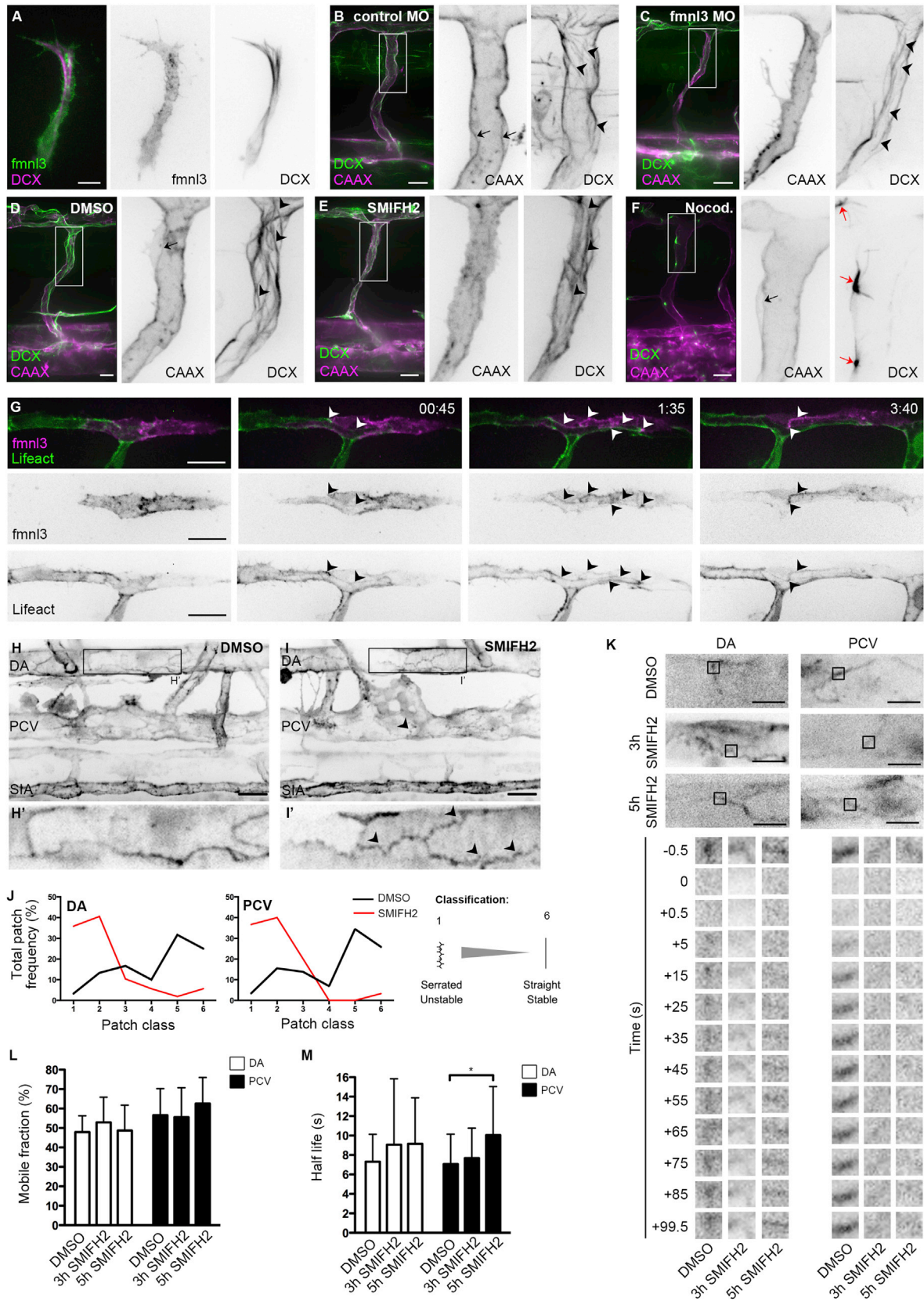
(legend on next page)

revealed a decrease in straight cables and an increase in serrated cables at the junctions of both the DA and PCV after 5 hr SMIFH2 treatment (Figures 2H–2J). Serrated junction profiles have been observed in vitro and in vivo at active junctions after VE growth factor (VEGF) treatment and at remodeling junctions (Bentley et al., 2014). Hence, the increase in serrated F-actin cables after formin inhibition suggests decreased F-actin stability at cell junctions.

As formins catalyze the nucleation of actin filaments, we examined whether the decrease in F-actin stability is a consequence of altered F-actin polymerization by measuring the fluorescence recovery of EGFP-Actin at cell junctions after photobleaching (FRAP) in Tg(fli1ep:EGFP-Actin) embryos (Figures S2B and S2C). FRAP experiments revealed that 47.9% and 57.4% of the F-actin population at junctions of the DA and PCV, respectively, are mobile (Figure 4L). The mobile fraction of EGFP-Actin at cell junctions of the DA and PCV of control embryos recovered rapidly after photobleaching (half-life of 7.3 ± 2.8 s at DA and 7.1 ± 3.1 s at PCV; Figures 2K and 2M). This recovery can occur through the diffusion of monomeric EGFP-Actin or through nucleation of EGFP-Actin at the junctions. As diffusive recovery occurs within 50 ms (Fritzsche et al., 2013), we assumed that monomeric EGFP-Actin distribution was homogeneous (Halavatyi et al., 2010) and that the recovery of the mobile EGFP-Actin fraction was a result of F-actin polymerization. Thus, our FRAP study revealed a mobile pool of dynamic F-actin with high turnover at EC junctions.

The mobile fraction of junctional EGFP-Actin in both the DA and PCV remained unaffected after formin inhibition (Figure 2L). However, 5 hr SMIFH2 treatment resulted in a significant increase of 3 s in half-life in the PCV compared with DMSO-treated embryos (p = 0.0481) (Figure 2M). Thus, formin-mediated F-actin polymerization contributes to the recovery of the mobile pool of junctional EGFP-Actin to maintain a stable F-actin content and, therefore, F-actin cable assembly, at EC junctions.

Junctional F-Actin Cables Assemble during Lumen Formation

To better understand how fmnl3 regulates ISV lumenization, we turned to live imaging of Tg(fli1ep:Lifeact-EGFP);Tg(kdr-l:ras-Cherry)^s916 embryos to visualize endothelial actin and membrane dynamics, respectively. In these embryos, the apical membrane can be clearly distinguished by mCherryCAAX enrichment at the apical membrane compared with the basal membrane (Figure 3B). Prior to lumenization, mCherryCAAX-rich membranes

accumulate along F-actin-positive cell junctions (35.5 hpf; Figures 3A and 3B) followed by their expansion along the junctions to form a lumen (Figure 3B). Cell rearrangements subsequently establish longitudinal junctions along ISVs (Figure 3B; Movie S1) (Herwig et al., 2011). However, in 5 of 10 ISVs of fmnl3 morphants, we were unable to observe this multistep process leading to lumen formation. Although we were able to detect F-actin in filopodia and at the cell cortex, we could not observe distinct F-actin cables at cell junctions upon knockdown of fmnl3 from 35.8 to 43 hpf (Figures 3C and 3D; Movie S2). Concomitantly, ISVs that did not establish distinct junctional F-actin cables failed to form lumen (five of five ISVs), suggesting that the formation of F-actin cables at EC junctions is functionally linked with lumen formation. Although mCherryCAAX-rich membranes accumulated in fmnl3 morphants (magenta arrows, Figure 3D), they formed vacuoles of variable sizes instead of a seamless lumen (Figure 3D). Furthermore, staining for podocalyxin-like 2 (Pdxl2), an apical membrane marker (Herwig et al., 2011), at 32 and 49 hpf showed that ECs of fmnl3 morphants can form apical domains (Figures S3A–S3D). These findings suggest that fmnl3 does not regulate endothelial apical polarity establishment that is required for lumen formation.

Occasionally, junctional F-actin assembly and lumenization occurred but were not maintained in fmnl3 morphants (2 of 10 ISVs). Figure 3E shows an example in which apical membranes expanded to form a continuous lumen within the ISV-DLAV network. However, the reactivation of an EC, as demonstrated by filopodia formation (from 40.7 hpf, Figure 3E; Movie S3), led the cell to slide over the neighboring cell, breaking cell contact and lumen continuity. Similarly, time-lapse movies of ISVs and DLAV with mosaic fmnl3ΔC expression showed defects in vessel lumenization or connection (9 of 21 vessels; Figure 3F; Movie S3).

Together, these observations suggest that, upon decreased fmnl3 or formin activity, diminished junctional F-actin assembly compromises junctional integrity, leading to disrupted lumen network within the vasculature.

Formin Activity Stabilizes Adherens Junctions

When grown to confluency, ECs form linear adherens junctions that are associated with parallel F-actin cables (Huveneers et al., 2012; Figures S4A and S4B). A second type of junction, focal adhesion junction (FAJ), shows perpendicular VE cadherin (VEC) orientation that is attached to radial actin bundles. FAJs are highly motile, constantly remodel, and commonly appear at

Figure 2. Formin Activity Promotes F-Actin Polymerization at EC Junctions
(A) Coexpression of fmnl3-EGFP and DCX-mCherry in ISV at 32 hpf. Scale bar represents 10 μm.
(B and C) ISVs of Tg(fli1ep:DCX-EGFP);Tg(kdr-l:ras-Cherry)^s916 embryos injected with control or fmnl3 morpholino at 49 hpf.
(D–F) Tg(fli1ep:DCX-EGFP);Tg(kdr-l:ras-Cherry)^s916 embryos were treated with DMSO, 10 μM SMIFH2, or 0.5 μg/ml nocodazole at 48 hpf for 2 hr and imaged at 51–52 hpf. Arrowheads show microtubule filaments. Black arrows show apical membrane, and red arrows show microtubule organizing center. Scale bars represent 20 μm.
(G) Mosaic endothelial fmnl3-mCherry expression in Tg(fli1ep:Lifeact-EGFP) embryo from 33 hpf. Arrowheads show localization of fmnl3 with F-actin at cell junctions. Scale bar represents 20 μm.
(H–J) 3 to 4 dpf Tg(fli1ep:Lifeact-EGFP) embryos were treated with DMSO or 10 μM SMIFH2 for 4–5 hr. Arrowheads show serrated F-actin cables. DA, dorsal aorta. PCV, posterior cardinal vein. SIA, subintestinal artery. Scale bars represent 20 μm. (J) Image analysis of F-actin cable profile at junctions of the DA or PCV.
(K–M) Fluorescence recovery of EGFP-Actin at cell junctions after photobleaching. Three dpf Tg(fli1ep:EGFP-Actin) embryos were treated with DMSO for 5 hr or 10 μM SMIFH for 3 or 5 hr prior to photobleaching. Scale bar represents 10 μm. Plots of EGFP-Actin mobile fraction (L) and half-life (M) are shown from different treatments. Data represent mean ± SD.
See also Figure S2.
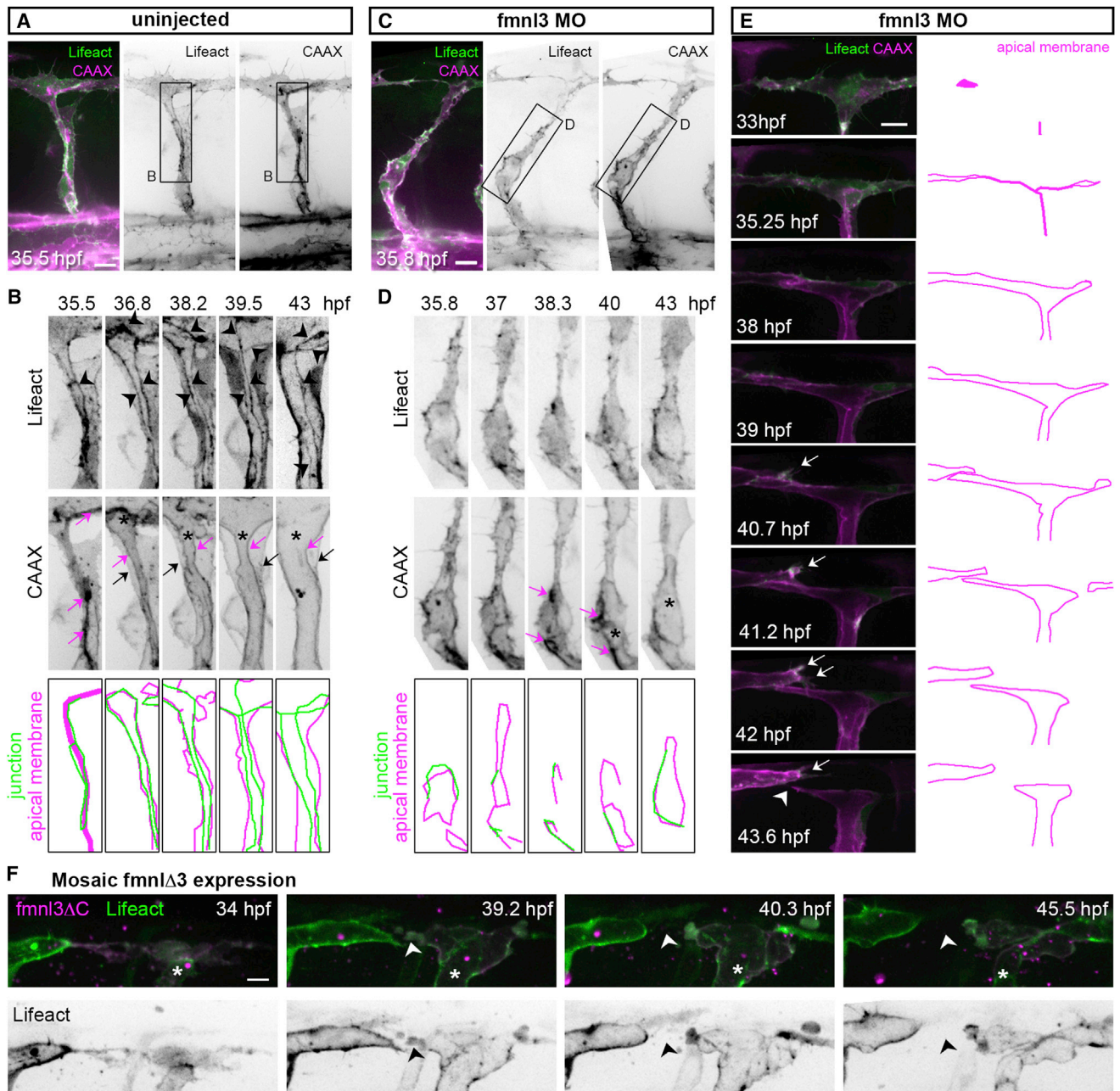
Figure 3. Junctional F-Actin Cables Assemble and Rearrange during Lumen Formation

(A–D) Stills from time-lapse movies illustrating ISV lumenization in uninjected and in fmnl3 morpholino-injected *Tg(fli1ep:Lifeact-EGFP)*;*Tg(kdr-l:ras-Cherry)*[s916] embryos. The magenta arrow shows apical membrane. The black arrow show basal membrane, and the arrowhead shows junctional F-actin cable. The asterisk shows lumen in (B) and vacuole in (D). Scale bars represent 10 μm.

(E and F) Stills from a time-lapse movie of the DLAV from a *Tg(fli1ep:Lifeact-EGFP)*;*Tg(kdr-l:ras-Cherry)*[s916] embryo injected with fmnl3 morpholino (E) or *Tg(fli1ep:Lifeact-EGFP)* embryo with mosaic fmnl3ΔC expression (*) (F). The arrow shows activated EC, and the arrowhead shows vessel disconnection. Scale bar represents 10 μm.

See also Figure S3 and Movies S1, S2, and S3.

the rear of cells (Huveneers et al., 2012). Live imaging of ECs expressing VEC-EGFP revealed that within minutes of SMIFH2 treatment linear junctions disassembled into clusters and FAJs were displaced (14 of 16 movies; Figure 4B; Movie S4). Consequently, cells recoiled from each other revealing high tension in

FAJs. In addition, ECs under shear stress displayed a change in junctional morphology after SMIFH2 treatment. Intercellular gaps formed at the long axis of the cells, as evidenced by two zona occludens 1 (ZO1)-positive membranes between ECs (Figure S4C). Furthermore, some of the remaining junctions were not

associated with F-actin cables (Figure S4D). These findings strongly implicate formins in stabilizing EC junctions.

In vivo, ISVs of 2 dpf embryos display VEC- and ZO1-positive junctions that are lined with F-actin cables and arranged in a multicellular organization with longitudinal and ring-shaped junctions (Figures 4C and 4E) (Herwig et al., 2011; Phng et al., 2013). Longitudinal junctions arise through cell rearrangements from ring-shaped junctions, which first form at sites of new EC contacts, during vessel development. They are therefore hallmarks of cell rearrangement and indicators of junction evolution. We next examined whether VEC binding to the actin cytoskeleton is required for junction stability and/or organization. To address this, we analyzed VEC mutant embryos (*VEC^ubs8*) expressing a truncated form of VEC in which the C terminus, which harbors the actin binding domain, is replaced by EGFP (VECΔC-EGFP). At 52 hpf, ISVs of WT and *Tg(UAS:VECΔC-EGFP)^ubs12* embryos displayed a complex organization of junctions with 69.6% ± 14% and 67% ± 12.8%, respectively, of the ISV displaying two parallel junctions extending along the vessel (Figures S4E and S4G). In *VEC^ubs8*;*Tg(UAS:VECΔC-EGFP)^ubs12* embryos, there was a decrease in the number of vessels segments with two junctions (52.3% ± 23.7%; Figures S4F and S4G) and an increase in variability in the number of parallel junctions (Figure S4G), suggesting a decrease in junctional stability when VEC is not linked to the actin cytoskeleton.

A more prominent effect on junction organization was observed when formin function was inhibited. Knockdown of fmnl3 resulted in discontinuous junctions with only ring-shaped junctions remaining within ISVs and the DLAV (Figure 4D). Occasionally, we observed remnants of a VEC- and ZO1-positive junction devoid of Lifeact (Figure 4D), suggesting that loss of junctional F-actin precedes junction destabilization. Similar discontinuous junction arrangements were also detected after SMIFH2 treatment in 2 dpf embryos (Figure 4F), and increasing the duration of formin inhibition increased the number of junctional gaps within ISVs (Figure 4G). Occasionally, we observed the detachment of cells from each other and disruption to vessel continuity (Figures 1O, 3E, and 3F), suggesting that prolonged decrease in junctional F-actin content can further lead to the disassembly of remaining ring-shaped junctions.

In summary, our results demonstrate a role of formin activity in promoting junctional F-actin assembly that is required for endothelial junction formation and for maintaining junctions in a multicellular configuration.

DISCUSSION

During vessel formation, F-actin cables are assembled and maintained at EC junctions (Fraccaroli et al., 2012; Phng et al., 2013). Here, we show that formin activity is selective for F-actin assembly at EC junctions, which, when depleted, leads to defects in lumen formation and maintenance. FRAP experiments revealed that F-actin cables at endothelial junctions are highly dynamic, show a high turnover rate, and are replenished by continuous actin polymerization to maintain a stable junctional F-actin content. While the half-life of junctional EGFP-Actin is similar in the DA and the PCV (~7 s), the mobile fraction of EGFP-Actin is 10% larger at the junctions of the PCV compared with the DA, suggesting that there is a higher turnover of, and

therefore less stable, junctional F-actin at the PCV. This may explain why junctions in the PCV are more sensitive to SMIFH2 treatment since EGFP-Actin half-life significantly increased in the PCV but not in the DA after formin inhibition. The observation of a complete recovery of the mobile EGFP-Actin fraction under formin inhibition suggests that other actin nucleating factors such as Arp2/3 and Spire contribute to actin assembly in EC junctions and junction stability. Indeed, Arp2/3 was shown to promote junctional actin nucleation at epithelial cell junctions (Kovacs et al., 2011; Tang and Brieher, 2012), and intercellular gaps appear between ECs after Arp2/3 inhibition (Abu Taha et al., 2014). However, other actin nucleators cannot fully compensate for reduced formin activity at EC junctions since we still observe defects in F-actin cable assembly and junction integrity after fmnl3 knockdown or SMIFH2 treatment.

Cadherin complexes exist dynamically to enable changes in cell adhesion, rearrangement, and junction permeability. The formation of cadherin junctions depends on extracellular intercadherin interaction and intracellular cadherin interaction with F-actin (Hong et al., 2013). Cadherins form clusters to strengthen adhesion, a process that requires both dynamic F-actin and myosin II-mediated contraction of F-actin (Ratheesh and Yap, 2012). Although cadherins can interact through *cis*- and *trans*-binding via their ectodomains, these clusters are unstable; it is the ability of cadherin binding to F-actin that stabilizes adherens junctions (Hong et al., 2013; Kametani and Takeichi, 2007; Noda et al., 2010). Thus, cadherin dynamics and adhesion are coupled to F-actin dynamics, and it is likely that the cadherin-actin interaction evolves during vessel morphogenesis.

During lumen formation of angiogenic vessels, ECs rearrange to form a multicellular tube in a process that is tightly associated with junction coalescence and reorganization (Lenard et al., 2013). In contrast, vasculogenic lumen formation commences in a multicellular configuration and involves junctional displacement from the apical to the lateral membrane and apical deadhesion of opposing membranes (Strilić et al., 2009). Intriguingly, although formin inhibition altered junctional F-actin both in ISV and in DA and PCV, angiogenic lumen formation and maintenance in the ISV were fully dependent on formin function. We propose that formin activity maintains a pool of F-actin at endothelial junction that reinforces junction stability by regulating the strength and organization of junctions. This process is critical for endothelial junctions during cellular rearrangements that drive lumen formation and stabilization in angiogenesis.

EXPERIMENTAL PROCEDURES

Fish Maintenance and Stocks

Zebrafish (*Danio rerio*) were raised and staged as previously described (Kimmel et al., 1995). The following transgenic lines were used: *Tg(fli:GFP)^y1* (Lawson and Weinstein, 2002), *Tg(kdr-l:ras-Cherry)^s916* (Hogan et al., 2009), and *Tg(fli1ep:Lifeact-EGFP)* (Phng et al., 2013).

Cloning and Constructs

All constructs were generated using the Tol2Kit (Kwan et al., 2007) and the Multisite Gateway system (Invitrogen). The *fli1ep* promoter (from Nathan Lawson) was used to drive endothelial expression of EGFP-human Actin (Clontech), zebrafish fmnl3 (from Shigetomo Fukuhara and Naoki Mochizuki), and EGFP-DCX (Distel et al., 2010). Fmnl3 was placed under the CMV/SP6 promoter (Kwan et al., 2007) for the generation of *fmnl3* capped mRNA. For inducible expression of fmnl3ΔC, LexPR transactivator was placed under the *fli1ep*
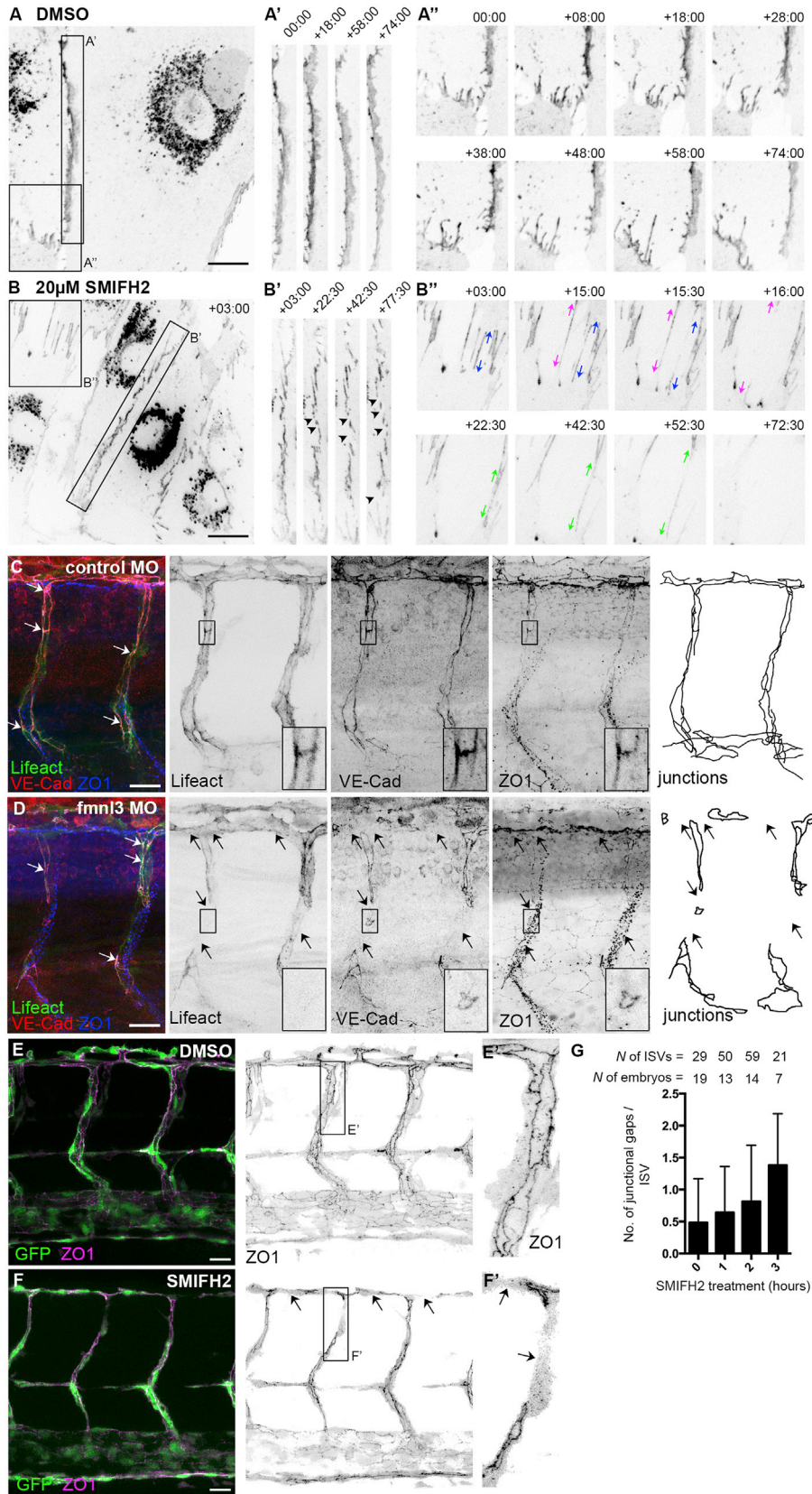
(legend on next page)

promoter, and a second plasmid encoding fmnlΔC was placed under the LexA operator (Emelyanov and Parinov, 2008). Embryos were injected with 25 plasmid and 25 ng/μl transposase RNA. Capped mRNAs were transcribed with the SP6 mMessage mMachine Kit (Ambion). Embryos injected with pDestTol2-*fli1ep*:EGFP-Actin and pDestTol2-*fli1ep*:EGFP-DCX plasmids were raised to adults and screened for founders.

Morpholino Injections, Chemical Treatments, and Microangiography

Ten ng standard control or fmnl3 translation blocking (Hetheridge et al., 2012) antisense morpholino (GeneTools) was injected into the yolk of one- to two-cell stage embryos. SMIFH2 (Merck Millipore) was dissolved in DMSO to 50 mM, stored at −20°C, and diluted in Danieau's Buffer containing 0.4% DMSO (control). To induce gene expression using the LexPR system, embryos were treated with 20 μM mifepristone (Sigma) for 3–4 hr and then washed. To assess vessel perfusion, 2 nl Qdot 705 Quantum Dots (Life Technologies) were injected into the sinus venosus at 2 dpf.

Live Imaging

Live embryos were mounted in 0.8% low melting agarose containing 0.01% Tricaine (Sigma) and bathed in Danieau's buffer. Cells were incubated at 37°C with 5% CO_2. Images and time-lapse movies were acquired using an Andor Revolution 500 spinning disk confocal built on a Nikon TiE inverted microscope; z stacks were flattened by maximum projection unless otherwise stated. Image processing, measurements, and stitching (Preibisch et al., 2009) were performed using ImageJ 1.47j software. XY drifts were corrected by using the StackReg Translation plugin (Thévenaz et al., 1998).

Statistical Analysis

Statistical analyses were performed using chi-squared test or Student's two-tailed t test in Prism 5.0 (GraphPad). A p value $\leq$ 0.05 was considered statistically significant.

SUPPLEMENTAL INFORMATION

Supplemental Information includes Supplemental Experimental Procedures, four figures, and four movies and can be found with this article online at http://dx.doi.org/10.1016/j.devcel.2014.11.017.

AUTHOR CONTRIBUTIONS

L.-K.P. conceived the project, designed and performed experiments, and analyzed data. L-K.P., V.G., T.M., and F.S. performed cell culture experiments. K.B. and A.P. analyzed junctional F-actin cables. A.W. generated *Tg(fli1ep: EGFP-DCX)* zebrafish. L.S., H.-G.B., and M.A. provided reagents. L-K.P. and H.G. wrote the paper.

ACKNOWLEDGMENTS

REFERENCES

Abu Taha, A., Taha, M., Seebach, J., and Schnittler, H.-J. (2014). ARP2/3-mediated junction-associated lamellipodia control VE-cadherin-based cell junction dynamics and maintain monolayer integrity. Mol. Biol. Cell *25*, 245–256.

Axnick, J., and Lammert, E. (2012). Vascular lumen formation. Curr. Opin. Hematol. *19*, 192–198.

Bartolini, F., and Gundersen, G.G. (2010). Formins and microtubules. Biochim. Biophys. Acta *1803*, 164–173.

Bentley, K., Franco, C.A., Philippides, A., Blanco, R., Dierkes, M., Gebala, V., Stanchi, F., Jones, M., Aspalter, I.M., Cagna, G., et al. (2014). The role of differential VE-cadherin dynamics in cell rearrangement during angiogenesis. Nat. Cell Biol. *16*, 309–321.

DeWard, A.D., Eisenmann, K.M., Matheson, S.F., and Alberts, A.S. (2010). The role of formins in human disease. Biochim. Biophys. Acta *1803*, 226–233.

Distel, M., Hocking, J.C., Volkmann, K., and Köster, R.W. (2010). The centrosome neither persistently leads migration nor determines the site of axonogenesis in migrating neurons in vivo. J. Cell Biol. *191*, 875–890.

Emelyanov, A., and Parinov, S. (2008). Mifepristone-inducible LexPR system to drive and control gene expression in transgenic zebrafish. Dev. Biol. *320*, 113–121.

Fraccaroli, A., Franco, C.A., Rognoni, E., Neto, F., Rehberg, M., Aszodi, A., Wedlich-Söldner, R., Pohl, U., Gerhardt, H., and Montanez, E. (2012). Visualization of endothelial actin cytoskeleton in the mouse retina. PLoS ONE *7*, e47488.

Fritzsche, M., Lewalle, A., Duke, T., Kruse, K., and Charras, G. (2013). Analysis of turnover dynamics of the submembranous actin cortex. Mol. Biol. Cell *24*, 757–767.

Halavatyi, A.A., Nazarov, P.V., Al Tanoury, Z., Apanasovich, V.V., Yatskou, M., and Friederich, E. (2010). A mathematical model of actin filament turnover for fitting FRAP data. Eur. Biophys. J. *39*, 669–677.

Harris, E.S., Gauvin, T.J., Heimsath, E.G., and Higgs, H.N. (2010). Assembly of filopodia by the formin FRL2 (FMNL3). Cytoskeleton (Hoboken) *67*, 755–772.

Hayashi, M., Majumdar, A., Li, X., Adler, J., Sun, Z., Vertuani, S., Hellberg, C., Mellberg, S., Koch, S., Dimberg, A., et al. (2013). VE-PTP regulates VEGFR2 activity in stalk cells to establish endothelial cell polarity and lumen formation. Nat. Commun. *4*, 1672.

Herwig, L., Blum, Y., Krudewig, A., Ellertsdottir, E., Lenard, A., Belting, H.-G., and Affolter, M. (2011). Distinct cellular mechanisms of blood vessel fusion in the zebrafish embryo. Curr. Biol. *21*, 1942–1948.

Hetheridge, C., Scott, A.N., Swain, R.K., Copeland, J.W., Higgs, H.N., Bicknell, R., and Mellor, H. (2012). The formin FMNL3 is a cytoskeletal regulator of angiogenesis. J. Cell Sci. *125*, 1420–1428.

Hogan, B.M., Bos, F.L., Bussmann, J., Witte, M., Chi, N.C., Duckers, H.J., and Schulte-Merker, S. (2009). Ccbe1 is required for embryonic lymphangiogenesis and venous sprouting. Nat. Genet. *41*, 396–398.

Figure 4. Formin Activity Is Essential for Junction Stability

(A and B) Still images of VEC-EGFP-expressing HDMEC treated with 0.02% DMSO or 20 μM SMIFH2. Imaging began 5 min after addition of SMIFH2. A′ and B′ show linear junctions. A″ and B″ show FAJs. The arrowheads show gaps within linear junctions, and arrows show the direction of FAJ displacement. Scale bars represents 20 μm.

(C–F) VEC and ZO1 immunostainings in ISVs and DLAV of control and fmnl3 morphants at 53 hpf (C and D) and in 2 dpf *Tg(fli1a:EGFP)*ʸ¹ embryos after 2 hr treatment with DMSO or 10μM SMIFH2 (E and F). Boxed regions in C and D show only endothelial staining. The arrows show junctional gaps. Scale bars represent 20 μm.

(G) Quantification of junctional gaps within ISVs at 0, 1, 2 or 3 hr after 10μM SMIFH2 treatment. Data represent mean ± SD.

See also Figure S4 and Movie S4.

Hong, S., Troyanovsky, R.B., and Troyanovsky, S.M. (2013). Binding to F-actin guides cadherin cluster assembly, stability, and movement. J. Cell Biol. *201*, 131–143.

Hultin, S., Zheng, Y., Mojallal, M., Vertuani, S., Gentili, C., Balland, M., Milloud, R., Belting, H.-G., Affolter, M., Helker, C.S.M., et al. (2014). AmotL2 links VE-cadherin to contractile actin fibres necessary for aortic lumen expansion. Nat. Commun. *5*, 3743.

Huveneers, S., Oldenburg, J., Spanjaard, E., van der Krogt, G., Grigoriev, I., Akhmanova, A., Rehmann, H., and de Rooij, J. (2012). Vinculin associates with endothelial VE-cadherin junctions to control force-dependent remodeling. J. Cell Biol. *196*, 641–652.

Kametani, Y., and Takeichi, M. (2007). Basal-to-apical cadherin flow at cell junctions. Nat. Cell Biol. *9*, 92–98.

Kimmel, C.B., Ballard, W.W., Kimmel, S.R., Ullmann, B., and Schilling, T.F. (1995). Stages of embryonic development of the zebrafish. Dev. Dyn. *203*, 253–310.

Kovacs, E.M., Verma, S., Ali, R.G., Ratheesh, A., Hamilton, N.A., Akhmanova, A., and Yap, A.S. (2011). N-WASP regulates the epithelial junctional actin cytoskeleton through a non-canonical post-nucleation pathway. Nat. Cell Biol. *13*, 934–943.

Kwan, K.M., Fujimoto, E., Grabher, C., Mangum, B.D., Hardy, M.E., Campbell, D.S., Parant, J.M., Yost, H.J., Kanki, J.P., and Chien, C.-B. (2007). The Tol2kit: a multisite gateway-based construction kit for Tol2 transposon transgenesis constructs. Dev. Dyn. *236*, 3088–3099.

Lampugnani, M.G., Orsenigo, F., Rudini, N., Maddaluno, L., Boulday, G., Chapon, F., and Dejana, E. (2010). CCM1 regulates vascular-lumen organization by inducing endothelial polarity. J. Cell Sci. *123*, 1073–1080.

Lawson, N.D., and Weinstein, B.M. (2002). In vivo imaging of embryonic vascular development using transgenic zebrafish. Dev. Biol. *248*, 307–318.

Lenard, A., Ellertsdottir, E., Herwig, L., Krudewig, A., Sauteur, L., Belting, H.-G., and Affolter, M. (2013). In vivo analysis reveals a highly stereotypic morphogenetic pathway of vascular anastomosis. Dev. Cell *25*, 492–506.

Martin, M., Geudens, I., Bruyr, J., Potente, M., Bleuart, A., Lebrun, M., Simonis, N., Deroanne, C., Twizere, J.-C., Soubeyran, P., et al. (2013). PP2A regulatory subunit Bα controls endothelial contractility and vessel lumen integrity via regulation of HDAC7. EMBO J. *32*, 2491–2503.

Montero-Balaguer, M., Swirsding, K., Orsenigo, F., Cotelli, F., Mione, M., and Dejana, E. (2009). Stable vascular connections and remodeling require full expression of VE-cadherin in zebrafish embryos. PLoS ONE *4*, e5772.

Noda, K., Zhang, J., Fukuhara, S., Kunimoto, S., Yoshimura, M., and Mochizuki, N. (2010). Vascular endothelial-cadherin stabilizes at cell-cell junctions by anchoring to circumferential actin bundles through alpha- and beta-catenins in cyclic AMP-Epac-Rap1 signal-activated endothelial cells. Mol. Biol. Cell *21*, 584–596.

Phng, L.K., Stanchi, F., and Gerhardt, H. (2013). Filopodia are dispensable for endothelial tip cell guidance. Development *140*, 4031–4040.

Preibisch, S., Saalfeld, S., and Tomancak, P. (2009). Globally optimal stitching of tiled 3D microscopic image acquisitions. Bioinformatics *25*, 1463–1465.

Ratheesh, A., and Yap, A.S. (2012). A bigger picture: classical cadherins and the dynamic actin cytoskeleton. Nat. Rev. Mol. Cell Biol. *13*, 673–679.

Rizvi, S.A., Neidt, E.M., Cui, J., Feiger, Z., Skau, C.T., Gardel, M.L., Kozmin, S.A., and Kovar, D.R. (2009). Identification and characterization of a small molecule inhibitor of formin-mediated actin assembly. Chem. Biol. *16*, 1158–1168.

Santos-Ledo, A., Jenny, A., and Marlow, F.L. (2012). Comparative gene expression analysis of the fmnl family of formins during zebrafish development and implications for tissue specific functions. Gene Expr. Patterns. *13*, 30–37.

Schönichen, A., and Geyer, M. (2010). Fifteen formins for an actin filament: a molecular view on the regulation of human formins. Biochim. Biophys. Acta *1803*, 152–163.

Strilić, B., Kucera, T., Eglinger, J., Hughes, M.R., McNagny, K.M., Tsukita, S., Dejana, E., Ferrara, N., and Lammert, E. (2009). The molecular basis of vascular lumen formation in the developing mouse aorta. Dev. Cell *17*, 505–515.

Tang, V.W., and Brieher, W.M. (2012). α-Actinin-4/FSGS1 is required for Arp2/3-dependent actin assembly at the adherens junction. J. Cell Biol. *196*, 115–130.

Thévenaz, P., Ruttimann, U.E., and Unser, M. (1998). A pyramid approach to subpixel registration based on intensity. IEEE Trans. Image Process. *7*, 27–41.

Wakayama, Y., Fukuhara, S., Ando, K., Matsuda, M., and Mochizuki, N. (2015). Cdc42 mediates Bmp-induced sprouting angiogenesis through Fmnl3-driven assembly of endothelial filopodia in zebrafish. Dev. Cell *32*, this issue, 109–122.

Wang, Y., Kaiser, M.S., Larson, J.D., Nasevicius, A., Clark, K.J., Wadman, S.A., Roberg-Perez, S.E., Ekker, S.C., Hackett, P.B., McGrail, M., and Essner, J.J. (2010). Moesin1 and Ve-cadherin are required in endothelial cells during in vivo tubulogenesis. Development *137*, 3119–3128.

Xu, K., Sacharidou, A., Fu, S., Chong, D.C., Skaug, B., Chen, Z.J., Davis, G.E., and Cleaver, O. (2011). Blood vessel tubulogenesis requires Rasip1 regulation of GTPase signaling. Dev. Cell *20*, 526–539.

Zovein, A.C., Luque, A., Turlo, K.A., Hofmann, J.J., Yee, K.M., Becker, M.S., Fässler, R., Mellman, I., Lane, T.F., and Iruela-Arispe, M.L. (2010). Beta1 integrin establishes endothelial cell polarity and arteriolar lumen formation via a Par3-dependent mechanism. Dev. Cell *18*, 39–51.

A.4. Ittig S., et al., in preparation

A bacterial type III secretion-based protein delivery tool for broad applications in cell biology

Simon J. Ittig[1], Christoph Schmutz[1], Christoph A. Kasper[1], Marlise Amstutz[1], Alexander Schmidt[1], Loïc Sauteur[1], Alessandra Vigano[1], Shyan Huey Low[1], Markus Affolter[1], Guy R. Cornelis[2], Erich A. Nigg[1] and Cécile Arrieumerlou[1,3,4,5]

[1]: Biozentrum, University of Basel, Klingelbergstrasse 50/70, 4056 Basel, Switzerland
[2]: URBM, Department of Biology, University of Namur, Namur, Belgium
[3]: INSERM, U1016, Institut Cochin, Paris, France
[4]: CNRS, UMR8104, Paris, France
[5]: Université Paris Descartes, Sorbonne Paris Cité, France

Abstract:

Methods enabling the delivery of proteins into eukaryotic cells are essential to address protein functions. Here we propose broad cell biology applications for a protein delivery tool based on bacterial type III secretion (T3S). We show that bacterial, viral and human proteins, fused to the N-terminal fragment of the *Yersinia enterocolitica* T3S substrate YopE, are effectively delivered into target cells in a fast and controllable manner via the injectisome of extracellular bacteria. This method enables functional interaction studies by the injection of multiple proteins simultaneously, and allows targeting intracellular proteins of different sub-cellular locations by translocated functional nanobody fusion proteins. After delivery, proteins can be freed from the YopE fragment by a T3S-translocated viral protease or fusion to ubiquitin and cleavage by endogenous ubiquitin proteases. Finally, we show that this delivery tool is suitable to inject proteins in living animals, and combine it with LC-MS/MS-based phosphoproteomics to characterize the systems-level impact of pro-apoptotic human truncated BID on the cellular network.

A.5. Supplemental discussion: Novel transgenic lines

In the zebrafish field, transgenic reporters have become routine. The establishment of novel transgenic lines allows detailed analysis of developmental processes but also genetic and pharmacological experiments on the scale of a whole organism.

We are interested in the cell behaviors that underlie vascular morphogenesis, which include cell migration, cell shape dynamics and cell division. The complex orchestration of these cell behaviors eventually leads to the formation of vascular tubes, with defined apical-basal polarization. However, how the apical-basal polarization is regulated during angiogenic sprouting is not known. As ECs arrange themselves in a growing sprout, they engage in homotypic manner with neighboring ECs and create new junctions. One important regulator of cell-cell contact formation, next to junctional proteins, is the actin cytoskeleton. And as a consequence of homotypic engagement the ECs have to redefine their polarity: an apical domain at the cell-cell interface.

A.5.1. Apical polarization during angiogenesis

The DA is a tube and each EC in this tube has a defined apical and basolateral polarity. ECs, which receive angiogenic stimuli, leave the tube and loose their apical-basolateral polarity (but gain front-rear polarity instead). New apical compartments form when angiogenic cells form contacts during anastomosis, and these contact sites are enriched with the apical marker Pdxl2. Apical markers also localize to cell-cell interfaces between neighboring stalk cells. How apical polarization is achieved at a molecular level is subject to many research fields and different cellular contexts might use different mechanisms.

In vitro studies showed that single cells are lined with the apical marker Pdxl2 at the cell-ECM boundary. When this single cell divides, the mother and daughter cell remain attached to each other by *de novo* formation of junctions. Integrin-dependent cues initiate the translocation of apical marker (Pdxl2) to

apical membrane initiation sites (AMIS) at the cell-cell interface (Bryant et al., 2014).

For the lumen formation in the mouse dorsal aorta, VE-cad is a prerequisite to localize CD34-sialomucins (a family of membrane proteins, to which Pdxl belongs) to the cell-cell interface (Strilić et al., 2009). In the absence of VE-cad, Pdxl was not targeted to the cell-cell interface in the forming dorsal aorta of mice. Therefore, the authors suggested that VE-cad is involved in the establishment for cell polarity. The requirement of VE-cad for EC polarization in zebrafish has not been investigated, neither for the DA, nor during angiogenic sprouting. However, similar to the loss of VE-cad, the genetic depletion of VE-PTP in mouse and zebrafish leads to the loss of EC polarity (Hayashi et al., 2013). Yet, we do not know if the same accounts for the loss of VE-cad in zebrafish.

The basic idea of having a live apical marker is to observe apical membrane polarization in real time. During anastomosis apical polarization could be induced by *de novo* contact formation, thus homotypic interactions of adhesion molecules. Therefore, an apical live marker and loss of function mutants of junctional components could reveal novel insights into apical polarization processes.

A.5.1.1. Podocalyxin-cherry

One main concern about transgenic lines is if the overexpression of the marker affects development *per se*. Here, the excess of Pdxl2 (remember, endogenous plus ectopic) could increase apical membrane repulsion and lead to abnormal luminal pocket formation. However, the line is viable and maybe due to the mosaic expression of the construct, seems not to induce such aberrant phenotypes. Furthermore, the relatively weak expression of this construct might favor the viability of the transgenic line.

The Pdxl2 construct is fused N-terminally to mCherry, which localizes the fluorescent protein extracellularly. How this affects the properties of the fusion protein I do not know. Ideally, I should have also generated a fish line with a cytoplasmic tagged Pdxl2, at the C-terminus and compared the two lines.

In cell culture, Pdxl is located at the MDCK cysts periphery before it is internalized and targeted to AMIS (Bryant et al., 2010; 2014). The

Tg(U*AS:mCherry-zfpdxl*) shows some spot-like localization in EC but if these spots represent AMIS needs further analysis. Staining endogenous Pdxl2 never indicated spot like localization, but the overall staining is very weak with high background and the EC specific signal is only observed within junctional rings. Therefore, other means to validate the vesicular nature of transgenic mCherry-zfpdxl spots are required.

A.5.1.2. FR-mKate2

In some aspects the FR-mKate2 apical marker behaves in a similar manner as the mCherry-zfpdxl construct. Both transgenic lines show spot-like accumulation, which locate where junctions are expected. In contrast to the mCherry-zfpdxl transgenic line, the FR-mKate2 spots are bigger in size, which could be explained by the stronger expression. But, as described above, more validation is needed to show that these spots represent vesicles that transport the marker to apical compartments.

The FR-mKate2 marker nicely marks the endothelial membrane but unfortunately both, apical and basolateral. Also in cell culture, such fluorescent fusions do not localize exclusively to apical membranes, although they are apically enriched (Paladino et al., 2008). Due to the UAS-dependent expression of the construct, excess protein might be targeted to the membrane. Therefore, the relative signal intensities of apical and basolateral compartments might be reduced and thus similar.

A.5.1.3. Conclusions

Although these apical markers (mCherry-zfpdxl and FR-mKate2) seem to stain the apical membrane, they also localize to the basolateral membrane. This makes these markers difficult to use as sole apical markers. The patches that localize in junction-like spots could represent AMIS, however, these spots are relatively big. Nevertheless, the size could be explained by the overexpression of the UAS-driven constructs. Staining with α-Pdxl2 antibody usually shows relatively weak staining of membrane compartments enclosed by junctions and I never observed AMIS-like spots with immunostains.

Furthermore, the overexpression could also explain the basolateral concentration of the markers, where apical saturation leads to the leaking of

the markers into the basolateral membrane compartments at stages where apical-basal polarity is well established (i.e. when patent lumen has formed).

Finally, these two live markers should localize to apical compartments subsequent to the polarization process and therefore represent a rather late stage of polarization. A marker that visualizes the aggregation of polarization components (e.g. Cdc42) would be state-of-the-art to follow apical membranes *in vivo*. Junctional accumulation of Cdc42, however, might not always coincide with apical-basolateral polarization. Therefore, the polarization process is difficult to observe with a single maker, especially *in vivo*.

A.5.2. Visualization of the actin cytoskeleton during angiogenesis

The actin cytoskeleton is involved in many biological processes. It is not only important for cell migration or cell shape definition, but also is needed for intracellular activities, such as trafficking.

We could show in our studies that the cytoskeleton plays important roles during angiogenesis, where it supports angiogenic sprouting by driving cell elongation, presumably by actin polymerization at cell-cell contacts (at the periphery of the junctions in stalk cells) (Sauteur et al., 2014). Furthermore, the actin cytoskeleton is also important for cell rearrangements and lumen formation. The lumen of vascular tubes is surrounded by ECs that are very flat and the cytoskeleton is probably involved in the maintenance of these cell shapes. Furthermore, junctions are reinforced by F-actin fibers that are polymerized by formins. Therefore, pharmacological inhibition of formins weakens the junctions, leading to the collapse of lumen (Phng et al., 2015). For these reasons the inspection of the actin cytoskeletal architecture helps understand the processes that underlie angiogenesis.

I looked at two different actin live markers: life-act and UCHD.

A.5.2.1. The life-act marker

Life-act is a versatile actin cytoskeleton marker and allows investigation of many different biological processes (Riedl et al., 2008), because it does not

interfere with actin dynamic, which is different for e.g. actin-GFP fusion proteins.

The life-act transgenic line I used to visualize the actin cytoskeleton is a line that was done by the Marina Mione lab and remains unpublished. I crossed this UAS reporter to our Tg(*fli1ep:GFF*)[ubs3] fish and observed the localization of the construct. At later stages, i.e. once lumen has formed and junctions have matured, the fusion protein localized weakly to the junctions. I expected to see more of the actin cytoskeletal architecture, which is predicted for life-act markers. Other labs, like Gerhard Holger or Wiebke Herzog, also generated transgenic zebrafish lines expressing the life-act-EGFP marker. When directly driven by the *fli1a* promoter actin fibers were observed in addition to the junctional localization (Phng et al., 2013). The different promoter and thus expression levels could explain the observed differences between these two lines, where the overexpression covers F-actin specific localization. However, in a similar manner, another UAS-driven life-act-GFP line [Tg(*UAS:lifact-GFP*)[mu271]] was crossed to our Gal4 driver fish (Helker et al., 2013). The resulting transgenic marker localized more to F-actin structures in EC of the CCV when compared to my images. This suggests that the transgenic line we obtained might not be the best transgenic insertion for a life-act marker. One explanation for that is a concatemer (tandem insertion of the transgenic construct). Here multiple tandem copies increase the protein level of the marker to the extent that single fibers become invisible.

A.5.2.2. UCHD as a versatile live-marker

While constructing the red version of UCHD I initially used a fusion to mKate2, because of its stability and high brightness. When I then looked at the localization of the reporter in transiently expressing embryos, I realized that it localized more cytoplasmicly. Although mKate2 is a monomeric fluorescent protein, it altered the localization of the fusion protein. Similar observations were made by Li-Kun Phng (personal communication, former Holger Gerhard lab member). Therefore, different fluorescent proteins fused to the UCHD domain can alter the binding dynamics of the actin binding domain. Finally, I generated an mRuby2-UCHD construct, which showed

similar localization as the EGFP fusion construct and thus did not interfere with the actin binding properties of UCHD.

With the UCHD cytoskeletal markers, we are able to visualize cytoskeletal structures in great detail. Already low magnification, i.e. using a 60x objective, allows the visualization of many cortical actin fibers *in vivo*, which, to my knowledge, has not been achieved to this extent in other studies. These transgenic lines will help to understand the role of the actin cytoskeleton in many different developmental contexts. Yet, we used the marker in ECs, which are relatively big compared to other cell types in zebrafish embryos. Smaller cells will not allow similar subcellular resolution. Even though we could visualize the cortical cytoskeleton of stalk cells, it is sometimes hard to tell two neighboring cells apart, especially, when the junctions have not been stabilized yet. Therefore, the combination with other transgenic lines (e.g. Zo-1 transgenes) is unavoidable.

Furthermore, the UCHD marker allows differentiation between stable and more dynamic actin cytoskeletal structures, if the structures can be isolated spatially, e.g. filopodia. Dynamics within a cell or at the cell-cell boundary (i.e. junctional actin) require the use of photoconvertible UCHD. Here, stable actin structures will be labeled by green fusion protein, while newer (more dynamic) portions will recruit red (photoconverted) protein, as it has been done in cultured cells (Burkel et al., 2007).

Table A- 1: Esama specific staining of animal derived sera

Antibody host	Dilution	Specificity
gp-pre	1:50	None
r1-pre	1:50	None
r2-pre	1:50	None
gp	1:50	Very little
gp	1:200	Little
r1	1:50	Some
r1 preabsorb.	1:200	Good
r2	1:50	Little, but also unspecific

A.6. PCR conditions on genomic *esama* loci

To assess transient mutation in embryos it is crucial to have only a single PCR product amplified. Therefore, different primer combinations were tested with different annealing temperatures; the results are listed Table A- 2.

To be mentioned: in the second intron of *esama*, in proximity of the third exon, there is the occurrence of an allele in wt ABC zebrafish that carries an insertion. Further, since I generated two different TALEN pairs for the third exon, the combination E31 (TALEN_E311 and TALEN_E312) was screened with NcoI (NEB) restriction polymorphism and the combination E32 (TALEN_E321 and TALEN_E322) with the enzyme XmaI (NEB).

Table A- 2: PCR conditions for *esama* loci

esama exon	Primers	Annealing	Extension (with Taq)	Product size	Enzyme
Exon 1	P51, P53	55.5°C	30sec	418bp	HpyCHIV4
Exon 2	P30, P55	60.3°C	30sec	482bp	StyI
Exon 3	P65, P66	54°C	45sec	722bp or 1092bp	E31: NcoI E32: XmaI/SmaI

A.7. Movie legends

Movie AMovie_1:

Time laps movie of ISV outgrowth of a Tg(*fli1ep:GFF*)^{ubs3}(*UAS:EGFP*)(*UAS:pdxl-mCherry*) starting around 24hpf, anterior to the left. On the left hand side both channels are shown (GFP in green and mCherry in red) and on the right hand side the mCherry channel is shown individually in inversed contrast. Single EC express the apical marker and the signal seems to accumulate in the luminal pocket, once lumen forms at the bottom of the ISV. But signal is also observed in the tip cell where at regions where apical membrane is not expected.

Movie AMovie_2:

Time laps movie of a Tg(*fli1ep:GFF*)^{ubs3}(*UAS:eGFP*)(4x*UAS:FR-mKate2*)^{ubs17} embryo starting around 30hpf, anterior to the left. In green the cytoplasmic GFP and in red or in inversed contrast (lower half) the apical marker FR-mKate2. Strong patches of FR-mKate2 aggregate in linear fashion, most probably at junctional interfaces. Sometimes these patches form and dissolve close to luminal compartments. Furthermore weaker signal is observed throughout the cells, which is signal in the membrane, most apparent above nuclei, which are lighter due to fewer superposed membranes.

Movie AMovie_X_3:

Time laps movie of a Tg(*fli1ep:GFF*)^{ubs3}(*UAS:eGFP*)(4x*UAS:FR-mKate2*)^{ubs17} embryo starting around 26hpf, anterior to the left. In green the cytoplasmic GFP and in red or in inversed contrast (lower half) the apical marker FR-mKate2. Strong patches of FR-mKate2 aggregate junction-like (see DA). Sometimes these patches form and dissolve close to luminal compartments. Furthermore weaker signal is observed throughout the cells, which is signal in the membrane, most apparent above nuclei, which are lighter due to fewer superposed membranes.

Movie AMovie_4:

Endothelial cells of the CCV on the yolk of a Tg(*fli1ep:GFF*)^{ubs3}(*UAS:mRFP*)(*4xUAS:EGFP-UCHD*)^{ubs18} at around 40hpf, imaged with a spinning disk confocal microscope (Ultraview). Stacks were acquired every two seconds. This high resolution visualizes the actin cytoskeleton, which is relatively rigid, but also dynamic actin that is being polymerized, as seen in filopodial extensions. To the right of the endothelial cells there is a macrophage passing by very quickly. Scalebar, 5µm.

Movie AMovie_5:

Time laps movie of tip cell ablated ISV of a Tg(*fli1ep:GFF*)^{ubs3}(*UAS:mRFP*)(*UAS:VEcad△C-EGFP*)^{ubs12}, starting around 30hpf, anterior to the left. The ectopic expression of a VE-cad construct, which lacks the cytoplasmic domain and was fused to EGFP (green), prevents the stalk from regenerating after tip cell ablation. Cytoplasmic mRFP (red) shows that the DLAV forms over the ablation area and the lumenization process appears normal too. Furthermore, the tip cell ablated partial sprout is also lumenized, but does not extend during observed time period.

Movie AMovie_6:

Time laps movie of tip cell ablated ISV of a Tg(*tp1:venus-PEST*)^{s940}BAC(*kdrl:mKate2-CAAX*)^{ubs16}, starting around 28hpf, anterior to the left. Top shows merged channels, middle the green tp1 notch reporter and at the top the red vascular specific membrane reporter (mKate2-CAAX). The Notch reporter is expressed in mosaic fashion, the marker labels i.e. only few EC. Furthermore, instead of only marking stalk cells, also tip cells are marked by the Notch reporter.

Movie AMovie_7:

Time laps movie of a Tg(*fli1a:EGFP*)^{y1} embryo starting around 28hpf in inversed contrast, anterior to the left. Tip cells seem to migrate out normally, however, stalk cells are very weakly attached to them and often detach. Furthermore, anastomosis is very inefficient, several filopodial extensions are needed to make contact and thus the process is greatly delayed. Finally, tip cells grow back down and try to make contact to the stalk cells that cluster close to the DA, but seem not to find them (i.e. tip cells that grow down seem to crawl over the stalk cells).

Movie AMovie_8:

Time laps movie of a Tg(*fli1ep:GFF*)^{ubs3}(*UAS:mRFP*) embryo starting around 28hpf in inversed contrast, anterior to the left. This movie shows stereotypical angiogenesis.

Movie AMovie_9:

Time laps movie of a Tg(*fli1a:EGFP*)^{y1} *esama*^{ubs19} embryo starting around 28hpf in inversed contrast, anterior to the left. The lack of Esama does not seem to alter the angiogenic cell behaviors or processes and is thus comparable to wt embryos.

Movie AMovie_10:

Time laps movie of a Tg(*fli1a:EGFP*)^{y1} *ve-cad*^{ubs8} embryo starting around 28hpf in inversed contrast, anterior to the left. The absence of VE-cad results in weak tip to stalk cell attachments and anastomosis is inefficient (resulting in multiple filopodial contacts). Furthermore, the lack of blood flow prevents the proper lumenization of ISVs.

Movie AMovie_11:

Time laps movie of a Tg(*fli1a:EGFP*)^{y1} *ve-cad*^{ubs8} *esama*^{ubs19} embryo starting around 28hpf in inversed contrast, anterior to the left. The absence of both junctional components worsens the phenotypes observed in the *ve-cad* mutant. Leading to more tip from stalk cell detachments, reduced tip cell recognition during anastomosis and in addition, the cell morphology of sprouting ECs is disturbed. The cell extensions appear thicker than the usual filopodia (compare to wt and *ve-cad*^{ubs8} movies). Furthermore, the migration polarity seems disturbed, leading to growth of tip cells into dorsally located somitic tissue. And finally, the double mutant seems unable to recover from the cell detachments, leaving the vasculature broken, while *ve-cad* mutants stalk cells reconnected to tip cells.

References

References

Abraham, S., Yeo, M., Montero-Balaguer, M., Paterson, H., Dejana, E., Marshall, C.J., and Mavria, G. (2009). VE-Cadherin-Mediated Cell-Cell Interaction Suppresses Sprouting via Signaling to MLC2 Phosphorylation. Curr. Biol. *19*, 668–674.

Abu Taha, A., Taha, M., Seebach, J., and Schnittler, H.-J. (2014). ARP2/3-mediated junction-associated lamellipodia control VE-cadherin-based cell junction dynamics and maintain monolayer integrity. Mol. Biol. Cell *25*, 245–256.

Affolter, M., Zeller, R., and Caussinus, E. (2009). Tissue remodelling through branching morphogenesis. Nat. Rev. Mol. Cell Biol. *10*, 831–842.

Akitake, C.M., Macurak, M., Halpern, M.E., and Goll, M.G. (2011). Transgenerational analysis of transcriptional silencing in zebrafish. Developmental Biology *352*, 191–201.

Andersson, E.R., Sandberg, R., and Lendahl, U. (2011). Notch signaling: simplicity in design, versatility in function. Development *138*, 3593–3612.

Arima, S., Nishiyama, K., Ko, T., Arima, Y., Hakozaki, Y., Sugihara, K., Koseki, H., Uchijima, Y., Kurihara, Y., and Kurihara, H. (2011). Angiogenic morphogenesis driven by dynamic and heterogeneous collective endothelial cell movement. Development *138*, 4763–4776.

Asakawa, K., Suster, M.L., Mizusawa, K., Nagayoshi, S., Kotani, T., Urasaki, A., Kishimoto, Y., Hibi, M., and Kawakami, K. (2008). Genetic dissection of neural circuits by Tol2 transposon-mediated Gal4 gene and enhancer trapping in zebrafish. Proc. Natl. Acad. Sci. U.S.a. *105*, 1255–1260.

Auer, T.O., Duroure, K., De Cian, A., Concordet, J.-P., and Del Bene, F. (2014). Highly efficient CRISPR/Cas9-mediated knock-in in zebrafish by homology-independent DNA repair. Genome Research *24*, 142–153.

Baer, M.M., Chanut-Delalande, H., and Affolter, M. (2009). Cellular and molecular mechanisms underlying the formation of biological tubes. Curr. Top. Dev. Biol. *89*, 137–162.

Bayless, K.J., Salazar, R., and Davis, G.E. (2000). RGD-dependent vacuolation and lumen formation observed during endothelial cell morphogenesis in three-dimensional fibrin matrices involves the alpha(v)beta(3) and alpha(5)beta(1) integrins. The American Journal of Pathology *156*, 1673–1683.

Bedell, V.M., Wang, Y., Campbell, J.M., Poshusta, T.L., Starker, C.G., Krug, R.G., Tan, W., Penheiter, S.G., Ma, A.C., Leung, A.Y.H., et al. (2012). In vivo genome editing using a high-efficiency TALEN system. Nature *491*, 114–118.

Bedell, V.M., Westcot, S.E., and Ekker, S.C. (2011). Lessons from morpholino-based screening in zebrafish. Brief Funct Genomics *10*, 181–188.

Bedell, V.M., Yeo, S.-Y., Park, K.W., Chung, J., Seth, P., Shivalingappa, V., Zhao, J., Obara, T., Sukhatme, V.P., Drummond, I.A., et al. (2005). roundabout4 is essential for angiogenesis in vivo. Proc. Natl. Acad. Sci. U.S.a. *102*, 6373–6378.

Benedito, R., and Hellström, M. (2013). Notch as a hub for signaling in angiogenesis. Experimental Cell Research *319*, 1281–1288.

Benedito, R., Trindade, A., Hirashima, M., Henrique, D., da Costa, L., Rossant, J., Gill, P.S., and Duarte, A. (2008). Loss of Notch signalling induced by Dll4 causes arterial calibre reduction by increasing endothelial cell response to angiogenic stimuli. BMC Dev Biol *8*, 117.

Bentley, K., Franco, C.A., Philippides, A., Blanco, R., Dierkes, M., Gebala, V., Stanchi, F., Jones, M., Aspalter, I.M., Cagna, G., et al. (2014). The role of differential VE-cadherin dynamics in cell rearrangement during angiogenesis. Nat Cell Biol *16*, 309–321.

Bill, B.R., Petzold, A.M., Clark, K.J., Schimmenti, L.A., and Ekker, S.C. (2009). A

242

Primer for Morpholino Use in Zebrafish. Zebrafish *6*, 69–77.

Blum, Y., Belting, H.-G., Ellertsdóttir, E., Herwig, L., Lüders, F., and Affolter, M. (2008). Complex cell rearrangements during intersegmental vessel sprouting and vessel fusion in the zebrafish embryo. Developmental Biology *316*, 312–322.

Boch, J., Scholze, H., Schornack, S., Landgraf, A., Hahn, S., Kay, S., Lahaye, T., Nickstadt, A., and Bonas, U. (2009). Breaking the code of DNA binding specificity of TAL-type III effectors. Science *326*, 1509–1512.

Bogdanove, A.J., Schornack, S., and Lahaye, T. (2010). TAL effectors: finding plant genes for disease and defense. Curr. Opin. Plant Biol. *13*, 394–401.

Boguslavsky, S., Grosheva, I., Landau, E., Shtutman, M., Cohen, M., Arnold, K., Feinstein, E., Geiger, B., and Bershadsky, A. (2007). p120 catenin regulates lamellipodial dynamics and cell adhesion in cooperation with cortactin. Proc. Natl. Acad. Sci. U.S.a. *104*, 10882–10887.

Bravi, L., Dejana, E., and Lampugnani, M.G. (2014). VE-cadherin at a glance. Cell Tissue Res *355*, 515–522.

Bryant, D.M., Datta, A., Rodríguez-Fraticelli, A.E., Peränen, J., Martín-Belmonte, F., and Mostov, K.E. (2010). A molecular network for de novo generation of the apical surface and lumen. Nat Cell Biol *12*, 1035–1045.

Bryant, D.M., Roignot, J., Datta, A., Overeem, A.W., Kim, M., Yu, W., Peng, X., Eastburn, D.J., Ewald, A.J., Werb, Z., et al. (2014). A molecular switch for the orientation of epithelial cell polarization. Developmental Cell *31*, 171–187.

Burkel, B.M., Dassow, von, G., and Bement, W.M. (2007). Versatile fluorescent probes for actin filaments based on the actin-binding domain of utrophin. Cell Motil. Cytoskeleton *64*, 822–832.

Bussmann, J., Wolfe, S.A., and Siekmann, A.F. (2011). Arterial-venous network formation during brain vascularization involves hemodynamic regulation of chemokine signaling. Development *138*, 1717–1726.

Cangara, H.M., Ishida, T., Hara, T., Sun, L., Toh, R., Rikitake, Y., Kundu, R.K., Quertermous, T., Hirata, K.-I., and Hayashi, Y. (2010). Role of endothelial cell-selective adhesion molecule in hematogeneous metastasis. Microvascular Research *80*, 133–141.

Carlson, D.F., Tan, W., Lillico, S.G., Stverakova, D., Proudfoot, C., Christian, M., Voytas, D.F., Long, C.R., Whitelaw, C.B.A., and Fahrenkrug, S.C. (2012). Efficient TALEN-mediated gene knockout in livestock. Proc. Natl. Acad. Sci. U.S.a. *109*, 17382–17387.

Carmeliet, P., Lampugnani, M.G., Moons, L., Breviario, F., Compernolle, V., Bono, F., Balconi, G., Spagnuolo, R., Oosthuyse, B., Dewerchin, M., et al. (1999). Targeted deficiency or cytosolic truncation of the VE-cadherin gene in mice impairs VEGF-mediated endothelial survival and angiogenesis. Cell *98*, 147–157.

Carroll, D. (2014). Genome engineering with targetable nucleases. Annu. Rev. Biochem. *83*, 409–439.

Caveda, L., Martin-Padura, I., Navarro, P., Breviario, F., Corada, M., Gulino, D., Lampugnani, M.G., and Dejana, E. (1996). Inhibition of cultured cell growth by vascular endothelial cadherin (cadherin-5/VE-cadherin). J. Clin. Invest. *98*, 886–893.

Cermak, T., Doyle, E.L., Christian, M., Wang, L., Zhang, Y., Schmidt, C., Baller, J.A., Somia, N.V., Bogdanove, A.J., and Voytas, D.F. (2011). Efficient design and assembly of custom TALEN and other TAL effector-based constructs for DNA targeting. Nucleic Acids Research *39*, e82.

References

Chakrabarti, S., Streisinger, G., Singer, F., and Walker, C. (1983). Frequency of gamma-Ray Induced Specific Locus and Recessive Lethal Mutations in Mature Germ Cells of the Zebrafish, BRACHYDANIO RERIO. Genetics *103*, 109–123.

Chapman, J.R., Taylor, M.R.G., and Boulton, S.J. (2012). Playing the end game: DNA double-strand break repair pathway choice. Mol. Cell *47*, 497–510.

Chappell, J.C., Mouillesseaux, K.P., and Bautch, V.L. (2013). Flt-1 (vascular endothelial growth factor receptor-1) is essential for the vascular endothelial growth factor-Notch feedback loop during angiogenesis. Arteriosclerosis, Thrombosis, and Vascular Biology *33*, 1952–1959.

Chappell, J.C., Taylor, S.M., Ferrara, N., and Bautch, V.L. (2009). Local guidance of emerging vessel sprouts requires soluble Flt-1. Developmental Cell *17*, 377–386.

Charpentier, E., and Marraffini, L.A. (2014). Harnessing CRISPR-Cas9 immunity for genetic engineering. Curr. Opin. Microbiol. *19C*, 114–119.

Chen, Q., Jiang, L., Li, C., Hu, D., Bu, J.-W., Cai, D., and Du, J.-L. (2012). Haemodynamics-driven developmental pruning of brain vasculature in zebrafish. Plos Biol *10*, e1001374.

Childs, S., Chen, J.-N., Garrity, D.M., and Fishman, M.C. (2002). Patterning of angiogenesis in the zebrafish embryo. Development *129*, 973–982.

Christian, M., Cermak, T., Doyle, E.L., Schmidt, C., Zhang, F., Hummel, A., Bogdanove, A.J., and Voytas, D.F. (2010). Targeting DNA double-strand breaks with TAL effector nucleases. Genetics *186*, 757–761.

Clasper, S., Royston, D., Baban, D., Cao, Y., Ewers, S., Butz, S., Vestweber, D., and Jackson, D.G. (2008). A novel gene expression profile in lymphatics associated with tumor growth and nodal metastasis. Cancer Research *68*, 7293–7303.

Clevers, H., and Nusse, R. (2012). Wnt/β-catenin signaling and disease. Cell *149*, 1192–1205.

Cong, L., Ran, F.A., Cox, D., Lin, S., Barretto, R., Habib, N., Hsu, P.D., Wu, X., Jiang, W., Marraffini, L.A., et al. (2013). Multiplex genome engineering using CRISPR/Cas systems. Science *339*, 819–823.

Conway, D.E., Breckenridge, M.T., Hinde, E., Gratton, E., Chen, C.S., and Schwartz, M.A. (2013). Fluid shear stress on endothelial cells modulates mechanical tension across VE-cadherin and PECAM-1. Curr. Biol. *23*, 1024–1030.

Corada, M., Zanetta, L., Orsenigo, F., Breviario, F., Lampugnani, M.G., Bernasconi, S., Liao, F., Hicklin, D.J., Bohlen, P., and Dejana, E. (2002). A monoclonal antibody to vascular endothelial-cadherin inhibits tumor angiogenesis without side effects on endothelial permeability. Blood *100*, 905–911.

Covassin, L.D., Villefranc, J.A., Kacergis, M.C., Weinstein, B.M., and Lawson, N.D. (2006). Distinct genetic interactions between multiple Vegf receptors are required for development of different blood vessel types in zebrafish. Proc. Natl. Acad. Sci. U.S.a. *103*, 6554–6559.

Dejana, E., Orsenigo, F., and Lampugnani, M.G. (2008). The role of adherens junctions and VE-cadherin in the control of vascular permeability. Journal of Cell Science *121*, 2115–2122.

Dejana, E. (2004). Endothelial cell-cell junctions: happy together. Nat. Rev. Mol. Cell Biol. *5*, 261–270.

Dejana, E., Tournier-Lasserve, E., and Weinstein, B.M. (2009). The Control of Vascular Integrity by Endothelial Cell Junctions: Molecular Basis and Pathological Implications. Developmental Cell *16*, 209–221.

Deng, D., Yan, C., Wu, J., Pan, X., and Yan, N. (2014). Revisiting the TALE repeat. Protein Cell *5*, 297–306.

Desai, R.A., Gao, L., Raghavan, S., Liu, W.F., and Chen, C.S. (2009). Cell polarity triggered by cell-cell adhesion via E-cadherin. Journal of Cell Science *122*, 905–911.

Djonov, V.G., Kurz, H., and Burri, P.H. (2002). Optimality in the developing vascular system: branching remodeling by means of intussusception as an efficient adaptation mechanism. Dev. Dyn. *224*, 391–402.

Dorrell, M.I., and Friedlander, M. (2006). Mechanisms of endothelial cell guidance and vascular patterning in the developing mouse retina. Progress in Retinal and Eye Research *25*, 277–295.

Doyon, Y., McCammon, J.M., Miller, J.C., Faraji, F., Ngo, C., Katibah, G.E., Amora, R., Hocking, T.D., Zhang, L., Rebar, E.J., et al. (2008). Heritable targeted gene disruption in zebrafish using designed zinc-finger nucleases. Nat Biotechnol *26*, 702–708.

Driever, W., Solnica-Krezel, L., Schier, A.F., Neuhauss, S.C., Malicki, J., Stemple, D.L., Stainier, D.Y., Zwartkruis, F., Abdelilah, S., Rangini, Z., et al. (1996). A genetic screen for mutations affecting embryogenesis in zebrafish. Development *123*, 37–46.

Ebnet, K. (2008). Organization of multiprotein complexes at cell–cell junctions. Histochem Cell Biol *130*, 1–20.

Ebnet, K., Aurrand-Lions, M., Kuhn, A., Kiefer, F., Butz, S., Zander, K., Meyer zu Brickwedde, M.-K., Suzuki, A., Imhof, B.A., and Vestweber, D. (2003). The junctional adhesion molecule (JAM) family members JAM-2 and JAM-3 associate with the cell polarity protein PAR-3: a possible role for JAMs in endothelial cell polarity. Journal of Cell Science *116*, 3879–3891.

Ebnet, K., Suzuki, A., Ohno, S., and Vestweber, D. (2004). Junctional adhesion molecules (JAMs): more molecules with dual functions? Journal of Cell Science *117*, 19–29.

Eisen, J.S., and Smith, J.C. (2008). Controlling morpholino experiments: don't stop making antisense. Development *135*, 1735–1743.

Ellertsdóttir, E., Lenard, A., Blum, Y., Krudewig, A., Herwig, L., Affolter, M., and Belting, H.-G. (2010). Vascular morphogenesis in the zebrafish embryo. Developmental Biology *341*, 56–65.

Esser, S., Lampugnani, M.G., Corada, M., Dejana, E., and Risau, W. (1998). Vascular endothelial growth factor induces VE-cadherin tyrosine phosphorylation in endothelial cells. Journal of Cell Science *111 (Pt 13)*, 1853–1865.

Fantin, A., Vieira, J.M., Gestri, G., Denti, L., Schwarz, Q., Prykhozhij, S., Peri, F., Wilson, S.W., and Ruhrberg, C. (2010). Tissue macrophages act as cellular chaperones for vascular anastomosis downstream of VEGF-mediated endothelial tip cell induction. Blood *116*, 829–840.

Farhadifar, R., Röper, J.-C., Aigouy, B., Eaton, S., and Jülicher, F. (2007). The Influence of Cell Mechanics, Cell-Cell Interactions, and Proliferation on Epithelial Packing. Current Biology *17*, 2095–2104.

Favier, B., Alam, A., Barron, P., Bonnin, J., Laboudie, P., Fons, P., Mandron, M., Hérault, J.-P., Neufeld, G., Savi, P., et al. (2006). Neuropilin-2 interacts with VEGFR-2 and VEGFR-3 and promotes human endothelial cell survival and migration. Blood *108*, 1243–1250.

Feng, Y., Santoriello, C., Mione, M., Hurlstone, A., and Martin, P. (2010). Live imaging of innate immune cell sensing of transformed cells in zebrafish larvae: parallels between tumor initiation and wound inflammation. Plos Biol *8*, e1000562.

Fu, Y., Sander, J.D., Reyon, D., Cascio, V.M., and Joung, J.K. (2014). Improving

References

CRISPR-Cas nuclease specificity using truncated guide RNAs. Nat Biotechnol *32*, 279–284.

Funahashi, Y., Shawber, C.J., Vorontchikhina, M., Sharma, A., Outtz, H.H., and Kitajewski, J. (2010). Notch regulates the angiogenic response via induction of VEGFR-1. J Angiogenes Res *2*, 3.

García-Vilas, J.A., Quesada, A.R., and Medina, M.Á. (2013). 4-methylumbelliferone inhibits angiogenesis in vitro and in vivo. J. Agric. Food Chem. *61*, 4063–4071.

Garrido-Urbani, S., Bradfield, P.F., and Imhof, B.A. (2014). Tight junction dynamics: the role of junctional adhesion molecules (JAMs). Cell Tissue Res *355*, 701–715.

Gavard, J., and Gutkind, J.S. (2006). VEGF controls endothelial-cell permeability by promoting the beta-arrestin-dependent endocytosis of VE-cadherin. Nat Cell Biol *8*, 1223–1234.

Gerhardt, H., Golding, M., Fruttiger, M., Ruhrberg, C., Lundkvist, A., Abramsson, A., Jeltsch, M., Mitchell, C., Alitalo, K., Shima, D., et al. (2003). VEGF guides angiogenic sprouting utilizing endothelial tip cell filopodia. The Journal of Cell Biology *161*, 1163–1177.

Goldstein, B., and Macara, I.G. (2007). The PAR proteins: fundamental players in animal cell polarization. Developmental Cell *13*, 609–622.

Grzegorski, S.J., Chiari, E.F., Robbins, A., Kish, P.E., and Kahana, A. (2014). Natural Variability of Kozak Sequences Correlates with Function in a Zebrafish Model. PLoS ONE *9*, e108475.

Gu, C., Rodriguez, E.R., Reimert, D.V., Shu, T., Fritzsch, B., Richards, L.J., Kolodkin, A.L., and Ginty, D.D. (2003). Neuropilin-1 conveys semaphorin and VEGF signaling during neural and cardiovascular development. Developmental Cell *5*, 45–57.

Haffter, P., Granato, M., Brand, M., Mullins, M.C., Hammerschmidt, M., Kane, D.A., Odenthal, J., van Eeden, F.J., Jiang, Y.J., Heisenberg, C.P., et al. (1996). The identification of genes with unique and essential functions in the development of the zebrafish, Danio rerio. Development *123*, 1–36.

Hara, T., Ishida, T., Cangara, H.M., and Hirata, K.-I. (2009). Endothelial cell-selective adhesion molecule regulates albuminuria in diabetic nephropathy. Microvascular Research *77*, 348–355.

Harris, E.S., and Nelson, W.J. (2010). VE-cadherin: at the front, center, and sides of endothelial cell organization and function. Curr. Opin. Cell Biol. *22*, 651–658.

Hayashi, M., Majumdar, A., Li, X., Adler, J., Sun, Z., Vertuani, S., Hellberg, C., Mellberg, S., Koch, S., Dimberg, A., et al. (2013). VE-PTP regulates VEGFR2 activity in stalk cells to establish endothelial cell polarity and lumen formation. Nat Commun *4*, 1672.

Helker, C.S.M., Schuermann, A., Karpanen, T., Zeuschner, D., Belting, H.-G., Affolter, M., Schulte-Merker, S., and Herzog, W. (2013). The zebrafish common cardinal veins develop by a novel mechanism: lumen ensheathment. Development *140*, 2776–2786.

Hellström, M., Phng, L.-K., Hofmann, J.J., Wallgard, E., Coultas, L., Lindblom, P., Alva, J., Nilsson, A.-K., Karlsson, L., Gaiano, N., et al. (2007). Dll4 signalling through Notch1 regulates formation of tip cells during angiogenesis. Nature *445*, 776–780.

Herbert, S.P., Huisken, J., Kim, T.N., Feldman, M.E., Houseman, B.T., Wang, R.A., Shokat, K.M., and Stainier, D.Y.R. (2009). Arterial-Venous Segregation by Selective Cell Sprouting: An Alternative Mode of Blood Vessel Formation. Science *326*, 294–298.

Herwig, L., Blum, Y., Krudewig, A., Ellertsdóttir, E., Lenard, A., Belting, H.-G., and

Affolter, M. (2011). Distinct cellular mechanisms of blood vessel fusion in the zebrafish embryo. Curr. Biol. *21*, 1942–1948.

Hirata Ki, Ishida, T., Penta, K., Rezaee, M., Yang, E., Wohlgemuth, J., and Quertermous, T. (2001). Cloning of an immunoglobulin family adhesion molecule selectively expressed by endothelial cells. J. Biol. Chem. *276*, 16223–16231.

Hodkinson, P.S., Elliott, P.A., Lad, Y., McHugh, B.J., MacKinnon, A.C., Haslett, C., and Sethi, T. (2007). Mammalian NOTCH-1 activates beta1 integrins via the small GTPase R-Ras. J. Biol. Chem. *282*, 28991–29001.

Hogan, B.M., Bos, F.L., Bussmann, J., Witte, M., Chi, N.C., Duckers, H.J., and Schulte-Merker, S. (2009). ccbe1 is required for embryonic lymphangiogenesis and venous sprouting. Nat. Genet. *41*, 396–398.

Holderfield, M.T., Henderson Anderson, A.M., Kokubo, H., Chin, M.T., Johnson, R.L., and Hughes, C.C.W. (2006). HESR1/CHF2 suppresses VEGFR2 transcription independent of binding to E-boxes. Biochemical and Biophysical Research Communications *346*, 637–648.

Huang, P., Xiao, A., Zhou, M., Zhu, Z., Lin, S., and Zhang, B. (2011). Heritable gene targeting in zebrafish using customized TALENS. Nat Biotechnol *29*, 699–700.

Huveneers, S., Oldenburg, J., Spanjaard, E., van der Krogt, G., Grigoriev, I., Akhmanova, A., Rehmann, H., and de Rooij, J. (2012). Vinculin associates with endothelial VE-cadherin junctions to control force-dependent remodeling. The Journal of Cell Biology *196*, 641–652.

Hwang, W.Y., Fu, Y., Reyon, D., Maeder, M.L., Tsai, S.Q., Sander, J.D., Peterson, R.T., Yeh, J.-R.J., and Joung, J.K. (2013). Efficient genome editing in zebrafish using a CRISPR-Cas system. Nat Biotechnol *31*, 227–229.

Hwang, W.Y., Peterson, R.T., and Yeh, J.-R.J. (2014). Methods for targeted mutagenesis in zebrafish using TALENS. Methods *69*, 76–84.

Inoue, M., Ishida, T., Yasuda, T., Toh, R., Hara, T., Cangara, H.M., Rikitake, Y., Taira, K., Sun, L., Kundu, R.K., et al. (2010). Endothelial cell-selective adhesion molecule modulates atherosclerosis through plaque angiogenesis and monocyte-endothelial interaction. Microvascular Research *80*, 179–187.

Irie, K., Shimizu, K., Sakisaka, T., Ikeda, W., and Takai, Y. (2004). Roles and modes of action of nectins in cell-cell adhesion. Semin Cell Dev Biol *15*, 643–656.

Iruela-Arispe, M.L., and Davis, G.E. (2009). Cellular and molecular mechanisms of vascular lumen formation. Developmental Cell *16*, 222–231.

Ishida, T., Kundu, R.K., Yang, E., Hirata, K.-I., Ho, Y.-D., and Quertermous, T. (2003). Targeted disruption of endothelial cell-selective adhesion molecule inhibits angiogenic processes in vitro and in vivo. J. Biol. Chem. *278*, 34598–34604.

Isogai, S. (2003). Angiogenic network formation in the developing vertebrate trunk. Development *130*, 5281–5290.

Isogai, S., Horiguchi, M., and Weinstein, B.M. (2001). The vascular anatomy of the developing zebrafish: an atlas of embryonic and early larval development. Developmental Biology *230*, 278–301.

Jakobsson, L., Franco, C.A., Bentley, K., Collins, R.T., Ponsioen, B., Aspalter, I.M., Rosewell, I., Busse, M., Thurston, G., Medvinsky, A., et al. (2010). Endothelial cells dynamically compete for the tip cell position during angiogenic sprouting. Nat Cell Biol *12*, 943–953.

Jao, L.-E., Wente, S.R., and Chen, W. (2013). Efficient multiplex biallelic zebrafish genome editing using a CRISPR nuclease system. Proc. Natl. Acad. Sci. U.S.a. *110*, 13904–13909.

Jin, S.-W., Beis, D., Mitchell, T., Chen, J.-N., and Stainier, D.Y.R. (2005). Cellular

and molecular analyses of vascular tube and lumen formation in zebrafish. Development *132*, 5199–5209.

Jin, S.-W., Herzog, W., Santoro, M.M., Mitchell, T.S., Frantsve, J., Jungblut, B., Beis, D., Scott, I.C., D'Amico, L.A., and Ober, E.A. (2007). A transgene-assisted genetic screen identifies essential regulators of vascular development in vertebrate embryos. Developmental Biology *307*, 29–42.

Jinek, M., Chylinski, K., Fonfara, I., Hauer, M., Doudna, J.A., and Charpentier, E. (2012). A programmable dual-RNA-guided DNA endonuclease in adaptive bacterial immunity. Science *337*, 816–821.

Kacso, I.M., Bondor, C.I., and Kacso, G. (2013). Low serum endothelial cell-selective adhesion molecule predicts increase in albuminuria in type 2 diabetes patients. Int Urol Nephrol *45*, 1319–1326.

Kaipainen, A., Korhonen, J., Mustonen, T., van Hinsbergh, V.W., Fang, G.H., Dumont, D., Breitman, M., and Alitalo, K. (1995). Expression of the fms-like tyrosine kinase 4 gene becomes restricted to lymphatic endothelium during development. Proc. Natl. Acad. Sci. U.S.a. *92*, 3566–3570.

Kamei, M., Saunders, W.B., Bayless, K.J., Dye, L., Davis, G.E., and Weinstein, B.M. (2006). Endothelial tubes assemble from intracellular vacuoles in vivo. Nature *442*, 453–456.

Kao, H.Y., Ordentlich, P., Koyano-Nakagawa, N., Tang, Z., Downes, M., Kintner, C.R., Evans, R.M., and Kadesch, T. (1998). A histone deacetylase corepressor complex regulates the Notch signal transduction pathway. Genes & Development *12*, 2269–2277.

Kappas, N.C., Zeng, G., Chappell, J.C., Kearney, J.B., Hazarika, S., Kallianos, K.G., Patterson, C., Annex, B.H., and Bautch, V.L. (2008). The VEGF receptor Flt-1 spatially modulates Flk-1 signaling and blood vessel branching. The Journal of Cell Biology *181*, 847–858.

Kawakami, K., Shima, A., and Kawakami, N. (2000). Identification of a functional transposase of the Tol2 element, an Ac-like element from the Japanese medaka fish, and its transposition in the zebrafish germ lineage. Proc. Natl. Acad. Sci. U.S.a. *97*, 11403–11408.

Kearney, J.B., Kappas, N.C., Ellerstrom, C., DiPaola, F.W., and Bautch, V.L. (2004). The VEGF receptor flt-1 (VEGFR-1) is a positive modulator of vascular sprout formation and branching morphogenesis. Blood *103*, 4527–4535.

Kendall, R.L., and Thomas, K.A. (1993). Inhibition of vascular endothelial cell growth factor activity by an endogenously encoded soluble receptor. Proc. Natl. Acad. Sci. U.S.a. *90*, 10705–10709.

Kettleborough, R.N.W., Busch-Nentwich, E.M., Harvey, S.A., Dooley, C.M., de Bruijn, E., van Eeden, F., Sealy, I., White, R.J., Herd, C., Nijman, I.J., et al. (2013). A systematic genome-wide analysis of zebrafish protein-coding gene function. Nature *496*, 494–497.

Khandoga, A., Huettinger, S., Khandoga, A.G., Li, H., Butz, S., Jauch, K.-W., Vestweber, D., and Krombach, F. (2009). Leukocyte transmigration in inflamed liver: A role for endothelial cell-selective adhesion molecule. J. Hepatol. *50*, 755–765.

Kimmel, C.B., Ballard, W.W., Kimmel, S.R., Ullmann, B., and Schilling, T.F. (1995). Stages of embryonic development of the zebrafish. Dev. Dyn. *203*, 253–310.

Kimura, R., Ishida, T., Kuriyama, M., Hirata, K.-I., and Hayashi, Y. (2010). Interaction of endothelial cell-selective adhesion molecule and MAGI-1 promotes mature cell-cell adhesion via activation of RhoA. Genes to Cells *15*, 385–396.

Koch, S., Tugues, S., Li, X., Gualandi, L., and Claesson-Welsh, L. (2011). Signal

transduction by vascular endothelial growth factor receptors. Biochem. J. *437*, 169–183.

Kochhan, E., Lenard, A., Ellertsdóttir, E., Herwig, L., Affolter, M., Belting, H.-G., and Siekmann, A.F. (2013). Blood Flow Changes Coincide with Cellular Rearrangements during Blood Vessel Pruning in Zebrafish Embryos. PLoS ONE *8*, e75060.

Kok, F.O., Shin, M., Ni, C.-W., Gupta, A., Grosse, A.S., van Impel, A., Kirchmaier, B.C., Peterson-Maduro, J., Kourkoulis, G., Male, I., et al. (2015). Reverse Genetic Screening Reveals Poor Correlation between Morpholino-Induced and Mutant Phenotypes in Zebrafish. Developmental Cell *32*, 97–108.

Kouklis, P., Konstantoulaki, M., and Malik, A.B. (2003). VE-cadherin-induced Cdc42 signaling regulates formation of membrane protrusions in endothelial cells. J. Biol. Chem. *278*, 16230–16236.

Kovacs, E.M., Goodwin, M., Ali, R.G., Paterson, A.D., and Yap, A.S. (2002). Cadherin-directed actin assembly: E-cadherin physically associates with the Arp2/3 complex to direct actin assembly in nascent adhesive contacts. Curr. Biol. *12*, 379–382.

Kraemer, A., Goodwin, M., Verma, S., Yap, A.S., and Ali, R.G. (2007). Rac is a dominant regulator of cadherin-directed actin assembly that is activated by adhesive ligation independently of Tiam1. Am. J. Physiol., Cell Physiol. *292*, C1061–C1069.

Krudewig, A. (2012). Junctional remodeling during angiogenesis : the role of Claudin5 during ISV formation in Zebrafish. PhD Thesis 1–182.

Krueger, J., Liu, D., Scholz, K., Zimmer, A., Shi, Y., Klein, C., Siekmann, A., Schulte-Merker, S., Cudmore, M., Ahmed, A., et al. (2011). Flt1 acts as a negative regulator of tip cell formation and branching morphogenesis in the zebrafish embryo. Development *138*, 2111–2120.

Kwan, K.M., Fujimoto, E., Grabher, C., Mangum, B.D., Hardy, M.E., Campbell, D.S., Parant, J.M., Yost, H.J., Kanki, J.P., and Chien, C.-B. (2007). The Tol2kit: a multisite gateway-based construction kit for Tol2 transposon transgenesis constructs. Dev. Dyn. *236*, 3088–3099.

Lam, A.J., St-Pierre, F., Gong, Y., Marshall, J.D., Cranfill, P.J., Baird, M.A., McKeown, M.R., Wiedenmann, J., Davidson, M.W., Schnitzer, M.J., et al. (2012). Improving FRET dynamic range with bright green and red fluorescent proteins. Nature Methods *9*, 1005–1012.

Lampugnani, M.G. (2006). Vascular endothelial cadherin controls VEGFR-2 internalization and signaling from intracellular compartments. The Journal of Cell Biology *174*, 593–604.

Lampugnani, M.G., Orsenigo, F., Rudini, N., Maddaluno, L., Boulday, G., Chapon, F., and Dejana, E. (2010). CCM1 regulates vascular-lumen organization by inducing endothelial polarity. Journal of Cell Science *123*, 1073–1080.

Lampugnani, M.G., and Dejana, E. (2007). Adherens junctions in endothelial cells regulate vessel maintenance and angiogenesis. Thromb. Res. *120 Suppl 2*, S1–S6.

Lampugnani, M.G., Zanetti, A., Breviario, F., Balconi, G., Orsenigo, F., Corada, M., Spagnuolo, R., Betson, M., Braga, V., and Dejana, E. (2002). VE-cadherin regulates endothelial actin activating Rac and increasing membrane association of Tiam. Mol. Biol. Cell *13*, 1175–1189.

Larrivée, B., Freitas, C., Suchting, S., Brunet, I., and Eichmann, A. (2009). Guidance of vascular development: lessons from the nervous system. Circulation Research *104*, 428–441.

References

Lawson, N.D., and Weinstein, B.M. (2002a). In vivo imaging of embryonic vascular development using transgenic zebrafish. Developmental Biology *248*, 307–318.

Lawson, N.D., and Weinstein, B.M. (2002b). Arteries and veins: making a difference with zebrafish. Nat Rev Genet *3*, 674–682.

Lawson, N.D., Vogel, A.M., and Weinstein, B.M. (2002). sonic hedgehog and vascular endothelial growth factor act upstream of the Notch pathway during arterial endothelial differentiation. Developmental Cell *3*, 127–136.

LeBlanc, A.J., Krishnan, L., Sullivan, C.J., Williams, S.K., and Hoying, J.B. (2012). Microvascular repair: post-angiogenesis vascular dynamics. Microcirculation *19*, 676–695.

Lecuit, T., Lenne, P.-F., and Munro, E. (2011). Force generation, transmission, and integration during cell and tissue morphogenesis. Annu. Rev. Cell Dev. Biol. *27*, 157–184.

Lenard, A., Daetwyler, S., Betz, C., Ellertsdóttir, E., Belting, H.-G., Huisken, J., and Affolter, M. Endothelial Cell Self-Fusion During Vascular Pruning. Plos Biol *in press*.

Lenard, A., Ellertsdóttir, E., Herwig, L., Krudewig, A., Sauteur, L., Belting, H.-G., and Affolter, M. (2013). In vivo analysis reveals a highly stereotypic morphogenetic pathway of vascular anastomosis. Developmental Cell *25*, 492–506.

Leong, K.G., Hu, X., Li, L., Noseda, M., Larrivée, B., Hull, C., Hood, L., Wong, F., and Karsan, A. (2002). Activated Notch4 inhibits angiogenesis: role of beta 1-integrin activation. Molecular and Cellular Biology *22*, 2830–2841.

Leslie, J.D., Ariza-McNaughton, L., Bermange, A.L., McAdow, R., Johnson, S.L., and Lewis, J. (2007). Endothelial signalling by the Notch ligand Delta-like 4 restricts angiogenesis. Development *134*, 839–844.

Lewis, J. (1998). Notch signalling and the control of cell fate choices in vertebrates. Semin Cell Dev Biol *9*, 583–589.

Lewis, K.L., Caton, M.L., Bogunovic, M., Greter, M., Grajkowska, L.T., Ng, D., Klinakis, A., Charo, I.F., Jung, S., Gommerman, J.L., et al. (2011). Notch2 receptor signaling controls functional differentiation of dendritic cells in the spleen and intestine. Immunity *35*, 780–791.

Li, L., Wu, L.P., and Chandrasegaran, S. (1992). Functional domains in Fok I restriction endonuclease. Proc. Natl. Acad. Sci. U.S.a. *89*, 4275–4279.

Lu, X., le Noble, F., Yuan, L., Jiang, Q., De Lafarge, B., Sugiyama, D., Bréant, C., Claes, F., De Smet, F., Thomas, J.-L., et al. (2004). The netrin receptor UNC5B mediates guidance events controlling morphogenesis of the vascular system. Nature *432*, 179–186.

Lubarsky, B., and Krasnow, M.A. (2003). Tube morphogenesis: making and shaping biological tubes. Cell *112*, 19–28.

Luissint, A.-C., Nusrat, A., and Parkos, C.A. (2014). JAM-related proteins in mucosal homeostasis and inflammation. Semin Immunopathol *36*, 211–226.

Maître, J.-L., Berthoumieux, H., Krens, S.F.G., Salbreux, G., Jülicher, F., Paluch, E., and Heisenberg, C.-P. (2012). Adhesion functions in cell sorting by mechanically coupling the cortices of adhering cells. Science *338*, 253–256.

Mak, A.N.-S., Bradley, P., Cernadas, R.A., Bogdanove, A.J., and Stoddard, B.L. (2012). The crystal structure of TAL effector PthXo1 bound to its DNA target. Science *335*, 716–719.

Makanya, A.N., Hlushchuk, R., and Djonov, V.G. (2009). Intussusceptive angiogenesis and its role in vascular morphogenesis, patterning, and remodeling. Angiogenesis *12*, 113–123.

Mao, Z., Bozzella, M., Seluanov, A., and Gorbunova, V. (2008). DNA repair by nonhomologous end joining and homologous recombination during cell cycle in human cells. Cell Cycle *7*, 2902–2906.

McKee, R., Gerlach, G.F., Jou, J., Cheng, C.N., and Wingert, R.A. (2014). Temporal and spatial expression of tight junction genes during zebrafish pronephros development. Gene Expr. Patterns *16*, 104–113.

Meeker, N.D., Hutchinson, S.A., Ho, L., and Trede, N.S. (2007). Method for isolation of PCR-ready genomic DNA from zebrafish tissues. Biotech. *43*, 610–612–614.

Meng, X., Noyes, M.B., Zhu, L.J., Lawson, N.D., and Wolfe, S.A. (2008). Targeted gene inactivation in zebrafish using engineered zinc-finger nucleases. Nat Biotechnol *26*, 695–701.

Michael, M., and Yap, A.S. (2013). The regulation and functional impact of actin assembly at cadherin cell-cell adhesions. Semin Cell Dev Biol *24*, 298–307.

Michaelis, U.R. (2014). Mechanisms of endothelial cell migration. Cell. Mol. Life Sci. *71*, 4131–4148.

Miller, J., McLachlan, A.D., and Klug, A. (1985). Repetitive zinc-binding domains in the protein transcription factor IIIA from Xenopus oocytes. The EMBO Journal *4*, 1609–1614.

Miyoshi, J., and Takai, Y. (2008). Structural and functional associations of apical junctions with cytoskeleton. Biochim. Biophys. Acta *1778*, 670–691.

Moscou, M.J., and Bogdanove, A.J. (2009). A simple cipher governs DNA recognition by TAL effectors. Science *326*, 1501.

Nasdala, I., Wolburg-Buchholz, K., Wolburg, H., Kuhn, A., Ebnet, K., Brachtendorf, G., Samulowitz, U., Kuster, B., Engelhardt, B., Vestweber, D., et al. (2002). A transmembrane tight junction protein selectively expressed on endothelial cells and platelets. J. Biol. Chem. *277*, 16294–16303.

Nasevicius, A., and Ekker, S.C. (2000). Effective targeted gene "knockdown" in zebrafish. Nat. Genet. *26*, 216–220.

Navarro, P., Caveda, L., Breviario, F., Mândoteanu, I., Lampugnani, M.G., and Dejana, E. (1995). Catenin-dependent and -independent functions of vascular endothelial cadherin. J. Biol. Chem. *270*, 30965–30972.

Nelson, C.M., and Chen, C.S. (2003). VE-cadherin simultaneously stimulates and inhibits cell proliferation by altering cytoskeletal structure and tension. Journal of Cell Science *116*, 3571–3581.

Nelson, C.M., Pirone, D.M., Tan, J.L., and Chen, C.S. (2004). Vascular endothelial-cadherin regulates cytoskeletal tension, cell spreading, and focal adhesions by stimulating RhoA. Mol. Biol. Cell *15*, 2943–2953.

Nicoli, S., Ribatti, D., Cotelli, F., and Presta, M. (2007). Mammalian tumor xenografts induce neovascularization in zebrafish embryos. Cancer Research *67*, 2927–2931.

Ninov, N., Borius, M., and Stainier, D.Y.R. (2012). Different levels of Notch signaling regulate quiescence, renewal and differentiation in pancreatic endocrine progenitors. Development *139*, 1557–1567.

Nitta, T. (2003). Size-selective loosening of the blood-brain barrier in claudin-5-deficient mice. The Journal of Cell Biology *161*, 653–660.

O'Connor, M.N., Salles, I.I., Cvejic, A., Watkins, N.A., Walker, A., Garner, S.F., Jones, C.I., Macaulay, I.C., Steward, M., Zwaginga, J.-J., et al. (2009). Functional genomics in zebrafish permits rapid characterization of novel platelet membrane proteins. Blood *113*, 4754–4762.

Ohno, S. (2001). Intercellular junctions and cellular polarity: the PAR-aPKC complex,

a conserved core cassette playing fundamental roles in cell polarity. Curr. Opin. Cell Biol. *13*, 641–648.

Orsenigo, F., Giampietro, C., Ferrari, A., Corada, M., Galaup, A., Sigismund, S., Ristagno, G., Maddaluno, L., Koh, G.Y., Franco, D., et al. (2012). Phosphorylation of VE-cadherin is modulated by haemodynamic forces and contributes to the regulation of vascular permeability in vivo. Nat Commun *3*, 1208.

Otani, T., Ichii, T., Aono, S., and Takeichi, M. (2006). Cdc42 GEF Tuba regulates the junctional configuration of simple epithelial cells. The Journal of Cell Biology *175*, 135–146.

Ozawa, M., Ringwald, M., and Kemler, R. (1990). Uvomorulin-catenin complex formation is regulated by a specific domain in the cytoplasmic region of the cell adhesion molecule. Proc. Natl. Acad. Sci. U.S.a. *87*, 4246–4250.

Pagès, G., and Pouysségur, J. (2005). Transcriptional regulation of the Vascular Endothelial Growth Factor gene--a concert of activating factors. Cardiovascular Research *65*, 564–573.

Paladino, S., Lebreton, S., Tivodar, S., Campana, V., Tempre, R., and Zurzolo, C. (2008). Different GPI-attachment signals affect the oligomerisation of GPI-anchored proteins and their apical sorting. Journal of Cell Science *121*, 4001–4007.

Park, K.W., Morrison, C.M., Sorensen, L.K., Jones, C.A., Rao, Y., Chien, C.-B., Wu, J.Y., Urness, L.D., and Li, D.Y. (2003). Robo4 is a vascular-specific receptor that inhibits endothelial migration. Developmental Biology *261*, 251–267.

Park, M., Vittinghoff, E., Ganz, P., Peralta, C.A., Whooley, M., and Shlipak, M.G. (2014). Role of soluble endothelial cell-selective adhesion molecule biomarker in albuminuria and kidney function changes in patients with coronary artery disease: the Heart and Soul Study. Arteriosclerosis, Thrombosis, and Vascular Biology *34*, 231–236.

Patan, S. (1998). TIE1 and TIE2 receptor tyrosine kinases inversely regulate embryonic angiogenesis by the mechanism of intussusceptive microvascular growth. Microvascular Research *56*, 1–21.

Patel-Hett, S., and D'Amore, P.A. (2011). Signal transduction in vasculogenesis and developmental angiogenesis. Int. J. Dev. Biol. *55*, 353–363.

Pelton, J.C., Wright, C.E., Leitges, M., and Bautch, V.L. (2014). Multiple endothelial cells constitute the tip of developing blood vessels and polarize to promote lumen formation. Development *141*, 4121–4126.

Phng, L.K., and Gerhardt, H. (2009). Angiogenesis: a team effort coordinated by notch. Developmental Cell *16*, 196–208.

Phng, L.-K., Gebala, V., Bentley, K., Philippides, A., Wacker, A., Mathivet, T., Sauteur, L., Stanchi, F., Belting, H.-G., Affolter, M., et al. (2015). Formin-mediated actin polymerization at endothelial junctions is required for vessel lumen formation and stabilization. Developmental Cell *32*, 123–132.

Phng, L.-K., Potente, M., Leslie, J.D., Babbage, J., Nyqvist, D., Lobov, I., Ondr, J.K., Rao, S., Lang, R.A., Thurston, G., et al. (2009). Nrarp Coordinates Endothelial Notch and Wnt Signaling to Control Vessel Density in Angiogenesis. Developmental Cell *16*, 70–82.

Phng, L.-K., Stanchi, F., and Gerhardt, H. (2013). Filopodia are dispensable for endothelial tip cell guidance. Development *140*, 4031–4040.

Puri, M.C., Rossant, J., Alitalo, K., Bernstein, A., and Partanen, J. (1995). The receptor tyrosine kinase TIE is required for integrity and survival of vascular endothelial cells. The EMBO Journal *14*, 5884–5891.

Quillien, A., Moore, J.C., Shin, M., Siekmann, A.F., Smith, T., Pan, L., Moens, C.B., Parsons, M.J., and Lawson, N.D. (2014). Distinct Notch signaling outputs pattern the developing arterial system. Development *141*, 1544–1552.

Ramirez, C.L., Foley, J.E., Wright, D.A., Müller-Lerch, F., Rahman, S.H., Cornu, T.I., Winfrey, R.J., Sander, J.D., Fu, F., Townsend, J.A., et al. (2008). Unexpected failure rates for modular assembly of engineered zinc fingers. Nature Methods *5*, 374–375.

Ratheesh, A., and Yap, A.S. (2012). A bigger picture: classical cadherins and the dynamic actin cytoskeleton. Nat. Rev. Mol. Cell Biol. *13*, 673–679.

Ren, X., Yang, Z., Xu, J., Sun, J., Mao, D., Hu, Y., Yang, S.-J., Qiao, H.-H., Wang, X., Hu, Q., et al. (2014). Enhanced Specificity and Efficiency of the CRISPR/Cas9 System with Optimized sgRNA Parameters in Drosophila. Cell Rep *9*, 1151–1162.

Reyon, D., Tsai, S.Q., Khayter, C., Foden, J.A., Sander, J.D., and Joung, J.K. (2012). FLASH assembly of TALENs for high-throughput genome editing. Nat Biotechnol *30*, 460–465.

Ribatti, D., and Crivellato, E. (2012). "Sprouting angiogenesis," a reappraisal. Developmental Biology *372*, 157–165.

Riedl, J., Crevenna, A.H., Kessenbrock, K., Yu, J.H., Neukirchen, D., Bista, M., Bradke, F., Jenne, D., Holak, T.A., Werb, Z., et al. (2008). Lifeact: a versatile marker to visualize F-actin. Nature Methods *5*, 605–607.

Rohatgi, A., Owens, A.W., Khera, A., Ayers, C.R., Banks, K., Das, S.R., Berry, J.D., McGuire, D.K., and de Lemos, J.A. (2009). Differential associations between soluble cellular adhesion molecules and atherosclerosis in the Dallas Heart Study: a distinct role for soluble endothelial cell-selective adhesion molecule. Arteriosclerosis, Thrombosis, and Vascular Biology *29*, 1684–1690.

Rojas, R., Ruiz, W.G., Leung, S.M., Jou, T.S., and Apodaca, G. (2001). Cdc42-dependent modulation of tight junctions and membrane protein traffic in polarized Madin-Darby canine kidney cells. Mol. Biol. Cell *12*, 2257–2274.

Sander, J.D., and Joung, J.K. (2014). CRISPR-Cas systems for editing, regulating and targeting genomes. Nat Biotechnol *32*, 347–355.

Sander, J.D., Cade, L., Khayter, C., Reyon, D., Peterson, R.T., Joung, J.K., and Yeh, J.-R.J. (2011a). Targeted gene disruption in somatic zebrafish cells using engineered TALENs. Nat Biotechnol *29*, 697–698.

Sander, J.D., Dahlborg, E.J., Goodwin, M.J., Cade, L., Zhang, F., Cifuentes, D., Curtin, S.J., Blackburn, J.S., Thibodeau-Beganny, S., Qi, Y., et al. (2011b). Selection-free zinc-finger-nuclease engineering by context-dependent assembly (CoDA). Nature Methods *8*, 67–69.

Santos, M.E., Braasch, I., Boileau, N., Meyer, B.S., Sauteur, L., Böhne, A., Belting, H.-G., Affolter, M., and Salzburger, W. (2014). The evolution of cichlid fish egg-spots is linked with a cis-regulatory change. Nat Commun *5*, 5149.

Sauteur, L., Krudewig, A., Herwig, L., Ehrenfeuchter, N., Lenard, A., Affolter, M., and Belting, H.-G. (2014). Cdh5/VE-cadherin Promotes Endothelial Cell Interface Elongation via Cortical Actin Polymerization during Angiogenic Sprouting. Cell Rep *9*, 504–513.

Schuermann, A., Helker, C.S.M., and Herzog, W. (2014). Angiogenesis in zebrafish. Semin Cell Dev Biol *31*, 106–114.

Schulte-Merker, S., and Stainier, D.Y.R. (2014). Out with the old, in with the new: reassessing morpholino knockdowns in light of genome editing technology. Development *141*, 3103–3104.

Scott, J.N.F., Kupinski, A.P., and Boyes, J. (2014). Targeted genome regulation and

modification using transcription activator-like effectors. Febs J. *281*, 4583–4597.

Seruggia, D., and Montoliu, L. (2014). The new CRISPR-Cas system: RNA-guided genome engineering to efficiently produce any desired genetic alteration in animals. Transgenic Res. *23*, 707–716.

Sessa, R., Seano, G., di Blasio, L., Gagliardi, P.A., Isella, C., Medico, E., Cotelli, F., Bussolino, F., and Primo, L. (2012). The miR-126 regulates angiopoietin-1 signaling and vessel maturation by targeting p85β. Biochim. Biophys. Acta *1823*, 1925–1935.

Siekmann, A.F., Affolter, M., and Belting, H.-G. (2013). The tip cell concept 10 years after: new players tune in for a common theme. Experimental Cell Research *319*, 1255–1263.

Smutny, M., and Yap, A.S. (2010). Neighborly relations: cadherins and mechanotransduction. The Journal of Cell Biology *189*, 1075–1077.

Smutny, M., Cox, H.L., Leerberg, J.M., Kovacs, E.M., Conti, M.A., Ferguson, C., Hamilton, N.A., Parton, R.G., Adelstein, R.S., and Yap, A.S. (2010). Myosin II isoforms identify distinct functional modules that support integrity of the epithelial zonula adherens. Nat Cell Biol *12*, 696–702.

Spindler, V., Schlegel, N., and Waschke, J. (2010). Role of GTPases in control of microvascular permeability. Cardiovascular Research *87*, 243–253.

Stalker, T.J., Wu, J., Morgans, A., Traxler, E.A., Wang, L., Chatterjee, M.S., Lee, D., Quertermous, T., Hall, R.A., Hammer, D.A., et al. (2009). Endothelial cell specific adhesion molecule (ESAM) localizes to platelet-platelet contacts and regulates thrombus formation in vivo. J. Thromb. Haemost. *7*, 1886–1896.

Stone, J., Itin, A., Alon, T., Pe'er, J., Gnessin, H., Chan-Ling, T., and Keshet, E. (1995). Development of retinal vasculature is mediated by hypoxia-induced vascular endothelial growth factor (VEGF) expression by neuroglia. J. Neurosci. *15*, 4738–4747.

Streubel, J., Blücher, C., Landgraf, A., and Boch, J. (2012). TAL effector RVD specificities and efficiencies. Nat Biotechnol *30*, 593–595.

Strilić, B., Eglinger, J., Krieg, M., Zeeb, M., Axnick, J., Babál, P., Müller, D.J., and Lammert, E. (2010). Electrostatic Cell-Surface Repulsion Initiates Lumen Formation in Developing Blood Vessels. Curr. Biol. *20*, 2003–2009.

Strilić, B., KuCera, T., Eglinger, J., Hughes, M.R., McNagny, K.M., Tsukita, S., Dejana, E., Ferrara, N., and Lammert, E. (2009). The molecular basis of vascular lumen formation in the developing mouse aorta. Developmental Cell *17*, 505–515.

Struhl, G., and Adachi, A. (1998). Nuclear access and action of notch in vivo. Cell *93*, 649–660.

Summerton, J., and Weller, D. (1997). Morpholino antisense oligomers: design, preparation, and properties. Antisense Nucleic Acid Drug Dev. *7*, 187–195.

Suri, C., Jones, P.F., Patan, S., Bartunkova, S., Maisonpierre, P.C., Davis, S., Sato, T.N., and Yancopoulos, G.D. (1996). Requisite role of angiopoietin-1, a ligand for the TIE2 receptor, during embryonic angiogenesis. Cell *87*, 1171–1180.

Taddei, A., Giampietro, C., Conti, A., Orsenigo, F., Breviario, F., Pirazzoli, V., Potente, M., Daly, C., Dimmeler, S., and Dejana, E. (2008). Endothelial adherens junctions control tight junctions by VE-cadherin-mediated upregulation of claudin-5. Nat Cell Biol *10*, 923–934.

Tammela, T., Zarkada, G., Nurmi, H., Jakobsson, L., Heinolainen, K., Tvorogov, D., Zheng, W., Franco, C.A., Murtomäki, A., Aranda, E., et al. (2011). VEGFR-3 controls tip to stalk conversion at vessel fusion sites by reinforcing Notch signalling. Nat Cell Biol *13*, 1202–1213.

Thisse, B., Wright, J.G., Thisse, C., and C (2008). Embryonic and Larval Expression Patterns from a Large Scale Screening for Novel Low Affinity Extracellular Protein Interactions (ZFIN Direct Data Submission (http://zfin.org)).

Thisse, B., and Thisse, C. (2014). In situ hybridization on whole-mount zebrafish embryos and young larvae. Methods Mol. Biol. *1211*, 53–67.

Thummel, R., Bailey, T.J., and Hyde, D.R. (2011). In vivo electroporation of morpholinos into the adult zebrafish retina. JoVE e3603.

Torregroza, I., Holtzinger, A., Mendelson, K., Liu, T.-C., Hla, T., and Evans, T. (2012). Regulation of a vascular plexus by gata4 is mediated in zebrafish through the chemokine sdf1a. PLoS ONE *7*, e46844.

Torres-Vázquez, J., Gitler, A.D., Fraser, S.D., Berk, J.D., Van N Pham, Fishman, M.C., Childs, S., Epstein, J.A., and Weinstein, B.M. (2004). Semaphorin-plexin signaling guides patterning of the developing vasculature. Developmental Cell *7*, 117–123.

Tu, T., Zhang, C., Yan, H., Luo, Y., Kong, R., Wen, P., Ye, Z., Chen, J., Feng, J., Liu, F., et al. (2015). CD146 acts as a novel receptor for netrin-1 in promoting angiogenesis and vascular development. Cell Res. Epub ahead of print.

Urnov, F.D., Rebar, E.J., Holmes, M.C., Zhang, H.S., and Gregory, P.D. (2010). Genome editing with engineered zinc finger nucleases. Nat Rev Genet *11*, 636–646.

Valton, J., Dupuy, A., Daboussi, F., Thomas, S., Maréchal, A., Macmaster, R., Melliand, K., Juillerat, A., and Duchateau, P. (2012). Overcoming transcription activator-like effector (TALE) DNA binding domain sensitivity to cytosine methylation. J. Biol. Chem. *287*, 38427–38432.

van Hinsbergh, V.W.M., and Koolwijk, P. (2008). Endothelial sprouting and angiogenesis: matrix metalloproteinases in the lead. Cardiovascular Research *78*, 203–212.

van Impel, A., Zhao, Z., Hermkens, D.M.A., Roukens, M.G., Fischer, J.C., Peterson-Maduro, J., Duckers, H., Ober, E.A., Ingham, P.W., and Schulte-Merker, S. (2014). Divergence of zebrafish and mouse lymphatic cell fate specification pathways. Development *141*, 1228–1238.

Vasioukhin, V., and Fuchs, E. (2001). Actin dynamics and cell-cell adhesion in epithelia. Curr. Opin. Cell Biol. *13*, 76–84.

Vincent, P.A., Xiao, K., Buckley, K.M., and Kowalczyk, A.P. (2004). VE-cadherin: adhesion at arm's length. Am. J. Physiol., Cell Physiol. *286*, C987–C997.

Wegmann, F., Ebnet, K., Pasquier, Du, L., Vestweber, D., and Butz, S. (2004). Endothelial adhesion molecule ESAM binds directly to the multidomain adaptor MAGI-1 and recruits it to cell contacts. Experimental Cell Research *300*, 121–133.

Wegmann, F., Petri, B., Khandoga, A.G., Moser, C., Khandoga, A., Volkery, S., Li, H., Nasdala, I., Brandau, O., Fassler, R., et al. (2006). ESAM supports neutrophil extravasation, activation of Rho, and VEGF-induced vascular permeability. J. Exp. Med. *203*, 1671–1677.

Westerfield, M. (2000). The Zebrafish Book. A guide for the laboratory use of zebrafish (Danio rerio). 4th Ed., Univ. of Oregon Press, Eugene.

Wiley, D.M., Kim, J.-D., Hao, J., Hong, C.C., Bautch, V.L., and Jin, S.-W. (2011). Distinct signalling pathways regulate sprouting angiogenesis from the dorsal aorta and the axial vein. Nat Cell Biol *13*, 686–692.

Wilkinson, R.N., Elworthy, S., Ingham, P.W., and van Eeden, F.J.M. (2013). A method for high-throughput PCR-based genotyping of larval zebrafish tail biopsies. Biotech. *55*, 314–316.

References

Williams, C.K., Li, J.-L., Murga, M., Harris, A.L., and Tosato, G. (2006). Up-regulation of the Notch ligand Delta-like 4 inhibits VEGF-induced endothelial cell function. Blood *107*, 931–939.

Wong, K.S., Proulx, K., Rost, M.S., and Sumanas, S. (2009). Identification of vasculature-specific genes by microarray analysis of etsrp/etv2 overexpressing zebrafish embryos. Dev. Dyn. *238*, 1836–1850.

Wu, X., Scott, D.A., Kriz, A.J., Chiu, A.C., Hsu, P.D., Dadon, D.B., Cheng, A.W., Trevino, A.E., Konermann, S., Chen, S., et al. (2014). Genome-wide binding of the CRISPR endonuclease Cas9 in mammalian cells. Nat Biotechnol *32*, 670–676.

Yamazaki, D., Oikawa, T., and Takenawa, T. (2007). Rac-WAVE-mediated actin reorganization is required for organization and maintenance of cell-cell adhesion. Journal of Cell Science *120*, 86–100.

Yarar, D., Waterman-Storer, C.M., and Schmid, S.L. (2005). A dynamic actin cytoskeleton functions at multiple stages of clathrin-mediated endocytosis. Mol. Biol. Cell *16*, 964–975.

Yokota, T., Oritani, K., Butz, S., Kokame, K., Kincade, P.W., Miyata, T., Vestweber, D., and Kanakura, Y. (2009). The endothelial antigen ESAM marks primitive hematopoietic progenitors throughout life in mice. Blood *113*, 2914–2923.

Zygmunt, T., Gay, C.M., Blondelle, J., Singh, M.K., Flaherty, K.M., Means, P.C., Herwig, L., Krudewig, A., Belting, H.-G., Affolter, M., et al. (2011). Semaphorin-PlexinD1 signaling limits angiogenic potential via the VEGF decoy receptor sFlt1. Developmental Cell *21*, 301–314.